A single-photon subtractor for spectrally multimode quantum states

Clément Jacquard

To cite this version:

Clément Jacquard. A single-photon subtractor for spectrally multimode quantum states. Optics [physics.optics]. Université Pierre et Marie Curie - Paris VI, 2017. English. NNT : 2017PA066155 . tel-01646428

HAL Id: tel-01646428
https://theses.hal.science/tel-01646428

Submitted on 23 Nov 2017

Thèse de doctorat de
l'Université Pierre et Marie Curie

présentée par

Clément Jacquard

pour obtenir le grade de Docteur de l'Université Pierre et Marie Curie
sur le sujet:

Soustracteur de photons uniques pour états quantiques multimode dans le domaine spectral

A single-photon subtractor for spectrally multimode quantum states

Membres du jury :

Pr. Rosa TUALLE-BROURI	Rapporteur
Dr. Marco BELLINI	Rapporteur
Pr. Akira FURUSAWA	Membre du jury
Pr. Agnès MAÎTRE	Membre du jury
Pr. Claude FABRE	Membre invité
Pr. Nicolas TREPS	Directeur de thèse

This page is reserved for latter use.

Contents

Introduction

At the heart of the scientific method lies the capability to evaluate the physical properties of nature through a quantitative measurement. In this context, an observer performs a targeted experiment that aims at isolating a physical phenomenon reduced to its core constituent. The common trait of every experiment is that while some preliminary work may be required by the observer, the process invariably ends with a measurement and an interpretation of its outcome. Light has been a medium of choice to understand the inner workings of reality much before the exact nature of light itself was sufficiently understood.

In particular, light has long been used to perform measurements sometimes leading to astonishing conclusions. Around 240 BC, the solar system and the concept of light still belonged to vague philosophical discussions at the margins. It did not stop Eratosthenes to estimate the Earth's radius with a 15% error from a simple geometric measurement and the sole assumption that Earth was a perfect sphere. In 1615, after having imaged the moons of Jupiter, Galileo is found "vehemently suspect of heresy" and arrested for defending an heliocentric system. The question of the finite speed of light remained in limbos after passing from the Greeks to early Islamic philosophers and late-seventeenth century scientists. Still, in 1675, Danish astronomer Ole Rømer used the eclipses of the Jupiter moon Io to come up with a measurement allowing him to evaluate the finite speed of light within 25% accuracy. It is worth stating that with the inherent limitations due to the technology available at those times, both outcomes mostly suffered from poorly measured or ill-defined distances they used as references.

Around the same period as the discovery of Rømer, Isaac Newton used a geometrical description of optics where light is composed of straight rays. The description of light as a wave appeared in 1803 when Thomas Young observed an interference pattern formed by light blocked by a narrow object. This representation is generalized in the middle of the nineteenth century, when James Clerk Maxwell elaborated a set of four famous equations describing the behavior of electromagnetic radiation. Using this description, Albert A. Michelson and Edward Morley failed to measure the motion of *luminiferous aether* in what is often referred to as the "most successful failed experiment" as it has spurred the community to elaborate alternative theories. Michelson soon realized that the extremely sensitive interference-based measurement they used was well suited for astronomical measurements [Michelson 94b] and to define standards in space and time from the wavelength of the light emitted by atomic transitions [Michelson 94a].

On the technical side, the nineteenth century is synonymous with the development of photographic plates allowing for the first time to fix images produced by advanced optical system. Those plates played a tremendous role in the development of experimental physics, as they allowed to detect phenomena never seen so far such as single particles decaying in cloud chambers [Anderson 33]. In 1909, Geoffrey I. Taylor used those plates in another “failed” experiment where he recorded the interference pattern in the shadow of a needle placed before a gas flame [Taylor 09]. He expected the interference pattern to fade out with extreme attenuation of the light as the quanta of energy would be reduced down to a single one, supposedly unable to interfere with any other, or itself. The pattern did not fade out, Taylor observed the interference of an extremely attenuated coherent state but still lacked the theoretical framework to know it so he set an upper bound on the amount of energy carried by a quantum of light. Physicists will wait seventy years to see an electron interfere with itself [Merli 76] and ten years more until a photon finally interferes with itself [Grangier 86].

Since the beginning of the twentieth century, quantum mechanics has been a reliable theoretical platform to model the behaviors of atoms, photons and their interactions. The invention of the laser in 1960 by Theodore H. Maiman has allowed physicists to create spatially and temporally coherent light and along with the progress made in material sciences, to use light as a measurement tool but also as a probe of light-matter interaction and the fundamentals of quantum mechanics, to manipulate atoms, etch materials and eventually seed thousands of applications in every engineering field from optical telecommunications to medical sciences.

Today, light is understood as a quantized electromagnetic radiation carrying one of the four fundamental interactions known by modern physics. The core activity in quantum optics consists in engineering the quantum states of light to create new breakthrough applications [O’Brien 09]. Because of the laws of quantum mechanics, light is thought of as a promising tool to distribute and process information better than the current classical schemes. Still, the intrinsic nature of light gives it advantages and downsides to perform different tasks. Its ever-propagating character makes it ideal to convey information but extremely challenging to store. The feeble interaction of the quanta composing it with the electromagnetic environment makes light robust to decoherence but equally hard to manipulate at will.

In this thesis, we aim at performing a genuinely selective and pure quantum operation at the single-photon level on an assembly of many quantum harmonic oscillators. Our approach is made possible by the recent developments in ultrafast optics. We have chosen ultrafast light as a platform to generate a spectrally multimode quantum state and ultrafast pulse shaping as a tool to measure and manipulate it.

Multimode quantum states have been generated previously using linear optics to mix together single-mode quantum states that were once spatially separated [Su 07, Yukawa 08]. This approach works and has led to great advances in the engineering of highly entangled multipartite states. But mixing spatially separated quantum states via linear optics lacks reconfigurability and the number of physical resources required (including PhD students) scales linearly with respect to the number of parties desired. If any quantum state of light is to be used to convey and process information in the form of quantum bits (qubits), or their higher dimensional counterpart known as qudits, they would be required in hundreds if not thousands just as in a traditional computer that uses billions of bits. It becomes necessary to find a way to easily scale up the production of the desired quantum states. Another successful approach has been developed based on continuous wave lasers and acousto-optic modulators [Chen 14].

Among the many states with high potential are squeezed quantum states of light. State of the arts generation of squeezed states includes different optical wavelengths in the optical spectrum [Baune 15] in the near infrared [Mehmet 10], at telecom wavelengths [Mehmet 11] and an ever-increasing amount of squeezing [Vahlbruch 16]. They constitute an important resource for high-precision measurements aiming at overcoming the standard quantum limit in, for instance, gravitational wave detection [Aasi 13] but also in the field of quantum information to perform various tasks such as teleportation, quantum cryptography, and distribution of entanglement in quantum computation networks [Furusawa 11].

Nevertheless, advances in the field of quantum information has highlighted that quantum states possessing Gaussian statistics, including squeezed states, are no sufficient resource to outperform classical resources and algorithms. Indeed, Gaussian statistics are synonymous of positive probability distributions, such as the Wigner function, and can efficiently be simulated and sampled by classical means. Additional quantum states exhibiting genuine quantum features such as non-classical statistics through the negativity of their Wigner function are required. Single photons are probably the best candidates that meet the requirements. While they remain difficult to create deterministically with sufficient purity, progress have been made toward that goal [Yoshikawa 13, Somaschi 15]. Still, performing a single-photon subtraction on a squeezed state is also known to create strongly negative Wigner functions [Nielsen 07].

Hence, the next step after the generation of any quantum state of light, and especially squeezed states, is to manipulate them with a genuine quantum operation at the level of the quantum such as single-photon subtraction or addition. Single-photon subtraction for instance has been widely used until today to probe quantum mechanics rules [Parigi 07], generate entanglement between different spatial or temporal modes [Ourjoumtsev 09, Takahashi 08], distillate entanglement [Takahashi 09, Ourjoumtsev 07a], generate superpositions of Fock states [Yukawa 13] and create hybrid entanglement [Morin 14b]. The problem of extending the technique previously used for single-photon subtraction is that it fails to address selectively a multimode quantum states generated in a scalable fashion. A new technique is required and this is what this thesis is about.

In the following chapters, we relate the study, design, construction and characterization of a single-photon subtractor, also known as the Quantum Pulse Gate (QPG) [Eckstein 11], meant to manipulate a spectrally multimode light field in a pure, selective and tunable fashion. This device is based on sum-frequency generation, ultrafast pulse shaping and single-photon detection and could eventually be performed an arbitrary number of times as proposed in [Huang 13].

This thesis is organized as followed. In the first chapter, we introduce a limited number of concepts of multimode quantum optics that we will use. In the second chapter, we describe a source of spectrally multimode squeezed vacuum that motivates the construction of a mode-selective single-photon subtractor. In the third chapter, we explain how a spectrally multimode quantum states can be analyzed with an homodyne detection enhanced by ultrafast pulse-shaping capabilities and we present the results of the analysis of our mutlimode squeezed vacuum. In the fourth chapter, we develop a theoretical framework for multimode single-photon subtraction and we apply it to spectrally multimode light. In the fifth chapter, we present our implementation of the single-photon subtraction, mention the problem related to mixing bright and low-power beams in the same optical setup and describe the solutions we have found to isolate the heralding signal from noise. In the sixth chapter, we present the results of a process tomography where we probe the single-photon subtractor to reveal the subtraction mode and assess the purity of the process.

Part I

Context and Tools

Chapter 1

Not an Introduction to Multimode Quantum Optics

> *[About me, miserably starting to write the present thesis in the darkness of the lab]*
> *“Almost done man! Almost done! (evil laughter)”*
>
> – Syamsundar “*Super Syam*” De

Contents

This chapter does not pretend to be a rigorous and thorough introduction to multimode quantum optics. The reader should consult [Grynberg 10, Walls 08, Vogel 06] for a full understanding of quantum optics. We also recommend [Thiel 15], [Morin 14a], and [Brecht 14a] as helpful PhD thesis giving good insights into multimode ultrafast optics, quantum optics and frequency conversion processes respectively.
In this chapter, we simply introduce some concepts proven useful to the understanding of the current work.

The first section defines different concepts and tools of quantum optics along with their notations. The second one will explain the nature of an optical mode and how optical process can be multimode. We will also extend the concepts developed in the first section in the multimode case.

1.1 Elements of quantum optics

1.1.1 The quantized electric field

Quantum optics describes the nature and the evolution of the electromagnetic radiation by quantizing the accessible levels of energy. In particular, the electric field is used to model the evolution of light and its interaction with various media. It is usually described in the space time basis at position $\boldsymbol{r}$ and time t. Since the electric field is an observable in the sense of quantum mechanics, it is described by an Hermitian operator $\hat{\mathbf{E}}$ and represented as a sum of a complex part $\hat{\mathbf{E}}^{(+)}$ (the analytic signal) and its Hermitian conjugate $\hat{\mathbf{E}}^{(-)}$:

$$\hat{\mathbf{E}}(\boldsymbol{r},t) = \hat{\mathbf{E}}^{(+)}(\boldsymbol{r},t) + \hat{\mathbf{E}}^{(-)}(\boldsymbol{r},t) \tag{1.1}$$

To obtain the expression of $\hat{\mathbf{E}}(\boldsymbol{r},t)$, we consider the energy of the field to be contained in an arbitrary volume V and we focus on the field in a single mode $\boldsymbol{u}$ in this volume. We calculate the expression of the Hamiltonian H of the field as if the field was classical through Maxwell's equations. In this mode, the Hamiltonian of the field is the one of an harmonic oscillator and satisfies the fundamental system of equations of the Hamiltonian mechanics thus introducing a pair of conjugate canonical variables of the Hamiltonian X and P. The quantization process turns the Hamiltonian into:

$$\hat{H} = \hbar\omega\left(\hat{a}^{\dagger}\hat{a} + \frac{1}{2}\right) \tag{1.2}$$

where $\hat{a}$ and $\hat{a}^\dagger$ are the annihilation and creation operator of the field and can be seen as the quantized counterpart of the field complex amplitude and its conjugate. Those operators always satisfy:

$$\left[\hat{a}, \hat{a}^\dagger\right] = 1 \tag{1.3}$$

The quantization process also turns X and P into a pair of Hermitian operators $\hat{X}$ and $\hat{P}$. Those operators are the field quadrature operators. In what is known in quantum optics as *Continuous Variables* (CV)[Lloyd 99, Furusawa 11], the information is encoded in the fluctuations of the field quadrature operators. The field quadratures are usually measured with an homodyne detection (see chapter 3). For vacuum, the field quadratures exhibit the same amount of fluctuations, known as *shot noise* in the context of homodyne measurement. For the experimental physicist in continuous variables, it constitutes a reference level for any other measurement, especially for the phase-dependent fluctuations of a squeezed vacuum state. For this reason, we denote σ_0 the standard deviation of the quadrature operators $\hat{X}$ and $\hat{P}$ associated to the fluctuations of vacuum:

$$\langle 0|\hat{X}^2|0\rangle = \langle 0|\hat{P}^2|0\rangle = \sigma_0^2 \tag{1.4}$$

With those definitions in mind, the expressions of $\hat{X}$, $\hat{P}$ and $\left[\hat{X}, \hat{P}\right]$ are:

$$\begin{cases} \hat{X} & = \sigma_0 \left(\hat{a} + \hat{a}^\dagger\right) \\ \hat{P} & = i\sigma_0 \left(\hat{a}^\dagger - \hat{a}\right) \end{cases} \quad \text{and} \quad \left[\hat{X}, \hat{P}\right] = 2i\sigma_0^2 \tag{1.5}$$

Many conventions exist in the literature regarding the value of the variance of vacuum σ_0^2 depending on the definitions of $\hat{X}$ and $\hat{P}$. This plethora of conventions leads to potential confusion when comparing even basic formulas. In the following sections and chapters, we try to keep σ_0 explicitly. If not, the reader should assume that for the sake of simplicity, everything is defined with $\sigma_0 = 1$.

Finally, a field constant $\mathscr{E}^{(1)}$ is introduced to link the annihilation operator and the field. The expression of the analytic signal $\hat{\mathbf{E}}^{(+)}$ decouples the temporal and spatial dependencies to satisfy Maxwell's equations:

$$\hat{\mathbf{E}}^{(+)}(\boldsymbol{r}, t) = \mathscr{E}^{(1)} \hat{a} \boldsymbol{u}(\boldsymbol{r}, t) \quad \text{with} \quad \mathscr{E}^{(1)} = \sqrt{\frac{\hbar\omega}{2\epsilon_0 V}} \tag{1.6}$$

where ϵ_0 is the permittivity of vacuum and $\hbar$ is the reduced Planck constant. Expression 1.6 is the starting point of quantum optics. It is very common to choose $\boldsymbol{u}$ to be a plane wave of wave vector $\mathbf{k}$ and frequency $\omega = c|\mathbf{k}|$ with c the speed of light in vacuum so that:

$$\boldsymbol{u}(\boldsymbol{r}, t) = \frac{1}{\sqrt{V}} e^{i(\mathbf{k}\boldsymbol{r} - \omega t)} \tag{1.7}$$

1.1.2 Quantum states of interests

In this work, we mainly focus on coherent states [Glauber 63] denoted $|\alpha\rangle$, single-photon states denoted $|1\rangle$ and squeezed vacuum states denoted $|\sigma\rangle$.
Fock states denoted $|n\rangle$ are the quantized level of excitation of the electric field. While particularly challenging to produce experimentally for arbitrary values of n, they form a convenient normalized basis of quantum states for theoretical discussions. Among them, the single-photon state is a single quantum of excitation of the electromagnetic field and is obtained formally by applying the creation operator $\hat{a}^\dagger$ on vacuum: $\hat{a}^\dagger|0\rangle = |1\rangle$.

A coherent state is the superposition of Fock states being an eigenstate of the annihilation operator: $\hat{a}|\alpha\rangle = \alpha|\alpha\rangle$. It is obtained by application of the displacement operator $\hat{D} = \exp[\alpha\hat{a}^\dagger - \alpha^*\hat{a}]$ on vacuum:

$$|\alpha\rangle = \hat{D}|0\rangle = e^{\alpha\hat{a}^\dagger}|0\rangle = e^{|\alpha|^2/2}\sum_{n\geq 0}\frac{\alpha^n}{\sqrt{n!}}|n\rangle \tag{1.8}$$

It is the quantum state whose properties are the closest to the classical description of light. It is generally used to represent the quantum state of light produced by a laser. Interestingly, the noise of the field quadratures for this state is equal to the ones of vacuum, i.e. σ_0^2.

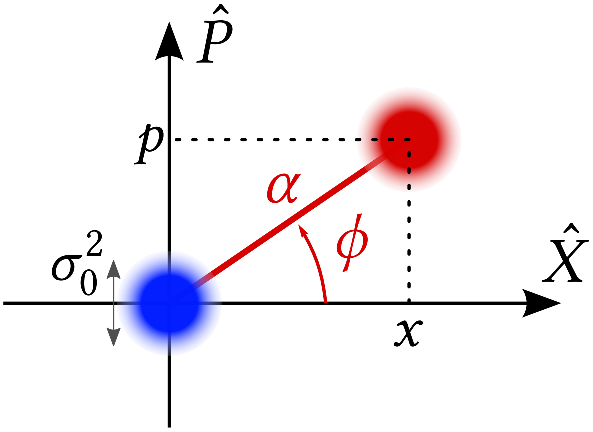

Figure 1.1: Phase space with the $\hat{X}$ and $\hat{P}$ quadratures with vacuum state (blue) and a coherent state (red) of amplitude α and phase ϕ. The coherent state can be localized in the phase space with its coordinate x and p along the $\hat{X}$ and $\hat{P}$ quadratures.

1.1.2.1 Squeezed vacuum states

As we will see in the next chapter, we will deal extensively with squeezed vacuum states $|\xi\rangle$ where $|\xi = 0\rangle$ is the vacuum state. A squeezed vacuum state is obtained by applying the squeezing operator $\hat{S}(\xi)$ to vacuum. It is defined as:

$$\hat{S}(\xi) = \exp\left[\xi\left(\hat{a}^2 - \hat{a}^{\dagger 2}\right)/\,2\right] \tag{1.9}$$

where for the sake of simplicity $\xi \in \mathbb{R}$. In the Heisenberg picture, the temporal evolution of the annihilation operator $\hat{a}$ through squeezing obeys:

$$\frac{\mathrm{d}\hat{a}}{\mathrm{d}t} = \frac{i}{\hbar}\left[\hat{H}_S, \hat{a}\right] = -\zeta\hat{a} \quad \text{where} \quad \hat{H}_S = i\hbar\frac{\zeta}{2}\left(\hat{a}^2 - \hat{a}^{\dagger 2}\right) \quad \text{and} \quad \zeta = \xi/t_{int} \tag{1.10}$$

where t_{int} is an interaction time during which the evolution trough $\hat{H}_S$ gives $\hat{S}(\xi)$ as the evolution operator. The quadratic Hamiltonian $\hat{H}_S$ associated to the squeezing operator leads to a unitary evolution of $\hat{a}$. In that picture, a squeezed vacuum state $|\xi\rangle = \hat{S}(\xi)|0\rangle$ should be understood as a squeeze and a stretch of the phase space (presented on figure 1.1) under a unitary transformation. When applied to vacuum, the expression of $\hat{S}(\xi)$ simplifies [Vogel 06]:

$$|\xi\rangle = \hat{S}(\xi)|0\rangle = \frac{1}{\sqrt{\mathrm{ch}\,(\xi)}}\exp\left(-\frac{\mathrm{th}(\xi)}{2}\hat{a}^{\dagger 2}\right)|0\rangle = \frac{1}{\sqrt{\mathrm{ch}\,(\xi)}}\sum_{n\geq 0}\left(-\frac{\mathrm{th}(\xi)}{2}\right)^n\frac{\sqrt{(2n)!}|2n\rangle}{n!} \tag{1.11}$$

This quantum state is of particular interest as the field quadratures exhibit quantum fluctuations below and above the shot noise. Indeed, using the properties of the squeezing operator $\hat{S}(\xi)$ and its action on the annihilation and creation operators $\hat{a}$ and $\hat{a}^\dagger$ (see e.g [Walls 08]), we can compute the variance of $\hat{X}$ and $\hat{P}$ for a squeezed vacuum state:

$$V_X = \langle\xi|\hat{X}^2|\xi\rangle = \sigma_0^2 e^{-2\xi} \tag{1.12}$$

$$V_P = \langle\xi|\hat{P}^2|\xi\rangle = \sigma_0^2 e^{2\xi} \tag{1.13}$$

Depending on the value of ξ, one quadrature of the field undergoes a reduction of its noise while the other one sees its noise increase according to the Heisenberg inequality:

$$\sqrt{V_X V_P} = \sigma_0^2 \tag{1.14}$$

An experimental Physicist often evaluates a squeezed state with the value of its variance below vacuum in decibels V_{dB}:

$$V_{dB} = 10\log_{10}\left(\frac{V_X}{\sigma_0^2}\right) \tag{1.15}$$

The generation of those states has been first demonstrated in [Wu 86, Slusher 87] and the maximum squeezing obtained has kept on growing to reach significant levels [Vahlbruch 16] as ambitious application are developed [Chua 14].

One last state of interest in quantum optics is the thermal state for which we need to introduce the density matrix.

1.1.3 The density matrix

The density matrix $\hat{\rho}$ is a key tool in describing quantum systems. The density matrix is used to introduce the concept of a mixed state as a statistical ensemble of many pure quantum states. Some classical uncertainty about the quantum state is thus introduced. For a pure state $|\psi\rangle$, the density matrix is: $|\psi\rangle\langle\psi|$. Among its many properties (see [Morin 14a]), the density matrix is positive semi-definite and Hermitian. The spectral theorem tells us that the density matrix of a mixed state can be written as a sum of density matrices of pure states $|\psi_i\rangle$:

$$\hat{\rho} = \sum_i w_i |\psi_i\rangle\langle\psi_i| \quad \text{with} \quad \mathrm{Tr}\left(\hat{\rho}\right) = 1 \tag{1.16}$$

The density matrix is useful to describe a quantum state onto a given basis of orthogonal quantum states. In quantum optics, the community of *Discrete Variables* (DV) usually characterizes quantum state of light through photon-counting. For this kind of measurement, the density matrix expressed in the basis of Fock states is particularly appropriate. A key quantity is the purity π of the density matrix defined as:

$$\pi = \mathrm{Tr}\left(\hat{\rho}^2\right) = \sum_i w_i^2 \tag{1.17}$$

This number represents the amount of "mixture" of a mixed quantum state. The purity of a pure state is equal to unity. It tends to zero for an extremely mixed state. As we will see later, the concept of purity can be extended to any positive semidefinite Hermitian matrix.

1.1.3.1 Losses at a detection

Any experimental setup suffers from losses affecting the quantum states of light. Those losses are usually modeled by an additional beamspitter mixing the signal electric field with vacuum and tracing out over the second output. The effect of losses on a quantum state at a detection, for instance a perfectly mode-matched homodyne detection (see chapter 3) with non-unit quantum efficiency, can be modeled by a mixed state where vacuum is introduced. The density matrix goes from $|\psi\rangle\langle\psi|$ to:

$$\hat{\rho} = \eta|\psi\rangle\langle\psi| + \sqrt{1-\eta^2}|0\rangle\langle 0| \quad \text{with} \quad 0 \leq \eta \leq 1 \tag{1.18}$$

1.1.3.2 Thermal states

In quantum optics, extra noise above the fluctuations of vacuum can be represented as a statistical mixture of Fock states weighted by the Boltzmann distribution. Those states are the thermal states of Planck and their density matrix is:

$$\hat{\rho}_{th} = \frac{1}{1+n_{th}} \sum_{n\geq 0} \frac{n_{th}^n}{\left(1+n_{th}\right)^n} |n\rangle\langle n| \tag{1.19}$$

where n_{th} is the average photon number: $n_{th} = \mathrm{Tr}\left(\hat{n}\hat{\rho}\right)$.

1.1.4 The Wigner function

As explained in [Ourjoumtsev 07b], the density matrix can sometimes be cumbersome to identify a quantum state qualitatively, especially when the electric field contains important phase-dependent properties. To answer this problem, there exists a continuous family of *s-parametrized* quasiprobability distributions for $-1 \leq s \leq 1$ [Cahill 69] (see e.g [Vogel 06, Leonhardt 97]). Those distributions describe the quantum state in the phase space where the x and p variables are coordinates along the $\hat{X}$ and $\hat{P}$ quadratures of the field. The most widely used are the Glauber-Sudarshan P function ($s = 1$) [Glauber 63], the Wigner function W ($s = 0$) [Wigner 32] and the Husimi Q function ($s = -1$) [Husimi 40]. Each of them have different advantages when it comes to identify different quantum states. The most widely used in quantum optics to characterize CV and hybrid (mixed CV and DV) quantum states is the Wigner function. It can be obtained from the density matrix $\hat{\rho}$ through:

$$W(x,p) = \frac{1}{2\pi\sigma_0^2} \int e^{iyp/\sigma_0^2} \langle x - y|\hat{\rho}|x + y\rangle \, \mathrm{d}y \tag{1.20}$$

As explained in [Morin 14a], this definition is handily extended to any Hermitian operator. The Wigner function is useful to compute, for instance, the average value of a Hermitian operator $\hat{O}$ as $\langle\hat{O}\rangle = \int \mathrm{d}x\,\mathrm{d}p W(x,p) O(x,p)$ where $O(x,p)$ is the Wigner function of $\hat{O}$.

The Wigner function of some standard quantum states can be computed with this definition, reminding that the wave function of the harmonic oscillator writes:

$$\langle x|n\rangle = \frac{1}{\sqrt{2^n n! \sigma_0 \sqrt{2\pi}}} H_n\left(\frac{x}{\sqrt{2}\sigma_0}\right) \exp\left(\frac{-x^2}{4\sigma_0^2}\right) \quad \text{where} \quad \hat{X}|x\rangle = x|x\rangle \tag{1.21}$$

where H_n is the n-th Hermite polynomial. The Wigner functions of the vacuum state $|0\rangle$ then is:

$$W_{|0\rangle}(x,p) = \exp\left(\frac{-(x^2+p^2)}{2\sigma_0^2}\right) \Big/ \, 2\pi\sigma_0^2 \tag{1.22}$$

The Wigner function of a pure squeezed vacuum state $|\xi\rangle$ can be deduced from the one of vacuum. The squeezing operator rescales the quadrature operators $\hat{X}$ and $\hat{P}$ with a factor e^{ξ} and $e^{-\xi}$ respectively [Walls 08]. It thus writes:

$$W_{|\xi\rangle}(x,p) = \exp\left(-\frac{x^2}{2V_x} - \frac{p^2}{2V_p}\right) \Big/ \, 2\pi\sigma_0^2 \quad \text{with} \quad \sqrt{V_X V_P} = \sigma_0^2 \tag{1.23}$$

In the scope of this thesis, we have a special interest in subtracting a single-photon from any quantum state. It is possible to compute the Wigner function of a pure quantum state $|\psi\rangle$ whom a single-photon has been subtracted from has a function of the original Wigner function $W_{|\psi\rangle}(x,p)$ [Ourjoumtsev 07b, Morin 14a]:

$$W_{\hat{a}|\psi\rangle}(x,p) = \frac{1}{2}\left(1 + \frac{x^2+p^2}{2\sigma_0^2} + x\partial_x + p\partial_p + \frac{\sigma_0^2}{2}\left(\partial_x^2 + \partial_p^2\right)\right) W_{|\psi\rangle}(x,p) \Big/ \, \mathrm{Tr}\left(\hat{a}|\psi\rangle\langle\psi|\hat{a}^\dagger\right) \tag{1.24}$$

where the factor Tr $\left(\hat{a}|\psi\rangle\langle\psi|\hat{a}^\dagger\right)$ guarantees the normalization of the Wigner function.
In the scope of this thesis, we give a particular interest to squeezed vacuum whose a single photon has been subtracted from, namely $\hat{a}|\sigma\rangle$. For a pure single-photon subtracted squeezed vacuum state, the Wigner function writes:

$$W_{\hat{a}|\xi\rangle}(x,p) = \frac{W_{|\xi\rangle}(x,p)}{\frac{1}{2}\left(V_X + V_P - 2\right)}\left(1 - \frac{\sigma_0^2}{2}\left(\frac{1}{V_X} + \frac{1}{V_P}\right) + x^2\left(\frac{1}{2\sigma_0^2} - \frac{1}{V_X} - \frac{\sigma_0^2}{2V_X^2}\right) + p^2\left(\frac{1}{2\sigma_0^2} - \frac{1}{V_P} - \frac{\sigma_0^2}{2V_P^2}\right)\right) \tag{1.25}$$

The Wigner function offers a certain readability of the states at play in a glance. The Wigner functions of the states introduced here are presented on figure 1.2. We may notice that after evolution through the squeezing operator, the Wigner function of vacuum remains Gaussian. After a single-photon subtraction is performed, a strong negativity appears in the Wigner function.

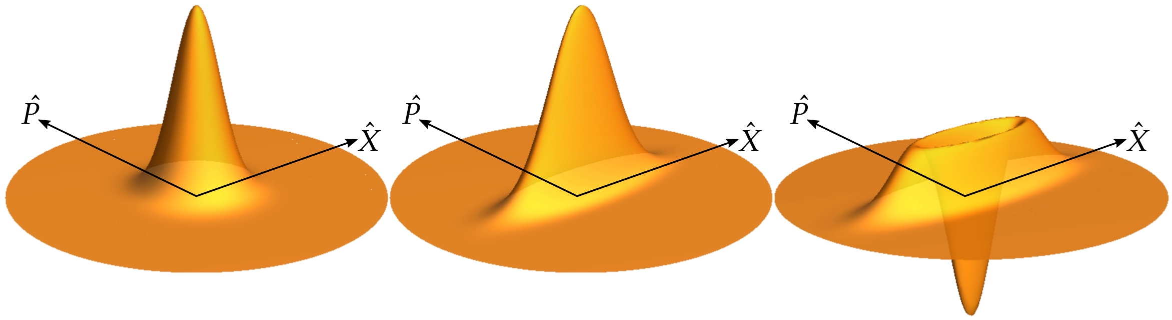

Figure 1.2: Wigner functions in a disk of phase space defined by $\sqrt{x^2 + p^2} < 9$. From left to right: vacuum, squeezed vacuum with 5dB of squeezing, single-photon subtracted squeezed vacuum with originally 5dB of squeezing.

1.2 Multimode generalization

During the quantization of the field mentioned in the previous section, we implicitly chose to express the electric field $\hat{\mathbf{E}}$ on the basis of plane waves. This choice forces to clarify the concept of optical mode.

1.2.1 Optical modes

A mode of the electromagnetic field $\hat{\mathbf{E}}$ is simply a normalized solution of Maxwell's equations [Kolobov 99, Treps 05]. As Maxwell's equations are classical, it should describe all the classically physical aspects of the field such as: spatial shape, polarization, spectral and temporal properties. A mode $\boldsymbol{u}(\boldsymbol{r}, t)$ can be mathematically expressed as a vector of a multi-dimensional Hilbert space where all the aforementioned physical characteristics are contained. The modal Hilbert space is given an inner product $\langle ., . \rangle$. It allows to compute the overlap $\langle \boldsymbol{u}, \boldsymbol{v} \rangle$ between two modes $\boldsymbol{u}(\boldsymbol{r}, t)$ and $\boldsymbol{v}(\boldsymbol{r}, t)$ as:

$$\langle \boldsymbol{u}, \boldsymbol{v} \rangle = \int_V \mathrm{d}\boldsymbol{r}\ \boldsymbol{u}^*(\boldsymbol{r}, t) \cdot \boldsymbol{v}(\boldsymbol{r}, t) \tag{1.26}$$

where $\boldsymbol{u}^*(\boldsymbol{r}, t)$ is the dual (or Hermitian conjugate) of $\boldsymbol{u}(\boldsymbol{r}, t)$ and where the above integration is only made over space since time and space are coupled by Maxwell's equations.
We have assumed the energy of the field to be bounded to a volume V so that there exist a countable basis of modes $\{\boldsymbol{u}_i\}$. The number of modes may be infinite while remaining countable. The basis notation implies an intrinsic truncation which is reasonable considering that only a finite number of modes may be populated. We often simply refer to modes as vectors $\boldsymbol{u}_i$, belonging to a basis $\{\boldsymbol{u}_i\}$ whose we drop the spatiotemporal dependence for the sake of simplicity. This basis is normalized and its vectors are orthogonal to each other, meaning:

$$|\langle \boldsymbol{u}_i, \boldsymbol{u}_i \rangle|^2 = 1 \quad \text{and} \quad \langle \boldsymbol{u}_i, \boldsymbol{u}_{i'} \rangle = \delta_{i,i'} \tag{1.27}$$

It is alway possible to perform a basis change from $\{\boldsymbol{u}_i\}$ to $\{\boldsymbol{v}_j\}$ such that:

$$\boldsymbol{v}_j = \sum_i \langle \boldsymbol{u}_i, \boldsymbol{v}_j \rangle \boldsymbol{u}_i \tag{1.28}$$

1.2.1.1 Modal algebra

Optical modes can be thought of as vectors of a Hilbert space of modal functions. For this reason, we introduce the notation $\boldsymbol{u}^\dagger$ as the Hermitian conjugate of mode $\boldsymbol{u}$. They can be thought respectively as a "row vector" for $\boldsymbol{u}^\dagger$ and a "column vector" for $\boldsymbol{u}$. Just like traditional vectors of any Hilbert space, the product $\boldsymbol{u}^\dagger \boldsymbol{v}$ is of dimension 1 (i.e. is a number) and is equal to $\langle u, v \rangle$ while the product $\boldsymbol{u}\boldsymbol{u}^\dagger$ is a matrix.

This notation allows us to write, for example a modal matrix $\mathbf{M}$ in the basis of modes $\{\boldsymbol{u}_i\}$ as:

$$\mathbf{M} = \sum_{i,j} m_{i,j}\, \boldsymbol{u}_i \boldsymbol{u}_j^\dagger \tag{1.29}$$

This notation will be helpful to seriously tackle the optical modes of a multimode single-photon subtraction in chapter 4.

1.2.1.2 The Schmidt decomposition

The Schmidt decomposition comes from the early works on integral equations [Schmidt 07] and is the continuous counterpart of the more famous but discrete Singular-Value decomposition [Townsend 14]. The Schmidt decomposition was made popular in quantum mechanics when it was applied to bipartite quantum states [Ekert 95, Averchenko 14]. In a nutshell, given a few mathematical conditions that we assume to be fulfilled here, it allows to decompose a cmatrix $A(x,y)$ into a sum of two sets of orthogonal functions $\{f_i\}$ and $\{g_i\}$ weighted by singular values $\{\lambda_i\}$ such that:

$$A(x,y) = \sum_i \lambda_i f_i(x) g_i^*(y) \tag{1.30}$$

and where one could define a *Schmidt number* K as the average number of terms in the sum such that:

$$K = \frac{\left(\sum_i \lambda_i^2\right)^2}{\sum_i \lambda_i^4} \tag{1.31}$$

We will use the Schmidt decomposition extensively in chapters 4 and 5 where we will apply it to obtain spectral modes.

1.2.1.3 Estimating the number of modes

We introduce an estimator of the multimode nature of the light field [Averchenko 16] inspired by the definition of the Schmidt number. If a basis of modes has an infinite but countable number of modes, they are not necessarily all excited. It can be useful, when considering a multimode light field, to assess the average number of modes populated by the quantum state carried by this light field. We define an efficient number N of non-vacuum modes, such that:

$$N = \frac{\left(\sum_k n_k\right)^2}{\sum_k n_k^2} \tag{1.32}$$

where n_k is the average photon number in mode "k". We notice that this definition is appropriate when a multimode quantum state of light is composed of many states of similar nature, or comparable energies. It will not be appropriate to describe an hybrid multimode quantum state composed for instance, of bright coherent states on one hand and low photon-number states on the other hand. The definition (1.32) could be modified to address this problem by weighting the sum by the fluctuations in each mode rather than the mean energy.

1.2.2 Multimode electric field

One way to introduce multiple modes of the electric field is to decompose the analytic signal on the basis of plane waves such that (1.6) becomes:

$$\hat{\mathbf{E}}^{(+)}(\boldsymbol{r},t) = \int \mathrm{d}\mathbf{k}\; \mathscr{E}^{(1)}(\omega)\; \boldsymbol{\varepsilon}(\mathbf{k}) \hat{a}(\mathbf{k},\omega) e^{i(\mathbf{k}\boldsymbol{r}-\omega t)} \tag{1.33}$$

where $\boldsymbol{\varepsilon}(\mathbf{k})$ is the polarization vector. This decomposition is not very convenient in our cases. There exist a countable basis of modes $\{\boldsymbol{u}_n\}$ with annihilation operators $\{\hat{a}_n\}$ with which we extend the definition (1.6) to a multimode electric field to this basis such that:

$$\hat{\mathbf{E}}^{(+)}(\boldsymbol{r},t) = \sum_n \mathscr{E}_n^{(1)} \hat{a}_n \boldsymbol{u}_n(\boldsymbol{r},t) \tag{1.34}$$

In this thesis, light is mostly composed of linearly polarized quasi Gaussian laser beams and we are interested into temporal/spectral properties. Hence we forget the polarization and following the formalism developed in [Thiel 15] we choose our modes to be single paraxial waves under the narrow spectrum approximation (i.e. $\Delta\omega \ll \omega_0$). This latter assumption allows us to split the temporal mode into a temporal envelope $u_n(t)$ and a oscillatory term $e^{-\omega_0 t}$ at the carrier frequency ω_0. We also assume the field constant in this mode to be equal to the one of the carrier frequency $\mathscr{E}^{(1)}(\omega_0)$. There is only one spatial mode g_0 (a TEM$_{00}$ in the scope of this thesis) and a mode $\boldsymbol{u}_n$ is:

$$\boldsymbol{u}_n(\boldsymbol{r},t) = g_0(\boldsymbol{r}) u_n(t) e^{i(\mathbf{k}_0\boldsymbol{r}-\omega_0 t)} \tag{1.35}$$

The multimode electric field $\hat{\mathbf{E}}^{(+)}(\boldsymbol{r},t)$ can then be expressed as a sum of temporal envelopes:

$$\hat{\mathbf{E}}^{(+)}(\boldsymbol{r},t) = \mathscr{E}_0^{(1)} g_0(\boldsymbol{r}) \sum_n \hat{a}_n u_n(t) e^{i(\mathbf{k}_0\boldsymbol{r}-\omega_0 t)} \tag{1.36}$$

We will refer to the Fourier Transform of $u_n(t)$ as the spectral mode denoted $\tilde{u}_n(\Omega)$ and defined relatively to the carrier frequency ($\Omega = \omega - \omega_0$):

$$\tilde{u}_n(\Omega) = \int \frac{\mathrm{d}t}{\sqrt{2\pi}}\, u_n(t) e^{i\Omega t} \tag{1.37}$$

1.2.3 Multimode quantum states

A single mode quantum state of the electromagnetic field consists of a coherent superposition of quanta of excitation in a given mode of the electromagnetic field. With this definition in mind, an optical mode should be seen as a classical container carrying the quantized excitation of the electromagnetic field. In this thesis, we specify the basis of optical modes in which a quantum state is represented by adding two subscripts: one to the state for the mode number and one to the Dirac notation for the basis. A single-mode state $|\psi\rangle$ contained in an optical mode $\boldsymbol{u}_n$ belonging to a basis $\{\boldsymbol{u}_n\}$ will be written $|\psi_n\rangle_u$.

According to the previous definitions, a single photon, defined as a single quantum of excitation of the electromagnetic field, is always single-mode. Indeed, a supposedly multimode single-photon state can be written in a basis of modes $\{\boldsymbol{u}_n\}$ whose associated annihilation operators are $\{\hat{a}_n\}$. A simple basis change shows that the state is single-mode:

$$\sum_n c_n |1_n\rangle_u = \sum_n c_n \hat{a}_n^\dagger |0\rangle = \hat{b}^\dagger|0\rangle = |1\rangle \quad \text{with} \quad \hat{b}^\dagger = \sum_n c_n \hat{a}_n^\dagger \quad \text{and} \quad \left[\hat{b},\hat{b}^\dagger\right] = 1 \tag{1.38}$$

In the rest of this thesis, we try to systematically separate the concepts of modes and states and avoid any abuse of language such as “squeezed mode”.

1.2.3.1 Factorizable multimode states

Factorizable multimode quantum states are a very particular and convenient case. It is possible to picture them as a collection of independent single-mode states although this description is not general. Still, for those multimode quantum states, there exists a modal basis $\{\boldsymbol{u}_n\}$ where the single-mode quantum states contained in each mode are independent from each other. We extend the previous notation to a multimode state $|\Psi\rangle$ composed of many single-mode states $|\psi_n\rangle$ contained in optical modes $\boldsymbol{u}_n$ so that:

$$|\Psi\rangle = |\psi_1\rangle_u \otimes \ldots \otimes |\psi_n\rangle_u = |\psi_1, \ldots, \psi_n\rangle_u \tag{1.39}$$

It is the case of multimode Gaussian states as we will discuss in section 1.3.

1.2.3.2 Entanglement

In the majority of cases, there is no simple way to write a multimode quantum state. One can still express a pure multimode quantum state $|\Psi\rangle$ on the basis of Fock states embedded in an arbitrary modal basis $\{\boldsymbol{u}_k\}$ as:

$$|\Psi\rangle = \sum_{n_1,\ldots,n_k,\ldots} C_{n_1,\ldots,n_k,\ldots} |n_1, \ldots, n_k, \ldots\rangle_u \quad \text{with} \quad \sum_{n_1,\ldots,n_k,\ldots} |C_{n_1,\ldots,n_k,\ldots}|^2 = 1 \tag{1.40}$$

The reason of such complexity is to be found in entanglement between the different modes that makes the state non-factorizable. Single photon subtraction for instance, can create such entanglement between states that were once factorizable. We will discuss this feature in chapter 4.

1.2.4 Multimode density matrix

The concept of density matrix can be extended to multimode states. Once again, the more general definition we can give for a pure multimode state is built on expression (1.40):

$$\hat{\rho} = |\Psi\rangle\langle\Psi| = \sum_{n_1,\ldots,n_k,\ldots} \sum_{n'_1,\ldots,n'_k,\ldots} C_{n_1,\ldots,n_k,\ldots} C^*_{n'_1,\ldots,n'_k,\ldots} |n_1, \ldots, n_k, \ldots\rangle\langle n'_1, \ldots, n'_k, \ldots|_u \tag{1.41}$$

where $|\Psi\rangle$ is explicitly written in expression (1.40). A mixed multimode state can be arbitrarily formed by a weighted sum of pure multimode density matrices.

Just like the single-mode version, it is possible to compute the purity of a multimode density matrix. The trace must then be taken over the whole modal space using for instance Fock states:

$$\pi = \operatorname{Tr}\left(\hat{\rho}^2\right) = \sum_{n_1,\ldots,n_k,\ldots} \langle n_1, \ldots, n_k, \ldots| \, \hat{\rho}^2 \, |n_1, \ldots, n_k, \ldots\rangle_u \tag{1.42}$$

For factorizable states, the expression of $\hat{\rho}$ is much simpler. Given a mode basis $\{\boldsymbol{u}_n\}$, for a pure factorizable multimode state $|\psi_1, ..., \psi_n\rangle_u$, the multimode density matrix $\hat{\rho}$ is: $\hat{\rho} = |\psi_1, ..., \psi_n\rangle\langle\psi_1, ..., \psi_n|_u$. The density matrix of any mixed multimode factorizable quantum state can be written as a sum of the density matrices of pure factorizable multimode states:

$$\hat{\rho} = \sum_i w_i |\psi_{i1}, ..., \psi_{in}\rangle\langle\psi_{i1}, ..., \psi_{in}|_u \tag{1.43}$$

1.2.5 Multimode Wigner function

It is possible to extend the definition of the single-mode Wigner function to a multimode Wigner function with a multimode density matrix. The definition remains the same, but the integral is extended over all modes:

$$W(x_1, p_1, \cdots, x_N, p_N) = \frac{1}{\left(2\pi\sigma_0^2\right)^N} \int \left(\prod_n \mathrm{d}y_n e^{iy_n p_n/\sigma_0^2}\right) \langle x_1 - y_1, \cdots, x_N - y_N|\, \hat{\rho}\, |x_1 - y_1, \cdots, x_N - y_N\rangle \tag{1.44}$$

where N is the number of modes. While straightforward, this expression can be cumbersome to manipulate and difficult to interpret. As long as the multimode state is factorizable (i.e. $\hat{\rho} = \otimes_n \hat{\rho_n}$), the phase space variables of different modes are separated and the multimode Wigner function is simply the product of the single-mode Wigner functions:

$$W(x_1, p_1, \cdots, x_N, p_N) = \prod_i W_i(x_i, p_i) \tag{1.45}$$

Again, in the scope of this thesis, we are interested in subtracting a single photon from multimode squeezed vacuum. In other word, creating entanglement between optical modes whose states were formerly separated. The density matrix after subtraction is no longer factorizable and the phase space variables of the Wigner function cannot be separated. The exact expression of the multimode Wigner function depends on which optical mode the subtraction is performed.

1.3 Multimode Gaussian states

Some quantum states of light belong to the family of Gaussian states. Those states possess certain properties that facilitate their understanding as multimode states.

1.3.1 Single-mode Gaussian state

A Gaussian state $|\psi\rangle$ is a state whose Wigner function is Gaussian. Such a Wigner function can be written in the form of expression (1.23) where we deliberately omit the mean field:

$$W_{|\psi\rangle}(x,p) = \exp\left(-\frac{x^2}{2V_x} - \frac{p^2}{2V_p}\right) \Big/ 2\pi\sqrt{V_x V_p} \tag{1.46}$$

where V_x and V_p are the variances of the Wigner function along the $\hat{X}$ and $\hat{P}$ quadratures and where we have put $\sigma_0 = 1$. Here we have considered the state to be centered on the origin of phase space. It is possible to displace this state with the displacement operator $\hat{D}$ while conserving all its properties but the average photon number that must reflect its average amplitude when the state is displaced.

The purity π and the average photon number of this state are:

$$\pi = 1/\sqrt{V_x Vp} \tag{1.47}$$

$$\langle\psi|\hat{n}|\psi\rangle = \frac{1}{4}\left(V_x + V_p - 2\right) \tag{1.48}$$

This state does not necessarily saturate the Heisenberg inequality and we have $\sqrt{V_x V_p} \geq \sigma_0^2$. It can be understood as a noisy squeezed state, or a mixture of a squeezed state with a thermal state. The Hudson-Piquet theorem guarantees that for a pure state, there is an equivalence between the positivity of the Wigner function and the Gaussian nature of the state and its Wigner function [Hudson 74]. As a consequence, if a pure state is non-Gaussian, it must possesses negativity.

1.3.2 The covariance matrix

The covariance matrix $\mathbf{\Gamma}$ offers a convenient formalism to describe the correlations in the fluctuations between different parties of a multimode state [Ferraro 05]. We denote $\hat{\boldsymbol{Q}} = (\hat{X}_1, ..., \hat{X}_n, \hat{P}_1, ..., \hat{P}_n)$ the vector of quadratures operators of every mode. The covariance matrix terms Γ_{ij} are:

$$\Gamma_{ij} = \frac{1}{2}\langle\{\hat{Q}_i\hat{Q}_j\}\rangle - \langle\hat{Q}_i\rangle - \langle\hat{Q}_j\rangle \tag{1.49}$$

This definition means that, by construction, a covariance matrix is always real positive definite so that the spectral theorem applies. With the previous definition in mind, we can write the multimode Wigner function of a multimode Gaussian states $|\Psi\rangle$ as:

$$W_{|\Psi\rangle}(\boldsymbol{q}) = \exp\left(-\frac{1}{2}\left(\boldsymbol{q} - \langle\hat{\boldsymbol{Q}}\rangle\right)^t \mathbf{\Gamma}^{-1}\left(\boldsymbol{q} - \langle\hat{\boldsymbol{Q}}\rangle\right)\right) \Big/ (2\pi)^{2n}\sqrt{\det(\mathbf{\Gamma})} \tag{1.50}$$

where $\boldsymbol{q} = (x_1, ..., x_n, p_1 ..., p_n)$ is the vector of every mode coordinates in the phase space. The covariance matrix can be seen as a four blocs matrix with the diagonal blocs being

$\mathbf{\Gamma}_X$ and $\mathbf{\Gamma}_P$, namely the covariance matrices limited to the amplitude and phase quadrature and the off-diagonal blocs $\mathbf{\Gamma}_{XP}$ being the covariance matrix of the correlations between quadratures. When the correlations between the amplitude and the phase quadratures are null, we only consider the diagonal blocs $\mathbf{\Gamma}_X$ and $\mathbf{\Gamma}_P$ of the covariance matrix as we will see later in chapter 3.

1.3.2.1 Purity

It is possible to compute the purity of a multimode Gaussian state multimode state from its covariance matrix as: $\pi = \det(\mathbf{\Gamma})$.

1.3.3 Multimode squeezed vacuum

In this work, one of the main quantum states of interest is multimode squeezed vacuum. Be it pure or not, two handy mathematical decompositions come at our rescue to gain some understanding on the properties of this multimode state.

1.3.3.1 Bloch-Messiah decomposition

The Bloch-Messiah reduction states that any general linear unitary Bogoliubov transformation on a finite number of modes (also known as a symplectic matrix) can be decomposed into a basis change, a set of single-mode linear Bogoliubov transformation independent from each other, and finally another basis change [Arvind 95]. The application of this reduction to a multimode optical setup described by linear and quadratic Hamiltonian (an arbitrary network of beamsplitters and second-order parametric processes) is that the setup can eventually be described by a multiport beamsplitter, followed by an assembly of individual squeezing operators in parallel and another multiport beamsplitter [Braunstein 05].

This result has an important consequence for pure Gaussian states of null mean field: one can always find a modal basis $\boldsymbol{u}_n$ where the initial multimode quantum state has been generated by a set of independent squeezing operators acting on vacuum. A pure multimode Gaussian state of zero mean field is consequently always a pure and factorizable multimode squeezed state in the form of expression (1.39), up to a basis change.

A multimode squeezed vacuum state with squeezing values $\{\sigma_1, ..., \sigma_n\}$ is always expressed as: $|\sigma_1, ..., \sigma_n\rangle$ and its multimode density matrix consists in a tensor product of the single-mode matrices of different modes, i.e.:

$$\hat{\rho} = \bigotimes_n \hat{\rho}_n \quad \text{where} \quad \hat{\rho}_n = |\sigma_n\rangle\langle\sigma_n|_u \tag{1.51}$$

For such a state, the covariance matrix in the basis $\{\boldsymbol{u}_n\}$ simply writes:

$$\mathbf{\Gamma} = \operatorname{diag}\left(\sigma_1^2, ..., \sigma_n^2, \frac{1}{\sigma_1^2}, ..., \frac{1}{\sigma_n^2}\right) \tag{1.52}$$

With this definition, the covariance matrix of vacuum or of a pure multimode coherent state is the identity matrix $\mathbb{1}$.

1.3.3.2 Williamson decomposition

The Williamson decomposition can be thought of a way to extend the consequences of the Bloch-Messiah reduction to multimode Gaussian states that are not required to be pure anymore. It states that for every real symmetric positive-definite matrix $\mathbf{V}$ of even dimension, there is a symplectic matrix $\mathbf{S}$ so that $\mathbf{S}\mathbf{V}\mathbf{S}^{\intercal} = \mathbf{D}^2$ where $\mathbf{D}^2$ is a diagonal matrix whose diagonal is repeated, i.e. $\mathbf{D}^2 = \text{diag}(d_1, \ldots, d_N, d_1, \ldots, d_N)$ [Simon 98]. The symplectic matrix $\mathbf{S}$ can be then decomposed by the Bloch-Messiah decomposition. Eventually, the matrix $\mathbf{V}$ is decomposed as:

$$\mathbf{V} = \mathbf{O}_1\mathbf{K}\mathbf{O}_2^{\intercal}\mathbf{D}^2\mathbf{O}_2\mathbf{K}\mathbf{O}_1^{\intercal} \tag{1.53}$$

where $\mathbf{O}_1$ and $\mathbf{O}_2$ are orthogonal matrices and $\mathbf{K}$ is diagonal.

This result applies to the covariance matrix Γ of any multimode Gaussian state [Weedbrook 12]. If this multimode Gaussian state has a zero mean field, the previous decomposition can be interpreted as follows:

- the diagonal $\mathbf{D}^2$ is an initial assembly of thermal states;
- a basis change described by $\mathbf{O}_2$ is performed between the basis of the initial thermal states and the basis of the diagonal matrix $\mathbf{K}$;
- the matrix $\mathbf{K}$ symbolizes a set of pure parallel squeezing operations according to the Bloch-Messiah decomposition;
- finally, a last basis change described by $\mathbf{O}_1$ is performed to obtained $\mathbf{\Gamma}$.

To sum up, the combination of the Williamson decomposition and the Bloch-Messiah reduction guarantees that a non-pure multimode Gaussian state of null mean field always results from the classical noise of an assembly of thermal states in some modes, a basis change and a set of parallel squeezing operation, up to a last basis change. The multimode state is not factorizable anymore, but one can retrieve the squeezing of each individual squeezer and the initial classical noise independently.

Chapter 2

A Source of Spectrally Multimode Quantum States

[About the last month of thesis writing] *"Yeah … you'll see. It's just no fun."*
– Every physics PhD I know

Contents

In this chapter, we briefly introduce ultrafast optics to model a source of spectrally multimode squeezed vacuum. Our source consists of an optical cavity and a non-linear medium pumped by a frequency comb. Such a setup is known to produce multimode squeezed vacuum in the spectral domain when pumped below threshold.

We start with a single-mode description of an Optical Parametric Oscillator (OPO), composed of a non-linear crystal and a lossy ring cavity, operated below threshold. We then describe our source of spectrally multimode squeezing and give theoretical predictions of its output quantum state.

2.1 A crash course of ultrafast optics

A significant addition to the physics of OPOs in our setup consists in the fact that our oscillator is pumped with a frequency comb produced by an ultrafast laser compared to the more common practice using Continuous Wave (CW) lasers [Vahlbruch 16]. Ultrafast pulses offer the advantage that the energy is focused in time, thus enhancing non-linear interactions. For this reason, we introduce a few concepts and definitions of ultrafast optics. For a detailed presentation, the reader should consult [Weiner 11b].

2.1.1 Generation of ultrafast pulses

We describe the classical electric field E as an infinite train of periodic ultrafast pulses with a repetition rate ω_r and a temporal envelope $u(t)$. Within each pulse, the field oscillates at the carrier frequency ω_0. From one pulse to the next one, the field and envelope are dephased by a Carrier-Envelope Offset (CEO) ω_{ceo} (see [Spence 91]). The pulse train $E(t)$ can be expressed as:

$$E(t) = A \sum_{n=-\infty}^{\infty} u\left(t - \frac{n}{f_r}\right) \, e^{-i\omega_0\left(t-\frac{2\pi n}{\omega_r}\right)} e^{-i\omega_{ceo}\frac{2\pi n}{\omega_r}} \tag{2.1}$$

where A is the amplitude of the field and $u(t)$ is in fact the normalized temporal mode of a single pulse. By taking the Fourier Transform of the previous expression, one gets the spectral profile of the electric field $\tilde{E}(\Omega)$ of the pulse train:

$$\tilde{E}(\Omega) = A \, \tilde{u}(\Omega) \sum_{n=-\infty}^{\infty} \delta\left(\Omega + \omega_0 - n\omega_r - \omega_{ceo}\right) \tag{2.2}$$

where $\tilde{u}$ is the Fourier Transform of u. An infinite pulse train in the time domain is thus a frequency comb in the spectral domain. The frequencies of the comb are $\omega_n = n\omega_r + \omega_{ceo}$ for $n \in \mathbb{N}$. The frequency comb is modulated by the Fourier Transform of the pulse shape.

In order to produce this train of ultrafast pulses, it is required to produce a large frequency comb whose all spectral components are in phase. It can be achieved with a laser possessing a large spectral gain profile as well as dispersion compensation in the optical resonator. A mode-locking mechanism is also required in order to initiate the pulsed regime. It is commonly achieved since the early 1990 with solid-state Kerr lens mode-locking lasers [Spence 91]. Those lasers use Titanium Sapphire (Ti:Sa) as a homogeneous gain medium due to its large spectral gain profile spanning from the red edge of the visible spectrum to more than 1.1μm [Rapoport 88]. Ultrafast pulses of light with duration down to a few optical cycles can be generated with such lasers [Asaki 93, Sutter 99, Morgner 99]. For a fundamental wavelength of $\lambda_0 = 800$nm, an optical cycle is about 3fs.

2.1.2 Pulse modeling

In this manuscript, we will consider that our pulses are well modeled by Gaussian profiles. While this choice is not appropriate for all ultrafast pulses (see previous references), it is still an excellent approximation given the spectrum of our laser source (see figure 2.1. This choice has some advantages as allowing analytical calculations and time/frequency symmetric definitions has a Gaussian is self Fourier-Transform. We will represent the Gaussian temporal envelopes as a normalized mode of the electric field in the following form:

$$u(t) = \exp\left(-\frac{t^2}{4\Delta t^2}\right) \Big/ \sqrt{\Delta t} 2\pi \tag{2.3}$$

where Δt is the standard deviation of the intensity envelope. This definition is convenient as, due to Fourier Transform, time and frequency definitions are the same. The spectral envelope is:

$$\tilde{u}(\Omega) = \int \frac{\mathrm{d}t}{\sqrt{2\pi}} u(t) e^{i\Omega t} = \exp\left(-\frac{\Omega^2}{4\Delta\omega^2}\right) \Big/ \sqrt{\Delta\omega} 2\pi \quad \text{with} \quad \Delta\omega = 1/2\Delta t \tag{2.4}$$

where $\Delta\omega$ is the standard deviation of the intensity envelope and $\Omega = \omega - \omega_0$.

An experimental physicist often characterizes optical pulses by the Full-Width-Half-Maximum (FWHM) of the intensity spectrum in the wavelength domain. As long as the narrow-spectrum approximation holds, the spectrum in this domain can be considered Gaussian as well. It is easily measured with a spectrometer and the relation between the FWHM and $\Delta\omega$ is:

$$\Delta\omega = \frac{\pi\ c\ \text{FWHM}}{\lambda_0^2 \sqrt{2\ln(2)}} \quad \text{where} \quad \lambda_0 = \frac{2\pi c}{\omega_0} \tag{2.5}$$

Another meaningful quantity is the pulse duration. We choose to refer to pulse duration τ as the full-width-half-maximum of the temporal intensity profile. This definition makes sense as long as the pulse is Gaussian. It can be useful to relate this quantity to the FWHM of the intensity profile in the wavelength domain:

$$\tau = \frac{\lambda_0^2 \, 2\ln(2)}{\pi \; c \; \mathrm{FWHM}} \tag{2.6}$$

2.1.2.1 Spectral Phase

With broad spectra comes the possibility that each optical frequency has, or acquires, its own phase $\phi(\omega)$ with respect to the others. In ultrafast optics, it is common to perform the Taylor expansion of the spectral phase around the carrier frequency ω_0 so that:

$$\phi(\omega) \approx \phi_0 + \phi'\Omega + \phi''\frac{\Omega^2}{2} + \phi^{(3)}\frac{\Omega^3}{3!} + \ldots \quad \text{with} \quad \begin{cases} \phi_0 & = \phi(\omega_0) \\ \phi' & = \frac{\mathrm{d}\phi}{\mathrm{d}\omega}(\omega_0) \\ & \ldots \end{cases} \tag{2.7}$$

The zero-order and first-order terms represents respectively a relative phase and a temporal delay (see [Weiner 11b]) with respect to the original pulse.

The second-order term, called *quadratic phase* has the effect of increasing the duration of a Gaussian pulse while conserving its shape. Assuming a Gaussian pulse with no spectral phase of duration τ_0, its duration τ after having acquired a quadratic phase ϕ'' is:

$$\tau = \tau_0 \sqrt{1 + \left(\frac{4\ln(2)\phi''}{\tau_0^2}\right)^2} \tag{2.8}$$

This formula shows that the shorter the initial pulse is, the greater the impact of the quadratic phase will be. To give some insight to the reader, a Gaussian pulse of duration $\tau_0 = 50$fs will see its duration increase to $\tau = 75$fs with a $\phi'' = 1000\text{fs}^2$ quadratic phase.

The third order term called *cubic phase* modifies strongly the pulse shape creating ripples in the pulse shape (see [Thiel 15] pulse spectrograms). Given our limited spectrum (shown on figure 2.1), we neglect any cubic phase and limit ourselves to quadratic phase.

2.2 Our light source

For all experiments described in this thesis, the light source we used is a MIRA® 900 from COHERENT pumped by a VERDI V18® provided by the same company. We pump the Ti:Sa oscillator with 13W of CW light at 532nm. When operated in ultrafast regime, the Ti:Sa oscillator delivers approximately 2W of power with a repetition rate f_r of 76MHz.

The output spectrum of our laser is presented on figure 2.1. The spectrum is centered at $\lambda_0 = 795$nm. A Gaussian fit leads to a FWHM of approximately 11nm. Such a FWHM is synonymous of a Fourier Transform limited pulse of duration approximately equal to 85fs.

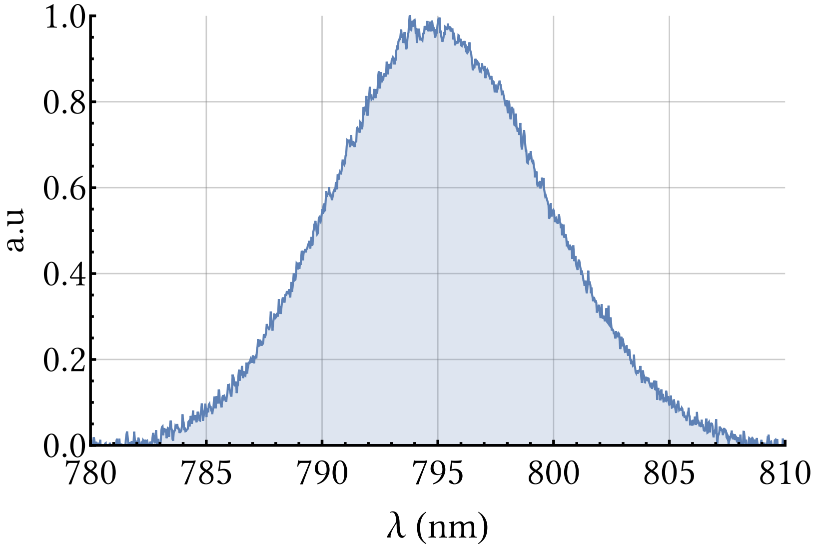

Figure 2.1: Output spectrum of our light source.

2.3 Single-mode OPO in a ring cavity

In order to predict the quantum state produced by a lossy below-threshold OPO, we use a simple model where a coherent state CW pump undergoes a degenerate parametric down-conversion process inside an optical cavity at resonance with the signal field. In the majority of the literature about OPOs and their below-threshold counterpart, the optical resonator is assumed to have low optical losses so that a first order development of the round trip equation can be performed (see e.g [Morin 14a]). It is generally a good assumption for high finesse cavities. For optical cavities of lower finesse, this assumption no longer holds so we use the full cavity transfer function. We will compute the variance of the quadratures of the output state by using the input/output relations of the ring cavity presented on figure 2.2.

2.3.1 Input/output relations

The input/output relations for the annihilation operators of the field at play in figure 2.2 are dictated by the beamsplitter transformation in the Heisenberg picture as well as the evolution of annihilation operators through the squeezing operator $\hat{S}(\xi)$. We get the following:

$$\begin{cases} \hat{a}_a & = t_i \hat{a}_i + r_i \hat{a}_c \\ \hat{a}_L & = t_i \hat{a}_c - r_i \hat{a}_i \\ \hat{a}_o & = t_o \hat{a}_b - r_o \hat{a}_b \\ \hat{a}_c & = t_o \hat{a}_e + r_o \hat{a}_b \\ \hat{a}_b & = \mathrm{ch}\left(\xi\right) \hat{a}_a - \mathrm{sh}\left(\xi\right) \hat{a}_a^\dagger \end{cases} \tag{2.9}$$

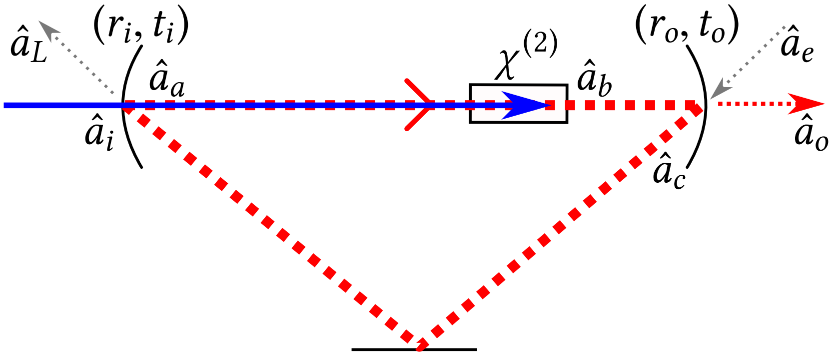

Figure 2.2: Ring cavity with an input coupler, an output coupler and non-linear gain medium ($\chi^{(2)}$). The annihilation operators of the electric field at different positions are represented. The subscripts i, o, L and e stand for input, output, losses and extra. The subscripts a, b and c just denote different useful position for calculus in the resonator.

where we have assumed the cavity to be resonant with the signal so that we could discard the phases due to propagation assuming they are multiples of 2π. We therefore lose generality and the capability to compute the squeezing in the sidebands of the resonance. The parameter ξ is the gain of the squeezing operator and we consider it being a real number. It ultimately depends of the non-linearity $\chi^{(2)}$, the pump amplitude $|\alpha_p|$, the medium length l_c as: $\xi = \epsilon_0 l_c |\alpha_p| \chi^{(2)}/2$

With the relations (2.9), we compute the value of the output fields quadratures $\hat{X}_o$ and $\hat{P}_o$ (note that the same is possible for $\hat{X}_L$ and $\hat{P}_L$) as functions of the input fields quadratures $\hat{X}_i$, $\hat{P}_i$, $\hat{X}_e$ and $\hat{P}_e$:

$$\begin{cases} \hat{X}_o &= \left(t_i t_o e^{-\xi} \hat{X}_i + \left(r_i e^{-\xi} - r_o\right) \hat{X}_e\right) \Big/ \left(1 - r_i r_o e^{-\xi}\right) \\ \hat{P}_o &= \left(t_i t_o e^{\xi} \hat{P}_i + \left(r_i e^{\xi} - r_o\right) \hat{P}_e\right) \Big/ \left(1 - r_i r_o e^{\xi}\right) \end{cases} \tag{2.10}$$

Interestingly, the expressions for $\hat{X}_o$ and $\hat{P}_o$ (and so $\hat{X}_L$ and $\hat{P}_L$) are symmetrical with respect to $\xi \rightarrow -\xi$.

Assuming the quantum states injected in both input are vacuum, we may compute the variance of the output field quadratures relatively to σ_0^2. One can show easily that given vacuum inputs, the average of the output field quadratures are null. Both vacuum inputs are not correlated so we get:

$$\begin{cases} \langle \hat{X}_o^2 \rangle / \sigma_0^2 &= \left(t_i^2 t_o^2 e^{-2\xi} + \left(r_i e^{-\xi} - r_o\right)^2\right) \Big/ \left(1 - r_i r_o e^{-\xi}\right)^2 \\ \langle \hat{P}_o^2 \rangle / \sigma_0^2 &= \left(t_i^2 t_o^2 e^{2\xi} + \left(r_i e^{\xi} - r_o\right)^2\right) \Big/ \left(1 - r_i r_o e^{\xi}\right)^2 \end{cases} \tag{2.11}$$

As expected, the equation for $\langle \hat{X}_L^2 \rangle$ and $\langle \hat{P}_L^2 \rangle$ are identical to the ones for $\langle \hat{X}_o^2 \rangle$ and $\langle \hat{P}_o^2 \rangle$ with respect to a substitution of input and output couplers coefficients.

2.3.2 OPO threshold

The expressions obtained above lead us to introduce a gain threshold ξ^{th} so that as:

$$\xi^{th} = \ln\left(\frac{1}{r_i r_o}\right) \tag{2.12}$$

For $\xi = \xi^{th}$, the expressions (2.11) diverge. Physically, the gain of the amplifier in the resonator equals losses and the threshold is reached. The OPO and like a laser, emitting bright light. We restrict ourselves to the below-threshold regime where it is convenient to reformulate expression (2.11) in terms of the ratio ε between the actual gain ξ and the gain threshold ξ_{th} (i.e. $\varepsilon = \xi/\xi_{th}$). The full expressions of the fluctuations for every output quadratures are:

$$\begin{cases} \langle \hat{X}_o^2 \rangle / \sigma_0^2 & = \left(t_i^2 t_o^2 / \left(r_i r_o\right)^{-2\varepsilon} + \left(\frac{r_i}{(r_i r_o)^{-\varepsilon}} - r_o \right)^2 \right) \Big/ \left(1 - (r_i r_o)^{1+\varepsilon} \right)^2 \\ \langle \hat{P}_o^2 \rangle / \sigma_0^2 & = \left(t_i^2 t_o^2 / \left(r_i r_o\right)^{2\varepsilon} + \left(\frac{r_i}{(r_i r_o)^{\varepsilon}} - r_o \right)^2 \right) \Big/ \left(1 - (r_i r_o)^{1-\varepsilon} \right)^2 \end{cases} \tag{2.13}$$

$$\begin{cases} \langle \hat{X}_L^2 \rangle / \sigma_0^2 & = \left(\left(\frac{r_o}{(r_i r_o)^{-\varepsilon}} - r_i \right)^2 + t_i^2 t_o^2 / \left(r_i r_o\right)^{-2\varepsilon} \right) \Big/ \left(1 - (r_i r_o)^{1+\varepsilon} \right)^2 \\ \langle \hat{P}_L^2 \rangle / \sigma_0^2 & = \left(\left(\frac{r_o}{(r_i r_o)^{\varepsilon}} - r_i \right)^2 + t_i^2 t_o^2 / \left(r_i r_o\right)^{2\varepsilon} \right) \Big/ \left(1 - (r_i r_o)^{1-\varepsilon} \right)^2 \end{cases} \tag{2.14}$$

Expressions (2.14) allow us to compute the values of the field quadratures variances for any arbitrary ring cavity configuration where vacuum is injected. Those expressions are valid for frequencies below the optical cavity bandwidth.

2.3.3 Predicting squeezing

With equations (2.14), we can predict the maximum expected squeezing for any optical ring cavity. We can tune the input/output couplers parameters in order to adapt to different situations. In particular, optical losses can be included in the value of r_i by taking it strictly smaller than the intrinsic reflectivity of the coupler.

For example, figure 2.3 shows the expected squeezing and antisqueezing for different values of r_i and r_o. We choose $r_o = \sqrt{.7}$ to analyze a ring cavity whose output coupler has a transmission T_o of 30%. This latter value being meaningful in our case as we will see later in 2.4.1. The value of r_i is varied in order to introduce some losses from the input coupler. As expected, squeezing becomes finite at threshold as soon as losses are introduced. The maximum squeezing that can possibly be produced with 3% losses and an output coupler with 70% of transmission is about −12dB.

This model is important because it allows to understand the effect of losses in a single-mode OPO below threshold. As we will see later, our multimode OPO can be treated as an assembly of single-mode OPOs. This former model shows that the maximum squeezing that

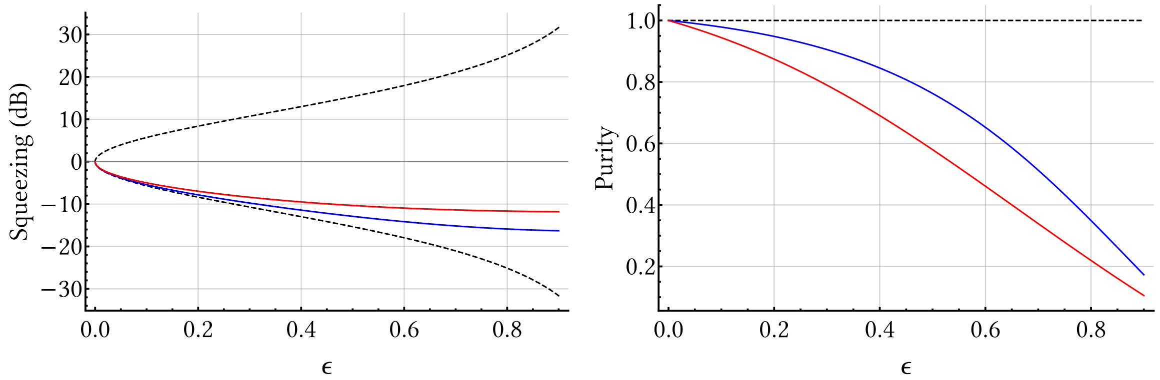

Figure 2.3: Left: Theoretical value of squeezing with respect to ε for $r_i = 1$ (dashed, along with antisqueezing), $\sqrt{r_i} = .99$ (blue) and $\sqrt{r_i} = .97$ (red). Right: Purity of the output state.

could be expected in a single mode of our lossy multimode OPO is bound by the maximum squeezing that can potentially be produced by a lossy single-mode OPO.

2.4 Measuring single-mode squeezing

2.4.1 A technical description of our OPO

In this section, we recall and update the technical description of the optical cavity used for our multimode OPO. A complete description is given in [Medeiros de Araujo 12]. Minor changes have been made since mostly consisting in replacing some mirrors.

In a nutshell, the optical resonator is a ring cavity designed for S-polarized light. Its length is about 3.95m ($L = c/f_r$) so that every optical frequency of the frequency comb produced by our light source (see figure 2.1) is resonant. For stability reasons, the ring cavity is folded several times in a complex fashion. A picture of the cavity can be seen in appendix A.

2.4.1.1 Finesse

The input coupler has a reflectivity of 99.85% and the output coupler has a reflectivity of 70%. The losses measured in the cavity due to the crystal interfaces and the numerous reflections are approximately 3%. To compute the finesse $\mathscr{F}$ of the cavity, we use a model cavity similar to the one introduced on figure 2.4 where the non-linear medium has been removed and where the third mirror has some non-unit reflectance r_L. The transfer function H of the cavity in terms of intensities for a monochromatic field at λ_0 is:

$$H = \frac{I_o}{I_i} = \frac{T_o T_i}{(1 - r_i r_o r_L)^2 \left(1 + \frac{4 r_i r_o r_L}{(1 - r_i r_o r_L)^2} \sin^2(\phi/2)\right)} \tag{2.15}$$

where ϕ is the phase on a round-trip in the cavity and $T = 1 - r^2$ is the transmission of a given mirror. The finesse $\mathscr{F}$ is defined as the Full Spectral Range (FSR) over the FWHM of a transmission peak. The expression of the finesse is:

$$\mathscr{F} = \frac{\pi}{2 \arcsin\left(\sqrt{\frac{(1 - r_i r_o r_L)^2}{4 r_i r_o r_L}}\right)} \tag{2.16}$$

The evolution of the finesse with respect to losses for our cavity is shown on figure 2.4.

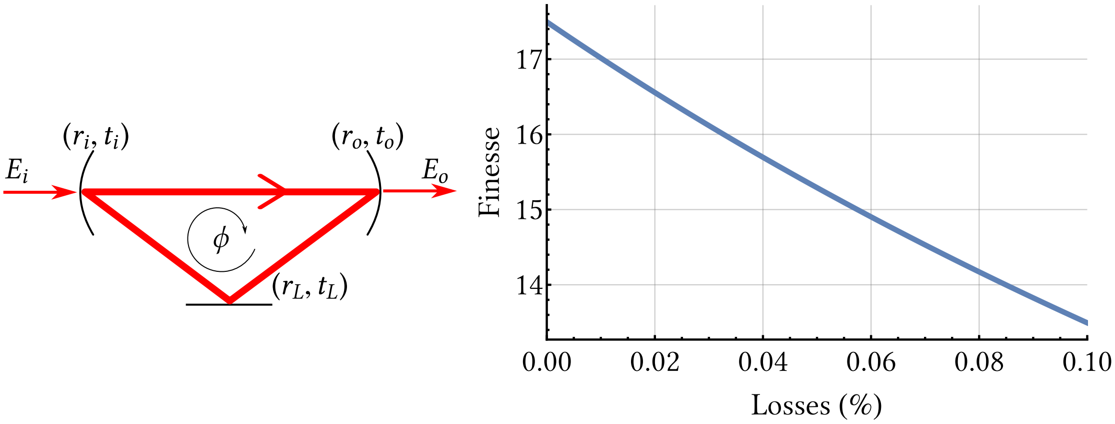

Figure 2.4: Left: Scheme of a lossy ring cavity. Right: Evolution of the finesse with respect to losses for our cavity parameters.

2.4.1.2 Spatial mode

The cavity is built from spherical mirrors and thus designed to be resonant for TEM_{nm} modes. It possesses four spherical mirrors disposed in a symmetric fashion around the BiBO crystal. The radii of curvature of the spherical mirrors are $R_1 = 250\text{mm}$ and $R_2 = 6000\text{mm}$. For symmetry reasons, it is possible to reduce the spatial analysis to half the length of the cavity, starting from the waist w_0 in the crystal until the waist w_1 encountered after a second spherical mirror as pictured on figure 2.5.

A ray transfer matrix analysis [Yariv 89] using the complex beam parameter of the spatial mode in the cavity reveals that for the given parameter, the cavity is stable for $120\text{mm} \leqslant L_1 \leqslant 140\text{mm}$ and $0 < L_2 \leqslant L/2 - L_1$. The mode and the waists, w_0 in particular, being much more sensitive to L_1 than to L_2. Still, the critical waist w_0 remains approximately equal to $50\mu\text{m}$ within a 5mm variation of L_1.

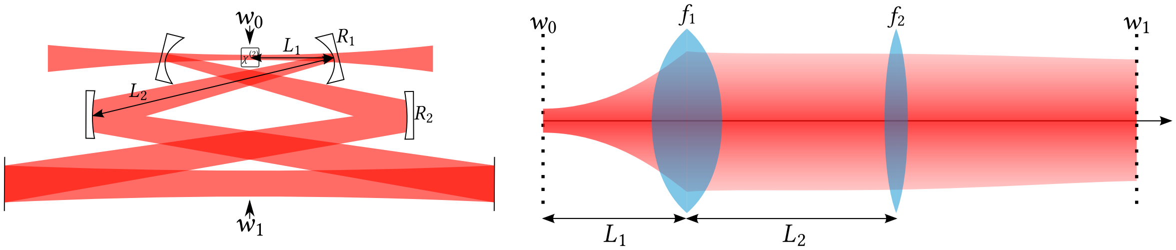

Figure 2.5: Left: Simplified scheme of the ring cavity with waists, radii of curvatures and important distances. Right: Equivalent optical scheme for ray transfer matrix analysis.

In its current configuration, the lengths are set so that $L_1 = 125\text{mm}$ and $L_2 = 472\text{mm}$. For those values, we have $w_0 = 52\mu\text{m}$ and $w_1 = 601\mu\text{m}$. With those parameters, if the mode TEM_{00} is resonant, the Gouy phase of the other TEM_{nm} is such that no other mode will be resonant before $n + m = 4$ where the Gouy Phase is about 0.08 of 2π.

2.4.1.3 Dispersion

The main source of dispersion in the cavity is the 2mm thick BiBO crystal that accounts for 332fs^2 as computed in appendix B. The length of the cavity adds some additional dispersion up to approximately 80fs^2 assuming an average 20fs^2 per meter in standard laboratory conditions [Jian 12]. Three mirrors in the cavity have a negative dispersion of about -50fs^2 each. The total dispersion in the cavity should not exceed 260fs^2 per round trip.

For a Fourier-Transform limited pulse of duration $\tau_0 = 85.0\text{fs}$ (like our laser source), the pulse duration after one round trip is increased to $\tau_0 = 85.4\text{fs}$ according to equation (2.8). Thus, on such an optical bandwidth, the effect of dispersion is almost negligible. Nevertheless, for larger bandwidths, the effect of dispersion can rapidly limit the transmission of the cavity and introduces extra frequency-dependent losses. It can be detrimental when trying to produce loss-sensitive quantum states in optical modes of large bandwidth. Ultimately, a dispersion of the order of 260fs^2 will limit the optical bandwidth of the cavity. Even for a low finesse cavity like ours, it is not reasonable to expect to go beyond a few tenth of nanometers of optical bandwidth without any dispersion compensation [Thiel 15].

2.4.1.4 Bandwidth

The bandwidth BW of an optical cavity is the FWHM of a transmission peak. It can be computed from the definition of the finesse $\mathscr{F}$ as:

$$\text{BW} = \text{FSR}/\mathscr{F} \tag{2.17}$$

The finesse of our cavity being approximately 16 and the FSR being 76MHz, the bandwidth is expected to be about 4.75MHz. **Refine those values**

The cavity was built to guarantee an optical bandwidth much greater than the bandwidth of the source (see figure 2.1). Given the typical reflectivity data provided by high reflectivity mirror manufacturers, it is safe to assume that the optical bandwidth spans from 750nm to 850nm with minimal losses.

2.4.2 Pump spectrum

In order to bring energy to the squeezing process of our OPO, we generate a pump beam by Second-Harmonic-Generation (SHG) of our laser source (whose spectrum is presented on figure 2.1) in BiBO [Ghotbi 04b]. We use a 0.5mm thick BiBO crystal phase-matched for SHG around our fundamental wavelength of $\lambda = 795$nm. The details of the phase-matching in BiBO for this process can be found in appendix B.

The fundamental wave interacts with itself due to the second-order non-linear polarization of the medium. We assume that the fundamental wave is composed of a single-mode coherent state and using the relationships between the field around frequency ω_0, the second-order non-linear polarization and the field around frequency $2\omega_0$, we can compute the expected spectral profile of the harmonic field $\tilde{u}_p$ as:

$$\tilde{u}_p(\omega) \propto \int_0^{+\infty} \mathrm{d}\omega' \ \tilde{u}_s(\omega') \ \tilde{u}_s(\omega - \omega') \ \operatorname{sinc}(\Delta k L/2) \tag{2.18}$$

Where $\tilde{u}_s$ is the spectral profile of the fundamental wave. Figure 2.6 shows the spectral profile $\tilde{u}_p$ of the pump assuming $\tilde{u}_s$ to be Gaussian with a FWHM of 11nm according to figure 2.1.

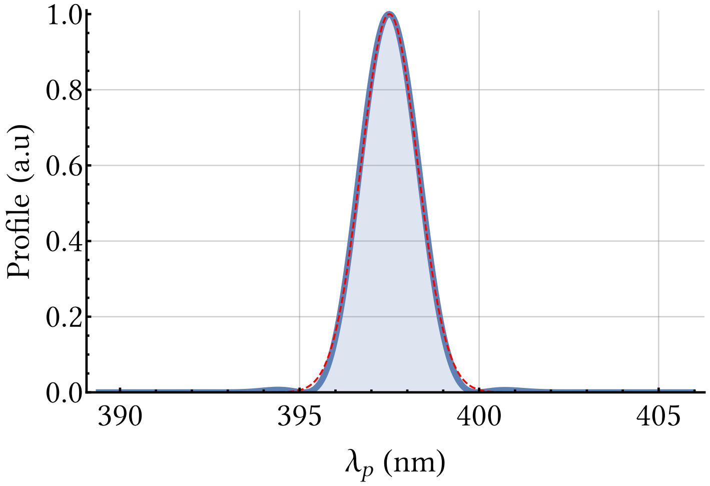

Figure 2.6: Pump spectrum intensity profile $\tilde{u}_p$ obtained from doubling the spectrum presented on figure 2.1 in a 0.5mm crystal of BiBO (blue) and a Gaussian fit of it (dashed red).

A Gaussian fit of the pump spectrum shown on figure 2.6 gives a FWHM of 1.85nm. The phase-matching function Φ_{SHG} is thus too narrow to consider that the doubled spectrum is simply a self convolution product of the spectral profile $\tilde{u}_s$. Indeed, if the phase-matching function was broadband enough, the FWHM of $\tilde{u}_p$ would be equal to the one of $\tilde{u}_s$ divided by $2\sqrt{2}$, hence 3.89nm. This factor comes from the self convolution of a Gaussian. The phase-matching function Φ_{SHG} acts here as a spectral filter.

2.4.3 Single-mode squeezing measurement

Despite the fact that an OPO pumped below threshold is inherently multimode, one may always try to measure the quantum state at the output by mixing it with a Local Oscillator (LO) in a homodyne detection scheme as presented in chapter 3. For this measurement, we use our laser source presented on figure 2.1 as a LO in a scheme shown on figure 2.7.

The noise power in the homodyne detection signal is detected at a single sideband frequency and acquired while the phase between the signal and the LO is swept. The measurement is shown on figure 2.7. It shows the signal alternating between below and above the shot noise power. The average squeezing measured is −2.78dB relatively to shot noise, not corrected from any losses. This result was obtained with diodes whose losses were at least 7% each due to poor quantum efficiency. For information, the best squeezing obtained with the aforementioned diodes was −3.5dB. Some higher squeezing of −5.5dB has been measured with diodes of near unity quantum efficiency (see [Cai 15]) in the same configuration.

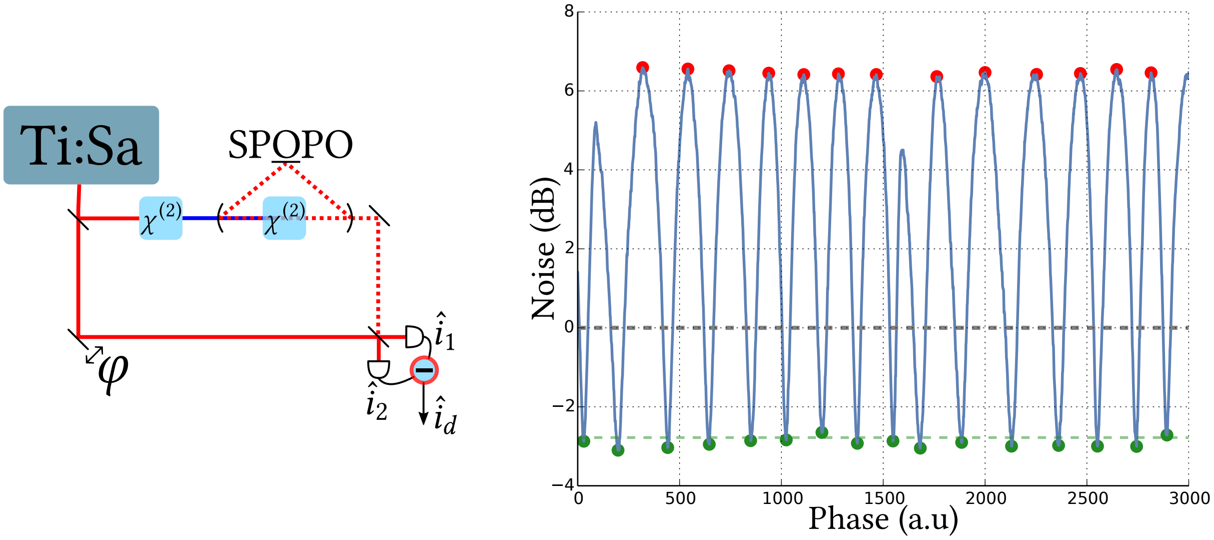

Figure 2.7: Left: Simplified scheme of the experimental setup used to measure the squeezing in the mode of the laser source. Right: Homodyne detection signal at a sideband frequency of 1MHz. The laser source is used as LO.

2.5 Lossless multimode OPO

A multimode description of the OPO has been first developed in [Jiang 12] and reformulated in [Medeiros de Araujo 12]. A description of the temporal properties of the output multimode quantum state can also be found in [Averchenko 11]. In order to provide a description accounting for the multimode aspect of an OPO below threshold, we assume that the optical resonator is lossless. Actually, it is possible to write the squeezing spectrum of a lossy cavity as long as losses are flat over the optical bandwidth. The optical resonator presented on figure 2.2 is modified so that $r_o = 1$ and the output field becomes $\hat{a}_L$.

2.5.1 Degenerate parametric down-conversion in a cavity

The Synchronously Pumped Optical Parametric Oscillator (SPOPO) is an OPO pumped by a frequency comb. The pump comb is generated through the doubling of the laser source as explained in section 2.4.2. The original field is a frequency comb of repetition rate ω_r and Carrier-Envelope-Offset (CEO) ω_{ceo}. The pump field is thus a frequency comb of repetition rate ω_r and Carrier-Envelope-Offset (CEO) $2\omega_{ceo}$ within the spectral envelope presented on figure 2.6.

In our Type-I degenerate Parametric Down-Conversion (PDC), each individual frequency $\omega_{p,i} = i\ \omega_r + 2\omega_{ceo}$ of the pump comb undergoes parametric down-conversion and creates a pair of correlated photons at the optical frequencies of the signal allowed by the optical cavity as illustrated on figure 2.8. For a pump frequency $\omega_{p,i}$, the possible signal frequencies are $\omega_{s,n} = n\omega_r + \omega_{ceo}$ and $\omega_{s,m} = m\omega_r + \omega_{ceo}$ with $m + n = i$ so that the energy is conserved: $\omega_{p,i} = \omega_{s,n} + \omega_{s,m}$.

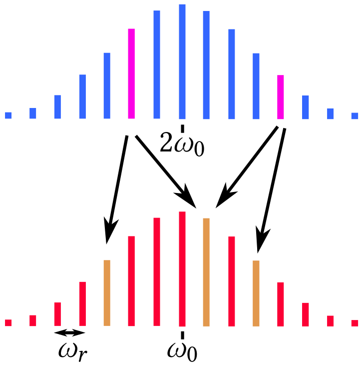

Figure 2.8: Parametric down-conversion from a pump frequency comb into the optical frequencies of the optical resonator.

One can show that the signal frequencies are all entangled with each other resulting in highly multipartite entanglement [Patera 08]. The different possible conversions are governed by the spectral profile $\tilde{u}_p$ of the pump and by the phase-matching function Φ_{PDC}

introduced in appendix B.

2.5.2 Parametric down-conversion in BiBO

We use a 2mm thick BiBO crystal as a gain medium to achieve Type-I degenerate PDC in our OPO. The details of the crystal orientation and phase-matching are also presented in appendix B. The advantage of BiBO is that its high non-linear coefficients allows to produce measurable significant squeezing without the need of a high finesse cavity.

Assessing the phase-matching function $\Phi_{PDC}(\omega_s, \omega_i)$ gives some insight about the correlation (or anticorrelation) between the signal and idler photons, ω_s and ω_i being the frequencies of the signal and idler beam. Figure 2.9 shows the phase-matching function $\Phi_{PDC}(\omega_s, \omega_i)$ for such a crystal where the angle θ of BiBO has been set so that the phase-matching Δk is null for $\lambda_0 = 795$nm.

Figure 2.9 reveals a strong anticorrelation between the signal and idler frequencies as expected from the conservation of energy. The actual range of possible phase-matching is much wider than the optical bandwidth depicted on figure 2.9 and is eventually limited by the decreasing value of the effective nonlinear coefficient of BiBO [Ghotbi 04a]. We will assume a constant non-linear coefficient $\chi^{(2)}$ over our optical bandwidth.

2.5.3 Hamiltonian of the conversion

In order to write the Hamiltonian of the conversion process, we assume the pump beam to be a coherent state. The other states at play having no mean field, we neglect the fluctuations of the pump and keep only the mean field of the pump. We therefore replace its frequency-dependent annihilation operator by its spectral profile $\tilde{u}_p$ in the expression oh the Hamiltonian. We also assume that the depletion of the pump is negligible which, in a weak conversion process, is a very good approximation. We denote $\hat{a}_n^\dagger$ and $\hat{a}_m^\dagger$ the creation operators at the signal frequencies $\omega_{s,n}$ and $\omega_{s,m}$. The Hamiltonian of the PDC described above is then:

$$\hat{H}_{PDC} \propto i \sum_{n,m} \tilde{u}_p(\omega_{s,n} + \omega_{s,m}) \Phi_{PDC}(\omega_{s,n}, \omega_{s,m}) \hat{a}_n^\dagger \hat{a}_m^\dagger + \text{h.c} \tag{2.19}$$

where h.c stands for *Hermitian conjugate*. The coupling function $L_{nm} = \tilde{u}_p(\omega_{s,n}+\omega_{s,m})\Phi_{PDC}(\omega_{s,n}, \omega_{s,m})$ is known as the Joint-Spectral Distribution [Grice 01, Mosley 08] (JSD, otherwise called JSA for Amplitude). It plays a central role in conversion processes and is generally a product of a phase-matching function and the spectral profile of a driving field. It is possible to perform a modal decomposition of this JSD [Eckstein 12, Medeiros de Araujo 12] through Mercer's theorem (in practice, an eigendecomposition) to assess the modal aspect of the process.

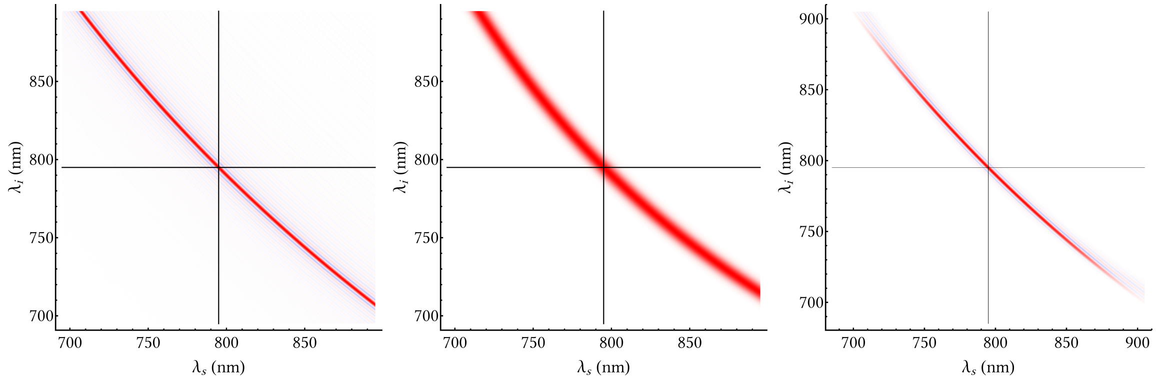

Figure 2.9: Left: Phase-matching function Φ_{PDC} for 2mm of BiBO. Center: Pump spectral profile $\tilde{u}_p$ as a function of λ_s and λ_i. The wavelength range is $\lambda_0 \pm 100$nm. Right: Joint spectral Distribution as a product of Φ_{PDC} and $\tilde{u}_p$. The wavelength range is $\lambda_0 \pm 110$nm. The black lines represent $\lambda_s = 795$nm and $\lambda_i = 795$nm.

2.5.4 Eigenmodes of the conversion

In the present case, the eigendecomposition of L_{nm} gives a set of eigenvalues $\{\Lambda_n\}$ associated with eigenmodes $\{v_n\}$ with their annihilation operators being $\{\hat{s}_n\}$. The Hamiltonian (2.19) becomes:

$$\hat{H}_{PDC} \propto i \sum_n \Lambda_n \hat{s}_n^{\dagger 2} + \text{h.c} \tag{2.20}$$

The evolution operator $\hat{U}_{PDC}$ associated to $\hat{H}_{PDC}$ is then :

$$\hat{U}_{PDC} = \bigotimes_n \hat{S}_n\left(\Lambda_n\right) \quad \text{with} \quad \hat{S}_n\left(\Lambda_n\right) = e^{\kappa \Lambda_n \left(\hat{s}_n^{\dagger 2} - \hat{s}_n^2\right)} \tag{2.21}$$

where κ is a constant that normalizes the distribution of $\{\Lambda_n\}$. It depends linearly on the pump amplitude and the crystal length l_c while the distribution of $\{\Lambda_n\}$ also depends on l_c.

Interestingly, the expression (2.21) shows that a parametric down-conversion process pumped by a frequency comb is equivalent to a set of squeezers in parallel when the down-converted modes are given by the optical resonator. The eigenmodes $\{v_n(\omega)\}$ of the process are called *supermodes* [Medeiros de Araujo 12].

We assume a Gaussian spectral profile in the frequency domain centered on $\lambda_0/2 = 397.5$nm with a FWHM of 1.85nm according to section 2.4.2. The pump spectral profile, the phase-matching function and the JSD are presented on figure 2.9. The eigenvalues and eigenmodes of the JSD are shown on figure 2.10. First, we notice that the sign of the eigenvalues alternates between positive-valued and negative-valued, meaning that the operators $\{\hat{S}_n\}$ squeeze alternatively the quadratures $\hat{X}_n$ or $\hat{P}_n$ of each mode v_n. The first four eigenmodes of the JSD are similar to a family of Hermite-Gaussian functions. A Gaussian fit of the first eigenmode gives a FWHM of about 6.4nm.

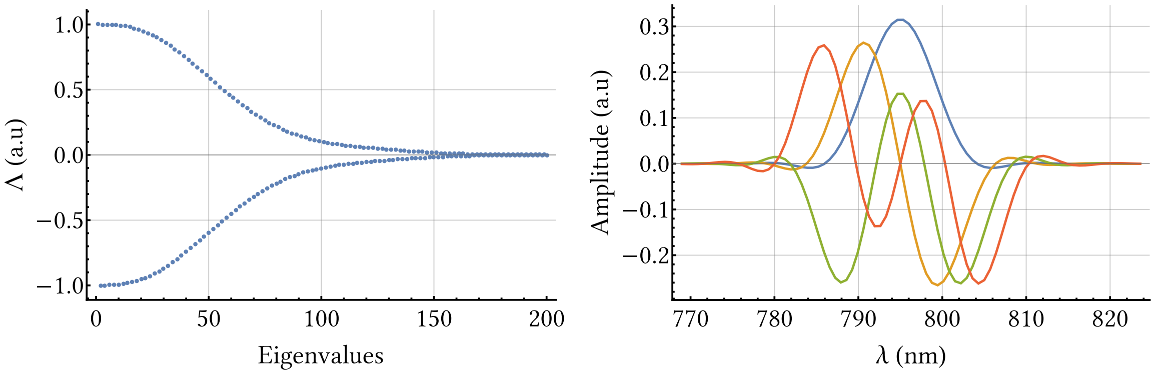

Figure 2.10: Left: Eigenvalues of the JSD $L_{n,m}$ for 2mm of BiBO. Right: First four normalized eigenmodes of the JSD $L_{n,m}$.

2.5.5 Toward a full model of SPOPO

In [Jiang 12] and [Medeiros de Araujo 12], a gap is bridged between the description of the multimode parametric down-conversion presented above and the full interpretation of the SPOPO as a multimode OPO in the spectral domain. To reach that conclusion, it is necessary to assume that optical losses are frequency independent within the optical bandwidth of the phase-matching function Φ_{PDC}. This assumption leads to the spectral eigenmodes of the PDC to be a also eigenmodes of the propagation in the optical resonator. Those eigenmodes of the SPOPO as a whole are frequency combs possessing different spectral envelopes and we call them *supermodes*.

A symplectic description of the SPOPO shows that each of those supermodes interacts independently with the pump beam to create squeezed states. Similarly to an OPO, the squeezed states are hosted in the correlated sidebands of the comb teeth at frequencies inferior to the bandwidth of the optical resonator. The squeezing spectrum is computed in [Medeiros de Araujo 12]. Characterizing such a state is not straightforward are requires the ability to engineer the LO spectrum [Pinel 12] in order to reveal the full multimode nature of the SPOPO output as we will see in the next chapter.

Finally, the theory developed previously fails to account for frequency-dependent losses in the resonator due to limited optical bandwidth and dispersion. We remain confident that this enrichment of the theoretical description may be within reach by adding frequency dependent losses and phase in equation (2.19).

Chapter 3

Tunable Projective Measurements

[About the advantages and trade-offs of blazed and holographic gratings]
“"Ain’t never been about that! Goldie don’t play with no blazed Newport grating! Just use that real good product from Spectrogon!”
– Jonathan “*Goldie*” Roslund

Contents

In this chapter, we explain that the well-known homodyne detection can be adapted to measure and characterize the multimode quantum state predicted in chapter 2. We show that different projective measurements can be performed by adapting the local oscillator of the homodyne detection. We introduce ultrafast pulse shaping as a way to manipulate the spectral phase and amplitude of an ultrafast pulse. We discuss the pulse shaping technique performed in the scope of this thesis and demonstrate how it was used to characterize the multimode quantum state introduced in the previous chapter.

3.1 Homodyne Detection

In this section, we recall why the well-known homodyne detection is adapted to measure and identify any single-mode quantum states of light [Grynberg 10]. We show that it can be easily adapted to measure different modes by tuning the mode of the local oscillator.

3.1.1 Single-mode homodyne detection

In a homodyne detection, a signal beam with an electric field $\hat{\mathbf{E}}_s^{(+)}$ is mixed with a Local Oscillator (LO) field $\hat{\mathbf{E}}_{lo}^{(+)}$ of the same optical carrier frequency ω_0 (otherwise, the detection is called *heterodyne*) on a balanced beamsplitter (see figure 3.1). Both outputs are detected by independent photodiodes of equal characteristics and their photocurrents are subtracted.

According to the beamsplitter equations, the electric field $\hat{\mathbf{E}}_1^{(+)}$ and $\hat{\mathbf{E}}_2^{(+)}$ at the output are:

$$\hat{\mathbf{E}}_1^{(+)} = \frac{1}{\sqrt{2}}\left(\hat{\mathbf{E}}_s^{(+)} + \hat{\mathbf{E}}_{lo}^{(+)}\right) \tag{3.1}$$

$$\hat{\mathbf{E}}_2^{(+)} = \frac{1}{\sqrt{2}}\left(\hat{\mathbf{E}}_s^{(+)} - \hat{\mathbf{E}}_{lo}^{(+)}\right) \tag{3.2}$$

For now, the input fields are assumed to be single-mode and mode-matched, meaning that they share the same spatial mode and temporal mode $u(\boldsymbol{r}, t)$. We thus forget the other modes in their expression and simply write:

$$\hat{\mathbf{E}}_s^{(+)}(\boldsymbol{r},t) = \mathscr{E}_0^{(1)}\hat{a}u(t) \tag{3.3}$$

$$\hat{\mathbf{E}}_{lo}^{(+)}(\boldsymbol{r},t) = \mathscr{E}_0^{(1)}\hat{l}u(t) \tag{3.4}$$

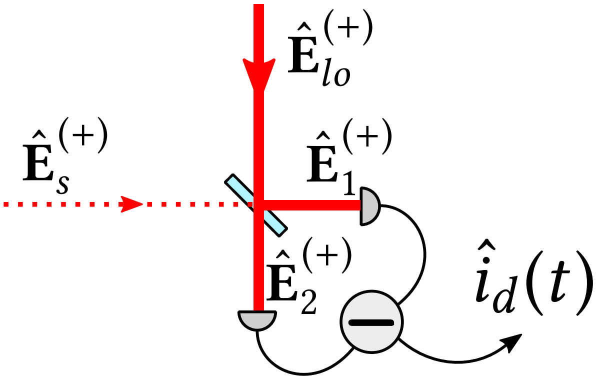

Figure 3.1: Standard homodyne detection scheme.

3.1.1.1 Homodyne photocurrent

Each field $\hat{\mathbf{E}}_1^{(+)}$ and $\hat{\mathbf{E}}_2^{(+)}$ is detected by a photodiode producing a pair of photocurrents $\hat{i}_1$ and $\hat{i}_2$ respectively proportional to $\int \mathrm{d}\boldsymbol{r}|\hat{\mathbf{E}}_1^{(+)}|^2$ and $\int \mathrm{d}\boldsymbol{r}|\hat{\mathbf{E}}_2^{(+)}|^2$. Those photocurrents are subtracted from each other and the difference $\hat{i}_d$ is:

$$\hat{i}_d(t) = \hat{i}_2(t) - \hat{i}_1(t) \propto \int \mathrm{d}\boldsymbol{r} \left(\hat{\mathbf{E}}_2^{(+)}\hat{\mathbf{E}}_2^{(-)}(\boldsymbol{r},t) - \hat{\mathbf{E}}_1^{(+)}\hat{\mathbf{E}}_1^{(-)}(\boldsymbol{r},t)\right) \tag{3.5}$$

$$\propto \mathscr{E}_0^{(1)2}\left[\hat{a}\hat{l}^\dagger + \hat{a}^\dagger\hat{l}\right] \tag{3.6}$$

where every spatial dependence has been integrated over the detectors area.

We can now calculate the expectation value of $\hat{i}_d$ given that the different quantum states for the LO and the signal are a coherent state $|\alpha\rangle_{lo}$ and an arbitrary state $|\psi\rangle_s$. Also, the detection is limited by the bandwidth of electronics so that the electrical signal is average over a time scale much longer than the typical time of the signal temporal mode. The expectation value of $\hat{i}_d$ is then:

$$\langle\hat{i}_d\rangle \propto \mathscr{E}_0^{(1)2}\langle\alpha|_{lo}\langle\psi|_s\left[\hat{a}_s\hat{l}^\dagger + \hat{a}_s^\dagger\hat{l}\right]|\alpha\rangle_{lo}|\psi\rangle_s \tag{3.7}$$

$$\propto \mathscr{E}_0^{(1)2}|\alpha|\langle\psi|_s\left[\hat{a}_s e^{-i\varphi} + \hat{a}_s^\dagger e^{i\varphi}\right]|\psi\rangle_s \tag{3.8}$$

where $\varphi = \mathrm{Arg}(\alpha)$ is the phase of the LO with respect to the signal. We notice that the signal retrieved is proportional to the amplitude $|\alpha|$ of the LO. We have only accounted here for the temporal mode but the same principle is at play for polarization and transverse modes.

3.1.1.2 Measuring the electric field quadratures

The expectation value of $\hat{i}_d$ allows us to measure the expectation value of either the $\hat{X}$ or the $\hat{P}$ quadrature of the signal as:

$$\langle \hat{i}_d \rangle \propto \mathcal{E}_0^{(1)2}\ |\alpha| \langle\psi| \left(\cos(\varphi)\, \hat{X}_s + \sin(\varphi)\, \hat{P}_s\right) |\psi\rangle_s \tag{3.9}$$

Through a similar calculation, we deduce the value of $\langle \hat{i}_d^2 \rangle = \langle \left(\hat{i}_1 - \hat{i}_2\right)^2 \rangle$. For this, we assume that the LO carries a coherent state whose average photon number is much higher photon number than the signal field (i.e. $|\alpha|^2 \gg \langle\psi|\hat{a}^\dagger \hat{a}|\psi\rangle_s$) so that only the term containing the LO energy dominates:

$$\begin{aligned} \langle \hat{i}_d^2 \rangle &\propto \mathcal{E}_0^{(1)4}\ |\alpha|^2\ \langle\psi| \left(e^{-i\varphi}\hat{a} + e^{i\varphi}\hat{a}^\dagger\right)^2 |\psi\rangle_s && (3.10) \\ &\propto \mathcal{E}_0^{(1)4}\ |\alpha_{lo}|^2\ \langle\psi| \left(\cos(\varphi)\, \hat{X} + \sin(\varphi)\, \hat{P}\right)^2 |\psi\rangle_s && (3.11) \end{aligned}$$

We can now compute the variance $\Delta^2 i_d$ of the photocurrent with expressions (3.9) and (3.11). We also introduce a variable quadrature operator $\hat{Q}(\varphi)$ dependent upon the relative phase φ as $\hat{Q}(\varphi) = \cos(\varphi)\, \hat{X} + \sin(\varphi)\, \hat{P}$ so that:

$$\Delta^2 i_d = \langle \hat{i}_d^2 \rangle - \langle \hat{i}_d \rangle^2 \propto \mathcal{E}_0^{(1)4}\ |\alpha_{lo}|^2 \left(\langle\psi|\hat{Q}^2(\varphi)|\psi\rangle_s - \langle\psi|\hat{Q}(\varphi)|\psi\rangle_s^2\right) = \Delta^2 Q(\varphi) \tag{3.12}$$

Expression (3.12) shows that as the assumption over the average photon number holds, the variance $\Delta^2 i_d$ of the difference photocurrent gives a direct measurement of the variance of any quadrature of the signal field depending on φ. For squeezed vacuum and other states of interest, the mean amplitude of the signal field is null and the variance is directly the fluctuations. The fluctuations of the LO have been neglected under the assumption of strong mean field. In a sense, homodyne detection amplifies the fluctuations of the signal field via the LO.

If the signal field is reduced to vacuum, the measurement reveals a flat frequency noise known as shot noise as long as the detection electronics are capable of subtracting the classical (technical) noise potentially contained in the LO. Measuring the shot noise is a direct measurement of the quantum fluctuations of vacuum.

Hence, homodyne detection allows to measure the field quadratures, both in terms of their average value and their fluctuations. For most of the quantum states of light of interest today (see chapter 1), the average photon number is of the order of magnitude of unity and the assumption previously mentioned holds for a LO of weak optical power (about 1mW or less).

3.1.2 Homodyne detection as a projective measurement

An interesting feature of homodyne detection is the optical mode investigated is exactly the one of the LO where there is a mean field. We change the expression of the signal and LO fields to multimode fields.

$$\hat{\mathbf{E}}_s^{(+)}(\boldsymbol{r},t) = \mathscr{E}_0^{(1)} \sum_n \hat{a}_n u_n(\boldsymbol{r},t) \tag{3.13}$$

$$\hat{\mathbf{E}}_{lo}^{(+)}(\boldsymbol{r},t) = \mathscr{E}_0^{(1)} \sum_n \hat{l}_n v_n(\boldsymbol{r},t) \tag{3.14}$$

We also assume that only one mode $v_0(\boldsymbol{r},t)$ of the LO hosts a coherent state $|\alpha\rangle$ with a significant mean field, the rest being vacuum. The signal contains a pure multimode state $|\Psi\rangle_s$. We introduce a new quadrature operator $\hat{Q}_n$ for each mode $\{u_n\}$ of the signal as: $\hat{Q}_n(\varphi) = \cos(\varphi)\,\hat{X}_n + \sin(\varphi)\,\hat{P}_n$ where $\hat{X}_n$ and $\hat{P}_n$ are the quadrature operator of the mode $u_n(\boldsymbol{r},t)$. Starting back from equation (3.5), equations (3.9) and (3.11) become:

$$\langle\hat{i}_d\rangle \propto \mathscr{E}_0^{(1)2}\ |\alpha|\langle\Psi|\left(\sum_n |\langle u_n, v_0\rangle|\hat{Q}_n(\varphi_n)\right)|\Psi\rangle_s \tag{3.15}$$

$$\langle\hat{i}_d^2\rangle \propto \mathscr{E}_0^{(1)4}\ |\alpha|^2\langle\Psi|\left(\sum_n |\langle u_n, v_0\rangle|\hat{Q}_n(\varphi_n)\right)^2 |\Psi\rangle_s \tag{3.16}$$

with $\varphi_n = \varphi + \text{Arg}(\langle u_n, v_0\rangle)$ and the scalar product $\langle u_n, v_0\rangle$ being defined in chapter 1. Similarly to the single-mode case, the last two equations lead to the variance $\Delta^2 i_d$ of the photocurrent to be proportional to the variance of the weighted sum of the $\hat{Q}_n(\varphi_n)$ operators.

The equations above show that by changing the temporal mode $v_0(\boldsymbol{r},t)$ of the LO, one can change the optical mode of the signal that is measured by the homodyne detection. Homodyne detection is thus appropriate to measure multimode quantum state when paired with a mode tuning device for the LO such as an ultrafast pulse-shaper that we describe later in section 3.2. We have only accounted here for the temporal and spatial mode but the same principle is at play for polarization.

3.1.2.1 Dynamical properties

Depending of the type of temporal mode of the signal that must be measured, the detection electronics must be adapted. For instance, in a pulsed single-pass setup, it is necessary to assess the quantum properties of a single pulse of light at a potentially fast repetition rate. For this purpose, a fast and broadband homodyne detection electronics is required [Cooper 13]. In the case of our SPOPO, the modes can be analysed at different sideband frequencies below the cavity bandwidth [Pinel 12]. It is then possible to measure the state at a single analysis frequency (either by demodulating or using a spectrum analyzer) and a resonant circuit at the analysis frequency can be used to improve the clearance of the detection electronics.

3.2 Ultrafast Pulse Shaping

Ultrafast pulse-shaping is a technique consisting in manipulating the temporal variation of the amplitude and phase of an optical pulse. It was originally developed for optical communications [Heritage 85] with picosecond pulses and has then been applied to femtosecond pulses [Weiner 88]. It has since found various applications everywhere ultrafast pulses are used [Weiner 00, Weiner 11a]. For pulses of light shorter than a fraction of a picosecond, it is not reasonable to try to shape a light pulse in the time domain directly [Wright 15]. Ultrafast pulse-shaping relies on the independent engineering of the optical frequencies composing a pulse. In ultrafast optics, a pair of identical prisms (more often gratings) are commonly employed for their dispersive properties to add or remove some quadratic phase from an ultrafast pulse [Weiner 11b]. Those devices are called optical compressors or optical stretchers depending on the sign of the quadratic phase. In this thesis, we use a Spatial Light Modulator (SLM) placed at the end of a folded $4f$ zero-dispersion optical compressor based on near-Littrow gratings. An extensive tutorial detailing this technique can be found in [Monmayrant 10].

Figure 3.2 details the optical setup used to achieve phase and amplitude shaping through diffraction by the 2D phase mask of the SLM. At first, a reflective grating diffracts a collimated input beam using the -1 order of diffraction. The different wavelengths and their wave vectors $\mathbf{k}(\lambda)$ are diffracted in different directions $\theta_{out}(\lambda)$ around $\theta_{out}(\lambda_0)$ corresponding to $\mathbf{k}(\lambda_0)$ according to the grating law:

$$\sin\left(\theta_{out}(\lambda)\right) = -\sin\left(\theta_{in}\right) + m\lambda g \tag{3.17}$$

where θ_{in} is the input angle on the grating, $m = -1$ is the order of diffraction and g is the number of grooves per mm of the grating. The separation of optical frequency is only angular at this point. Then, a cylindrical lens of focal f (preferably a mirror to avoid any additional dispersion and for ease of alignment) images the grating so that the different wave vectors $\mathbf{k}(\omega)$ are parallel. The 2D mask of a SLM is set in the focal plane where the different optical frequencies are mapped to space horizontally. If the SLM reflects light like in our setup, the beam returns on its initial path. A slight vertical tilt of the SLM surface allows to pick up the output beam once the wave vectors have been recombined together by the grating. A description of the step-by-step alignment of such a setup can be found in [Weiner 00].

If the SLM transmits light, a symmetric optical setup must be built after the SLM to combine the different wave vectors $\mathbf{k}(\omega)$ along a single direction. This solution suffers from the difficulty to easily tune the optical compressor to avoid the spatiotemporal distortion of the ultrafast pulses as we will discuss later.

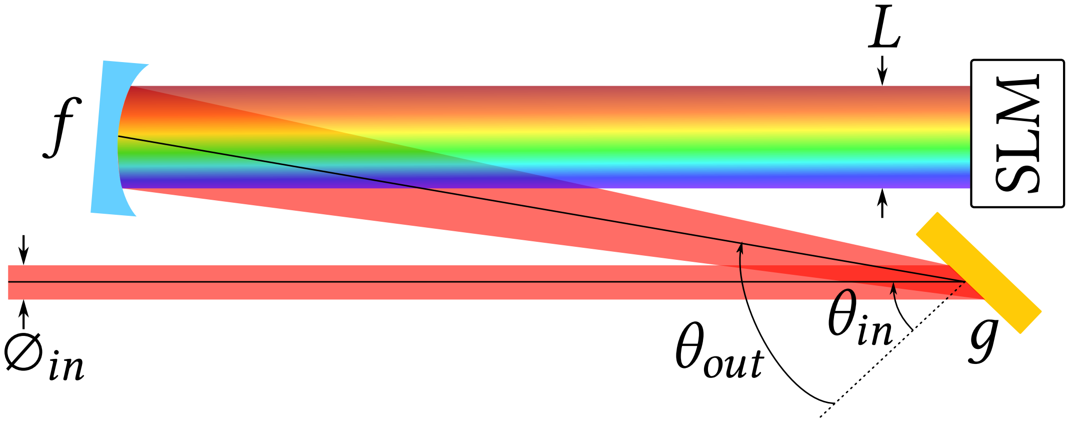

Figure 3.2: Optical pulse-shaper in a near-Littrow $4f$ line. It consists of a grating with g grooves per mm, a cylindrical mirror of focal f and a SLM whose mask size is L.

3.2.1 Diffraction-based amplitude shaping

With the previous configuration, the different wavelengths are mapped horizontally on the SLM while the input beam vertical profile has not been transformed by the $4f$ line. At this point, the spectral phase can be controlled by adjusting the voltage of an entire column of pixel.

3.2.1.1 Effect of a linear phase

It is possible to achieve amplitude shaping by diffracting the beam reflected by the SLM. Let us consider the vertical transverse profile of the collimated beam at the center: $\mathrm{E}(y) \propto \exp\left(-y^2/w_{in}^2\right)$ where w_{in} is the input beam waist. During the reflection on the mask, it acquires a linear spatial phase $\phi(y) = k_0 y$ where k_0 has the dimension of a wave vector. In the Fourier space, the vertical part of the beam is:

$$\mathrm{E}(k_y) \propto \int_{-\infty}^{\infty} \frac{\mathrm{d}y}{\sqrt{2\pi}} \mathrm{E}(y) e^{i\left(k_0 - k_y\right)y} \propto e^{-\left(k_0 - k_y\right)^2} \tag{3.18}$$

The beam coming out of the pulse-shaper is propagating into an order of diffraction determined by the value of k_0. The phase mask then behaves like a tilted mirror. By adjusting k_0 for different columns of pixels and selecting a given order of diffraction with a spatial filter in the Fourier plane (with an optical telescope and a pinhole for instance), it is possible to achieve amplitude shaping.

3.2.1.2 Effect of a blazed grating structure

It is shown in [Vaughan 05] that a phase mask consisting of a blazed grating structure allows to conveniently shape both the spectral phase and amplitude. The phase $\phi(y)$ is wrapped (the SLM dynamics being limited to 2π) to form a sawtooth grating of period d. For such a grating, the direction of the first order of diffraction is only determined by the grating period d (or the number of grooves g per mm). Indeed, the phase mask $M(\omega, y)$, where the x dimension has been replaced by the optical frequencies ω, applied on the SLM is:

$$M(\omega, y) = 2\pi \left(\frac{1}{2} + A(\omega) \sum_{n=-\infty}^{\infty} f_d \left(y - \frac{d\phi(\omega)}{2\pi} - nd \right) \right) \tag{3.19}$$

where $A(\omega)$ is the amplitude ($0 \leq A(\omega) \leq 1$) of the grating for the frequency ω, f_d is a standard sawtooth function of period d ($-1/2 \leq f_d(y) \leq 1/2$ for $y \in [0, d]$) and $\phi(\omega)$ is the desired phase for the frequency ω. The periodic sawtooth function f_d and the phase mask M are represented on figure 3.3.

We can compute the field $\mathrm{E}(k_y, \omega)$ in the Fourier plane for a single optical frequency ω assuming a plane wave at the input and an infinite grating for simplicity. In the Fourier plane, the field $\mathrm{E}(k_y, \omega)$ is:

$$\mathrm{E}(k_y, \omega) \propto \int_{-\infty}^{\infty} \frac{\mathrm{d}y}{\sqrt{2\pi}} \exp\left(-ik_y y + iM(\omega, y)\right) \tag{3.20}$$

$$\propto \exp\left(-i\phi(\omega)\right) \operatorname{sinc}\left(\pi A(\omega) - \frac{k_y d}{2}\right) \sum_{n=-\infty}^{+\infty} \delta\left(k_y - \frac{2\pi n}{d}\right) \tag{3.21}$$

Expression (3.21) shows that the orders of diffraction only depends on the period of the grating d. Also, as shown in [Vaughan 05], the amplitude $A(\omega)$ of the grating controls the amplitude-shaping while the phase $\phi(\omega)$ of the grating creates a relative phase for the diffracted light at the optical frequency ω.

It is possible to model the effect of the finite size of the phase mask. The sum of δ functions in expression (3.21) is changed for a function of the mask size $L = Nd$, where N is the number of grating structures. This function[1] creates some potential overlap between orders of diffraction for small values of N. It is also possible to assume that the input beam transverse profile is Gaussian and that the mask size is finite but the analytical calculation becomes less meaningful. On top of the non-zero widths of the orders of diffraction due to the finite mask, the Gaussian transverse profile induces an additional width for each order of diffraction. A numerical simulation is required to make sure that in the Fourier space (or in the focal plane of the spatial filter), the different orders of diffraction do not overlap.

3.2.1.3 Efficiency of diffraction

The efficiency of diffraction in first order depends on the capability of the SLM to create the periodic sawtooth function. The phase-mask suffers from many imperfections such as

---

[1] is exactly $\exp\left(-ik_y d\frac{(N-1)}{2}\right) \sin\left(k_y dN/2\right) / \sin\left(k_y d/2\right)$, which tends to a sum of δ functions for $N \to \infty$

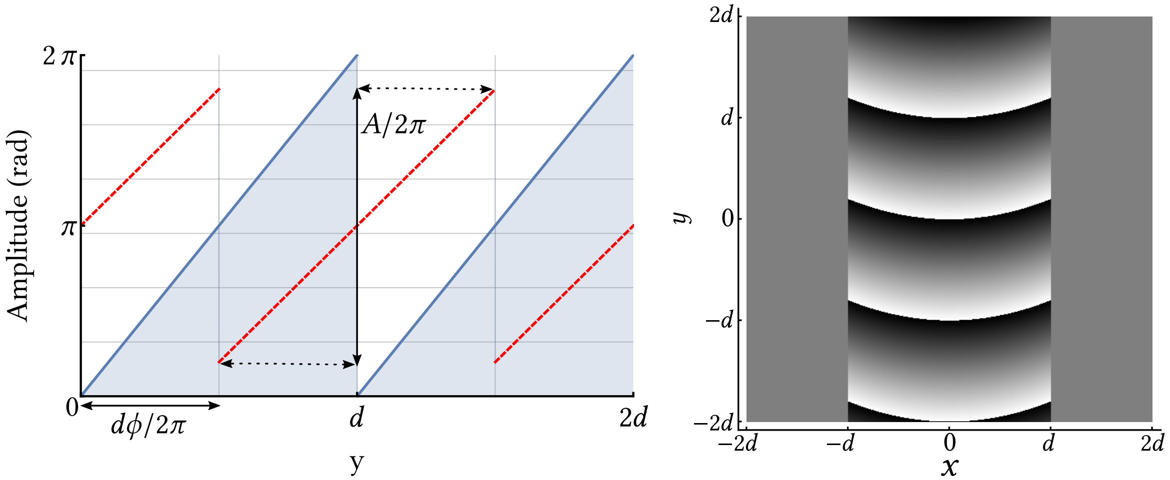

Figure 3.3: Left: the sawtooth structure printed on a single column of pixels. The dashed red curve represent a grating structure of the same period with reduced amplitude $A = 0.8$ and a phase $\phi = \pi$. Right: the 2D phase mask printed on the SLM for a grating structure with only four phase wraps (white is 0, black is 2π). The light is diffracted in the direction of the negative y. We added a flat phase mask for $|x| > d$ so that the light in those regions is not diffracted. We also added a quadratic spectral phase for $|x| < d$.

pixel sampling and dependence of the pixels to their nearest neighbors. For those reasons, it becomes quite challenging for a SLM to mimic a blazed grating structure when the period becomes short.

The decay of the efficiency of diffraction is shown on Figure 3.4. Notice that for up to 10 phase wraps printed on the SLM, the efficiency of diffraction in the first order is almost constant.

3.2.1.4 Advantages of diffraction-based pulse-shaping

As explained in [Vaughan 05], this technique is free of short time temporal pulse replicas generally encountered in previous techniques used to shape both the amplitude and spectral phase [Weiner 92, Wefers 95]. Another advantage of this diffraction-based technique is that the spatial filter only lets the first order of diffraction pass through. If no grating structure is printed, no light will pass through the spatial filter. It is thus a zero-background technique.

3.2.2 Pulse-shaper design

In this section, we explain how to choose the optical elements to build a diffraction-based pulse-shaper with maximal resolution in a $4f$ configuration. The optical setup must preferably be compact for stability and easy to build with in-stock optical parts.

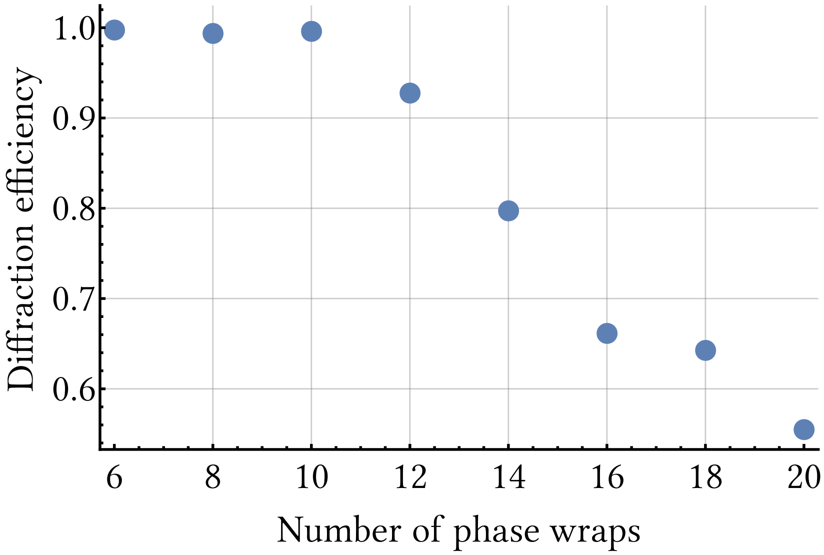

Figure 3.4: Evolution of the efficiency of diffraction in the first order with the number of phase wraps of the grating printed on the SLM. The efficiencies are normalized to the efficiency for 6 phase wraps.

3.2.2.1 Parameters and objectives

We assume that the SLM is chosen and we use the data of our P512-0785 BNS SLM whose meaningful parameters are:

- the physical size of the phase mask: $L = 7.65\text{mm}$,
- the number of pixels: $N_p = 512$,
- the characteristics of our laser source such as its carrier wavelength $\lambda_0 = 795\text{nm}$ and its FWHM, here $\Delta\lambda = 11\text{nm}$.

The free parameter that we need to determine are the number of grooves g of the grating, the cylindrical mirror focal length f and the input beam diameter[2] $2w_{in}$. Manufacturers usually provide stock gratings with $100 \leq g \leq 2000\text{mm}^{-1}$ and cylindrical mirrors with $100 \leq f \leq 5000\text{mm}$. A quick analysis can help determine the most convenient pair of values for g and f. Commercially available values can then be chosen and tested with the same equations and principles described below.

The optical setup will spread optical frequencies horizontally and focus them in the focal plane while letting the beam unchanged vertically. The objectives and constraints are the following:

---

[2] The beam diameter is defined as twice the beam waist and known as the intensity full width at 13.5% (e^{-2}).

- spread the input spectrum on the phase mask to maximize spectral resolution without clipping,
- fit the vertical profile of the beam within the phase mask to avoid losses and scattering by the edges,
- maximize the optical resolution of the imaging system.

Additionally, the angles must be kept small to avoid spatial chirp as we will explain in section 3.2.3. For this reason, the grating is operated near Littrow configuration.

3.2.2.2 Finding a grating/mirror pair

We need to determine first an approximate pair of values for f and g with which we will check wether all objectives can be met within acceptable bounds. We can do that while trying to achieve the first objective.

We can reformulate equation (3.17). First we need to compute the input and output angles θ_{in} and θ_{out}. The grating is used in a near-Littrow configuration. The Littrow angle θ_{Lit} for a blazed grating depends on the blazed design wavelength λ_d. We can approximate by using the formula for an holographic grating with g grooves:

$$\theta_{Lit}(\lambda) = \arcsin\left(\frac{\lambda g}{2}\right) \tag{3.22}$$

For the input and output angles, we can tolerate a ±5° deviation from Littrow. Equation (3.17) becomes:

$$g\Delta\lambda = 2\cos\left(\theta_{out}(\lambda_0)\right)\sin\left(\frac{\Delta\theta_{out}}{2}\right) \tag{3.23}$$

where $\Delta\theta_{out}$ is the angular spread of the diffracted angles $\theta_{out}(\lambda)$ corresponding to the FWHM $\Delta\lambda$. The spatial spread Δl at the mirror corresponding to this angular spread is:

$$\Delta l = f\tan\left(2\arcsin\left(\frac{\Delta\lambda g}{2\cos\left(\theta_{out}(\lambda_0)\right)}\right)\right) \tag{3.24}$$

After the mirror, the different wave vectors $\mathbf{k}(\lambda)$ are parallel and the spatial separation that corresponds to $\Delta\lambda$ is Δl. We can then compute the ratio $\Delta l/L$.

Assuming the distribution is Gaussian, Δl is here the FWHM associated to $\Delta\lambda$. To fit the Gaussian over a length L, we use the 6σ rule where σ is the standard deviation of the distribution. This rule states that about 99% of the energy will be within L for $L = 6\sigma$. In terms of FWHM, it is equivalent to $\Delta l = L\sqrt{2\log(2)}/3 \approx 0.39$. Figure 3.5 shows the focal length f as a function of g where we have assumed $\Delta l/L = \sqrt{2\log(2)}/3$. Thanks to figure 3.5, we can choose a pair of off-the-shelf available values for f and g keeping in mind the constraints of space on an optical table. Also, the shorter f, the more compact and stable the pulse-shaper will be. For our pulse-shaper, we have chosen a blazed grating (contrary to what the introduction quote might suggest) of $g = 1200$ grooves per mm^{-1} whose blazed design wavelength is $\lambda_d = 1\mu\text{m}$ and a cylindrical mirror of $f = 190\text{mm}$.

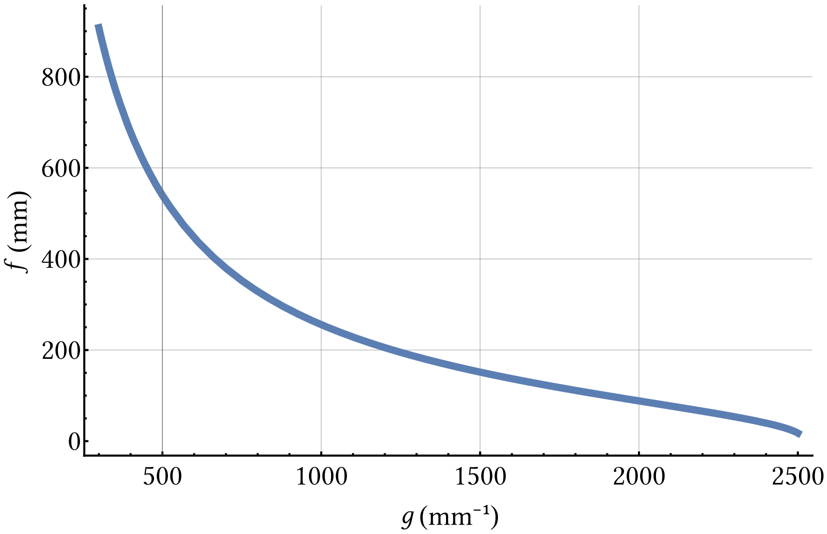

Figure 3.5: Focal length f as a function of g, assuming the spatially spread spectrum fits within the SLM length L according to the 6σ rule.

3.2.2.3 Assessing optical performance

With the parameters determined in the previous paragraph, we check that the two other objectives mentioned previously are met and the constraints are respected. We consider an input collimated beam of waist w_{in} with a single optical frequency ω_0. The grating diffracts the beam and the cylindrical mirror images it on the SLM thus forming a vertical line. We compute the ratio between the waist w_f of the focused beam at the focal plane[3] and the size of a pixel $p = L/N_p$. This ratio is a direct estimate of the optical resolution of the setup. According to the figure 3.2, this ratio is:

$$w_f/p = \frac{\lambda_0 f}{\pi w_{in} p} \times \frac{\cos(\theta_{in})}{\cos(\theta_{out}(\lambda_0))} \tag{3.25}$$

Ideally, this ratio would be equal to unity or slightly inferior to ensure that the focal spot is contained in a pixel. The evolution of this ratio is shown on figure 3.6.

For the values of f and g of our setup, the value of w_{in} required to have $2w_f/p = 1$ is 7.7mm.

Vertically, the beam is not transformed by the setup so its diameter is still $2w_{in}$ in the focal plane. As the SLM is only reflective within the size of its phase mask, the vertical spatial profile of the beam must be contained within the phase mask to avoid any additional losses and diffraction by the edges of the mask as stated in the second objective. The SLM size L thus constitutes an upper bound for w_{in}.

---

[3] The half-width in terms of intensity half-width at 13.5% of the vertical line.

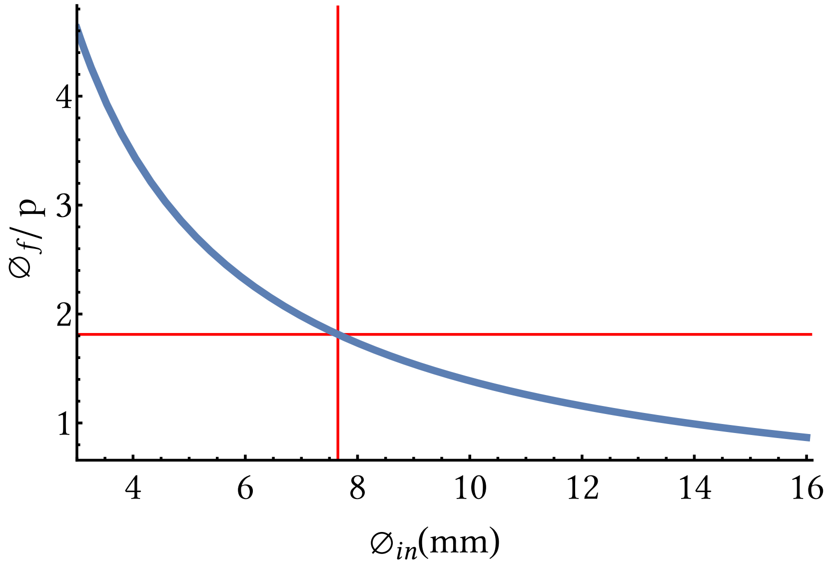

Figure 3.6: Ratio of focal spot diameter $\varnothing_f$ and pixel size p versus input beam diameter $\varnothing_{in}$. Red lines: SLM size L (vertical), ratio for $\varnothing_{in} = L$ (horizontal).

The input diameter computed to achieve $2w_f/p = 1$ is well beyond L and is thus unrealistic. For an input diameter of 7mm, we get $2w_f/p = 1.98$ which means that a single-wavelength spot in the focal plane is more or less spread onto 2 pixels. It is the optical resolution of the setup.

The spectral resolution can be estimated accounting that the setup was designed according to the 6σ rule. Indeed, we have assumed that the spectrum of the input beam of FWHM $\Delta\lambda$ would be spread horizontally on the SLM so that L would be equal to 6σ of the spatial distribution. The spectral resolution R_s can be estimated as:

$$R_s = \frac{3\Delta\lambda}{N_p\sqrt{2\ln 2}} \approx 2.5\frac{\Delta\lambda}{N_p} \tag{3.26}$$

For our setup, we have $R_s = 0.054$nm meaning that a single pixel represents about an eighteenth of a nanometer. This spectral resolution is limited by the optical resolution if the focal spot diameter is bigger than a pixel. It is the case of our setup where the actual spectral resolution is $2w_f R_s/p = 0.10$nm.

3.2.3 Potential problems

In ultrafast optics, a number of specific problems can appear on top of the common ones encountered in CW optics.

3.2.3.1 Optical losses

First, the technique described above is not unitary when it comes to amplitude shaping. Amplitude shaping basically consists in introducing frequency-dependent losses. If the optical beam to be shaped carries some loss-sensitive quantum states such as squeezed vacuum or Fock states (with more than a single photon), amplitude shaping is probably not adapted.

Even for phase shaping only, the technique suffers from the important optical losses of the grating whose diffraction efficiency is currently about 80% and can hardly be better than 90%. The surface of the SLM is also lossy (about 2%) even if a suited dielectric mirror is located behind the liquid crystal. When used in the diffraction-based phase and amplitude shaping configuration explained above, the diffraction efficiency of the SLM is also a source of losses as it rarely exceeds 90%. On top of those losses come additional ones when a spatial filter is required to separate the shaped light from the remaining original one. This technique is thus appropriate in situations where roughly 50% losses can be tolerated.

3.2.3.2 Scattering by the mask

Even if the phase mask composed of liquid crystals is fairly transparent, the presence of pixels along with the edges of the mask constitute a source of scattering. If the input light transverse profile is a well collimated Gaussian, the output profile may contain light in some Fourier components that were previously empty. When the pulse-shaper is paired with a spatial filter to achieve amplitude shaping, the filter lets only the ±1 order of diffraction pass. Some scattered light may still pass through the filter even for a grating amplitude $A(\omega) = 0$. The technique is eventually not exactly zero-background and the weak scattered light passing trough the filter may become comparable to the signal for low values of $A(\omega)$.

3.2.3.3 Output beam geometry

The folded optical compressor composing the pulse-shaper separates a collimated beam composed of many wave vectors $\mathbf{k}(\omega)$ traveling in the same direction, first angularly, then spatially. Those different optical frequencies must be recombined in a collimated beam at the output. If the distance between the cylindrical mirror and the SLM is not perfectly f, some geometric problems may appear in the output beam. The first problem is that the output beam will not be collimated. This distance can be roughly adjusted with the laser source operating CW until the output beam is sufficiently collimated.

Then, one must check that the different wave vectors $\mathbf{k}(\omega)$ are recombined in the same direction. If not, the different wave vectors associated to different optical frequencies propagate in different direction. This phenomenon is known in ultrafast optics as *angular chirp* and is commonly created by dispersive optical elements. It can be measured with a spectrometer placed after an optical telescope by moving a pinhole located near the Fourier plane and monitoring any change of spectrum. Some angular chirp in the horizontal direction generally comes from a slight mismatch of the distance between the cylindrical mirror and the SLM. For angular chirp in the vertical direction, the grating should probably be adjusted to make sure its lines are perfectly perpendicular to the plane of the input beam.

3.2.3.4 Temporal chirp

Once all geometrical problems are solved, temporal problems can still arise. Though, if the distance l between the grating and the lens is not exactly equal to the focal length f, the compressor creates a quadratic spectral phase ϕ'' whose expression is:

$$\phi'' = \frac{\lambda_0^3 g^2 (l - f)}{\pi c^2 \cos^2\left(\theta_{out}(\lambda_0)\right)} \tag{3.27}$$

where g and θ_{out} are defined above.

This temporal chirp can be measured with a self-referencing technique such as spectral interferometry [Lepetit 95, Weiner 11b] or a Frequency-Resolved Optical Gating (FROG) technique [Trebino 93, Trebino 02]. To check that no quadratic phase is added by the optical compressor, one can adjust the distance between the grating and the cylindrical mirror in the setup described on figure 3.2.

3.2.4 Dual beam pulse-shaping

As we will see in chapter 5 and 6, we needed two independent shaped beams instead of only one as in [Medeiros de Araujo 12] and [Cai 15]. A simple solution is to build a second pulse-shaper. While being expensive, this solution is space-consuming, space being a critical resource on an optical table. We explain in the following subsections how we achieved an independent dual beam shaping.

3.2.4.1 Do not try this (it does not work)

The perfect solution to the aforementioned problem is to find a phase mask that could be put onto the SLM and would turn a single light beam (the previous optical configuration) into two independent light beam at the output. Unfortunately, we will see that this transformation is not unitary and should consequently suffer from losses. Indeed, if the field profile $\tilde{\mathrm{E}}(k_y)$ in the Fourier space is a couple of equally spaced Gaussian, we can compute the inverse Fourier Transform to retrieve the field $\mathrm{E}(y)$ at the SLM surface:

$$\tilde{\mathrm{E}}(k_y) \propto \left(e^{-(k_y-k_0)^2/4\Delta k^2} + e^{-(k_y+k_0)^2/4\Delta k^2}\right) \tag{3.28}$$

$$\begin{aligned} \mathrm{E}(y) &\propto \int_{-\infty}^{\infty} \tilde{\mathrm{E}}(k_y) e^{ik_y y} && (3.29) \\ &\propto \cos\left(2k_0 y\right) e^{-4y^2\Delta k^2} && (3.30) \end{aligned}$$

In the expression (3.30) above, the exponential is the Gaussian transverse profile of the input beam. The cosine though can be interpreted as an amplitude and phase mask, its negative sign being a π phase. As its absolute value is less than unity, losses are necessarily required in order to turn one beam into two diffracted beams in ± 1 orders at the output.

To obtain two independent, phase and amplitude shaped beams at the output, we tried two different types of phase masks. A first one, were the phase mask was composed of two sawtooth gratings diffracting light respectively in the $+1$ and -1 orders. The two gratings were printed by alternating one row of pixels out of two for each. The second attempt was to print a triangular grating consisting of two sawtooth gratings back to back, each missing one tooth out of two.

For each order of diffraction (± 1), those two solutions can be seen as two standard sawtooth gratings modulated by an array of lossy slits. In the first case, the slits have the width of a pixel and are spaced by the size of a pixel. In the second case, the slits have the widths corresponding to the grating period d and are separated by d. The arrays of lossy slits introduce higher orders of diffraction in each order leading to extra losses.

At the end of the day, none of those solutions proved reliable to achieve independent diffraction-based pulse shaping simply in terms of diffracted power. We thus decided to inject two identical beams in the pulse-shaper as described in the next section.

3.2.4.2 What works

After trying the aforementioned shaping techniques to turn one beam into two, we decided to simply duplicate the input beam with a polarizing beamsplitter and a waveplate to adjust the relative power. Those two identical beams were overlapped horizontally while being spatially separated but close along the vertical direction. They were brought together and made parallel before being injected in the pulse shaper. The upper beam uses only the upper half of the SLM while the lower one uses only the lower half as depicted on figure 3.7.

To achieve this, the input beam size was downsized by half, impacting the optical resolution of the pulse shaper. The new input beam diameter is $\varnothing_{in} = 3.5$mm. The expected optical resolution then drops by half as the ratio $\varnothing_f / p$ becomes 3.96. In the plane of the SLM, the horizontal diameter of a single-wavelength focal spot is now spread on 4 pixels. The spectral resolution R_s remains the same but is limited by the new optical resolution.

Those optical capabilities can be assessed experimentally. For the spectral resolution, a standard sawtooth grating is printed and modulated horizontally by a regular array of slits. The first order of diffraction is sent to a spectrometer and the position of the peaks allow to check the spectral resolution R_s as shown on figure 3.8. The measurement gives .056nm per pixel, very close to what was predicted by equation (3.26).

To asses how limiting the optical resolution is, we print a standard sawtooth grating on a single column of pixels and feed the diffracted light to a spectrometer as shown on figure 3.8. A Gaussian fit of the peak gives a diameter of .24nm, meaning that it is the smallest feature that can be reasonably shaped. This value coincide with the previous prediction of

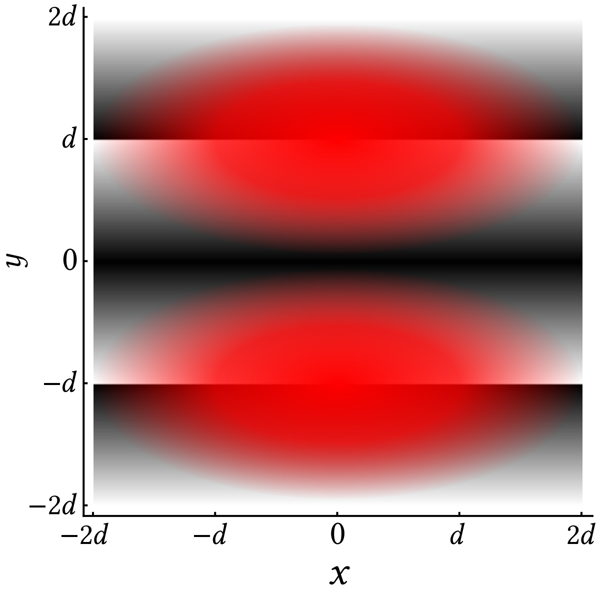

Figure 3.7: Phase mask of the SLM with a two-parts grating structure with only 4 wraps (white is 0, black is 2π) along with the two beams being spread on the SLM surface. The lower part diffracts the lower beam in the direction of negative y ($k_y = -2\pi/d$) and the upper part diffracts the upper beam in the direction of positive y ($k_y = 2\pi/d$).

equation (3.25) that the $\varnothing_f/p$ ratio should know be about 4.

Once the optical pulse shaper is built and potential problems are eliminated, it is necessary to check its capacity to achieve both phase and amplitude shaping. Amplitude shaping can be easily checked by sending the first order of diffraction to a spectrometer as demonstrated on figure 3.8. For phase shaping, a phase-retrieval measurement such as spectral interferometry [Lepetit 95, Weiner 11b] is required. It is usually the final performance check for an optical pulse-shaper.

3.3 Measuring multimode squeezed vacuum

As underlined above, homodyne detection is able to measure the fluctuations in the quadratures of a signal field whose optical mode matches the one of the LO. By tuning the LO temporal mode with a pulse shaper (see section 3.2), one may investigate a spectrally multimode quantum state such as the one described in chapter 2. The measurement scheme is similar to the one pictured on figure 2.7 with an additional diffraction-based pulse shaper in the lower arm.

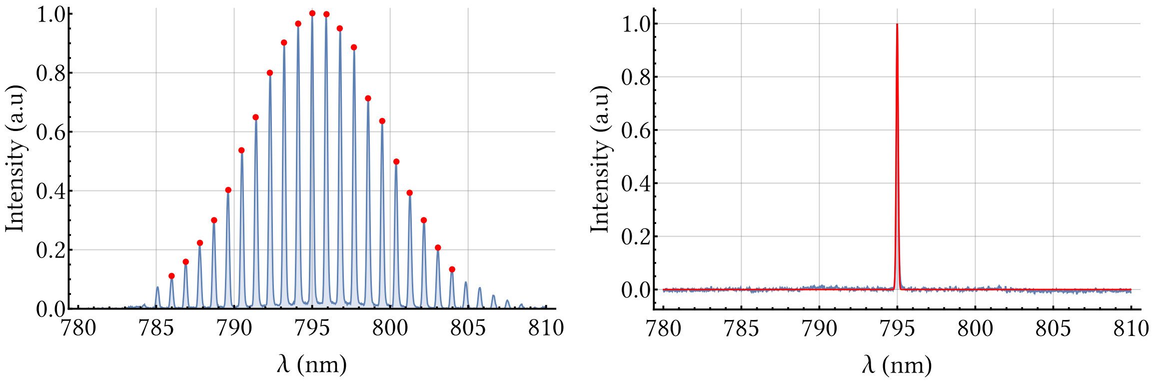

Figure 3.8: Left: Spectrum diffracted (blue) in first order by a sawtooth grating modulated horizontally by losses to assess the spectral resolution. The peak detected for the computation are marked as red dots. Right: Spectrum diffracted (blue) in first order by a single column of pixels and its Gaussian fit (red) to assess optical resolution.

3.3.1 Principle

As the expected multimode state to measure is Gaussian, it can be fully characterized by its covariance matrix $\mathbf{\Gamma}$ in a basis of measurement modes $\{\boldsymbol{m}_i\}$. For each mode $\boldsymbol{m}_i$, the fluctuations of both quadratures $\langle \hat{X}_i^2 \rangle$ and $\langle \hat{P}_i^2 \rangle$ is measured. To measure the correlations between different modes, we measure the fluctuations $\langle \hat{X}_{ij}^2 \rangle$ and $\langle \hat{P}_{ij}^2 \rangle$ of a new set of quadratures [Roslund 13, Medeiros de Araújo 14] belonging to a set of modes $\{\boldsymbol{m}_{ij}\}$ formed by the former basis and defined as:

$$\boldsymbol{m}_{ij} = \frac{\sqrt{\mathcal{P}_i}\boldsymbol{m}_i + \sqrt{\mathcal{P}_j}\boldsymbol{m}_j}{\sqrt{\mathcal{P}_i + \mathcal{P}_j}} \tag{3.31}$$

where $\mathcal{P}_i$ and $\mathcal{P}_j$ are the optical powers in modes $\boldsymbol{m}_i$ and $\boldsymbol{m}_j$ which are a priori not balanced during the measurement. The quadrature operators $\hat{X}_{ij}$ and $\hat{P}_{ij}$ associated to the mode m_{ij} being:

$$\hat{X}_{ij} = \frac{\sqrt{\mathcal{P}_i}\hat{X}_i + \sqrt{\mathcal{P}_j}\hat{X}_j}{\sqrt{\mathcal{P}_i + \mathcal{P}_j}} \quad \text{and} \quad \hat{P}_{ij} = \frac{\sqrt{\mathcal{P}_i}\hat{P}_i + \sqrt{\mathcal{P}_j}\hat{P}_j}{\sqrt{\mathcal{P}_i + \mathcal{P}_j}} \tag{3.32}$$

The cross-correlations elements $\langle \hat{X}_i \hat{X}_j \rangle$ and $\langle \hat{P}_i \hat{P}_j \rangle$ of the covariance matrices $\mathbf{\Gamma}_X$ and $\mathbf{\Gamma}_P$ are reconstructed through:

$$\langle \hat{X}_i \hat{X}_j \rangle = \left[\langle \hat{X}_{ij}^2 \rangle - \frac{\mathcal{P}_i}{\mathcal{P}_i + \mathcal{P}_j} \langle \hat{X}_i^2 \rangle - \frac{\mathcal{P}_j}{\mathcal{P}_i + \mathcal{P}_j} \langle \hat{X}_j^2 \rangle \right] \frac{\mathcal{P}_i + \mathcal{P}_j}{2\sqrt{\mathcal{P}_i \mathcal{P}_j}} \tag{3.33}$$

The last equation has the tremendous advantage that the covariance matrices are directly normalized to shot noise as long as the classical noise of the LO is correctly suppressed by the detection electronics. The same equation stands for the $\hat{P}$ quadrature. The correlations between $\hat{X}_i$ and $\hat{P}_j$ can also be measured by forming a new set of modes $\{\boldsymbol{m}'_{ij}\}$ similar to the one introduced in expression (3.31) but with a *pi* phase on the second mode:

$$\boldsymbol{m}_{ij} = \frac{\sqrt{\mathcal{P}_i}\boldsymbol{m}_i + i\sqrt{\mathcal{P}_j}\boldsymbol{m}_j}{\sqrt{\mathcal{P}_i + \mathcal{P}_j}} \tag{3.34}$$

3.3.2 Measurement

To measure multimode squeezed vacuum, we first choose a modal basis to be investigated with the homodyne detection. The covariance matrices obtained will give all information on the modes in which the multimode squeezed vacuum is carried along with the full individual squeezed state characteristics.

3.3.2.1 Basis of measurement

In order to measure the covariance matrix, one must choose a basis of modes $\{\boldsymbol{m}_i\}$ in which to perform the measurement. Given the theory developed in chapter 2, we choose a basis of spectral modes sharing the same Gaussian spatial mode and the same linear polarization. Given the laser source available (see 2.1), we choose to flatten the spectrum and cut it into sixteen spectral bands with the optical pulse-shaper in order to produce the LO (see figure 3.9). The spectrum is flattened to limit the power discrepancy between different spectral bands. The bands are separated by two columns of non-diffracting pixels to avoid spectral overlap.

For this measurement, only a single beam was injected in the pulse-shaper hence maximizing the optical resolution.

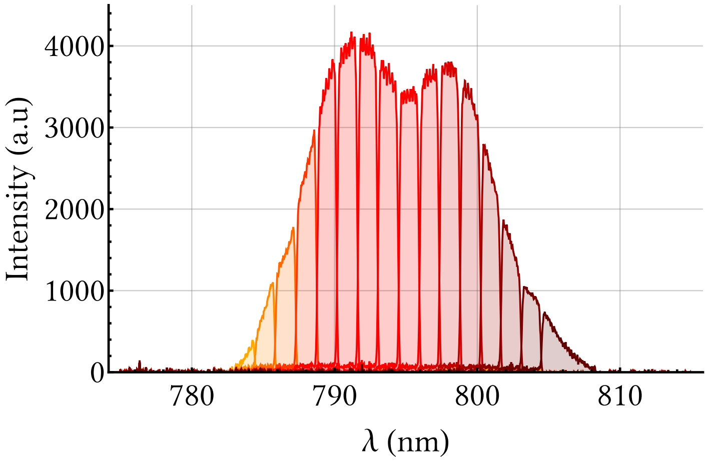

Figure 3.9: Spectral modes of LO used to measure the covariance matrix through homodyne detection.

3.3.2.2 Experimental techniques

The noise at the high-frequency output of the homodyne detection is measured with a spectrum analyzer at the detection frequency of 1MHz. The phase of the LO is swept by a piezoelectric element at a frequency of 50mHz. At lower frequencies, some phase instabilities in the whole experiment decrease the amount of squeezing measured. At higher frequencies, the squeezing dip is swept too fast to be measured it correctly. For those reasons, 50mHz is the sweeping frequency that allowed us to measure the best squeezing.

3.3.3 The covariance matrices

From the measurements obtained with the spectral basis shown on figure 3.9 and equation (3.33), we reconstruct the diagonal blocs $\mathbf{\Gamma}_X$ and $\mathbf{\Gamma}_P$ of the covariance matrix of the multimode quantum state produced by the SPOPO below threshold. Those matrices exhibit some noise on the diagonal along with correlations between different parties on the off-diagonal terms. We also measured the correlations between the $\hat{X}$ and $\hat{P}$ quadratures of different frequency bands but the signal was too small to be distinguished from shot noise (i.e. the noise of plain vacuum). As a consequence, the off-diagonal bloc $\mathbf{\Gamma}_{XP}$ of the covariance matrix (see chapter 1) is considered to be null. Figure 3.10 shows both covariance matrices $\mathbf{\Gamma}_X$ and $\mathbf{\Gamma}_P$ from which we subtracted the covariance matrix of vacuum, namely the identity matrix $\mathbb{1}$.

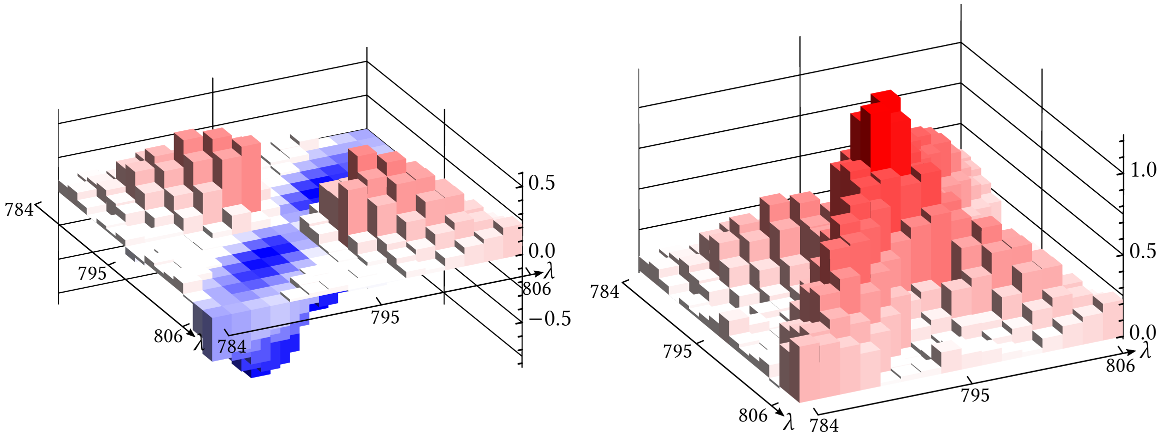

Figure 3.10: Covariance matrices $\mathbf{\Gamma}_X$ (left) and $\mathbf{\Gamma}_P$ (right) from which we have subtracted the identity matrix $\mathbb{1}$ to eliminate the diagonal elements due to shot noise in a single band.

Both matrices clearly exhibit correlations whose magnitude is a significant fraction of shot noise between different frequency bands. Both matrices being symmetric and real by construction, we perform an eigendecomposition to compute eigenmodes and eigenvalues in order to learn more about the multimode quantum state at play.

3.3.4 Eigenvalues and eigenmodes

An eigendecomposition of the covariance matrices gives two sets of eigenvalues $\{\nu_n^X\}$ and $\{\nu_n^P\}$ for $\mathbf{\Gamma}_X$ and $\mathbf{\Gamma}_P$ respectively. Those eigenvalues do not coincide exactly as shown on figure 3.11 and both eigendecomposition unfortunately give slightly different sets of eigenmodes $\{v_n^X\}$ and $\{v_n^P\}$. Because the multimode state is not perfectly pure, the Williamson decomposition (see chapter 1) states that the state can be seen as a squeezed thermal state [Weedbrook 12]. The classical noise embedded in the state leads to the discrepancy between the eigenmodes of $\mathbf{\Gamma}_X$ and $\mathbf{\Gamma}_P$.

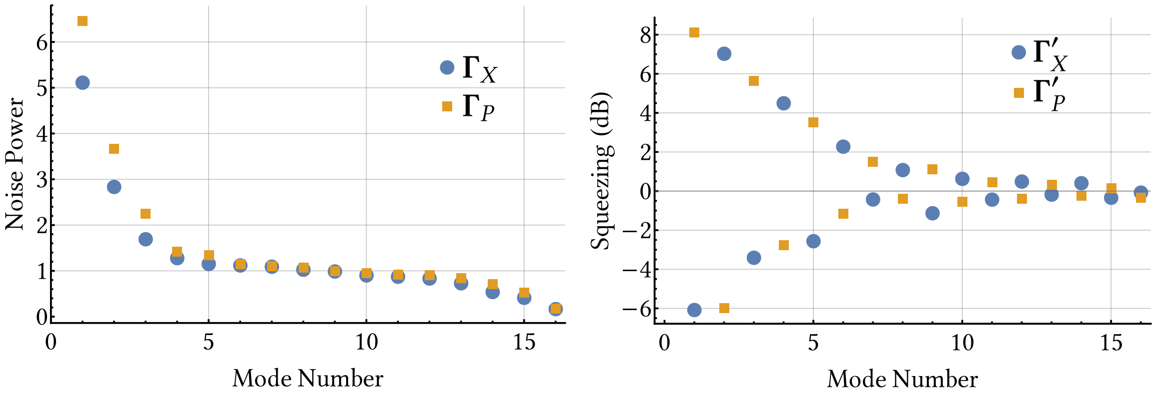

Figure 3.11: Left: Eigenvalues of $\mathbf{\Gamma}_X$ and $\mathbf{\Gamma}_P$, in units of shot noise. Right: diagonal terms of $\mathbf{\Gamma}'_X$ and $\mathbf{\Gamma}'_P$ in dB for each mode of the common basis $\{v'_n\}$.

Nevertheless, those eigenvalues give the variances V_{Xn} and V_{Pn} on each quadratures of the field in each mode with respect to shot noise $\sigma_0^2 = 1$. In the light of the theoretical prediction of chapter 2, we can interpret figure 3.11 as follows: the first eight eigenvalues are the anti-squeezing measured in each mode while the last 8 correspond to squeezing. We also expect from theory the squeezed vacuum states to be alternatively squeezed along each quadrature which the first eight eigenvalues for both matrices seem to confirm.

3.3.4.1 Finding a common basis

One way to overcome the discrepancy between the eigenmodes of $\mathbf{\Gamma}_X$ and the ones of $\mathbf{\Gamma}_P$ is reported in [Roslund 13, Medeiros de Araújo 14]. The eigenmodes showing the strongest anti-squeezing are usually the most stable when the measurement is repeated. We thus choose the first eight modes of $\{v_n^X\}$ and $\{v_n^P\}$ to form a new modal basis $\{v'_n\}$ through a Gram-Schmidt process leading to a basis change $\boldsymbol{V}$ matrix where the new modes $\{v'_n\}$ are expressed in the basis of the measurement modes $\{\boldsymbol{m}_i\}$. We compute a pair of new covariance matrices $\mathbf{\Gamma}'_X$ and $\mathbf{\Gamma}'_P$ by performing a basis change in order to represent them in the basis of modes $\{v'_n\}$:

$$\mathbf{\Gamma}'_X = \boldsymbol{V}\mathbf{\Gamma}_X\boldsymbol{V}^{-1} \tag{3.35}$$

$$\mathbf{\Gamma}'_P = \boldsymbol{V}\mathbf{\Gamma}_P\boldsymbol{V}^{-1} \tag{3.36}$$

Both covariance matrices represented in the new modal basis $\{v'_n\}$ are almost diagonal, up to residual off-diagonal terms accounting for the small classical noise (see figure 3.12). Both matrices diagonal terms represent the amount of squeezing or anti-squeezing in each mode of the new modal basis $\{v'_n\}$. Those values are depicted on figure 3.11 in dB.

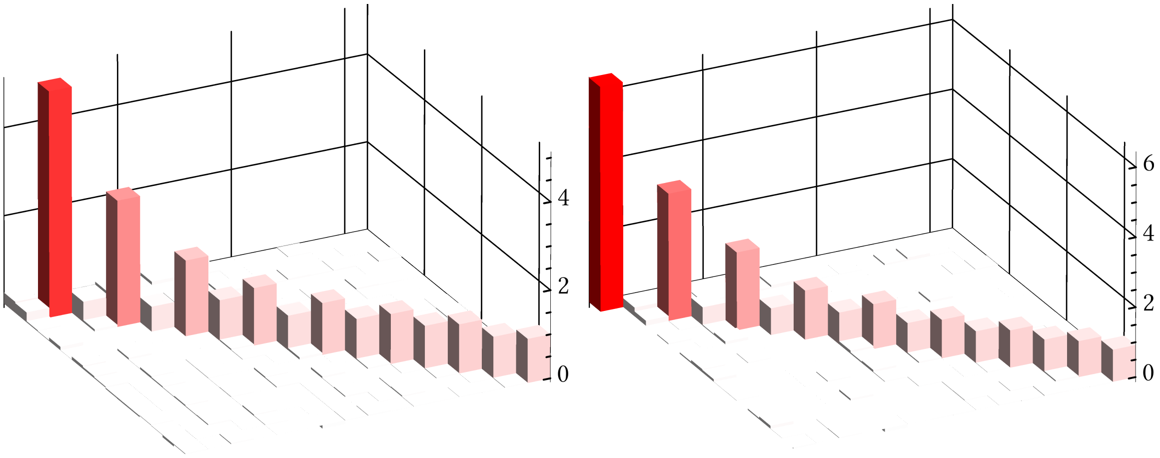

Figure 3.12: Covariance matrices $\mathbf{\Gamma}'_X$ (left) and $\mathbf{\Gamma}'_P$ represented in the basis of the the modes spectral modes $\{v'_n\}$.

The modes $\{v'_n\}$ are presented on figure 3.13. They resemble a family of Hermite-Gaussian functions matching the theoretical predictions depicted in figure 2.10. Still, there is a sensible difference between the measured FWHM of the first mode (about 10nm) and the one predicted in chapter 2 (about 6.4nm). A thorough investigation of the width of the modes $\{v'_n\}$ should be performed by changing the key parameters such as the FWHM of the pump spectrum, the crystal length in the SPOPO and comparing with the above-threshold output of the SPOPO.

3.3.5 Going further in multipartite entanglement

The zoology of multipartite entangled states is rich. Among other states are cluster states [Raussendorf 01] where N parties, or nodes, are entangled with each others according to an arbitrary graph described by an adjacency matrix A as presented on figure 3.14. The entanglement between the different nodes of a cluster is characterized by a set of nullifier $\{\hat{\delta}_i\}$ associated to each node i. In CV, those nullifiers are defined as:

$$\hat{\delta}_i = \hat{X}_i - \sum_{j\neq i} A_{i,j}\hat{P}_j \xrightarrow[\text{Inf. Sqz}]{} 0 \tag{3.37}$$

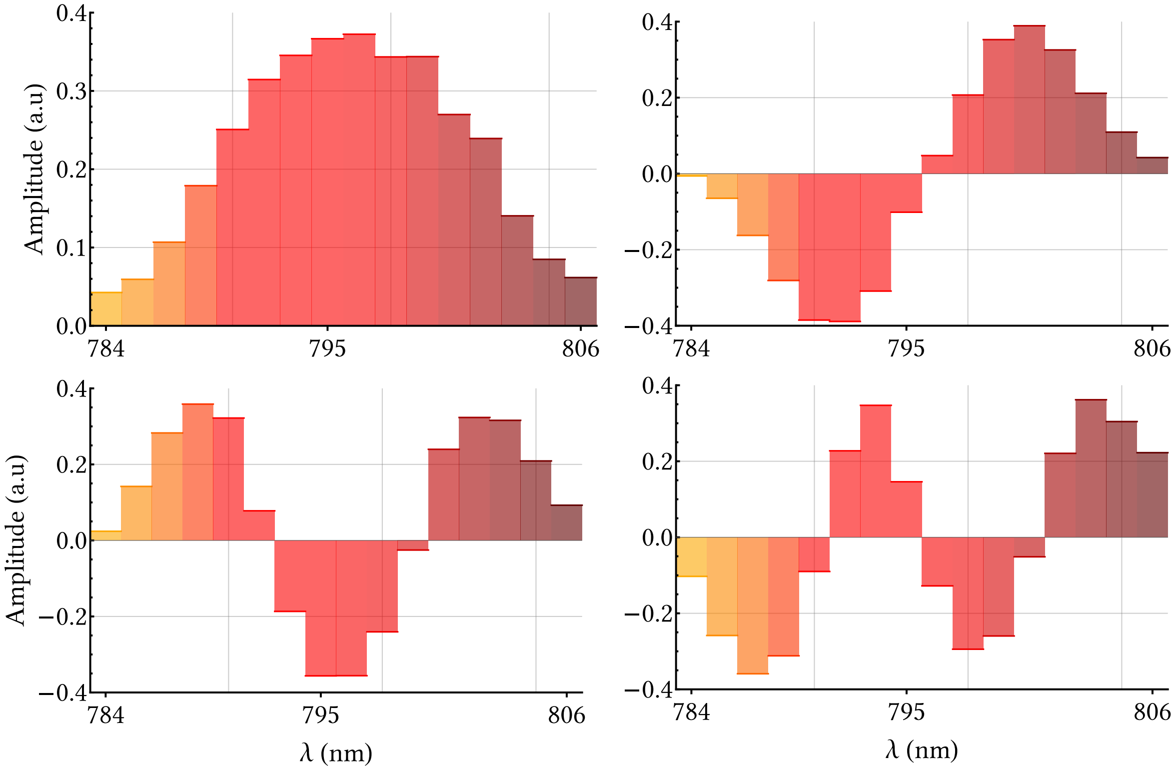

Figure 3.13: First four spectral modes $\{v'_n\}$.

meaning that the amplitude quadrature $\hat{X}_i$ is entangled with a sum of phase quadrature $\hat{P}_j$ or the other modes. In the limit of infinite squeezing, the nullifier tends to zero, meaning there is a perfect correlation between quadratures belonging to different nodes.

A cluster state can be generated through a simple basis change given a multimode squeezed state as input [Van Loock 07]. CV cluster states have been previously generated by mixing single-mode squeezed states on beamsplitters in a fixed configuration[Su 07, Su 13] but also in a frequency comb [Pysher 11]. With the multimode resource presented in this chapter, it is possible to reveal arbitrary Gaussian cluster states in the multimode structure. Indeed, the basis change is simply performed by changing the basis of measurement used for the LO [Cai 15, Cai 16] or using a multi-pixel detector where different spectral bands are detected simultaneously [Ferrini 13].

The interest for cluster states is fueled by their theoretical capability to perform Gaussian quantum computation [Menicucci 06, Gu 09] using measurement-based quantum computation [Raussendorf 03]. Still, the measurement of Gaussian cluster states with our setup has been extensively discussed in the previous references and does not constitute the core of this work. In the next part, we focus on developing a single-photon subtraction scheme for the multimode quantum states presented in the current chapter. This single-photon subtractor is meant to be tunable so that a subtraction could be performed either on a frequency mode

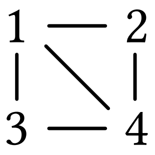

$$A = \begin{pmatrix} 0 & 1 & 1 & 1 \\ 1 & 0 & 0 & 1 \\ 1 & 0 & 0 & 1 \\ 1 & 1 & 1 & 0 \end{pmatrix}$$

Figure 3.14: A four nodes cluster state graph and its adjacency matrix.

generated by our SPOPO or a node of an arbitrary cluster state.

Part II

Single-Photon Subtraction

Chapter 4

A Theoretical Framework for Multimode Single-Photon Subtraction

[About manipulating the temporal mode of a single photon]
"It's quantum mechanics, it's not magic!"

– Nicolas "Da Boss" Treps

Contents

In this chapter, we develop a theoretical framework meant to describe the subtraction of a single photon from a multimode quantum resource. This framework was first introduced in [Averchenko 16]. It provides a way to model the single-photon subtraction process independently of its physical nature and of the multimode basis concerned.

It can be used to describe the Quantum Pulse Gate (QPG) first introduced in [Eckstein 11] and can be seen as a generalization of it.

4.1 Modeling single-photon subtraction

We first recall the results of the single-mode subtraction of a photon from a single-mode light field for clarity before extending the process to the multimode situation.

4.1.1 Detecting a single photon

The subtraction of a single photon relies on the detection, either of the subtracted photon or of another single photon created from the subtracted one. For this purpose, we use a single-photon detector generally consisting of an avalanche photodiode operated above breakdown voltage. Those detectors do not resolve the number of photon and should be modeled by a Positive Operator of Measurement (POM) [Barnett 09] $\hat{\Pi} = \gamma \left(\hat{\mathbb{1}} - |0\rangle\langle 0|\right)$ where γ is the quantum efficiency of the detection. In the next sections, we assume that only a single-photon is subtracted and detected. We intentionally reduce the detection operator $\hat{\Pi}$ to a mixture of lossy single-photon measurements on a set of detection modes $\{\boldsymbol{\delta}_m\}$ whose annihilation operators are denoted $\hat{D}_m$:

$$\hat{\Pi} = \sum_m \gamma_m |1_m\rangle\langle 1_m|_\delta \tag{4.1}$$

$$\text{where: } |1_m\rangle_\delta = |0, \ldots, 0, \underset{m}{1}, 0, \ldots\rangle_\delta = \hat{D}_m^\dagger |0\rangle \tag{4.2}$$

$$\text{and } 0 \leq \gamma_m \leq 1 \tag{4.3}$$

where the coefficients $\{\gamma_m\}$ are the detection efficiencies associated with the detection modes $\{\boldsymbol{\delta}_m\}$. The measurement being imperfect, the detection operator $\hat{\Pi}$ should eventually be written in terms of Kraus operators as:

$$\hat{\Pi} = \sum_m \hat{\kappa}_m^\dagger \hat{\kappa}_m \quad \text{with} \quad \hat{\kappa}_m = \sqrt{\gamma_m} |1_m\rangle\langle 1_m|_\delta \tag{4.4}$$

The evolution of the density matrix through the Kraus operators being:

$$\hat{\rho}^{after} = \sum_m \hat{\kappa}_m \hat{\rho} \hat{\kappa}_m^\dagger \tag{4.5}$$

A more complete multimode model of photon-counting can be found in [Tualle-Brouri 09] but the one developed here is sufficient to serve our purpose.

4.1.2 Single-mode case

We first consider a single-mode light field whose quantum state is described by its density matrix $\hat{\rho}$. The subtraction process is performed by first splitting the light field. While this splitting can be performed via different physical mechanisms (optical beam-splitter [Dakna 97], weak parametric up-conversion [Averchenko 14]), we model it via a simple beamsplitter. The split signal is sent to a single-photon detection device. A detection events conditions the quantum state of the output signal light field as pictured on figure 4.1.

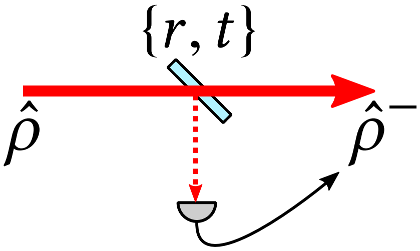

Figure 4.1: A trivial scheme of single-mode photon subtraction: an input light field carries a quantum state $\hat{\rho}$, hits a weak beamsplitter (of reflectance r and transmittance t) that splits the light field into two, a detection event in the split arm heralds the subtraction of a single-photon.

In order to calculate the evolution of the input quantum state, we consider an enlarged system composed of the input signal field and an auxiliary optical bath composed of vacuum. The light is split from an optical mode $\boldsymbol{\alpha}(\boldsymbol{r}, t)$ with annihilation operator $\hat{A}$ to the bath mode $\boldsymbol{\beta}(\boldsymbol{r}, t)$ with annihilation operator $\hat{B}$. It is modeled via a beam-splitting unitary transformation $\hat{U}$ acting on the joint state represented by the separable density matrix: $\hat{\rho} \otimes |0\rangle\langle 0|$. The aforementioned unitary transformation reads:

$$\hat{U} = \exp\left[i\theta\left(\hat{B}^\dagger \hat{A} + \hat{B}\hat{A}^\dagger\right)\right] \approx \hat{\mathbb{1}} + i\theta\left(\hat{B}^\dagger \hat{A} + \hat{B}\hat{A}^\dagger\right) \tag{4.6}$$

where we have assumed the interaction to be weak (i.e. the coefficient θ to be weak: $\theta = 2\arccos(2t) \ll 1$) so that a first order Taylor development could be performed.

On the split side, we assume the single-photon detector to be very multimode, i.e. the efficiencies γ_m are all equal: $\gamma_m = \gamma \, \forall \, m$. The quantum state of the output signal light is conditioned on a single-photon detection event and its density matrix $\hat{\rho}^-$ is computed by performing a partial trace over the mode of the split signal:

$$\hat{\rho}^{-} \propto \mathrm{Tr}_{\delta}\left[\sum_{m} \hat{\kappa}_m \hat{U}\left(\hat{\rho} \otimes |0\rangle\langle 0|_{\beta}\right) \hat{U}^{\dagger} \hat{\kappa}_m^{\dagger}\right] \tag{4.7}$$

$$\hat{\rho}^{-} = \gamma\, \theta^2\, \hat{A}\hat{\rho}\hat{A}^{\dagger}/P \tag{4.8}$$

$$\text{with} \quad P = \gamma\, \theta^2\, \mathrm{Tr}\left(\hat{A}^{\dagger}\hat{A}\hat{\rho}\right) \tag{4.9}$$

The constant P is exactly $\mathrm{Tr}\left(\hat{U}\left(\hat{\rho} \otimes |0\rangle\langle 0|\right) \hat{U}^{\dagger}\, \hat{\Pi}\right)$ and corresponds to the expectation value of the measurement operator. It is interpreted as the probability of success to subtract and detect a single photon and consequently depends on the number of photons in the signal light, the splitting efficiency and the detection efficiency.

4.1.3 General multimode case

We extend the previous description to a multimode subtraction process acting on an input multimode light field carrying an arbitrary multimode quantum state $\hat{\rho}$.
The input light field goes through a two-port multimode beamsplitter that couples two sets of input modes: $\{\boldsymbol{\alpha}_i(\boldsymbol{r}, t)\}$ with annihilation operators $\{\hat{A}_i\}$ and $\{\boldsymbol{\beta}_j(\boldsymbol{r}, t)\}$ with annihilation operators $\{\hat{B}_j\}$. Their arbitrary coupling is defined by complex coefficients $\{r_{ij}\}$ so that the multimode beamsplitter Hamiltonian writes:

$$\hat{H} \propto \sum_{i,j} r_{ij}\left(\hat{A}_i\hat{B}_j^{\dagger} + \hat{A}_i^{\dagger}\hat{B}_j\right) \tag{4.10}$$

This description is valid regardless of the physical nature of the modes. As the transformation is necessarily unitary, a Singular-Value Decomposition is performed to obtain two sets of modes representing the input port and the vacuum port. For the sake of simplicity, we will keep $\{\boldsymbol{\alpha}_n(\boldsymbol{r}, t)\}$ and $\{\boldsymbol{\beta}_n(\boldsymbol{r}, t)\}$ for those modes and $\{\hat{A}_n\}$ and $\{\hat{B}_n\}$ for their annihilation operators. Those two sets now form two orthonormal basis of a space of mode functions with its proper scalar product $\langle ., . \rangle$. The SVD also gives a set of real non-negative singular values $\{\theta_n\}$ representing the coupling between modes $\{\boldsymbol{\alpha}_n\}$ and $\{\boldsymbol{\beta}_n\}$.

The splitting of the input signal light is represented as depicted on figure 4.2 via a multimode beamsplitter transformation $\hat{U}$ as follows:

$$\hat{U} = \exp\left[i \sum_{n} \theta_n\left(\hat{A}_n\hat{B}_n^{\dagger} + \hat{A}_n^{\dagger}\hat{B}_n\right)\right] \tag{4.11}$$

$$\approx \hat{\mathbb{1}} + i \sum_{n} \theta_n\left(\hat{A}_n\hat{B}_n^{\dagger} + \hat{A}_n^{\dagger}\hat{B}_n\right) \tag{4.12}$$

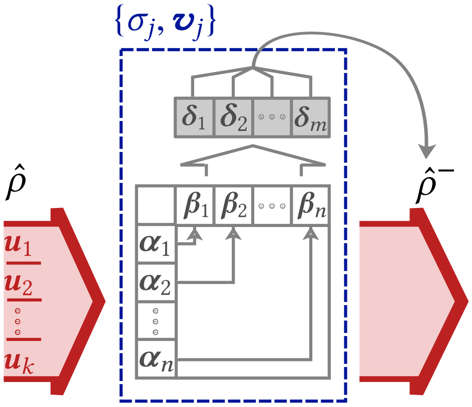

Figure 4.2: Single-photon subtraction from a multimode light field in a quantum state $\hat{\rho}$. The subtraction is modeled by the following steps: (1) splitting of the signal light from modes $\{\boldsymbol{\alpha}_n\}$ into the corresponding vacuum modes $\{\boldsymbol{\beta}_n\}$ of the auxiliary port; (2) detection of a single photon in one of the detection modes $\{\boldsymbol{\delta}_n\}$; (3) heralding conditional photon-subtracted state $\hat{\rho}^-$ of the multimode light, given by expression (4.14). The overall subtraction scheme can be equivalently described in terms of the subtraction modes and corresponding subtraction efficiencies $\{\boldsymbol{v}_j, \sigma_j\}$ using expression (4.18)

where we have assumed the coupling efficiencies $\{\theta_n\}$ to be small (i.e. $\theta_n \ll 1 \,\forall\, n$) to guarantee that only a single photon is exchanged and consequently use a first-order Taylor development.

A single photon is to be detected in the split arm by a multimode detector introduced in expression (4.1). The detection modes $\{\boldsymbol{\delta}_m\}$ are a priori different from the light splitting modes $\{\boldsymbol{\beta}_n\}$. The output density matrix is conditioned on the detection of a single photon. We compute it by performing a partial trace over the single photon output modal subspace:

$$\hat{\rho}^- = \mathrm{Tr}_\delta \left[\sum_m \hat{\kappa}_m \hat{U} \left(\hat{\rho} \otimes |0\rangle\langle 0|_\beta \right) \hat{U}^\dagger \hat{\kappa}_m^\dagger \right] \tag{4.13}$$

$$\hat{\rho}^- = \sum_{n,n'} S_{nn'} \, \hat{A}_{n'} \hat{\rho} \hat{A}_n^\dagger \Big/ P \tag{4.14}$$

$$\text{with } S_{nn'} = \sum_m \gamma_m \, \langle \boldsymbol{\delta}_m, \boldsymbol{\beta}_{n'} \rangle \theta_{n'} \theta_n^* \langle \boldsymbol{\beta}_n, \boldsymbol{\delta}_m \rangle \tag{4.15}$$

$$\text{and } P = \sum_{n,n'} S_{nn'} \, \mathrm{Tr} \left(\hat{A}_{n'} \hat{\rho} \hat{A}_n^\dagger \right) \tag{4.16}$$

where the normalization constant P is the total probability to subtract a single photon for a given optical setup. The weak coupling assumption ensures that $P \ll 1$. Equation (4.14) is an important expression. It describes the multimode subtraction of a single-photon from an arbitrary multimode state.

4.1.3.1 The Subtraction Matrix

While different physical mechanisms can be applied to split light, expression (4.14) shows that the subtraction of a single-photon is always characterized by a modal matrix S of coefficients $S_{nn'}$ that we refer to as the subtraction matrix. This matrix describes the whole multimode aspect of the physical process. According to expression (4.15), S is guaranteed to be positive-definite and hermitian. Hence, there exists a basis change that transforms S into a diagonal matrix with orthonormal eigenmodes $\{\boldsymbol{v}_j\}$ and nonnegative eigenvalues $\{\sigma_j\}$. The subtraction matrix can then be written using the notations introduced in chapter 1 as:

$$\mathrm{S} = \sum_{n,n'} S_{nn'}\ \boldsymbol{\alpha}_n \boldsymbol{\alpha}_{n'}^{\dagger} = \sum_j \sigma_j\ \boldsymbol{v}_j\ \boldsymbol{v}_j^{\dagger} \tag{4.17}$$

By substituting the diagonal decomposition of S into exp. (4.14), we get:

$$\hat{\rho}^{-} = \sum_j \sigma_j\ \hat{s}_j \hat{\rho} \hat{s}_j^{\dagger}\ \Big/\ P \tag{4.18}$$

$$\text{with} \quad \hat{s}_j = \sum_n \langle \boldsymbol{v}_j, \boldsymbol{\alpha}_n \rangle \hat{A}_n \tag{4.19}$$

Expression (4.18) is the most important result of this section. It proves that the overall single-photon subtraction procedure involving multimode light splitting and detection can be described in terms of orthogonal subtraction modes $\{\boldsymbol{v}_j\}$ with their annihilation operators $\{\hat{s}_j\}$ and efficiencies $\{\sigma_j\}$ as summarized on figure 4.2. But expression (4.18) is not an eigendecomposition of the density matrix $\hat{\rho}^{-}$. The efficiencies σ_j are all smaller than unity according to exp. (4.15) and are interpreted as subtraction probabilities per photon per subtraction mode. The total subtraction probability P reads:

$$P = \sum_j\ \sigma_j \,\mathrm{Tr}\left(\hat{s}_j^{\dagger} \hat{s}_j \hat{\rho}\right) \tag{4.20}$$

4.1.3.2 Number of subtraction modes

The effective number of subtraction modes is fully determined by the set of efficiencies $\{\sigma_j\}$ and quantified by the Schmidt number (see chapter 1) of the process:

$$K = \frac{\left(\sum_j \sigma_j\right)^2}{\sum_j \sigma_j^2} \tag{4.21}$$

In analogy with the density matrix with which the subtraction matrix shares the same mathematical properties, we can define a process purity as $\mathrm{Tr}\left(\mathrm{S}^2\right) / \mathrm{Tr}\,(\mathrm{S})^2$. Interestingly, the purity of the single-photon subtraction process is the exact inverse of the Schmidt number: $1/K$. One should not confuse the three different purities at play here: the one of the input multimode state, the one of the process and finally the one of the output multimode state.

4.1.4 Application to multimode squeezed vacuum

Some additional insight into the properties of the conditioned state $\hat{\rho}^-$ of expression (4.18) can be obtained by calculating the reduced density matrices of a given mode.

In the following, we apply the framework developed in the previous subsection to the subtraction of a single photon from multimode squeezed vacuum. All the properties of any photon-subtracted quantum state can be calculated with expression (4.14) and (4.18) as no assumption was made regarding the nature of $\hat{\rho}$. For the sake of simplicity, we now consider that the input quantum state $\hat{\rho}$ is pure and separable. There is a basis of modes $\{\boldsymbol{u}_k\}$, with annihilation operators $\{\hat{a}_k\}$, in which the quantum state $\hat{\rho}$ is factorized:

$$\hat{\rho} = \bigotimes_k \hat{\rho}_k \tag{4.22}$$

We consider that each single-mode state $\hat{\rho}_k$ is pure and solely composed of a squeezed vacuum state $|\xi_k\rangle_k$ so that: $\hat{\rho}_k = |\xi_k\rangle\langle\xi_k|_k$.

The next results in the rest of this section assume only a null mean field for the multimode state and consequently for each single mode state. Those results can easily be extended to other quantum states of interests sharing the same property such as Fock states, cat states [Ourjoumtsev 07a] and their superpositions.

In order to ease the calculation, we introduce an expansion of the subtraction modes over the modes of the input light field:

$$\hat{s}_j = \sum_k c_{jk}\hat{a}_k \quad \text{with} \quad c_{jk} = \langle \boldsymbol{v}_j, \boldsymbol{u}_k \rangle \tag{4.23}$$

Using expression (4.23), we write expression (4.18) in the basis of the input modes:

$$\hat{\rho}^- = \sum_j \sigma_j \sum_{k,k'} c_{jk}c^*_{jk'}\ \hat{a}_k\hat{\rho}\hat{a}^\dagger_{k'} \Big/ P \tag{4.24}$$

4.1.4.1 Multimode state purity

In general, the single-photon subtraction is multimode and the output state $\hat{\rho}^-$ is mixed according to equation (4.18). The multimode purity π of the output quantum state can be expressed using the expansion (4.23):

$$\pi = \mathrm{Tr}\left(\hat{\rho}^{-2}\right) = \sum_{j,j'} \sigma_j\sigma_{j'} \left| \sum_k c_{jk}c^*_{j'k} n_k \right|^2 \Big/ P^2 \tag{4.25}$$

where the n_k is the average photon number in mode "k". Expression (4.25) provides a way to calculate the purity when the subtraction modes and associated efficiencies are known. An alternative possibility to express π is to use expression (4.14) and, expansion of operators $\{\hat{A}_n\}$ similar to (4.23) and a basis change like (1.28). The purity becomes:

$$\pi = \sum_{k,k'} n_k n_{k'} \, |\langle \boldsymbol{u}_k, \mathrm{S}\boldsymbol{u}_{k'}\rangle|^2 \Big/ P^2 \tag{4.26}$$

$$\text{with} \quad \langle \boldsymbol{u}_k, \mathrm{S}\boldsymbol{u}_{k'}\rangle = \sum_{n,n'} S_{nn'} \langle \boldsymbol{u}_k, \boldsymbol{\alpha}_n\rangle\langle \boldsymbol{\alpha}_{n'}, \boldsymbol{u}_{k'}\rangle \tag{4.27}$$

This expression is useful to compute the multimode purity from the input modes and the subtraction matrix. In general, the multimode state purity depends both on the input quantum state and on the applied subtraction procedure, described by S. We also calculate the single-photon subtraction probability P with expressions (4.20) or (4.16):

$$P = \sum_{j,k} \sigma_j |c_{jk}|^2 n_k \tag{4.28}$$

$$= \sum_k n_k \langle \boldsymbol{u}_k, \mathrm{S}\boldsymbol{u}_k\rangle \tag{4.29}$$

We distinguish two extreme cases. In the case of non-selective photon subtraction, the subtraction matrix is proportional to identity: $\mathrm{S} \propto \hat{\mathbb{1}}$ implying $K \gg 1$. As long as the modes of the input multimode state are contained in the modes of S the expression of the output multimode state purity is equal to the definition of $1/N$:

$$\pi_{K \gg 1} = \frac{1}{N} \tag{4.30}$$

where N quantifies the number of modes in the input state as introduced in chapter 1.

In the opposite case, when the subtraction is perfectly selective, i.e. there is only one subtraction mode $\boldsymbol{v}$ with non-null efficiency σ, and using either equations (4.25) or (4.26), we have $\pi = 1$.

4.1.4.2 Matching the single-photon subtraction

According to our model of the single-photon subtraction, the subtraction procedure is single-mode ($K = 1$) in the following cases:

- the beam-splitter operation is single-mode for the mode $\boldsymbol{v}$;
- the single-photon detector detects only the photons in a single-mode $\boldsymbol{\delta}$, and the single photon is subtracted from the mode $\boldsymbol{v} \propto \sum_n \langle \boldsymbol{\delta}, \boldsymbol{\beta}_n\rangle \theta_n \boldsymbol{\alpha}_n$.

The only subtraction mode $\boldsymbol{v}$ is associated with an annihilation operator $\hat{s}$. The sum in expression (4.18) has only a single term and the output multimode quantum state simply is:

$$\hat{\rho}^{-} = \hat{s}\,\hat{\rho}\,\hat{s}^{\dagger} \Big/ \mathrm{Tr}\left(\hat{s}^{\dagger}\hat{s}\,\hat{\rho}\right) \tag{4.31}$$

Nevertheless, while the output multimode state is pure, the subtraction mode $\boldsymbol{v}$ does not necessarily matches a mode of the input state basis $\{\boldsymbol{u}_k\}$ (4.22). The following scenarios, schematically shown in figure 4.3, can be achieved:

- the subtraction mode is matched to one of the modes of the input signal light $\boldsymbol{u}_k$ (4.22) so that :

$$\hat{s} = \hat{a}_k \tag{4.32}$$

$$\hat{\rho}^{-} = \hat{\rho}_k^{-} \bigotimes_{k' \neq k} \hat{\rho}_{k'} \quad \text{where} \quad \hat{\rho}_k^{-} = \hat{a}_k\,\hat{\rho}_k\,\hat{a}_k^{\dagger}/n_k \tag{4.33}$$

- the subtraction mode is not matched with any particular mode of the input signal light. A single photon is subtracted from a coherent superposition of the input light modes (4.22):

$$\hat{s} = \sum_k c_k\,\hat{a}_k \quad \text{with} \quad c_k = \langle \boldsymbol{v}, \boldsymbol{u}_k \rangle \tag{4.34}$$

$$\hat{\rho}^{-} \propto \sum_{k,k'} c_k c_{k'}^{*}\,\hat{a}_k \hat{\rho} \hat{a}_{k'}^{\dagger} \tag{4.35}$$

  In the second scenario, a single-photon subtraction entangles the quantum states embedded into the input light modes. This procedure is used to perform entanglement distillation [Ourjoumtsev 07a, Takahashi 10, Kurochkin 14]. In the context of this thesis, we intend to use it in order to generate a non-Gaussian gate on a controllable optical mode such as the node of an optically implemented cluster state [Yokoyama 13, Medeiros de Araújo 14].

4.1.4.3 A two-mode example

In this section, we consider the subtraction of a single photon from a two-mode only input whose initial quantum state is separable:

$$|\Psi\rangle_{\mathrm{in}} = |\psi_1\rangle_1 |\psi_2\rangle_2 \tag{4.36}$$

We illustrate the difference between the multimode and the single-mode operation of the single-photon subtraction.

In the first case, there are two subtraction modes $\boldsymbol{v}_1$ and $\boldsymbol{v}_2$ with their subtraction efficiencies, σ_1 and σ_2, and their annihilation operators $\hat{s}_1$ and $\hat{s}_2$. We assume that $\hat{s}_1 = \hat{a}_1$,

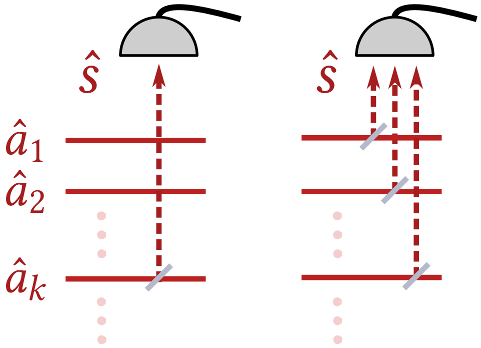

Figure 4.3: Difference between a subtraction scheme matched to an input mode (left) and a coherent subtraction scheme that is not matched to the input modes (right).

$\hat{s}_2 = \hat{a}_2$ (i.e. $c_{11} = c_{22} = 1$) and $\sigma_1 = \sigma_2$ so that a single photon is subtracted with equal probabilities from each input light mode. The purity of the output state, according to (4.25), becomes:

$$\pi = \frac{n_1^2 + n_2^2}{(n_1 + n_2)^2} \tag{4.37}$$

A near unit purity is then achieved only if one of the two modes totally overcomes the other with a much higher photon number which is synonymous of having a single mode input in terms of (1.32).

In the second case, there is only one subtraction mode $\boldsymbol{v}$ with unit subtraction efficiency and its subtraction operator $\hat{s}$. We assume that $\hat{s} = (\hat{a}_1 + \hat{a}_2)/\sqrt{2}\,(c_1 = c_2 = 1/\sqrt{2})$. The single-photon subtraction is pure and the photon is subtracted from a coherent superposition of the two input modes. The purity of the output state is then necessarily equal to unity. The output state is given by the following superposition of states:

$$|\Psi\rangle_{\text{out}} \propto \hat{a}_1|\psi_1\rangle_1|\psi_2\rangle_2 + |\psi_1\rangle_1\hat{a}_2|\psi_2\rangle_2 \tag{4.38}$$

In general, the output state can not be factorized in the original basis and the quantum state is entangled. What is at stake here is the interplay between the input light modes and the modes of the single-photon subtraction.

4.1.4.4 State in a single mode of light

After the properties of the multimode state as a whole, it is possible to focus on the quantum state in a single-mode of the input field. In this section, we investigate the evolution of the quantum state embedded in a single mode "k" of the multimode input state (4.22) through the single-photon subtraction process. The conditional probability that the subtracted photon belongs to the mode "k" is given by the expression:

$$p_k = n_k \langle \boldsymbol{u}_k, \mathbf{S}\boldsymbol{u}_k \rangle / P \tag{4.39}$$

$$= n_k \sum_j \sigma_j |c_{jk}|^2 / P \tag{4.40}$$

The conditioned density matrix of the mode "k", denoted as $\hat{\rho}^-|_k$, is a statistical mixture of two density matrices representing two possibilities. Either the photon was subtracted from the mode "k" or not:

$$\hat{\rho}^-|_k = p_k \; \hat{\rho}_k^- + (1 - p_k) \;\; \hat{\rho}_k \tag{4.41}$$

This result can be also formally obtained by tracing out all the modes except mode "k" in the output multimode state (4.18). The subtraction probability p_k is equal to the definition of the fidelity [Jozsa 94] of the resulting single-mode state $\hat{\rho}^-|_k$ with the "ideal" single-photon subtracted state $\hat{\rho}_k^-$:

$$F\left(\hat{\rho}^-|_k, \hat{\rho}_k^-\right) = \mathrm{Tr}\left(\hat{\rho}^-|_k \; \hat{\rho}_k^-\right) = p_k \tag{4.42}$$

The purity of the state (4.41) is calculated as:

$$\pi_k = \mathrm{Tr}\left(\hat{\rho}^-|_k^2\right) = p_k^2 + (1 - p_k)^2 \leq 1 \tag{4.43}$$

There are then two reasons for the single-mode state $\hat{\rho}^-|_k$ to be mixed. Firstly, when the single-photon subtraction itself is not pure and results in a non-pure multimode state $\hat{\rho}^-$. Secondly, if the subtraction mode is not exactly matched to the mode "k" (i.e. $|c_{jk}|^2 < 1$ for any j), the quantum state in mode "k" is entangled with the states in other modes. If taken apart, the quantum state in mode "k" becomes mixed.

4.2 Photon subtraction from spectrally/temporally multimode light

The framework developed above is applicable for any type of modes of the electric field. Herein, we focus on spectrally (or temporally) multimode light and we consider two subtraction methods. The first one uses a using a weak beamsplitter [Dakna 97, Wenger 04] and is a linear optics device. The second one is based on sum-frequency generation and depicted on figure 4.4. An input field interacts with a strong control field in a non-linear medium making this method a non-linear optics device. The sum-frequency generation converts a signal photon into an up-converted field whose photons are used for heralding [Averchenko 14]. The case of weak up-conversion will be extensively analyzed in chapter 5.

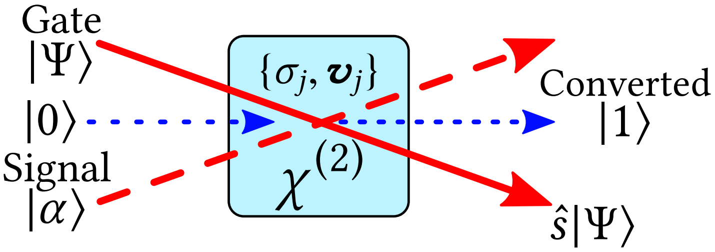

Figure 4.4: Simple sum-frequency generation scheme used for weak up-conversion.

4.2.1 Linear and non-linear photon subtraction

Both the optically linear and non-linear methods of photon subtraction are probabilistic and linear in the sense of quantum mechanics. We assume that the probability to extract more than one photon from a signal field is negligibly small. This assumption is reasonable for low reflectivity beamsplitters (about 1%) and weak up-conversion. In general, the extraction of a single photon from a signal field with annihilation operator $\hat{a}$ into an auxiliary field with creation operator $\hat{b}^\dagger$ can be described in the frequency domain by the following evolution operator:

$$\hat{U} \approx \mathbb{1} + i \iint \mathrm{d}\omega\, \mathrm{d}\omega'\; R(\omega, \omega')\, \hat{b}^\dagger(\omega)\, \hat{a}(\omega') \tag{4.44}$$

where $R(\omega, \omega')$ is the interaction kernel containing all the physics of the subtraction. It is written in the frequency basis because it is the mode appropriate to describe the physical nature of the subtraction. Once the physics is modeled with R, we can investigate the modal properties. Expression (4.44) is the frequency domain version of expression (4.12).

4.2.1.1 Weak beamsplitter

In the case of a beamsplitter, the interaction kernel R_{bs} reflects the fact that the photon energy is preserved during the exchange:

$$R_{bs}(\omega, \omega') = r\; \delta(\omega - \omega') \tag{4.45}$$

where r is the reflectance of the beamsplitter, assumed to be independent of the optical frequency and $r \ll 1$.

4.2.1.2 Weak up-conversion

The case of weak up-conversion is extensively developed in chapter 5. For now, we simplify the process to reduce it to its fundamental working principles. In weak up-conversion, the input field interacts with a control field of amplitude $\alpha(\omega)$ in a non-linear medium with phase-matching function $\Phi(\omega, \omega')$. While the up-conversion can be performed in different geometries and configurations (e.g. non-collinear [Averchenko 14] or collinear [Eckstein 11]), we consider a model case described by the following interaction kernel:

$$R_{up}(\omega,\omega') = C\,\alpha(\omega-\omega')\,\Phi(\omega,\omega') \tag{4.46}$$

$$= C\sum_n r_n\,\psi_n(\omega)\,\varphi_n^*(\omega') \tag{4.47}$$

where expression (4.47) is the Schmidt decomposition of the kernel of parametric interaction [Law 00]. When expression (4.47) is injected in equation (4.44), it results in the frequency domain version of equation (4.12). The decomposition (4.47) shows that the parametric up-conversion process operates as a beamsplitter but for broadband frequency modes [Eckstein 11, Brecht 14b] of signal $\{\varphi_n\}$ and up-converted fields $\{\psi_n\}$ with reflection coefficients $\{r_n\}$. The constant C is proportional to the length of the non-linear medium and the square root of the energy of the gate pulses in pulsed regime [Averchenko 14].

4.2.1.3 Spectral Filtering

Spectral filtering of the extracted photon with transmission $F(\omega)$ (such that $|F(\omega)| \leq 1$) can be implemented by substituting $F(\omega)\hat{b}^\dagger(\omega)$ to $\hat{b}^\dagger(\omega)$ in expression (4.44). This substitution is not unitary. Indeed, we only consider the situation where the output state is conditioned upon a successful photon detection. For this reason, we do not need the former substitution to be unitary and we do not account for the term describing the loss of an extracted photon due to filtering.

4.2.2 Time-resolved detection of a photon

Detecting the heralding photon is part of the subtraction scheme. When the multimode nature is temporal or spectral, it becomes necessary to give a temporally or spectrally multimode description of the photon detection through the POM $\hat{\Pi}$ introduced in section 4.1.1. The modeling of frequency resolving photon detection has been considered before [Rohde 06, Tualle-Brouri 09] and we focus here on the temporal aspect. While photon detection can be performed with detectors resolving the photon-number or not (creating a mixed state [Barnett 98]), we assume that the probability to measure more than one photon is negligibly small as mentioned in the previous sections.

The detection of a single photon at time t can be modeled by the projection operator $\hat{\Pi}(t)$[1]

$$\hat{\Pi}_t = |1_t\rangle\langle 1_t| \tag{4.48}$$

$$\text{with}\quad |1_t\rangle = \hat{D}^\dagger(t)|0\rangle = \left(\int \hat{D}(\omega)e^{-i\omega t}\,\mathrm{d}\omega/\sqrt{2\pi}\right)^\dagger |0\rangle$$

---

[1] This detection operator is not physical because it has the dimension of the inverse of a time and should be seen as a probability density. The physical operator is introduced two equations later.

We consider a realistic photodetectors that exhibits a finite temporal resolution, known as timing jitter, due to the temporal randomness of the avalanche process. We account for this timing jitter by averaging the previous projection operator with a detector response function $\gamma(t)$ defining a temporal window upon a detection event and thus introducing a multimode description of the detector. It is important to state that $\gamma(t)$ does not represent a coherent response of the detector. The detection of a photon at time t is thus a statistical mixture of instantaneous photodetections:

$$\hat{\bar{\Pi}}_t = \int \mathrm{d}\tau \; \gamma(\tau - t) \, \hat{\Pi}_\tau \tag{4.49}$$

In the limiting case where the temporal uncertainty is infinite (i.e. $\gamma(t) = 1$), the photon detection is fully mixed:

$$\hat{\bar{\Pi}} = \int \mathrm{d}t \; |1_t\rangle\langle 1_t| = \int \mathrm{d}\omega \; |1_\omega\rangle\langle 1_\omega| \tag{4.50}$$

where we have introduced a monochromatic single-photon state: $|1_\omega\rangle = \hat{b}^\dagger(\omega)|0\rangle$. Expression (4.50) means that the detected photon is also not resolved in the spectral domain. While it may seem puzzling that a detection over an infinite time does not resolve infinitely the optical frequency, one should remind that this property is limited to coherent detectors. A single-photon detector does not have that kind of capability.

4.2.3 Single-photon subtraction kernel

We aggregate all elements developed above to analyze the multimode aspect of the single-photon subtraction. The detection of a photon on the detector side (δ) results in a conditionally single-photon subtracted state of the signal output light. The state $\hat{\rho}^-$ is calculated as in (4.7):

$$\hat{\rho}^- \propto \mathrm{Tr}_\delta \left[\hat{U} (\hat{\rho} \otimes |0\rangle\langle 0|_\beta) \hat{U}^\dagger \hat{\bar{\Pi}}_t \right] \tag{4.51}$$

$$\hat{\rho}^- \propto \int \mathrm{d}\omega \, \mathrm{d}\omega' \; S(\omega, \omega', t) \; \hat{a}(\omega') \hat{\rho} \hat{a}^\dagger(\omega) \tag{4.52}$$

where $S(\omega, \omega', t)$ is the subtraction kernel, the frequency domain version of the subtraction matrix as expressed in (4.14). It incorporates all the elements introduced above and its expression is:

$$S(\omega, \omega', t) = \int \mathrm{d}\omega_1 \, \mathrm{d}\omega_2 R(\omega_2, \omega') R^*(\omega_1, \omega) F(\omega_2) F^*(\omega_1) \Gamma(\omega_1 - \omega_2) e^{i(\omega_1 - \omega_2)t} \tag{4.53}$$

where $\Gamma(\omega) = \int \gamma(\tau) \, e^{i\omega\tau} \, \mathrm{d}\tau / \sqrt{2\pi}$ is the Fourier transform of the detector temporal response function $\gamma(t)$.

Expressions (4.52) and (4.53) show that the conditioned quantum state $\hat{\rho}^-$ depends on an arbitrary detection time t whose value introduces a phase term $e^{i(\omega_1-\omega_2)t}$. In the rest of this chapter, we simply choose $t = 0$ for convenience. The kernel $S(\omega, \omega')$ is Hermitian and the subtraction modes $\{v_j(\omega)\}$ and the corresponding subtraction efficiencies $\{\sigma_j\}$ can be found through Mercer's theorem (in practice, an eigendecomposition). This decomposition is:

$$S(\omega, \omega') = \sum_j \sigma_j \, v_j(\omega) v_j^*(\omega') \tag{4.54}$$

where the modes $\{v_j\}$ are the frequency domain version of the subtraction modes of the signal introduced in (4.17). We state for clarity that the subtraction modes $\{v_j\}$ are not the modes $\{\varphi_n\}$ of expression (4.47) even if the subtraction modes were obtained from those.

4.2.3.1 Beamsplitter with filtering

We develop the kernel of subtraction $S(\omega, \omega')$ in the case where the subtraction is performed with a simple beamsplitter and a spectral filter. With the interaction R_{bs} of expression (4.45), the subtraction kernel S_{bs} is:

$$S_{bs}(\omega, \omega') = r^2 F^*(\omega) F(\omega') \Gamma(\omega - \omega') \tag{4.55}$$

where we have omitted the phase term $e^{i(\omega_1-\omega_2)t}$ of expression (4.53) by taking $t = 0$. It is possible to use a Gaussian approximation to obtain an explicit expression of the eigenmodes $v_j(\omega)$ and efficiencies σ_j. The spectral filter is given a bandwidth $\Delta\omega_f$ and the detector response function is taken to be $\gamma(t) = \exp(-t^2/\tau_d^2)$ with τ_d being the response time. In the frequency domain, both expressions are:

$$F(\omega) = \exp(-\omega^2/2\,\Delta\omega_f^2) \tag{4.56}$$

$$\Gamma(\omega) \propto \exp(-\tau_d^2\omega^2/4) \tag{4.57}$$

The subtraction modes $\{v_j(\omega)\}$ of S_{bs} are then Hermite-Gaussian functions:

$$v_j(\omega) \propto H_j(\tau\omega)\ \exp(-\tau^2\omega^2/2) \tag{4.58}$$

where H_j is the j-th Hermite polynomial and τ is the characteristic temporal width of the subtraction modes:

$$\tau = \sqrt[4]{1 + \tau_d^2\Delta\omega_f^2}/\Delta\omega_f \tag{4.59}$$

The subtraction efficiencies $\{\sigma_j\}$ are:

$$\sigma_j = r^2 \frac{\varepsilon^{2j-1}}{(1 + \sqrt{1+\varepsilon^2})^{2j-1}} \quad \text{with} \quad \varepsilon = \tau_d\Delta\omega_f \tag{4.60}$$

Given expression (4.60), it is easy to compute the Schmidt number K that characterizes how multimode the process is. It is given by:

$$K = \frac{\left(\sum_j \sigma_j\right)^2}{\sum_j \sigma_j^2} = \sqrt{1 + \tau_d^2 \Delta\omega_f^2} \tag{4.61}$$

We can distinguish two different regimes for single-photon subtraction in expression (4.61) depending on the interplay between the filter and the photodetector parameters:

- a single-mode operation with a fast detector and a narrow filter ($\tau_d \Delta\omega_f \ll 1$). Then $K = 1$ and the only subtraction mode is $v(\omega)$ is equal to the filter function $F(\omega)$.
- a multimode operation with a slow detector and a broad filter ($\tau_d \Delta\omega_f \gg 1$). Then $K = \tau_d \Delta\omega_f \gg 1$ and the characteristic temporal width of the modes is $\tau = \sqrt{\tau_d / \Delta\omega_f}$

4.2.3.2 Alternative temporal approach

It is possible to reach similar conclusions using a time domain approach. Starting back from the expression (4.44) and adding the filtering introduced previously, the transformation $\hat{U}_{bs}$ can be written as:

$$\hat{U}_{bs} \propto \mathbb{1} + r \int \mathrm{d}t\ \hat{b}^\dagger(t) \left(\int \mathrm{d}t'\ f(t'-t)\ \hat{a}(t') \right) \quad \text{with} \quad f(t) = \int F(\omega) e^{-i\omega t} \frac{\mathrm{d}\omega}{2\pi} \tag{4.62}$$

where $f(t)$ is the response function of the filter in the temporal domain. An instant detection of a photon at time t with operator $\hat{\Pi}_t$ (see expression (4.48)) on the detector side turns the evolution operator $\hat{U}_{bs}$ into a subtraction operator $\hat{a}_t$ expressed as a time average instant subtraction:

$$\hat{a}_t \propto \int \mathrm{d}t' f(t'-t) \hat{a}(t') \tag{4.63}$$

This last expression means that a single photon is subtracted from a time-frequency mode defined by the filter. The finite temporal resolution of the detector introduced in (4.49) can be accounted for and the conditioned signal state $\hat{\rho}^-$ becomes mixed:

$$\hat{\rho}^- \propto \int \mathrm{d}\tau\, \gamma(\tau - t)\ \hat{a}_\tau\ \hat{\rho}\ \hat{a}_\tau^\dagger \tag{4.64}$$

Interestingly, expression (4.64) shows that the subtraction modes defined for different values of τ overlap in the temporal basis. The reason is that the eigenmodes of the subtraction process are spectral modes and can only be obtained via the eigendecomposition of the spectral subtraction kernel $S(\omega, \omega')$ performed above.

4.2.3.3 Weak parametric up-conversion

The time scale of the parametric up-conversion is defined by the duration of the gate pulses and the inverse bandwidth of the phase-matching. For femtosecond pulses and bandwidths typical of non-linear media used at our wavelengths (see appendix B), the time scale of up-conversion is much shorter than the temporal resolution of a single-photon detector (typically hundreds of picoseconds). For this reason, we treat the photodetector as a slow one and replace the detector response function in the spectral domain $\Gamma(\omega_1 - \omega_2)$ by a Dirac function $\delta(\omega_1 - \omega_2)$ in expression (4.53). The subtraction kernel S_{up} is then:

$$S_{up}(\omega, \omega') = \int \mathrm{d}\omega_1 \; R^*_{up}(\omega_1, \omega) R_{up}(\omega_1, \omega') |F(\omega_1)|^2 \tag{4.65}$$

In the continuity of subsection 4.2.1.2, we assume a model case interaction between the signal and gate fields in a non-linear medium. The interaction kernel R_{up} is the product of the spectral profile of the gate field $\alpha(\omega - \omega')$ and the phase-matching function $\Phi(\omega')$ where ω' is the optical frequency of the up-converted photon. The subtraction kernel S_{up} is:

$$S_{up}(\omega, \omega') \propto \int \mathrm{d}\omega_1 \; \alpha(\omega_1 - \omega')\alpha^*(\omega_1 - \omega)\Phi^2(\omega_1)|F(\omega_1)|^2 \tag{4.66}$$

As in the case of a simple beamsplitter, it is possible to get analytic results for this subtraction scheme through a Gaussian approximation of the phase-matching function Φ with a width $\Delta\omega_{ph}$ [Grice 01], assuming the gate pulses are Gaussian and using the same Gaussian filter function as above:

$$F(\omega) = \exp(-\omega^2/2\,\Delta\omega_f^2) \tag{4.67}$$

$$\alpha(\omega) \propto \exp(-\tau_g^2\omega^2/2) \tag{4.68}$$

$$\Phi(\omega) \approx \exp(-\omega^2/2\Delta\omega_{ph}^2) \tag{4.69}$$

For a type-I degenerate up-conversion process, the phase-matching width can be approximated to the inverse of the difference of group velocities multiplied by crystal length. Under those approximations, the subtraction modes $\{v_j(\omega)\}$ are Hermite functions (4.58) with a duration τ equal to:

$$\tau = \tau_g \sqrt[4]{1 - \frac{1}{1 + \tau_g^{-2}(\Delta\omega_{ph}^{-2} + \Delta\omega_f^{-2})}} \tag{4.70}$$

The subtraction efficiencies are:

$$\sigma_j = \sigma \frac{\varepsilon^{2j-1}}{(1 + \sqrt{1-\varepsilon^2})^{2j-1}} \quad \text{with} \quad \begin{cases} \sigma \propto 2\sqrt{\pi}|C|^2/\tau_g \\ \varepsilon = 1/\sqrt{1 + \tau_g^{-2}(\Delta\omega_{ph}^{-2} + \Delta\omega_f^{-2})} \end{cases} \tag{4.71}$$

where the C constant was introduced in equation (4.47). Similarly to the cases of the simple beamsplitter, it is possible to compute the Schmidt number of subtraction process. Its expression is:

$$K = \sqrt{1 + \frac{\tau_g^2}{\Delta\omega_{ph}^{-2} + \Delta\omega_f^{-2}}} \tag{4.72}$$

To conclude, expression (4.72) shows that a single-mode operation can be achieved when the ratio between the pulse duration and the inverse of the phase-matching bandwidth is close to zero. Also, a narrow filtering of the up-converted photon can further reduce the Schmidt number of the process. The only subtraction mode left should be identical to the gate pulse profile in the Gaussian approximation of phase-matching.

Chapter 5

Single-Photon Subtraction via Parametric Up-Conversion

> *"So, when are you done with your exams?"*
>
> – My neighbor

Contents

In this chapter, we use the theory developed in [Averchenko 14] to model a single-photon subtraction device based on Sum-Frequency Generation (SFG). This device is called a Quantum Pulse Gate (QPG)[Eckstein 11] and is meant to manipulate the light field at the single photon level. We explain the design chosen to implement this device and investigate its modal properties.

5.1 Theory of sum-frequency

When a single-photon subtractor is based on Sum-Frequency Generation (SFG) in a non-linear medium, it is called a Quantum Pulsed Gate (QPG). In an ideal representation of this single-photon subtractor, a input quantum state is sent in order to undergo a controlled single-photon subtraction, ideally with no extra losses. In the QPG, a signal beam is mixed in a non-linear medium with a potentially strong gate beam used as a control. A converted photon is created at the sum of the signal and gate frequencies, possibly filtered and detected by a Single-Photon Counting Module (SPCM). The quantum state carried by the signal beam has undergone a single-photon subtraction when a converted photon is detected. This single-photon subtractor is thus probabilistic and relies on weak parametric interaction. A single photon, at maximum, is to be converted.

In this picture, the single-photon subtractor is composed of various optical elements: a gate beam, a non-linear medium where parametric interaction takes place and a SPCM. As we will see, the modal properties of this single-photon subtractor arise from the interplay of those various elements.

Our implementation of the QPG relies on a non-collinear optical configuration detailed on figure 5.1. A signal beam and a gate beam overlap in a non-linear medium placed in the focal plane of an optical telescope. At the input of the telescope, both beams are shifted from the optical axis of the telescope while remaining parallel to it as shown on figure 5.1. The signal beam is shifted by 6.25mm in the horizontal plane. The gate beam is shifted by 6.25mm in the horizontal plane and 2.5mm in the vertical plane. Given a focal length of 210mm for the first lens of the telescope, the angles α_h and α_v on figure 5.1 are respectively 1.70° and 0.68°. Those angles will be modified by refraction in the crystal and we will account for this effect later.

To model the subtraction of a single photon from the signal field, we express the electric field $\hat{\mathbf{E}}^{(+)}(\boldsymbol{r}, t)$ on the basis of plane waves as in (1.33). We add the narrow-spectrum approximation ($\mathscr{E}^{(1)} \approx \mathscr{E}_0^{(1)}$). We also assume the distribution of wave vectors $\mathbf{k}$ to be narrow and

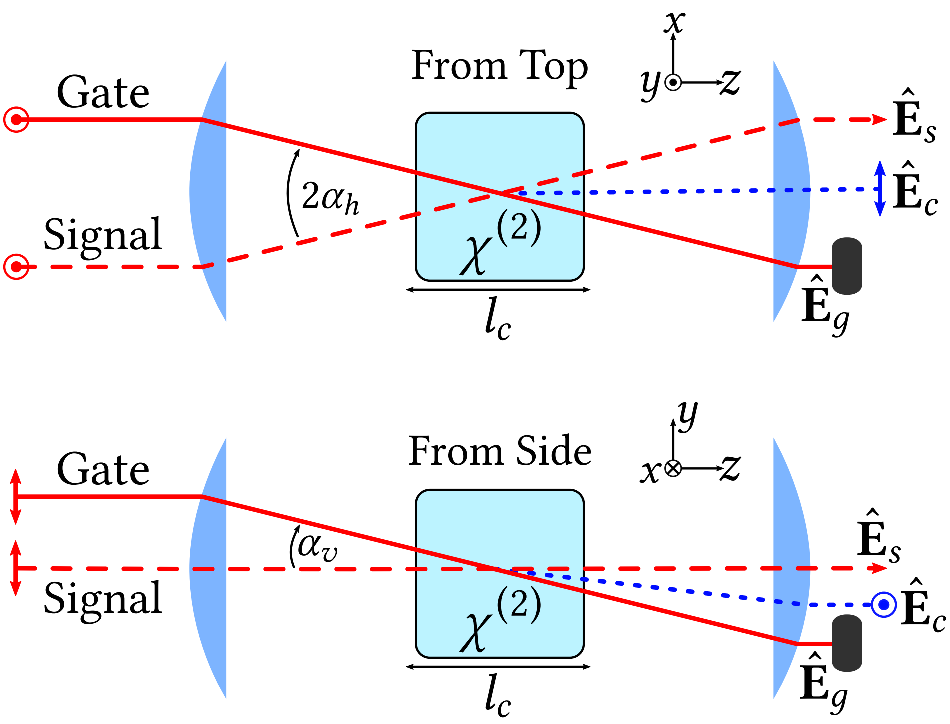

Figure 5.1: SFG optical setup consisting in an optical telescope and a non-linear medium at the Fourier plane. A single mode gate beam (solid red) and a multimode signal beam (dashed red) mix in a type I non-collinear configuration to create a converted beam (dashed blue). The gate beam is dumped after interaction while the signal and the converted ones can be analyzed. The x axis corresponds to the x axis of the ellipsoid of indices of BiBO (see appendix B.

centered around $k_z(\omega) = \omega n(\omega)/c$ where z denotes the propagation direction of the beam. We have $\mathbf{k} \approx k\boldsymbol{e}_z + \mathbf{q}$ where $\mathbf{q}$ contains the transverse components of $\mathbf{k}$. Expression (1.33) becomes similar to the ones of [Kolobov 99]:

$$\hat{\mathbf{E}}^{(+)}(\boldsymbol{r}, t) = \mathscr{E}_0^{(1)} \hat{a}(\boldsymbol{r}, t) \tag{5.1}$$

$$= \mathscr{E}_0^{(1)} \int \frac{\mathrm{d}\omega\, \mathrm{d}\mathbf{q}}{(2\pi)^{3/2}} \hat{a}(\omega, \mathbf{q}) e^{ik_z z} e^{i(\mathbf{q}\boldsymbol{r} - \omega t)} \quad \text{with} \quad \mathscr{E}_0^{(1)} = \sqrt{\frac{\hbar\omega_0}{2n\varepsilon_0 V}} \tag{5.2}$$

where n is the index of the material seen by the field. In the non-linear medium, the parametric interaction between the gate $\hat{\mathbf{E}}_g$, signal $\hat{\mathbf{E}}_s$ and converted electric fields $\hat{\mathbf{E}}_c$ (whose we drop space-time dependence) is governed by the Hamiltonian $\hat{H}_I$:

$$\hat{H}_I(t) = \varepsilon_0 \int_V \mathrm{d}V \chi^{(2)} \hat{\mathbf{E}}_g^{(+)} \hat{\mathbf{E}}_s^{(+)} \hat{\mathbf{E}}_c^{(-)} + \text{h.c} \tag{5.3}$$

where h.c stands for Hermitian conjugate, V is the volume of the non-linear medium and $\chi^{(2)}$ is the second order non-linear susceptibility of the non-linear medium for the sum-frequency process.

Given an input state $|\Psi_{in}\rangle$, the output state $|\Psi_{out}\rangle$ is obtained through the application of the evolution operator on $|\Psi_{in}\rangle$:

$$|\Psi_{out}\rangle = \exp\left(\frac{1}{i\hbar}\int \mathrm{d}t\ \hat{H}_I(t)\right)|\Psi_{in}\rangle \tag{5.4}$$

Assuming the interaction is weak, which is reasonable for parametric processes, a Taylor development can be performed and the output state becomes:

$$|\Psi_{out}\rangle \approx |\Psi_{in}\rangle + |\Psi^{-}\rangle \quad \text{where} \quad |\Psi^{-}\rangle = \frac{1}{i\hbar}\int \mathrm{d}t\ \hat{H}_I(t)|\Psi_{in}\rangle \tag{5.5}$$

$$= \frac{\varepsilon_0\chi^{(2)}}{i\hbar}\int_V \mathrm{d}\boldsymbol{r}\ \mathrm{d}t\ \hat{\mathbf{E}}_g^{(+)}\hat{\mathbf{E}}_s^{(+)}\hat{\mathbf{E}}_c^{(-)}|\Psi_{in}\rangle \tag{5.6}$$

In order to compute the photon-subtracted state $|\Psi^{-}\rangle$, we express all fields in their own coordinate systems with subscripts g, s and c. Given the geometry introduced, each coordinate can be explicitly written in terms of the general system of figure 5.1. The output state is then:

$$|\Psi^{-}\rangle = \frac{\varepsilon_0\chi^{(2)}\mathscr{E}_g^{(1)}\mathscr{E}_s^{(1)}\mathscr{E}_c^{(1)}}{i\hbar\,(2\pi)^{9/2}}\int \mathrm{d}\omega_g\,\mathrm{d}\omega_s\,\mathrm{d}\omega_c\,\mathrm{d}\mathbf{q}_g\,\mathrm{d}\mathbf{q}_s\,\mathrm{d}\mathbf{q}_c$$

$$\hat{a}_g(\omega_g,\mathbf{q}_g)\hat{a}_s(\omega_s,\mathbf{q}_s)\hat{a}_c^{\dagger}(\omega_c,\mathbf{q}_c)\int_V \mathrm{d}\boldsymbol{r}\,\mathrm{d}t\exp\left(i\ \phi(\boldsymbol{r},t)\right)|\Psi_{in}\rangle \tag{5.7}$$

$$\text{with}\quad \phi(\boldsymbol{r},t) = k_g z_g + \mathbf{q}_g\boldsymbol{r}_g - \omega_g t + k_s z_s + \mathbf{q}_s\boldsymbol{r}_s - \omega_s t - (k_c z_c + \mathbf{q}_c\boldsymbol{r}_c - \omega_c t) \tag{5.8}$$

In order to compute the integral over the volume V and time of the function $\phi(\boldsymbol{r},t)$, one needs to express every beam-specific coordinate (i.e. z_g, z_s, z_c, $\mathbf{q}_g$, $\mathbf{q}_s$ and $\mathbf{q}_c$) in terms of the general coordinates (x, y and z) of figure 5.1. The expressions are the following:

$$\underline{\text{Gate:}}\quad \begin{cases} x_g &= x\cos(\alpha_h) + z\sin(\alpha_h) \\ y_g &= y\cos(\alpha_v) - \sin(\alpha_v)\left[\cos(\alpha_h)z - \sin(\alpha_h)x\right] \\ z_g &= y\sin(\alpha_v) + \cos(\alpha_v)\left[\cos(\alpha_h)z - \sin(\alpha_h)x\right] \end{cases} \tag{5.9}$$

$$\underline{\text{Signal:}}\quad \begin{cases} x_s &= x\cos(\alpha_h) - z\sin(\alpha_h) \\ y_s &= y \\ z_s &= z\cos(\alpha_h) + x\sin(\alpha_h) \end{cases} \tag{5.10}$$

$$\underline{\text{Converted:}}\quad \begin{cases} x_s &= x \\ y_s &= y\cos(\alpha_v/2) + z\sin(\alpha_v/2) \\ z_s &= z\cos(\alpha_v/2) - y\sin(\alpha_v/2) \end{cases} \tag{5.11}$$

The integration of the function $\phi(\boldsymbol{r}, t)$ over time and space gives four different factors. The integration over transverse direction (x and y) and time are carried between $-\infty$ and ∞. It results in three factors whose values are null unless an equality is fulfilled for each. Those equations link the different geometrical parameters. They are:

$$\begin{aligned}
&\underline{\text{On t:}} \quad && \omega_g + \omega_s - \omega_c = 0 && (5.12)\\
&\underline{\text{On x:}} \quad && -\cos(\alpha_v)\sin(\alpha_h)k_g + q_g^x\cos(\alpha_h) + \sin(\alpha_v)\sin(\alpha_h)q_g^y + \sin(\alpha_h)k_s && \\
& && +\cos(\alpha_h)q_s^x - q_c^x = 0 && (5.13)\\
&\underline{\text{On y:}} \quad && \sin(\alpha_v)k_g + q_g^y\cos(\alpha_v) + q_s^y - \cos(\alpha_v/2)q_c^y + \sin(\alpha_v/2)k_c = 0 && (5.14)
\end{aligned}$$

The integration over the main propagation direction z is carried between $-l/2$ and $l/2$ with l being the crystal length. In the case of sum-frequency in a birefringent medium, at least one of the beams experiences spatial walk-off. It means that their Poynting vector is not collinear to their propagation (see appendix B). This spatial walk-off should result in additional terms in the expression of the phase-matching function (see [Averchenko 14] for instance). In our model, we choose to exclude the spatial walkoff for simplicity and because the additional complexity does not provide more insight. The integration over z leads to the well known phase-matching function:

$$\int_{-l_c/2}^{l_c/2} \mathrm{d}z e^{i\Delta k z} = l_c\sqrt{2\pi}\,\mathrm{sinc}\,(l_c\Delta k/2) = l_c\sqrt{2\pi}\Phi_{SFG}(\Delta k) \tag{5.15}$$

$$\begin{aligned}
\text{with} \quad \Delta k = {}& k_g\cos(\alpha_v)\cos(\alpha_h) + q_g^x\sin(\alpha_h) - \cos(\alpha_h)\sin(\alpha_h)q_g^y + \cos(\alpha_h)k_s\\
& - \sin(\alpha_h)q_s^x - k_c\cos(\alpha_v/2) - q_c^y\sin(\alpha_v/2)
\end{aligned} \tag{5.16}$$

where the different wave vectors k_s, k_c and k_g depend respectively of ω_s, ω_c and, through conservation of energy, $\omega_c - \omega_s$.

The phase-matching Δk is the critical parameter for every parametric process and the non-linear medium must be set so that $\Delta k = 0$ around the fundamental wavelength. The most important information contained in expression (5.16) is that the non-collinear geometry introduces a coupling between longitudinal and transverse components of momenta [Caspani 10, Averchenko 14]. It should actually be seen as a coupling between the transverse components of momenta and optical frequencies as different optical frequencies have the opportunity to phase-match differently in the non-collinear configuration. It is possible to take advantage of those coupling effects to diagnose ultrashort pulses [Sacks 01, Trebino 02, Akturk 10].

In order to compute the output state $|\Psi_{out}\rangle$ of expression (5.7), we do a certain number of assumptions:

- The spatial modes of the signal and gate fields are assumed to be TEM$_{00}$ so that the spatial distribution of the transverse components $\mathbf{q}_g$, $\mathbf{q}_s$ and $\mathbf{q}_c$ in the focal plane are simply Gaussian and described by the function g:

$$g(q^x) = \sqrt{\frac{w}{\sqrt{\pi}}} e^{-\frac{w^2 q^{x2}}{2}} \tag{5.17}$$

where w is the optical waist in the focal plane. As a consequence, the signal and gate fields are single mode spatially and their annihilation operators $\hat{a}_s$ and $\hat{a}_g$ depend only on optical frequencies ω_s and ω_g so that we can separate the frequency dependence from the spatial one:

$$\hat{a}_s(\omega_s, \mathbf{q}_s) = \hat{a}_s(\omega_s) g(q_s^x) g(q_s^y) \quad \text{and} \quad \hat{a}_g(\omega_g, \mathbf{q}_g) = \hat{a}_g(\omega_g) g(q_g^x) g(q_g^y) \tag{5.18}$$

- The gate field quantum state is a coherent state with spectral amplitude $\alpha_g(\omega_g)$ and is not subject to depletion. We assume that we can readily substitute the annihilation operator $\hat{a}_g(\omega_g)$ with the spectral classical amplitude $\alpha_g(\omega_g)$. As a consequence, the input state $|\Psi_{in}\rangle$ is no longer the same as we have taken out the gate quantum state. For the sake of simplicity, we keep the same notation.

With those assumptions at hand, the photon-subtracted state $|\Psi^-\rangle$ can be written as:

$$|\Psi^-\rangle = \frac{\varepsilon_0 \chi^{(2)} \mathcal{E}_g^{(1)} \mathcal{E}_s^{(1)} \mathcal{E}_c^{(1)}}{i\hbar\,(2\pi)^{9/2}} \int \mathrm{d}\omega_c\, \mathrm{d}\omega_s \int \mathrm{d}\mathbf{q}_c\; L(\omega_c, \mathbf{q}_c, \omega_s) \hat{a}_s(\omega_s) \hat{a}_c^\dagger(\omega_c, \mathbf{q}_c) |\Psi_{in}\rangle \tag{5.19}$$

$$\text{with} \quad L(\omega_c, \mathbf{q}_c, \omega_s) = \int \mathrm{d}\mathbf{q}_g\, \mathrm{d}\mathbf{q}_s \alpha_g(\omega_c - \omega_s) \Phi_{SFG}\left(\Delta_k\right) g(q_s^x) g(q_s^y) g(q_g^x) g(q_g^y) \tag{5.20}$$

As we will see in the next sections, the reduced transfer function $L(\omega_c, \mathbf{q}_c, \omega_s)$ of expression (5.19) is the key to the modal decomposition [Caspani 10] of the single-photon subtraction.

5.1.1 Modes of the process

In order to obtain the eigenmodes of the single-photon subtraction, we perform a Schmidt decomposition [Ekert 95] on the reduced transfer function $L(\omega_c, \mathbf{q}_c, \omega_s)$.

5.1.1.1 Schmidt decomposition

The Schmidt decomposition is formally a discrete decomposition of the reduced transfer function:

$$L(\omega_c, \mathbf{q}_c, \omega_s) = \sum_n \sqrt{\sigma_n} w_n(\omega_c, \mathbf{q}_c) v_n^*(\omega_s) \tag{5.21}$$

where $\{\sigma_n\}$ and $\{v_n\}$ are respectively the subtraction efficiencies and the subtraction modes obtained in chapter 4. The set of modes $\{w_n\}$ are the modes of the up-converted photon.

There is no a priori reason to factorize the momentum dependence from the spectral one in the modes $\{w_n\}$ [Caspani 10, Averchenko 14]. An alternative way to compute the modes $\{v_n\}$ and $\{w_n\}$ is to apply Mercer's theorem (in practice an eigendecomposition) to two auxiliary Hermitian functions $G_s(\omega_s, \omega_s')$ and $G_c(\omega_c, \omega_c', \mathbf{q}_c)$:

$$G_s(\omega_s, \omega_s') = \int \mathrm{d}\omega_c\, \mathrm{d}\mathbf{q}_c\; L^*(\omega_c, \mathbf{q}_c, \omega_s) L(\omega_c, \mathbf{q}_c, \omega_s') = \sum_n \sigma_n v_n(\omega_s) v_n^*(\omega_s') \tag{5.22}$$

$$G_c(\omega_c, \omega_c', \mathbf{q}_c) = \int \mathrm{d}\omega_s L^*(\omega_c', \mathbf{q}_c, \omega_s) L(\omega_c', \mathbf{q}_c, \omega_s) = \sum_n \sigma_n w_n(\omega_c, \mathbf{q}_c) w_n^*(\omega_c', \mathbf{q}_c) \tag{5.23}$$

It is worth noticing that the auxiliary Hermitian function $G_s(\omega_s, \omega_s')$ is the continuous version of the subtraction matrix introduced in chapter 4.

5.1.1.2 Schmidt number

As introduced in chapter 1 and used in chapter 4, the multimode aspect of the process can be quantified through the computation of the Schmidt number K as:

$$K = \frac{\left(\sum_n \sigma_n\right)^2}{\sum_n \sigma_n^2} \tag{5.24}$$

In the next sections, we will pay particular attention to the values of K and we will try to design the SFG process so that K is as close to unity as possible, i.e. the process is single-mode.

5.2 Collinear SFG in BiBO

From now on, we consider BiBO as the medium for SFG. In the collinear case, degenerate SFG is formally equivalent to SHG. The collinear configuration simplifies greatly the model, allows us to gain insight on the process and choose the appropriate crystal length assuming the non-collinear configuration will be only a small perturbation away from the collinear conclusions.

In the rest of this section, we choose $\alpha_h = \alpha_c = 0°$.

5.2.1 Phase-matching

The phase matching Δk of expression (5.16) along with equalities (5.13) and (5.14) are greatly simplified by the collinear assumption:

$$\Delta k(\omega_s, \omega_c) = k_g(\omega_c - \omega_s) + k_s(\omega_s) - k_c(\omega_c) \quad \text{and} \quad \begin{cases} q_g^x + q_s^x - q_c^x = 0 \\ q_g^y + q_s^y - q_c^y = 0 \end{cases} \tag{5.25}$$

Expressions (5.25) show a very important aspect of the collinear configuration: even with broad spectrum ultrafast light, there is no space-time (or rather frequency-momentum) coupling due to focusing.

5.2.1.1 Joint Spectral Distribution (JSD)

As explained in appendix B, Type I ($e + e \rightarrow o$) phase-matching for $\lambda = 795$nm can be achieved in BiBO with $\phi = 90°$ and $\theta = 150.81°$. The reduced transfer function L introduced in expression (5.19) can be factorized into a Gaussain spatial part and a frequency-dependent part $L_c(\omega_s, \omega_c)$. The expression of frequency-dependent part $L_c(\omega_s, \omega_c)$ is simply:

$$L_c(\omega_s, \omega_c) = \alpha_g(\omega_c - \omega_s)\Phi_{SFG}\left(\Delta_k\right) \tag{5.26}$$

This expression is exactly the definition of the JSD introduced in chapter 2.

The phase-matching function Φ_{SFG} and the JSD L_c are represented on figure 5.2 for a crystal length $l_c = 2$mm. We take as a gate profile α_g, the unshaped spectrum provided by our laser source whose intensity FWHM is 11nm (see figure 2.1). The phase-matching function and JSD show that for the chosen crystal length, the phase-matching function Φ_{SFG} is “horizontal” in the wavelength space and so is the JSD. This property comes from the fact that the signal and gate group velocities in the medium are equal [Brecht 14a]. The same principal can be used to engineer a “vertical” JSD [Mosley 08]. This shape of the JSD has the following consequence: if a photon is created and detected at a given up-converted frequency, there is no way to correlate it with a specific signal frequency. The main result is that the conversion is then single-mode.

The spectrum of the converted photon is exactly centered at $\lambda_0/2 = 397.5$nm.

5.2.1.2 Schmidt decomposition

In order to obtain the signal modes $\{v_n\}$ of the subtraction, we perform a Schmidt decomposition of L_c. In practice, it is achieved by performing a Singular Value Decomposition (SVD). The eigenvalues obtained are depicted on figure 5.3 along with the subtraction efficiencies $\{\sigma_n\}$ obtained by squaring the eigenvalues. The distribution of efficiencies gives $K \approx 1.08$ and a process purity $(1/K)$ of 92.5%. The process is then almost single-mode.

The converted mode $\{w_n\}$ can be investigated but we choose not focus on them. We are only interested in the signal modes $\{v_n\}$ whose first three are shown on figure 5.3. They resemble a family of Hermite functions. The first one can be fitted with a Gaussian profile and the fitting leads to an Intensity FWHM of 11nm. It matches exactly the gate spectral profile.

5.2.2 Choosing the crystal length

As the single-photon subtraction process is based on SFG, it relies strongly on the crystal length that impacts the bandwidth of the phase-matching function Φ_{SFG}. A short crystal

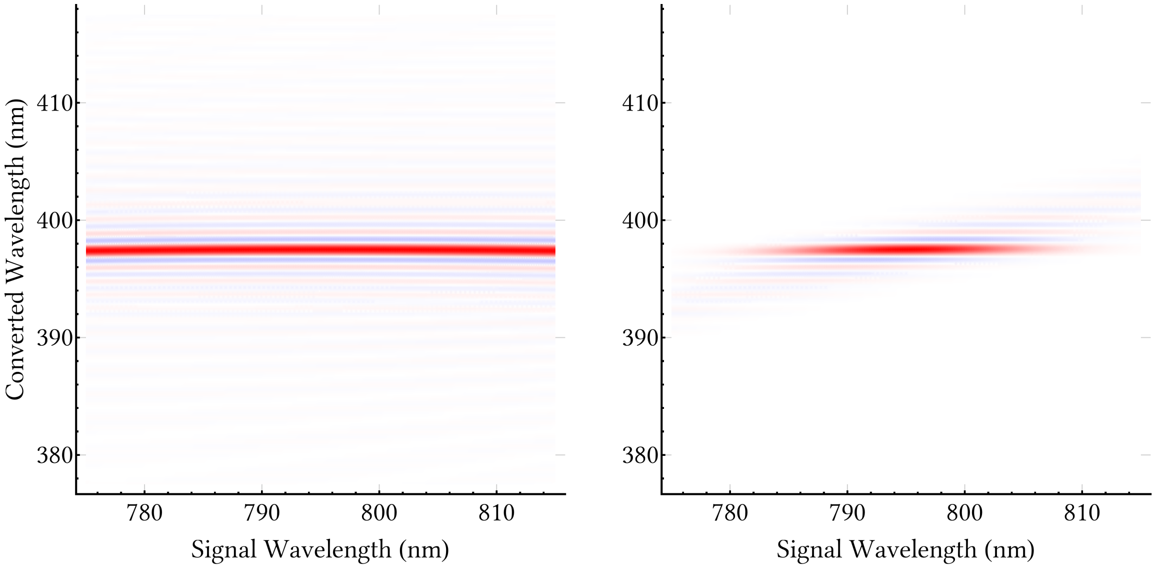

Figure 5.2: Left: Phase-matching function Φ_{SFG}. Right: Joint spectral distribution L_c for a Gaussian gate of 11nm intensity FWHM. The non-linear medium chosen is BiBO with a length of $l_c = 2$mm.

leads to broadband phase-matching while a long one leads to infinitely narrowband phase-matching.

5.2.2.1 Impact on the Schmidt number

The Schmidt number depends on the JSD L_c that directly depends on the crystal length l_c. For a single-mode interaction, we want a Schmidt number as close as possible to unity. We compute the value of K for different crystal length and a fixed gate of 11nm intensity FWHM (see figure 5.4). We find the following different regimes:

- a first regime of short crystals where the Schmidt number is high and drops as the crystal length increase ($l_c < 1$mm on figure 5.4);
- an optimum where the Schmidt number is near unity ($l_c \approx 6$mm on figure 5.4);
- a region where K increases while remaining small ($K \leq 1.2$) as the crystal length increases.

In the first regime, the phase-matching function Φ_{SFG} is just not selective enough to decorrelate the signal and converted frequencies hence leading to a high-valued K. In the last regime, the phase-matching function becomes too narrowband and limits the bandwidth of the optical frequencies that can be converted.

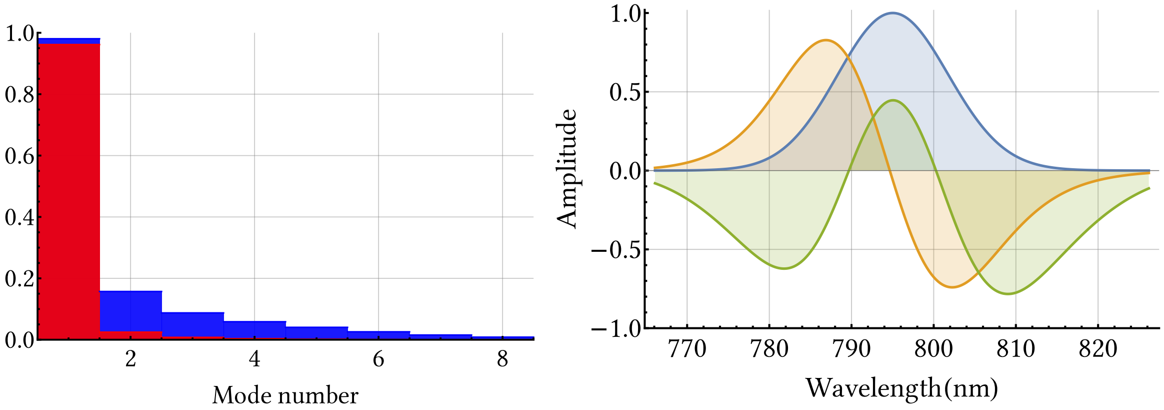

Figure 5.3: Left: first eight eigenvalues of L_c obtained through SVD (blue) and first eight subtraction efficiencies $\{\sigma_n\}$ (red). Right: amplitudes of the first three signal eigenmodes obtained through SVD of L_c. The gate spectrum here has a bandwidth of 11nm in terms of intensity FWHM.

5.2.2.2 Impact on subtraction modes

From figure 5.4, it may seem that increasing the crystal length to higher values can be a solution to maximize interaction while conserving a near unity Schmidt number. This is misleading. Indeed, for long crystal lengths, the phase-matching function Φ_{SFG} becomes extremely narrowband and may ultimately limit the spectral mode that can be converted.

For instance, with $l_c = 20$mm, the Schmidt number remains low ($K = 1.10$) but the width of the first subtraction mode no longer matches the width of the gate spectrum (see figure 5.5). The intensity FWHM is now less than 10nm compared to the 11nm of the gate. For an even longer crystal of $l_c = 100$mm, the first subtraction mode looks like a flat top function but clearly exhibits ripples which are the stigmata of the sinc function contained in Φ_{SFG}. The overall shape is clearly different from a Gaussian potentially imposed by the gate spectrum. The Schmidt number also increases to $K = 1.88$.

5.2.3 Playing with the gate

One of the main advantage of the QPG is the tunability of the process. In our setup, it is implemented through the pulse-shaping of the gate beam in our ultrafast pulse-shaper introduced in chapter 3.

5.2.3.1 Changing the width

It is possible to change the width of the gate beam to control the modes of the single-photon subtraction. We present on figure 5.6 the evolution of the Schmidt number with the width of the gate beam in a crystal of length $l_c = 2$mm. Similarly to figure 5.4, for low values of

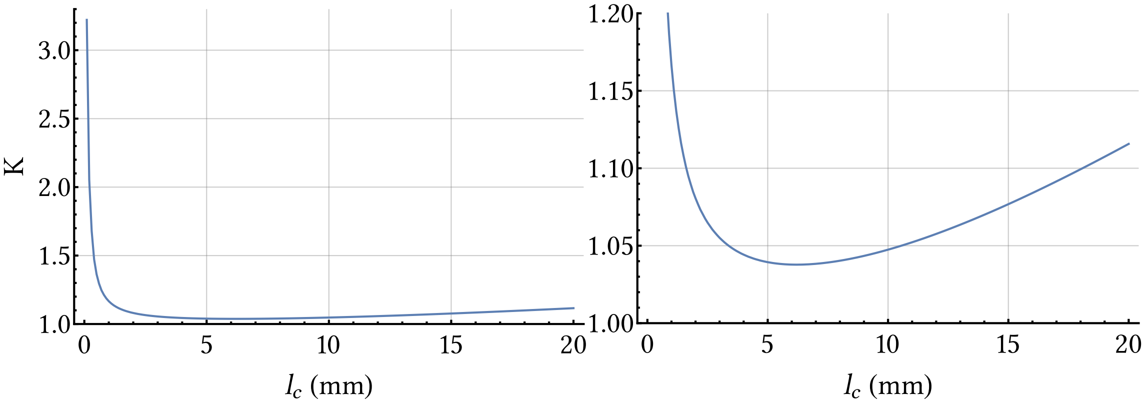

Figure 5.4: Left: Schmidt number K as a function of l_c for a Gaussian gate of 11nm intensity FWHM. Right: Same than left, zoomed for small values of K

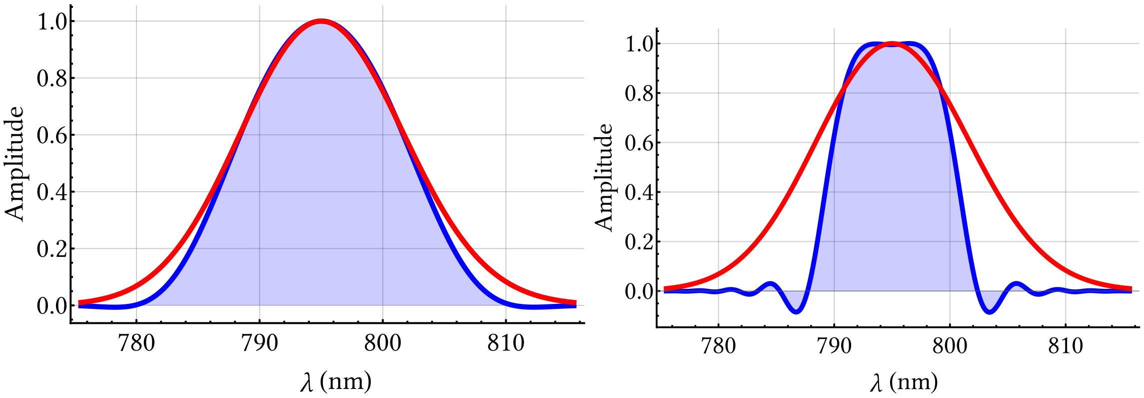

Figure 5.5: First subtraction mode amplitude (blue) and gate pulse spectral amplitude (red) for a crystal length of 20mm (left) and 10mm (right).

the gate bandwidth (intensity FWHM), the phase-matching function is too broadband for the gate pulse and the Schmidt number is high. As the gate width is increased, the Schmidt number drops at a minimum value of approximately 1.04 for a Gate FWHM of approximately 24nm. Finally, the Schmidt number increases again while remaining near minimum as the gate width keeps increasing. As explained in the previous section, the values of K for broadband gate pulses are misleading as the subtraction modes start to exhibit the features of a constraining phase-matching function.

Figure 5.6 shows that provided a adapted crystal length, it is possible to operate the single-photon subtraction process over a varying bandwidth of gate pulses while conserving a reasonably small Schmidt number.

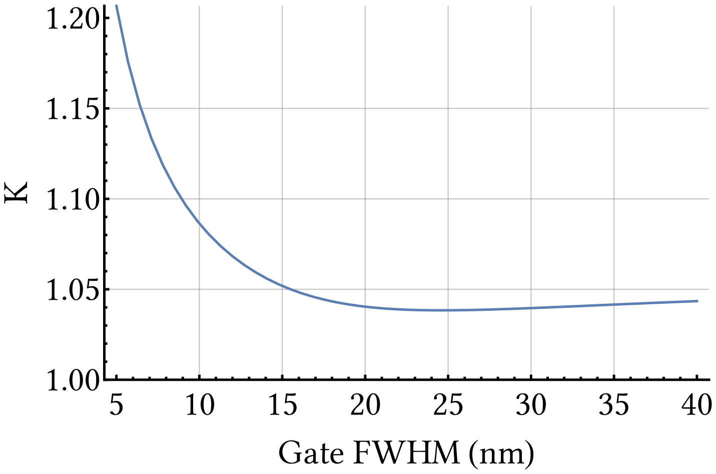

Figure 5.6: Evolution of the Schmidt number with respect to the gate bandwidth (intensity FWHM) for a crystal length $l_c = 2\text{mm}$

5.2.3.2 Changing the shape

Ultimately, it is not only important to be able to change the width of a Gaussian gate, but given the ultrafast pulse-shaping capabilities (and the potential target modes depicted on figure 3.13), to be able to tune the subtraction mode into any spectral shape.

Figure 5.7 compares the gate mode and the first subtraction mode for two different gate profiles: a second Hermite function H_1 and a superposition of the first two Hermite functions $H_0 + H_1$ of the same family. The Schmidt number remains close to unity for both: $K = 1.16$ for H_1, and $K = 1.09$ for $H_0 + H_1$.

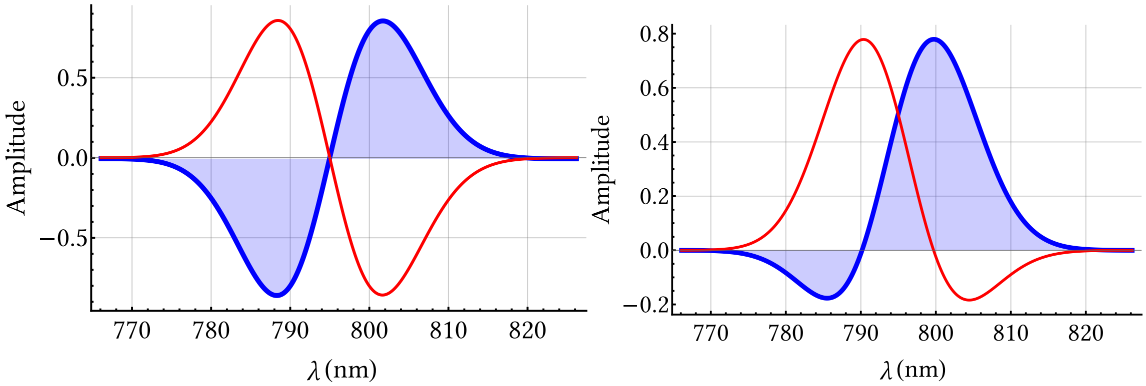

Figure 5.7: First subtraction mode amplitude (blue) and gate pulse spectral amplitude (red) for a crystal length $l_c = 2\text{mm}$. The gate profiles correspond to a second Hermite function H_1 whose corresponding H_0 possesses an intensity FWHM of 11nm (left) and to a coherent superposition of H_0 and H_1 (right).

Figure 5.7 reveals some interesting features in the conversion induced by the conservation of energy. Two conditions are required and met in our case:

- the phase-matching is broadband enough to allow a perfect and undistorted conversion of the gate mode (see previous section and figure 5.5),
- the phase-matching is narrowband enough so that the bandwidth of the up-converted photon is narrow compared to the gate one (see figure 5.2).

With those conditions, the conservation of energy makes the subtraction mode exactly symmetric to the gate mode with respect to the phase-matching center wavelength (here $\lambda_0 = 795\text{nm}$) as depicted on the right side of figure 5.7. As a consequence, when the gate mode is an odd function with respect to λ_0, the subtraction mode will be identical but with a π phase shift. This phase is irrelevant for a single-mode but we have kept it on the left side of figure 5.7 as it explains the right side of the figure.

Let us develop this explanation with the example of figure 5.7. The gate mode is $H_0 + H_1(\Omega_g)$. In the conditions set above, the conservation of energy can be approximated to:

$$\omega_g + \omega_s - \omega_c = \Omega_g + \Omega_s - \Omega_c \approx \Omega_g + \Omega_s = 0 \tag{5.27}$$

And in a single-mode operation of the parametric process, the signal mode should match the gate mode but using the simplified conservation of energy we get: $H_0 + H_1(-\Omega_s) = H_0 - H_1(\Omega_s)$ as H_1 is an odd function with respect to λ_0.

It is thus possible to use different spectrally shaped profile for the gate beam in order to control precisely the first subtraction mode while being conscious that the conservation of energy create the “mirror” effect explained above.

5.3 Non-collinear SFG in BiBO

The main issue with collinear Type I interaction is that both signal and gate beam are in the same spatial mode and have the same polarization. It is then impossible to combine them without losses (which might be detrimental for the signal) and to separate them after their interaction. Also, if the conversion is degenerate, the SHG of the gate beam and the SFG between the gate and the signal are formally equivalent and take place in the same optical mode. It is then impossible to isolate the SFG photons from the SHG ones and additionally, in the case of weak signal, the SHG may be orders of magnitude stronger than the SFG. If the conversion is non-degenerate with no spectral overlap between gate and signal light, the collinear configuration remains meaningful as beams can be separated by a wavelength-selective optical element. If the conversion is degenerate, it can be tempting to use a type-II up-conversion but it is not possible to achieve a good modal selectivity as explained in appendix C.

For this reason, we have introduced the angle α_h and α_v in the horizontal and vertical planes of the optical table leading to a non-collinear configuration. In the next sections, we discuss how the non-collinear configuration impacts the SFG, what problems we have encountered and how we solved them.

5.3.1 Effect of focusing

We start by reminding the expression (5.16) of the non-collinear phase-matching Δk for clarity:

$$\begin{aligned}\Delta k =& k_g \cos(\alpha_v)\cos(\alpha_h) + q_g^x \sin(\alpha_h) - q_g^y \cos(\alpha_h)\sin(\alpha_h) + k_s \cos(\alpha_h)\\ &- q_s^x \sin(\alpha_h) - k_c \cos(\alpha_v/2) - q_c^y \sin(\alpha_v/2)\end{aligned}$$

This expression shows that the non-collinear configuration of the optical telescope depicted on figure 5.1 and the presence of focusing create a space-time coupling in the phase-matching of the SFG [Valencia 07, Averchenko 14] (more precisely a frequency-momentum coupling). We can compare the orders of magnitude of the terms containing the transverse components of momenta (q_g^x, q_g^y, q_s^x and q_c^y) and the ones containing the longitudinal components of momenta (k_g, k_s and k_c) in expression (5.16). Also, the longitudinal components are products of cosines of the angles α_h and α_v while the transverse components are systematically products of sines of the same angles. As the incident angles are small (about 1°), it is reasonable to make the approximations $\cos(\alpha) \approx 1$ and $\sin(\alpha) \approx \alpha < .02$.

5.3.1.1 Transverse terms

First, we investigate the transverse terms. The optical beams entering the telescope are both collimated to 1.6mm of diameter. With a lens of focal length $f = 210$mm, the waist w in the focal plane of the telescope is about 63µm. Using equation (5.17), we can compute a value q_{typ} for which $g(q)/g(0) = e^{-1}$. It leads to $q_{typ} = \sqrt{2}/w \approx 22\text{mm}^{-1}$.

5.3.1.2 Longitudinal terms

In comparison, the longitudinal terms depend on the FWHM of the spectrum of the light carried by those beams. We approximate the spectral amplitude $A(\lambda)$ of the spectrum shown on figure 2.1 by a Gaussian function similar to the one used in expression (2.4): $\exp\left(-(\lambda-\lambda_0)^2/4\sigma_\lambda^2\right)$. For a FWHM of the intensity profile of 11nm, the standard deviation σ_λ is equal to approximately 4.7nm. Using the latest expression, one can compute a typical value k_{typ} for which $A(k_{typ}) = e^{-1}$. It leads to $k_{typ} - k_0 = 4\pi n_r(\lambda_0)\sigma_\lambda/\lambda_0^2 \approx 170\text{mm}^{-1}$ where $k_0 = 2\pi n_r(\lambda_0)/\lambda_0$.

5.3.1.3 Neglecting focusing terms

Hence the ratio between the transverse terms and the longitudinal terms of expresion (5.16) for the typical values q_{typ} and k_{typ} is less than 2.5×10^{-3}. It is thus reasonnable, in this "weak" focusing regime, to neglect the focusing terms and keep only the longitudinal terms in expression (5.16).

5.3.2 Effect of birefringence

BiBO being a bi-axial crystal, there is no reason that any beams in a non-collinear configuration has the appropriate polarization to propagate in the crystal and experience the same refractive index than in the collinear case. Using the ellipsoid of indices of BiBO (as explained in appendix B), we can compute the new refractive index each beam experiences and assess the discrepancy between their input polarizations and the directions where a linear polarization is allowed to propagate in the crystal.

When they enter the crystal, both beams are deviated by refraction at the interface. The angles α_h^{in} and α_v^{in} inside the crystal are:

$$\alpha_h^{in} \approx \alpha_h / n_r(\lambda_0) \approx 0.93^\circ \tag{5.28}$$

$$\alpha_v^{in} \approx \alpha_v / n_r(\lambda_0) \approx 0.37^\circ \tag{5.29}$$

where $n_r(\lambda_0)$ is the refractive index of BiBO at our fundamental wavelength for linearly-polarized light in the yz plane and is approximately equal to 1.82 for $\theta = 150.81^\circ$. We will replace α_h and α_v with α_h^{in} and α_h^{in} in the rest of this chapter.

We compare the values of the trigonometric factors of expression (5.16) with the unity terms of the expression of the collinear phase-matching function (5.25). We find the following differences:

$$\underline{\text{For } k_g}: \quad 1 - \cos\left(\alpha_v^{in}\right)\cos\left(\alpha_h^{in}\right) \approx 1.5 \times 10^{-4} \tag{5.30}$$

$$\underline{\text{For } k_s}: \quad 1 - \cos\left(\alpha_h^{in}\right) \approx 1.3 \times 10^{-4} \tag{5.31}$$

$$\underline{\text{For } k_c}: \quad 1 - \cos\left(\alpha_v^{in}/2\right) \approx 2.1 \times 10^{-5} \tag{5.32}$$

In the following subsections, we use the notations of appendix B for the ellipsoid of indices $\mathscr{E}$, the plane perpendicular to the wave vector Π and their intersection E. We compute a new ellipse E for each case and compare it to E_{coll} which is the ellipse in the collinear case. If the direction of the main axes of E and E_{coll} do not coincide, the linear polarizations authorized to propagate in the crystal have changed. If the input polarization is not adapted in consequence, it will be decomposed into two orthogonal linear components experiencing different refractive indices in the crystal and thus creating an elliptically polarized light at the output (in the presence of walkoff, those components will ultimately be spatially separated). We assume that the amount of light being projected in the orthogonal component is lost and we estimate this loss from the angle θ_{pol} between the main axes of E and E_{coll} as $\sin^2\left(\theta_{pol}\right)$. We also compute the difference Δn between the refractive indices obtained from E_{coll} and the ones obtained from E.

5.3.2.1 Effect of the horizontal angle

In presence of an horizontal angle $\alpha_h^{in} \approx 0.93°$ only (the vertical angle α_v^{in} is assumed to be null in this subsection), the gate and signal beams are still contained in the xz plane of figure 5.1. The SFG beam direction and polarization is identical to the one of the collinear configuration and the gate SHG beam propagates with the gate beam. We summarize our findings in the following table:

Beam	Angle	θ_{pol}	Losses	Δn
Signal	α_h^{in}	0.69°	1.44×10^{-4}	8.69×10^{-6}
Gate	$-\alpha_h^{in}$	−0.69°	1.44×10^{-4}	8.69×10^{-6}
SFG	0	0	0	0
Gate SHG	$-\alpha_h^{in}$	−0.62°	1.17×10^{-4}	1.28×10^{-4}

The values of Δn given in the table above are the maxima that can be obtained by changing the crystal phase-matching angle θ.

Given the low values of θ_{pol} and the losses that each beam experience, we do not adapt the polarization and neglect the losses. Nevertheless, the values of Δn are not really negligible when compared to the values of the trigonometric functions shown in (5.32), especially for the gate SHG. It would be quite an approximation to treat the conversion as if the change in indices due to the non-collinear geometry did not exist. Let us add the vertical angle before we conclude.

5.3.2.2 Effect of both horizontal and vertical angles

We now consider the configuration where both angles α_h^{in} and α_v^{in} are non-null. The signal beam is unchanged and the gate beam propagates with an additional vertical angle. The SFG beam now propagates in the yz plane but deviates of the z axis by an angle $-\alpha_v^{in}/2$ as indicated on figure 5.1. The gate SHG still propagates along the gate beam. The values of θ_{pol}, the losses and Δn are now: Interestingly, the introduction of the vertical angle has had no effect on the propagation properties of the SFG beam. It is because introducing a vertical angle is equivalent to a rotation of the ellipsoid of indices around the x axis, which is the direction of polarization of the SFG beam. It is thus absolutely normal that those properties remain unaltered.

Given the new value of Δn for the gate beam especially, we can no longer neglect the change of indices when compared to the values of the trigonometric functions (see (5.32)) of expression (5.16). In the rest of this chapter, we will account for this change of index when computing phase-matching.

Beam	Angles	θ_{pol}	Losses	Δn
Signal	$\{\alpha_h^{in}, 0\}$	$0.69°$	1.44×10^{-4}	8.69×10^{-6}
Gate	$\{-\alpha_h^{in}, -\alpha_v^{in}\}$	$-0.62°$	1.17×10^{-4}	7.30×10^{-4}
SFG	$\{0, -\alpha_v^{in}/2\}$	0	0	0
Gate SHG	$\{-\alpha_h^{in}, -\alpha_v^{in}\}$	$-0.56°$	9.73×10^{-5}	1.50×10^{-4}

Table 5.1: test

5.3.3 The problem of gate SHG

We first introduced only the horiontal angle α_h^{in} in order to create the non-collinear configuration where the SFG and the gate SHG beams are spatially separated. The photons in the SFG beam must be detected by a SPCM to act as heralds of the single-photon subtraction. The first step to take in order to enable the single-photon subtraction is to check that the SPCM is indeed detecting photons from the SFG beam and not background noise. To test that, we generated a bright SFG beam between a gate and a signal of comparable powers, coupled this SFG beam into a six meters long SM-300 single-mode optical fiber. We blocked the signal beam before the telescope and kept only the gate beam. We finally connected the single-mode fiber to a low-noise SPCM (dark counts < 10Hz). We counted the number of events detected by the SPCM with the gate beam but in the absence of signal beam and we refer to this count simply as *noise count.*

As a first test, the SPCM exhibited an important noise count consistently over 70kHz (and much beyond) for only 2mW of gate power. In a nutshell, the gate SHG was scattered by imperfections in the crystal and at the output interface as depicted in figure 5.8. The spatial mode of SFG captured by the fiber was polluted by this scattering and the single-photon detector was “blinded” by this pollution. One should keep in mind that regarding spatial filtering, a single-mode fiber is the best device available.

The noise count exhibited important variations (from 70kHz to 1MHz) depending on the position of the beams in the crystal. At first, lowering the noise resulted in manually scanning the crystal position at random in order to find a “soft spot” minimizing the noise count. In spite of our best efforts, it was not sufficient. However, we realized that the non-collinear geometry resulted in different phase-matching for SFG and gate SHG with the following consequences:

- if the crystal was set to optimize the phase-matching of the SFG, the phase-matching of the gate SHG should be detuned, resulting in a shifted sepctrum for the SHG;
- as the gate SHG was detuned, the efficieny of the SHG should be greatly decreased.

We decided to take advantage of this detuning effect to discriminate the photons coming from the SFG and the gate SHG. Firstly, by separating their spectra for further spectral filtering and secondly by weakening the power of the gate SHG. In the following we discuss how both conversions are affected by the horizontal angle α_h^{in} and then by the combination of α_h^{in} and α_v^{in}.

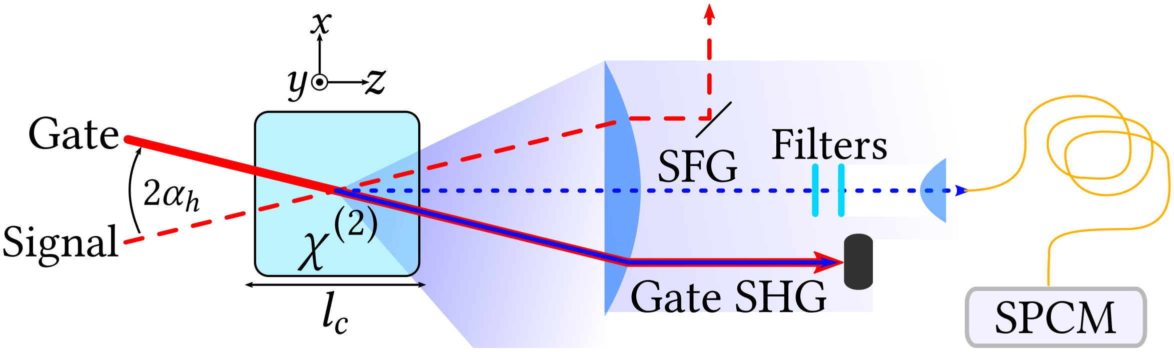

Figure 5.8: Optical setup of the SFG seen from top. The gate SHG propagates along the gate. Its scattering is shown as a blue shaded area. The SFG beam is injected into a single-mode optical fiber connected to a Single-Photon Counting Module (SPCM) for subtrction heralding. The spectral filters block the scattered gate SHG.

5.3.3.1 SFG and SHG Phase-matching

The phase matching of SFG Δk_{SFG} of expression (5.16) and gate SHG Δk_{SHG} are the following:

$$\begin{aligned}\Delta k_{SFG}(\omega_s,\omega_c) &= \left(k_g(\omega_c-\omega_s)\cos\left(\alpha_v^{in}\right)+k_s(\omega_s)\right)\cos\left(\alpha_h^{in}\right)-k_c(\omega_c)\cos\left(\alpha_v^{in}/2\right)\\ \Delta k_{SHG}(\omega_g,\omega_c) &= k_g(\omega_c-\omega_g)+k_g(\omega_g)-k_d(\omega_c)\end{aligned} \tag{5.33}$$

where k_d is the wave vector of the frequency-doubled light. The wave vectors k_g, k_s, k_c and k_d depend on the phase-matching angle θ. This angle must be adapted for each values of α_h^{in} and α_v^{in} in order to optimize the SFG process. Indeed, the cosines inherited from the non-collinear geometry in expression 5.16 must be compensated for so that $\Delta k_{SFG} = 0$. Experimentally, it is achieved by performing SFG between a signal and a gate beam of identical spectra (and comparable optical powers) while monitoring the spectrum of the converted light. The phase-matching angle θ is adapted by tilting the crystal along the x axis (see figure 5.1) until the spectrum of the converted light is centered at $\lambda_0/2 = 397.5$nm.

Figure 5.9 presents an explanation for our configuration. The phase-matching θ is adapted in order to center the JSD of the SFG at λ_0 for the signal wavelength and $\lambda_0/2$ for the up-converted wavelength. We treat the gate SHG as a detuned sum frequency between the gate pulse and another virtual pulse that propagates along the gate beam. In this picture, the phase-matching of this virtual sum frequency is detuned compared to the one of the non-collinear SFG. In particular, on the right side of figure 5.9, the JSD of the virtual sum frequency is detuned by approximately 10nm for the signal and 2.5nm for the up-converted when compared to the JSD shown on the left side. It means that to perform efficient collinear sum frequency in the direction of the gate beam, a virtual pulse should be centered at $\lambda_0 - 10\text{nm} = 785\text{nm}$. As the gate SHG is in fact a sum frequency of the gate with itself, it cannot be performed efficiently due to the detuned phase-matching.

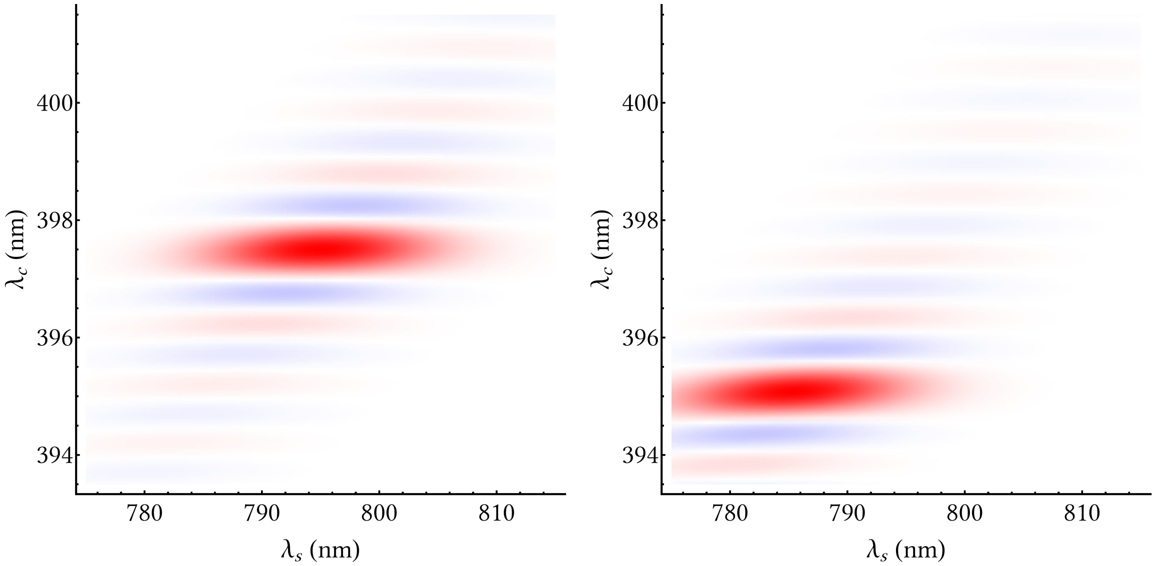

Figure 5.9: JSD of SFG (left) and gate SHG (right) for a crystal length $l_c = 2\text{mm}$. The gate profiles correspond to the first Hermite function H_0 whose bandwidth is 11nm (intensity FWHM). The vertical axis has been zoomed five times with respect to the horizontal one.

To conclude, this detuning has two effects that we exploit: a great reduction of the conversion efficiency for the gate SHG and a shift of its spectrum.

5.3.3.2 Horizontal only tuning

At first, the horizontal separation between signal and gate beam was only 7mm and there was no vertical angle. We tried to increase the horizontal separation up to 19.5mm. The reduction of efficiency conversion for the gate SHG was greatly reduced and so was the noise count on the single-photon detector which dropped down to a few kilohertz for about 2mW of gate power. The situation was not fully satisfying for the following reasons:

- the noise count was still not low enough;
- the spectra of SFG and gate SHG still overlapped as shown on figure 5.10;
- a large horizontal separation meant that the beams were far from the center of our spherical lens thus inducing angular chirp in both beams [Weiner 11b].

For those reasons, we decided to introduce the vertical separation by shifting the gate beam in the upper direction with the idea that a vertical angle α_v^{in} would have a stronger impact to detune the phase-matching of the gate SHG.

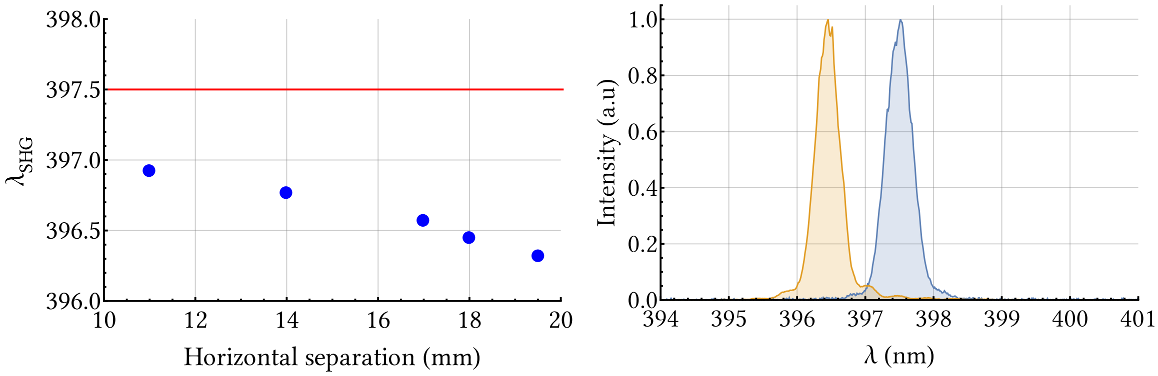

Figure 5.10: Left: central wavelengths of gate SHG spectra (blue dots) with respect to the horizontal separation between gate and signal beam. The crystal is consistently adapted so that the spectrum of SFG is centered at $\lambda_0/2 = 397.5$nm (red line). Right: spectra of SFG (blue) and gate SHG (yellow) for a 18mm of horizontal separation. Both spectra have been normalized to their respective maxima.

5.3.3.3 Killing the noise

In spite of keeping a reasonable horizontal separation (about 12mm) between the signal and the gate beams, the introduction of a vertical shift of the gate beam (about 3mm) kept the noise count on the single-photon detector down to the same level achieved for the largest horizontal only separation (a few kilohertz) for the same gate power. It meant that the slight vertical angle compensated the smaller horizontal angle in reducing the efficiency of the gate SHG phase-matching. Increasing the vertical shift of the gate beam to 6mm decreased that efficiency further as depicted on the left side of figure 5.11. More interestingly, the spectrum of the gate SHG was shifted further in the direction of shorter wavelengths.

We then used a pair of optical filters with a narrow spectral bandwidth (0.5nm FWHM) and a decent peak transmission (over 90%) at 398nm. The filters were tuned sequentially with a bright SFG beam centered at $\lambda_0/2 = 397.5$nm by maximizing the integrated signal of a spectrometer located after the filters. The SFG spectrum was narrowed from 0.6nm to 0.4nm.

We then sent the gate SHG beam through the filters to assess the filtering achieved on the scattered light coming from this beam. The first filter allowed us to reduce the power transmitted almost by a factor 20. The second filter offered an additional factor 7. The overall power reduction on the spectrally shifted gate SHG beam was over 100. As shown on figure 5.11, there is still a little bit of the gate SHG spectrum leaking through the double filter system. The power reduction was enough to allow us to drop the noise count of the single-photon detector to less than 100Hz for approximately 1mW of gate beam power.

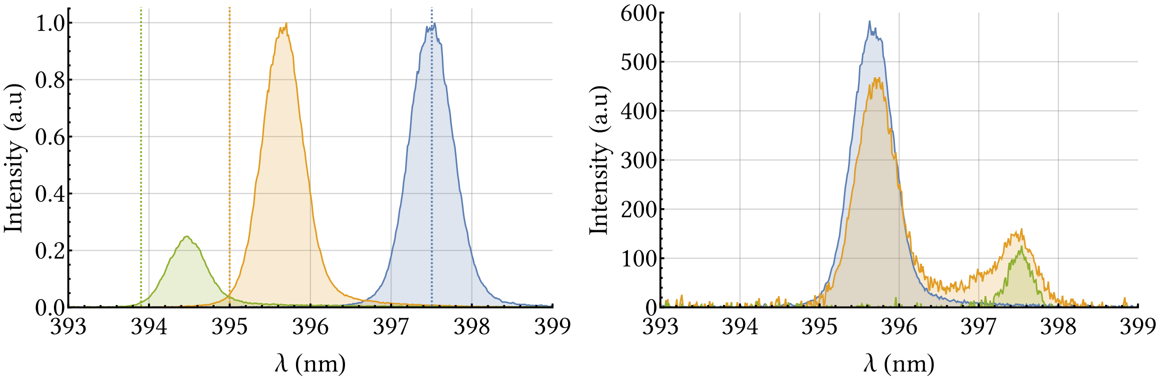

Figure 5.11: Left: spectra of the gate SFG (blue), gate SHG with 3mm of vertical separation (yellow), 6mm of vertical separation (green) and the theoretical predictions for their central wavelengths (dashed vertical lines). The theoretical predictions of their central wavelengths are consistently too optimistic by approximately 25%. Blue and yellow spectra have been normalized to their respective maxima while the green spectrum has been normalized to the maximum of the yellow spectrum to highlight the reduction of the conversion efficiency. Right: gate SHG spectra with no filter and reduced by a factor 20 for readability (blue), with one spectral filter (yellow), with two spectral filters (green).

Finally, we mixed the gate beam with a signal beam of identical spectrum but whose power had been attenuated by neutral densities down to a few photon per pulse. We could observe a count of approximately 200kHz meaning that the signal to noise ratio reached a satisfying value of about 2×10^3. The capability to suppress the noise count was a necessity in order to perform any experiment of single-photon subtraction. Obtaining a significant signal from the up-conversion of a beam carrying an average photon per pulse close to unity was the key capability to perform a modal tomography of the single-photon subtraction as we will see in the next chapter.

5.3.4 Eigenmodes of non-collinear subtraction

Before describing the tomography of the single-photon subtraction, we briefly discuss the theoretical expectations. We eventually used a 2.5mm long crystal. The non-collinear geometry reduces the effective interaction length to approximately 2.3mm. We build the JSD of SFG similarly to section 5.2 with the addition of two filtering Gaussian functions of FWHM 0.5nm in order to model the spectral filters used for the up-converted photon before fiber injection. The JSD is depicted on figure 5.12.

We perform a Schmidt decomposition to obtain the subtraction efficiencies $\{\sigma_n\}$, compute the Schmidt number and obtain the eigenmodes of the up-conversion and consequently, of the single-photon subtraction. The Schmidt number is $K = 1.004$ meaning that the process can hardly be more single-mode, thanks to the spectral filtering of the up-converted photon. The amplitude of the first three signal modes of the process are shown on figure 5.12. The only mode that really matters is only the first one (due to the extremely low Schmidt number) and it matches the gate mode exactly.

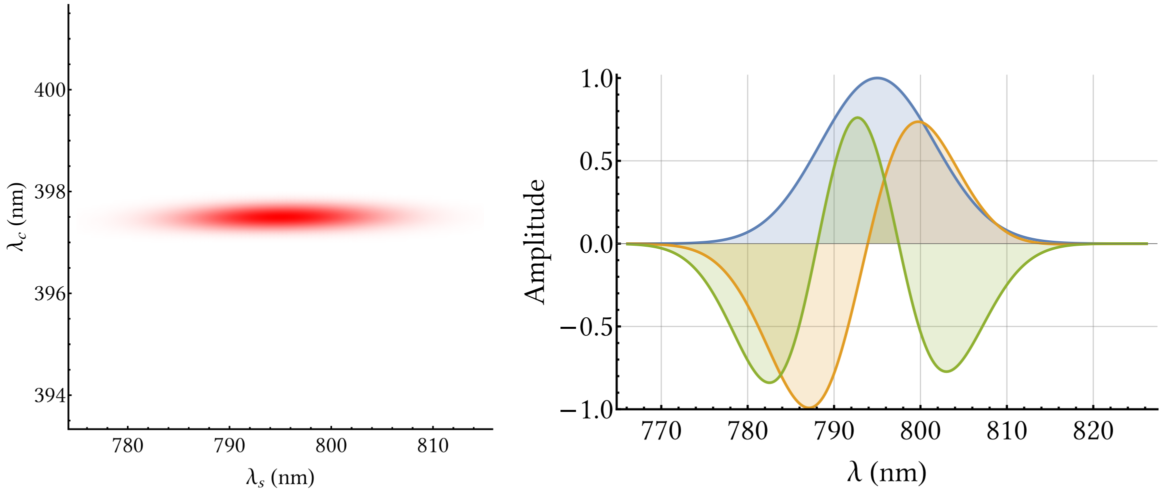

Figure 5.12: Left: JSD of the non-collinear SFG with two spectral filters for the up-converted photon. Right: amplitudes of the first three signal eigenmodes.

We can now move on to describe the process tomography of the single-photon subtractor.

Part III

Process Tomography

Chapter 6

Tomography of the single-photon subtractor

[About physics as a whole] *"Everything is the cause of what happens after!"*
– Valérian "Wunderval" Thiel

Contents

In this chapter, we adopt a similar but different approach than the one developed in chapter 4. We show how the subtraction matrix (4.17) of the Quantum Pulse Gate (QPG), or any single-photon subtraction process, can be retrieved by probing the device with weak coherent states and measuring conversion rates with a single-photon detector. This technique allows us to retrieve the modal matrix of the process.

6.1 Quantum process tomography

Tomography is the mathematical reconstruction of a high dimension object from several partial measurements. In quantum optics, tomography is usually performed on states, processes and finally detectors. In this section, we introduce the concept of Quantum Process Tomography (QPT) and explain how it adapts to our particular case.

6.1.1 Tomography of a quantum black box

Quantum process tomography was first suggested to assess the properties of a quantum-mechanical *black box* as an arbitrary open quantum system [Chuang 97]. A linear map (a tensor) $\mathcal{E}$ would transform an input quantum state $\hat{\rho}$ into $\mathcal{E}(\hat{\rho})$. A natural form to describe the process is a sum of operators similar to expressions (4.14) and (4.18) introduced in chapter 4 where $\hat{\rho}^-$ is $\mathcal{E}(\hat{\rho})$.

Process tomographies were limited at first to processes acting on qubits of low dimensionality. The standard way to characterize those processes was to produce a complete set of quantum states, have each of them undergo the quantum process and measure the ouput density matrix elements. In other words, perform a state tomography before, and after the process. If the process had dimension N, a set of N^2 states should be prepared in order to recover all the elements of the tensor through the measurement of the elements of each output density matrices as:

$$\hat{\rho}_{i,j}^{out} = \sum_{n,m} \mathcal{E}_{i,j}^{n,m} \hat{\rho}_{n,m} \tag{6.1}$$

where $\mathcal{E}_{i,j}^{n,m}$ are the elements of the tensor $\mathcal{E}$.

While this method works when the black box acts on system of low dimensionality, it becomes quite impractical when the dimension increases. To address this problem, it is possible to perform process tomography with coherent states.

6.1.1.1 Coherent states quantum process tomography

As the process tomography requires the synthesis of arbitrarily complex quantum states to probe the quantum black box, it is extremely appealing to perform it with coherent states only. This technique has been introduced and exploited for the first time recently [Lobino 08]. An arbitrary quantum state can be written as a weighted continuous superposition of coherent states thanks to the Glauber-Sudarshan P function. It is then possible to use coherent state for the measurement and still reconstruct the process tensor $\mathcal{E}$ using the same tools.

A quantum state $\hat{\rho}$ is written with its Glauber-Sudarshan $\mathrm{P}_{\hat{\rho}}$ function as:

$$\hat{\rho} = \int \mathrm{d}\alpha^2 \; \mathrm{P}_{\hat{\rho}}(\alpha)|\alpha\rangle\langle\alpha| \tag{6.2}$$

A single-mode density matrix can be written in the Fock basis as a decomposition over the Fock states:

$$\hat{\rho} = \sum_{n,m} \rho_{n,m}|n\rangle\langle m| = \sum_{n,m} \rho_{n,m} \int \mathrm{d}\alpha^2 \; \mathrm{P}_{|n\rangle\langle m|}(\alpha) \; |\alpha\rangle\langle\alpha| \tag{6.3}$$

and with this decomposition[1], it is possible to express the density matrix $\mathcal{E}(\hat{\rho})$ transformed by the quantum process $\mathcal{E}$ as:

$$\mathcal{E}(\hat{\rho}) = \sum_{n,m} \rho_{n,m} \int \mathrm{d}\alpha^2 \; \mathrm{P}_{|n\rangle\langle m|}(\alpha) \; \mathcal{E}(|\alpha\rangle\langle\alpha|) \tag{6.4}$$

Then each element $\mathcal{E}_{i,j}^{n,m}$ of the process tensor can be reconstructed as:

$$\mathcal{E}_{i,j}^{n,m} = \int \mathrm{d}\alpha^2 \; \mathrm{P}_{|n\rangle\langle m|}(\alpha) \; \mathcal{E}_{i,j}(|\alpha\rangle\langle\alpha|) \tag{6.5}$$

where the values $\mathcal{E}_{i,j}(|\alpha\rangle\langle\alpha|) = \langle i|\mathcal{E}(|\alpha\rangle\langle\alpha|)|j\rangle$ can be retrieved, for instance from the measurement of the output state field quadratures with an homodyne detection [Lobino 08]. With those measurement, it is possible to reconstruct the entire process $\mathcal{E}$.

6.1.1.2 Working around the traditional characterization

As explained above, even in the context of coherent states quantum process tomography, the process tomography is still a quantum state tomography. In our case, the situation becomes different because of the very nature of our process. We restrain our analysis by assuming

---

[1] Actually, the P function needs to be regularized using Klauder theorem, $\tilde{\mathrm{P}}$ (the Fourier transform of the P function) and an exponentially decaying regularizing function over an arbitrarily large volume of the space. It is then possible to write the following equation. We treat the P function as regular here, see [Lobino 08] for full details about this regularization

that the input density matrix can be factorized on a basis of modes $\{\boldsymbol{u}_k\}$ and express each single-mode quantum state in terms of its coherent states decomposition using Glauber-Sudarshan P function:

$$\hat{\rho} = \bigotimes_k \int \mathrm{d}\alpha_k^2 \; \mathrm{P}_k(\alpha) |\alpha\rangle\langle\alpha|_k \tag{6.6}$$

We now come back to the expression (4.14) of the evolution of the density matrix through the multimode subtraction procedure introduced in chapter 4. We can calculate the output density matrix by introducing a basis change between the modes of the input state and the modes of the operators $\{\hat{A}_n\}$:

$$\begin{aligned}
\hat{\rho}^- &\propto \sum_{n,n'} S_{nn'} \; \hat{A}_{n'} \hat{\rho} \hat{A}_n^\dagger \qquad (6.7)\\
&\propto \sum_{n,n'} S_{n,n'} \sum_{k,k'} v_{n',k} v_{n,k'}^* \hat{a}_k \hat{\rho} \hat{a}_{k'}^\dagger \quad \text{where} \quad v_{n,k} = \langle \boldsymbol{\alpha}_n, \boldsymbol{u}_k \rangle \qquad (6.8)\\
&\propto \sum_{n,n'} S_{n,n'} \sum_{k,k'} v_{n',k} v_{n,k'}^* \bigotimes_i \int \mathrm{d}\alpha_i^2 \; \mathrm{P}_i(\alpha) |\alpha\rangle\langle\alpha|_i \qquad (6.9)
\end{aligned}$$

Expression (6.9) is greatly simplified if the input state consists of coherent states in each modes $\{\boldsymbol{u}_k\}$. The Glauber-Sudarshan $\mathrm{P}_i(\alpha)$ become Dirac delta functions and expression (6.9) simply gives:

$$\hat{\rho}^- \propto \left(\sum_{n,n'} S_{n,n'} \sum_{k,k'} v_{n',k} v_{n,k'}^* \alpha_k \alpha_{k'}^* \right) \hat{\rho} \tag{6.10}$$

Hence an input state constituted of coherent states is not transformed by a single-photon subtraction. This result is absolutely normal as coherent states are eigenstates of the annihilation operator. But for this reason, it does not make any sense in our case to try to reconstruct the process tensor $\mathcal{E}$ through the state tomography of the output state $\hat{\rho}^-$ as in [Fedorov 15, Cooper 15].

Nevertheless, we can measure the success rate of the single-photon subtraction. Indeed, the normalization constant P is exactly equal to the probability to subtract a photon and is equal, in the case of an input consisting in coherent states, to:

$$\begin{aligned}
P &= \sum_{n,n'} S_{n,n'} \operatorname{Tr}\left(\hat{A}_{n'} \left(\otimes_i |\alpha\rangle\langle\alpha|_i \right) \hat{A}_n^\dagger \right) \qquad (6.11)\\
&= \sum_{n,n'} S_{n,n'} \sum_{k,k'} v_{n',k} v_{n,k'}^* \alpha_k \alpha_{k'}^* \qquad (6.12)
\end{aligned}$$

The success rate of the process is thus expected to change depending on the amplitudes $\{\alpha_i\}$ of the input state. By measuring the success rate, we perform a tomography of our single-photon subtractor.

6.1.2 Checking the quantum process

Before performing a quantum process tomography, it is necessary to verify that the quantum process at play is a single-photon subtraction and not a multi-photon subtraction. Our subtraction process is equivalent to a simple beamsplitter mixing a single-mode signal field with a vacuum bath as described on figure 4.1 and we use the formalism of chapter 4 in the following. The evolution operator $\hat{U}$ is the one introduced in expression (4.6) although we do not limit the Taylor development to the first order:

$$\hat{U} = \hat{\mathbb{1}} + \sum_{n\geq 1} \frac{\left[i\theta\left(\hat{A}\hat{B}^{\dagger} + \hat{A}^{\dagger}\hat{B}\right)\right]^n}{n!} \tag{6.13}$$

The signal field is single-mode and we assume its annihilation operator to be $\hat{A}$. It carries a coherent state $|\alpha\rangle$ and the input state of the beamsplitter is $\hat{\rho} = |\alpha\rangle\langle\alpha| \otimes |0\rangle\langle 0|$. We assume that the detection operator $\hat{\Pi}$ of the single-photon detector is $\hat{\mathbb{1}} - |0\rangle\langle 0|$, i.e. a photon detector with unit efficiency unable to resolve the photon number. We compute the evolution of the density matrix through the evolution operator and the average number of counts c recorded by the single-photon detector:

$$\hat{U}\hat{\rho}\hat{U}^{\dagger} = \hat{\rho} + \sum_{n\geq 1} |\theta|^{2n}|\alpha|^{2n}\frac{|\alpha\rangle\langle\alpha| \otimes |n\rangle\langle n|}{n!} + \text{Cross Terms} \tag{6.14}$$

$$c = \mathrm{Tr}\left(\hat{\Pi}\hat{U}\hat{\rho}\hat{U}^{\dagger}\right) = \sum_{n\geq 1}\left(\frac{|\theta|^{2n}|\alpha|^{2n}}{n!}\right) \tag{6.15}$$

where the cross terms in expression (6.14) contain non-symmetric terms in terms of photon numbers such as $|n\rangle\langle m|$ with $n \neq m$ in the part of the density matrix about to be detected by the single-photon detector.

Expression (6.15) is a well-known result: the photon arrival statistics of an attenuated coherent state is still a coherent state. The potentially non-unit quantum efficiency γ of the single-photon detector can be accounted for and would only results in a modification of the constant θ into $\theta\gamma$.

As a consequence, we can interpret the evolution of the number of counts of the single-photon detector. One can see that the term corresponding to the detection of n photons is weighted by $|\alpha|^{2n}$. One way to verify that only a single-photon is subtracted from the input light field is to assess the evolution of the number of counts when increasing the power of the input coherent state. If the evolution remains linear, then only a single-photon is subtracted.

We present an experimental verification of the linearity of the evolution with respect to the power of the signal beam on figure 6.1. We fit the detection count c with a quadratic function of the average photon number per pulse $|\alpha|^2$ in the signal beam according to:

$$c = c_0\left(a_0 + |\alpha|^2 + a_2\left(|\alpha|^2\right)^2\right) \tag{6.16}$$

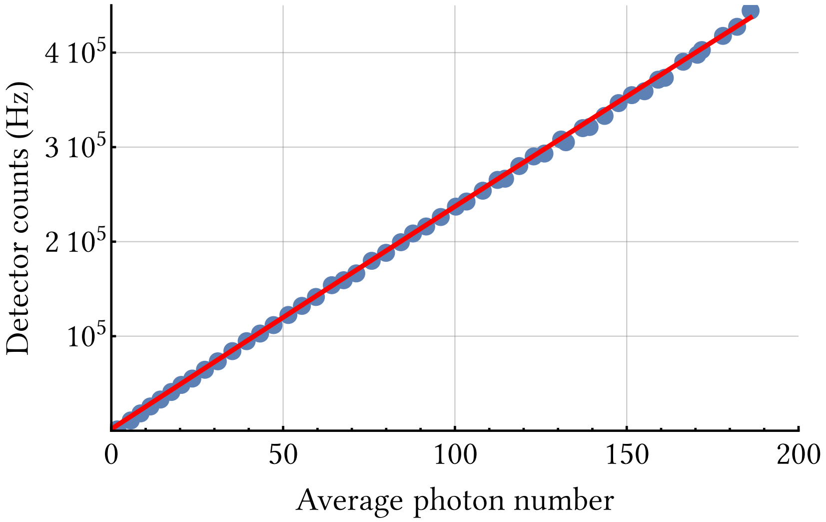

Figure 6.1: Detection count of our single-photon detector with respect to the average photon number per pulse in the probe beam (blue dots) and a quadratic fit of the data (red). The gate power is approximately 1mW, the gate mode is H_0 with 6nm bandwidth.

The fit parameters obtained are detailed in the following table:

Parameter	Fitting value	Standard deviation	Confidence interval
c_0	2372.16	22.95	[2325.99, 2418.32]
a_0	0.716439	0.379329	[−0.0462534, 1.47913]
a_2	-7.26201×10^{-5}	5.09087×10^{-5}	$\left[-1.74979 \times 10^{-4}, 2.97387 \times 10^{-5}\right]$

The confidence interval of the a_2 parameter proves that the the quadratic term of the evolution of the detection count with respect to the probe beam can be neglected. The subtraction that we perform is then a single-photon only subtraction. For each process tomography that we have performed, we have checked the linearity of this evolution to be sure that the quantum process we were looking at did not include any multiphoton subtraction.

6.2 Probing the subtraction matrix

In this section, we investigate our single-photon subtractor as a multimode quantum process mixing two input ports. The evolution operator is exactly the one of exp. (4.12), namely:

$$\hat{U} \approx \hat{\mathbb{1}} + i \sum_n \theta_n \left(\hat{A}_n \hat{B}_n^\dagger + \hat{A}_n^\dagger \hat{B}_n \right) \tag{6.17}$$

6.2.1 The probing basis

In order to perform a process tomography of our single-photon subtractor, we send a probe beam as input. This probe beam carries a weak coherent state. The average number of photon of this coherent state must be low enough to satisfy a low conversion rate compatible with the first-order Taylor development of (4.12). The basis $\{\boldsymbol{u}_k\}$ chosen for the probing modes is composed of frequency bands called *pixels* obtained by chopping the original spectrum via ultrafast pulse-shaping (see chapter 3) as shown on figure 6.2. In order to perform the tomography, we use the maximum optical power available in each band so that the signal-to-noise ratio is maximized for each measurement.

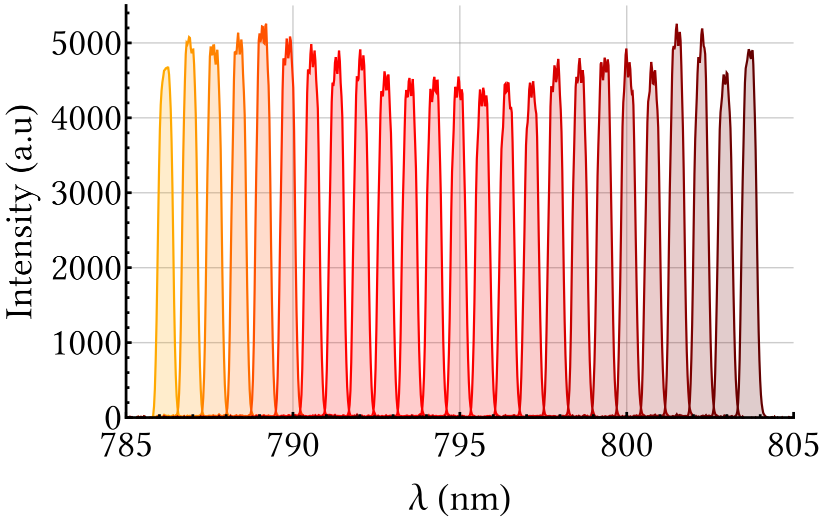

Figure 6.2: Spectra of the 25 pixel modes used to probe the subtraction matrix.

We use the formalism developed in chapter 4. For simplicity, we choose the arbitrary input basis $\{\boldsymbol{\alpha}_n\}$ used to describe the single-photon subtraction process to be the same than our probing basis $\{\boldsymbol{u}_k\}$ whose annihilation operators are $\{\hat{a}_k\}$. In what follows, we compute the probability to detect a single photon with the single-photon detector, given a combination of non-vacuum input modes. For that purpose, we first express the evolution operator in the basis the pixel modes of the probe:

$$\hat{U} \approx \hat{\mathbb{1}} + i \sum_k \theta_k \left(\hat{a}_k \hat{B}_k^\dagger + \hat{a}_k^\dagger \hat{B}_k \right) \tag{6.18}$$

We assume for simplicity that the single-photon measurement operator $\hat{\Pi}$ of exp. (4.1) is lossless (i.e $\gamma_m = 1 \ \forall \ m$). We compute the quantum state $\hat{\rho}^-$ at the output of the single-photon subtractor similarly to expression (4.14) and we obtain:

$$\hat{\rho}^{-} = \sum_{k,k'} S_{kk'}\ \hat{a}_{k'}\hat{\rho}\hat{a}_{k}^{\dagger}\ /P \tag{6.19}$$

$$\text{with } S_{kk'} = \theta_{k'}\theta_{k}^{*}\sum_{m}\langle\vec{\boldsymbol{\delta}}_m, \vec{\boldsymbol{\beta}}_{k'}\rangle\langle\vec{\boldsymbol{\beta}}_k, \vec{\boldsymbol{\delta}}_m\rangle \tag{6.20}$$

6.2.2 Accessing the elements of the subtraction matrix

By computing the trace of the output state $\hat{\rho}^{-}$, we can now compute the probability to detect a single-photon with the single-photon detector given the input multimode state. In order to probe the subtraction matrix S in the $\{\boldsymbol{u}_k\}$ basis, we populate only one or a pair of modes with a coherent state as input via ultrafast pulse shaping.

6.2.2.1 Diagonal terms

For example, exciting only one mode "i" of the basis $\{\boldsymbol{u}_k\}$ gives the probability P_i to convert a photon from this given mode, hence the diagonal terms of the subtraction matrix in this basis:

$$P_i = \mathrm{Tr}\left(\sum_{k,k'} S_{kk'}\ \hat{a}_{k'}\hat{\rho}_i\hat{a}_{k}^{\dagger}\right) \quad \text{with} \qquad \hat{\rho}_i = |\alpha_i\rangle\langle\alpha_i|_i \tag{6.21}$$

$$= S_{ii}|\alpha_i|^2 \tag{6.22}$$

The diagonal terms $\{S_{ii}\}$ of the subtraction matrix are then easily deduced from those one mode measurements.

6.2.2.2 Off-diagonal terms

In order to access the off-diagonal terms of the subtraction matrix, we populate a two-modes coherent state from the $\{\boldsymbol{u}_k\}$ basis as probing inputs. We compute the probability to measure a single photon with the single-photon detector:

$$P_{i,i'} = Tr\left(\sum_{k,k'} S_{ii'}\ \hat{a}_{k'}\left(\hat{\rho}_i \otimes \hat{\rho}_{i'}\right)\hat{a}_{k}^{\dagger}\right) \tag{6.23}$$

$$= S_{ii}|\alpha_i|^2 + S_{i'i'}|\alpha_{i'}|^2 + S_{ii'}\alpha_i\alpha_{i'}^{*} + S_{i'i}\alpha_i^{*}\alpha_{i'} \tag{6.24}$$

The subtraction matrix being Hermitian by construction (see expression (4.15)), we have $S_{i'i} = S_{ii'}^{*}$. We access the real and imaginary parts of the off-diagonal terms by setting the phase between $|\alpha_i\rangle$ and $|\alpha_{i'}\rangle$ respectively to 0 and $\pi/2$. We assume the amplitude α_i and $\alpha_{i'}$ to be equal and we denote the probabilities to detect a single photon associated to those two modes $P^{0}_{i,i'}$ and $P^{\frac{\pi}{2}}_{i,i'}$ for respectively a 0 and $\pi/2$ phase difference. We can then easily compute the real and imaginary parts as:

$$\begin{cases} P^{0}_{i,i'} & = S_{ii} + S_{i'i'} + S_{ii'} + S^{*}_{ii'} \\ P^{\frac{\pi}{2}}_{i,i'} & = S_{ii} + S_{i'i'} - iS_{ii'} + iS^{*}_{ii'} \end{cases} \tag{6.25}$$

$$\Rightarrow \begin{cases} \Re\left(S_{ii'}\right) & = \left(P^{0}_{i,i'} - S_{ii} - S_{i'i'}\right)/2 \\ \Im\left(S_{ii'}\right) & = \left(P^{\frac{\pi}{2}}_{i,i'} - S_{ii} - S_{i'i'}\right)/2 \end{cases} \tag{6.26}$$

Once the elements of the subtraction matrix are known in the $\{\boldsymbol{u}_k\}$ basis, it is possible to diagonalize S in order to access its eigenvalues and eigenvectors. We can then deduce the Schmidt number of the process (or the purity) as well as the optical modes that will undergo a single-photon subtraction.

6.2.3 Experimental subtraction matrices

In order to perform a process tomography using the single-photon detector and the probing modes pictured in figure 6.2, we had to slightly change the phase mask printed on the SLM. We initially used a grating structure made of five wrappings for each beam in the dual beam shaping configuration introduced in chapter 3. When the amplitude of the grating supposed to diffract the probe beam was null, a little bit of light was still diffracted into the first order of diffraction and was passing through the spatial filter. This leak led to unwanted detection events by the single-photon detector. We got rid of those events by increasing the wrappings up to seven on the lower part of the SLM used to shape the probe beam and changing the spatial filter accordingly.

Technically, we perform the measurement of each term of the subtraction matrix through the following sequence:

- we first measure the number of counts detected by the single-photon detector for each of the N individual pixel of the probing basis shown on figure 6.2 utilizing the maximum optical power available;
- we measure the count of the single-photon detector and the optical power of the probe beam for a superposition of two pixels where we exploit as much optical power as we can from the pair of pixels. For this, we set the grating structure on the SLM phase mask to reach a maximum amplitude for one of the two pixels;
- we perform the same measurement again introducing a $\pi/2$ phase between each couple of pixel.

We take N extra measurements at the beginning of the sequence for calibration so at the rate of one measurement per second, the measurement time of subtraction matrix is actually $N + N \times N = 25 + 25^2 = 650$ seconds. Also, we used enough optical densities to keep the average photon number per pulse in each pixel between 5 and 42 ensuring the subtraction of a single-photon at best as guaranteed by figure 6.1. We present here the results of the different subtraction matrices obtained experimentally.

6.2.3.1 Tomography for different gate modes

We have measured several subtraction matrices corresponding to the following gate spectral profiles:

- different zero-order H_0 Hermite functions modes with bandwidths between 2 to 10 nm (intensity FWHM);
- a family of Hermite functions H_n based on a 4nm H_0 with n up to 6 (see figure 6.3);
- various coherent superpositions of the previous family, sometimes including a $\pi/2$ phase, thus taking advantage of the spectral phase shaping capability of our pulse shaper to introduce non-trivial spectral phase (other that π phase jump) in the subtraction modes.

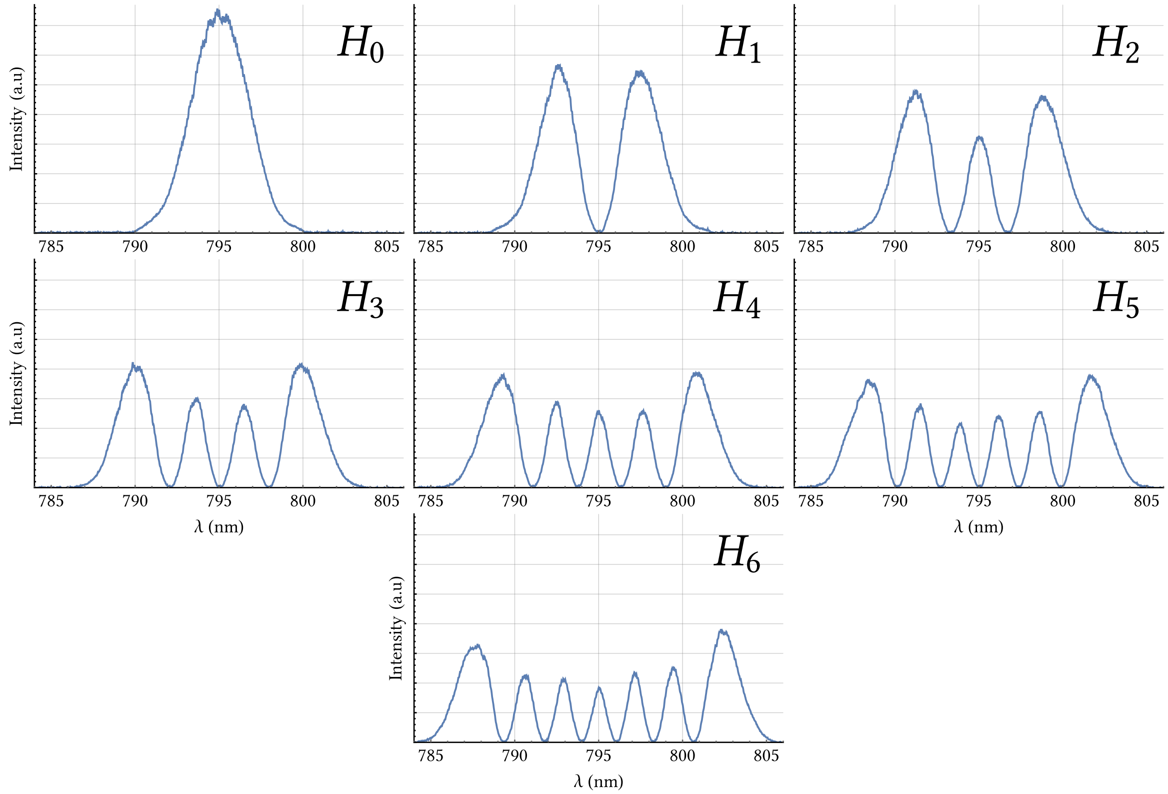

Figure 6.3: Spectral intensity profiles of the gate modes for the family of H_n Hermite functions whose H_0 has a bandwidth of 4nm.

We present some experimental matrices in the following subsection.

6.2.3.2 Experimental matrices

Figure 6.4 shows the subtraction matrices reconstructed in the probing basis introduced in figure 6.2. For each of those different matrices, the imaginary part should be null but we still retrieve a few weak components due to noise and some experimental imperfections. All the measured matrices prove the tunability of our single-photon subtractor and its capability to address any arbitrary broadband frequency mode within a given optical bandwidth and spectral complexity. The main limitations are, in descending order of importance, the bandwidth of the phase-matching, the bandwidth of the gate available and the optical resolution of the pulse shaper. To demonstrate the capability to engineer the spectral phase of a subtraction mode, we present on figure 6.5 the subtraction matrix where the gate mode was a coherent superposition of H_1 and H_2 with a $\pi/2$ phase. We also measured the subtraction matrices (not displayed here) for the following coherent superpositions: $H_0 + H_1$, $H_0 + H_2$, $H_0 + iH_2$, $H_2 + H_3$, $H_3 + H_4$, $H_0 + H_1$, $H_0 + H_1 + H_2$, $H_1 + H_3 + H_4$, $H_1 + iH_3 + H_4$, $H_0 + H_1 + H_2 + H_3 + H_4$ and finally $H_0 + H_1 + H_2 + H_3 + H_4 + H_5 + H_6$.

We do not directly compute the purity of the experimental subtraction matrices. Indeed, those matrices suffer from experimental errors. Those errors come from the noise of the single-photon detector and the imperfections of our measurement. The noise from the detector in particular, becomes annoying when the signal to be measured is null, or extremely weak. The noise being constant, the signal ratio for the small terms of the subtraction matrix becomes low, hence those small terms are most likely quite inaccurate. One of the annoying manifestation of those experimental errors is to be found in the properties of the experimental subtraction matrices.

For instance, for the subtraction matrix where the gate mode is a H_0 function with 4nm bandwidth, some of the eigenvalues obtained through eigendecomposition are negative as depicted on figure 6.6. Those negative eigenvalues mean that the experimental subtraction matrices are not semi-definite positive, hence physical, which contradicts the theoretical predictions of chapter 4 (see equation (4.15)). Those negative eigenvalues could lead to a Schmidt number lower than unity, or a process purity greater than unity which is non physical. Still, figure 6.6 provides a very valuable information. We see that one eigenvalue is clearly dominating meaning that one mode of subtraction dominates over all the others. We will discuss the reconstruction of physical subtraction matrices later in this chapter and focus now on the eigenmodes of those subtraction matrices.

6.2.3.3 Eigenmodes

We present on figure 6.7 the first and dominating eigenmode of the matrices displayed in the previous subsection. Those first eigenmodes show the expected features, namely:

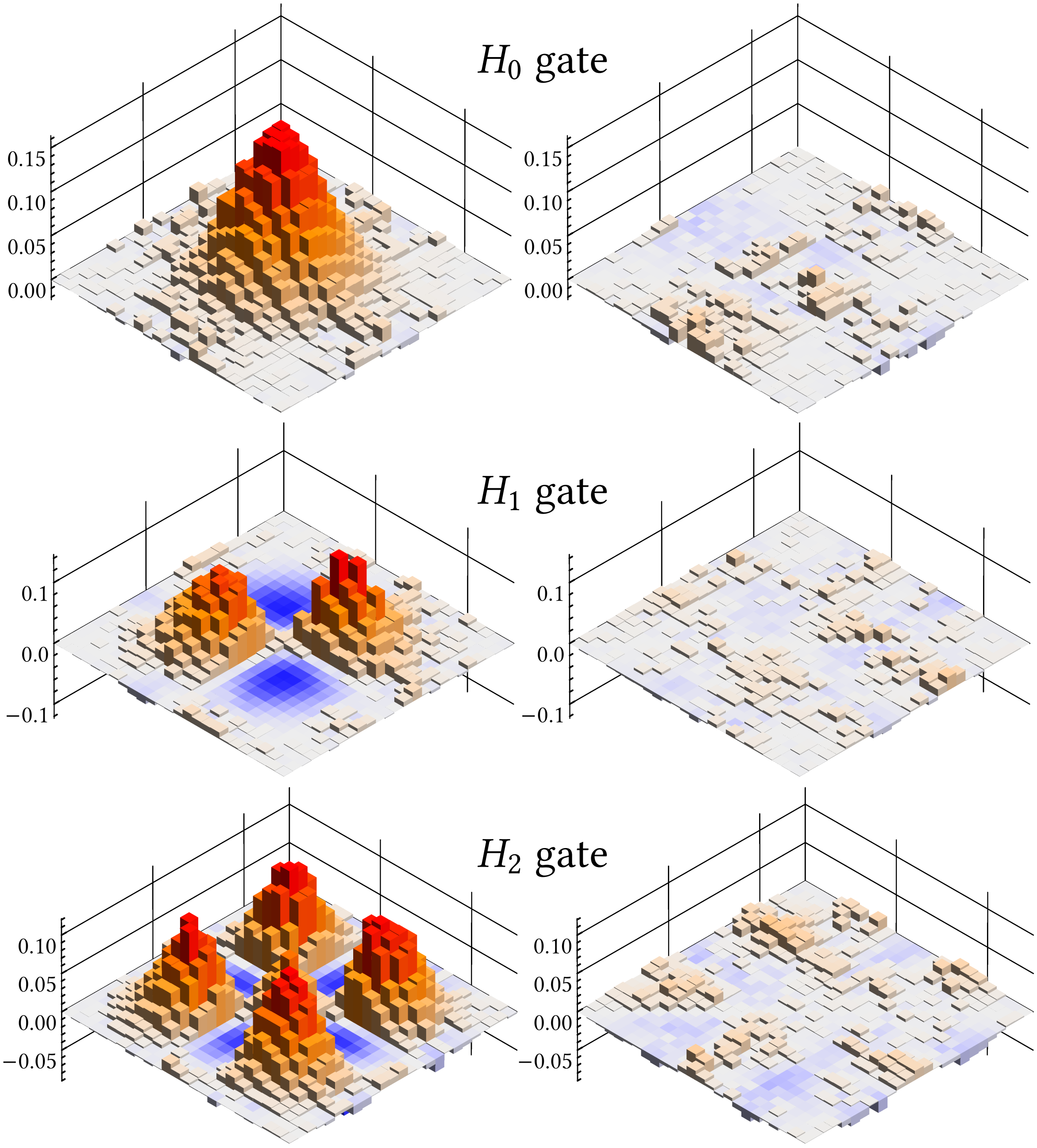

Figure 6.4: Real (left column) and imaginary (right column) parts of experimental subtraction matrices obtained for different gate modes presented on figure 6.3: H_0 with a bandwidth of 4nm (first row), H_1 of the same family (second row) and H_2 (last row). Matrices are shown from their lower left corner.

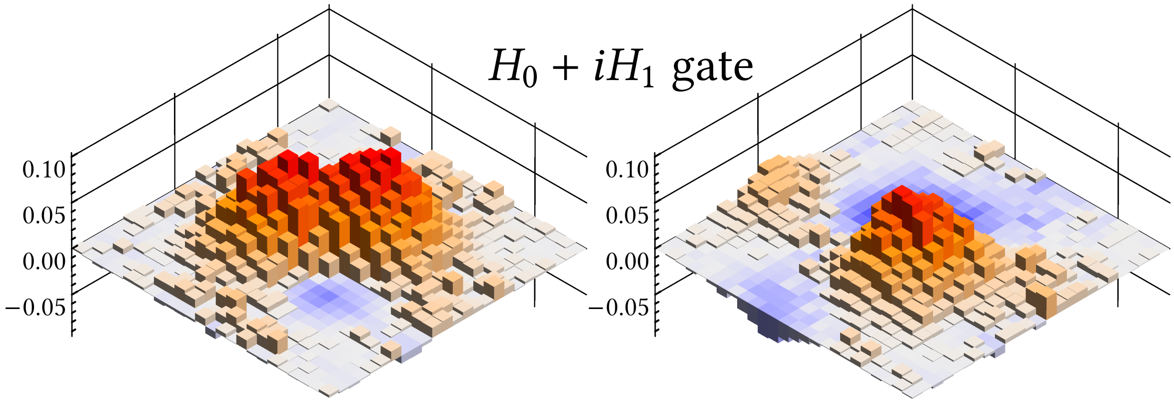

Figure 6.5: Real (left column) and imaginary (right column) parts of the experimental subtraction matrix obtained for a gate mode consisting in a coherent superposition of H_0 and H_1 wih a $\pi/2$ phase. Matrices are shown from their lower left corner.

- a Gaussian profile of bandwidth (intensity FWHM) of about 4nm and a flat phase for the H_0 gate,
- a H_1 profile with a π phase shift at the center for the H_1 gate,
- a H_2 profile with two π phase at the nodes for the H_2 gate
- a super-Gaussian like amplitude profile wider than the H_0 with a dip in the middle and a linearly increasing phase π for the $H_0 + iH_1$ gate.

The phase of each of those subtraction modes only makes sense for the frequency bands where there is actually some amplitude. In the frequency bands where there is no energy, the phase is not defined and gets more noisy. It leads to random phase jumps from negative values close to $-\pi$ to positive values close to π as the phase has been wrapped between those bounds. Also, the average value of the phase does not have a particular physical meaning here as those modes are only defined up to an arbitrary relative phase.

Those first eigenmodes are proofs that our single-photon subtractor is capable of reproducing the spectral mode imposed by the gate mode as explained in 5. In order to fully assess the performance of our single-photon subtractor, we should compute the Schmidt number K of the subtraction matrices (or the process purity $1/K$) as well as the first eigenvalues. For this, we reconstruct physical matrices through Maximum-Likelihood.

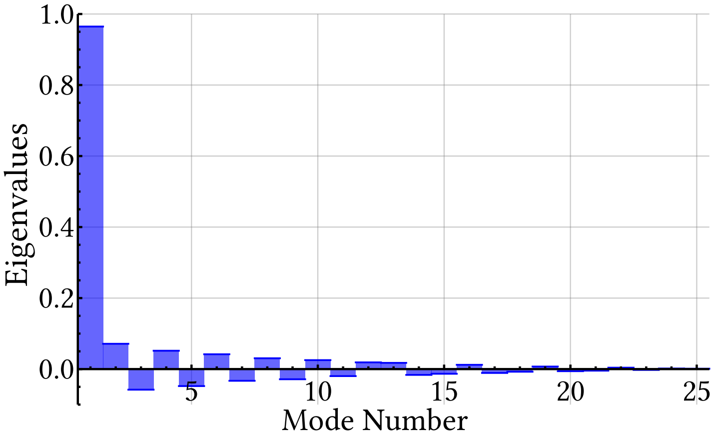

Figure 6.6: Eigenvalues of an experimental subtraction matrix whose gate mode is a H_0 of 4nm bandwidth (intensity FWHM).

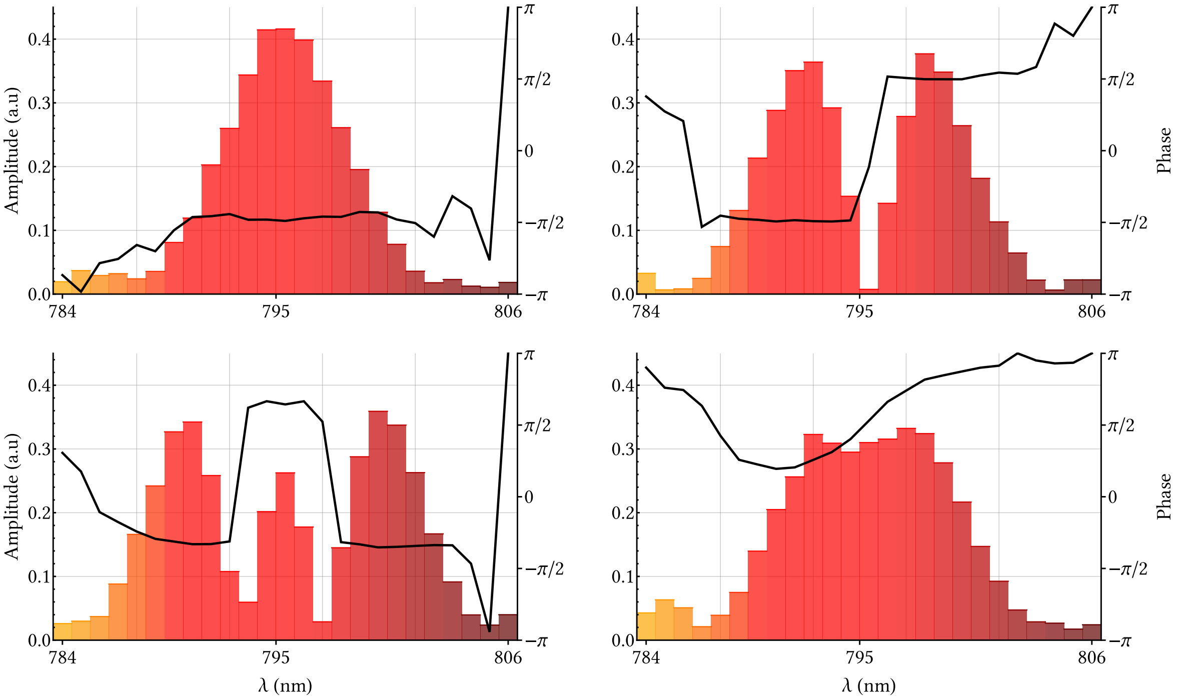

Figure 6.7: Amplitude (colored bars) and phase (solid black line) of the first eigenmode of the experimental subtraction matrices displayed on figures 6.4 and 6.5: H_0 gate (upper left), H_1 gate (upper right), H_2 gate (lower left) and $H_0 + iH_1$ gate (lower right).

6.3 Maximum-Likelihood reconstruction

As explained in the previous section, the experimental subtraction matrices are not physical (precisely not semi-definite positive), mostly because of the incorrect values of their small terms. Those errors might be partly suppressed by further optimizing the experimental setup to make sure that the supposedly null terms of the subtraction matrices are correctly canceled when computed from the measurement data. Also, integrating the signal for each measurement on a longer time may help but the overall acquisition time would be increased proportionally, leading to time-consuming experiments.

Because of our guilty laziness, and the fact that we already spent significant time optimizing this measurement, we rather perform a Maximum-Likelihood reconstruction of the subtraction matrix similarly to [Fedorov 15].

6.3.1 Principle of Maximum-Likelihood reconstruction

For a given experimental subtraction matrix S, we want to find a positive semi-definite matrix S^{Lik} that maximizes the likelihood to obtain the measurement data associated to S.

6.3.1.1 Single-photon detection as a random process

The physical process that we try to assess is a parametric process. It is inherently probabilistic. The up-converted photons are also subject to many optical losses, namely:

- losses at the interfaces of the second lens of the telescope (the coating is not adapted to UV light) for about 40%,
- losses in the spectral filter for about 40%,
- losses at the fiber injection the coupling being limited to 50% at best,
- losses at the detector whose quantum efficiency is approximately 40%.

Hence approximately 95% of the up-converted photons are lost between the bulk BiBO crystal and the detector avalanche process. On top of that, the detector has an inherent noise, even if we worked hard toward minimizing it (see chapter 5). For all those reasons, we assume that the count number of the detector eventually given by the detector follows a binomial distribution of probability p. For a large number of counts the probability mass function can be approximate to be Gaussian (according to the central limit theorem) and we model the probability to get a count number c as:

$$P\left(c\right) \propto \exp\left[-\frac{\left(c-\langle c\rangle\right)^2}{2\sigma_c^2}\right] \tag{6.27}$$

where $\sigma_c^2 = \langle c\rangle(1-p)p$ is the variance of the probability mass function and $\langle c\rangle$ is the average of the probability mass function of the detection count, i.e. the most likely value to be measured [James 01].

To reconstruct a subtraction matrix, we perform N^2 measurements leading to a set $\{c_i\}$ of measurement values. Each measurement obeys to the probability law (6.27) with a different parameter $\langle c_i \rangle$ for each. The likelihood $\mathcal{L}$ that a given set of values $\{\langle c_i \rangle\}$ could produce the N^2 measurements $\{c_i\}$ is the product of each individual measurement probabilities:

$$\mathcal{L} = \prod_i P\left(c_i\right) \propto \prod_i \exp\left[-\frac{\left(c_i - \langle c_i \rangle\right)^2}{2\sigma_{c_i}^2}\right] \tag{6.28}$$

It is very common to treat maximum-likelihood problems by maximizing the log-likelihood $\log\left(\mathcal{L}\right)$ as this quantity is much simpler to compute. We choose the fitness function $\mathcal{F}$ of our evolution strategy (see next subsection) to be proportional to the log-likelihood $\log\left(\mathcal{L}\right)$:

$$\mathcal{F} = -\sum_i \frac{\left(c_i - \langle c_i \rangle\right)^2}{\langle c_i \rangle} \propto \log\left(\mathcal{L}\right) \tag{6.29}$$

According to expressions (6.22) and (6.26), the sets $\{c_i\}$ and $\{\langle c_i \rangle\}$ can be computed from the subtraction matrices S and S^{Lik}.

6.3.1.2 Search and optimization under constraints

The reconstructed subtraction matrix S^{Lik} must satisfy the following mathematical criterion: be semi-definite positive with unity trace. To guarantee this, we actually look for a lower triangular complex matrix $\mathbf{T}$ that is the Cholesky decomposition of the matrix S^{Lik}, i.e. $\mathrm{S}^{Lik} = \mathbf{T}^\dagger\mathbf{T}$ [James 01]. The matrix S^{Lik} is then necessarily semi-definite positive. The optimization must thus be performed on the N^2 values $\{t_k\}$ composing the matrix $\mathbf{T}$. The fitness function $\mathcal{F}$ is computed from $\mathbf{T}$ by computing S^{Lik} and then the set of associated measurement values $\{\langle c_i \rangle\}$ that are compared with the experimental counts $\{c_i\}$ through expression (6.29).

6.3.2 Optimizing with evolutionary strategies

Evolutionary Strategies (ES) is a general term grouping all search and optimization algorithms inspired by organic evolution based on Darwinian theory [Back 96]. They are close but conceptually different from Genetic Algorithms (GA) [Chambers 98] in the sense that GA optimize a set of discrete-valued (often binary) parameters while ES optimize continuous-valued parameters. Those algorithms are particularly well suited to find a global solution in a high dimensional complex landscape of peaks, ridges and valleys because of their stochasticity. Those algorithms can be described by two parameters (μ, λ). They search and optimize a problem of dimension N in the following way:

- at first, a set of μ individuals $\{\vec{x}_k\}$ (where the dimension of $\vec{x}_k$ is N) is generated at random;

- from this first set, a set of λ offspring are generated through recombination of the of the μ parents; each offspring is also authorized to have some mutations;
- the performance of each offspring is tested with a fitness function $\mathcal{F}$;
- among the λ offspring, only the μ first that performs the best with respect to $\mathcal{F}$ are kept, the others are discarded (survival of the fittest);
- the set of μ selected offspring becomes the next generation of individuals $\{\vec{x}_k\}$ and the process iterates.

Different variations exist depending on the ratio μ/λ and the importance given to recombination or mutations and we will detail ours in a following subsection.

Evolutionary algorithms allow to find a numerical solution to an optimization problem of high dimensionality when a lack of analytic solution makes a fitness function the only available measure of success. A thorough and detailed review of evolutionary algorithms can be found in [Roslund 10] (in the context of quantum coherent control) and its references.

6.3.2.1 The failure of standard regression methods

In [James 01], an identical search and optimization problem is solved using the Mathematica FindMinimum routine. In their case, the dimension of the target matrix is only $4\times4 = 16$. In order to converge to a solution, this routine may use different well-known regression methods such as the Gradient Descent or the Levenberg-Marquardt algorithm[2]. While this routine and its methods are well adapted for search and optimization problems of low dimensionality, they are doomed to fail in our case by the *curse of dimensionality*[3]. For instance, we tried to perform the aforementioned Maximum-Likelihood optimization procedure with tomography matrices whose dimensions was $16\times16 = 256$. The routine eventually converged to some solution using a single-core i7-3770 CPU clocked at 3.4GHz after a random computation time between twenty minutes and thirteen hours depending on the experimental matrix to replicate. This is simply not practical. We did not even try with our $25\times25 = 625$ matrices, knowing beforehand that there existed search-and-optimize algorithms capable of dealing with our higher dimensionality.

6.3.2.2 Our evolutionary algorithm

The exact (μ, λ) evolutionary strategy we use is a Covariance Matrix Adaptation Evolutionary Strategy (CMAES) where we choose $\mu = 1$, i.e. no recombination and only one parent individual. This algorithm is a *derandomized evolution strategy* where it is sufficient to take $\lambda \propto \log(dim)$ where $dim = N^2$ is the dimension of the problem (in practice, $\lambda = 4 + \lfloor 3\log(dim)\rfloor$ where $\lfloor x\rfloor$ is floor of x). The algorithm uses a covariance matrix $\mathbf{C}$ that

---

[2] Check FindMinimum in the Mathematica documentation for a full list of the available methods

[3] see Curse of dimensionality on Wikipedia

defines which directions of the multidimensional landscape should be preferably explored through mutations. The offspring are generated only by mutations of the parent individual and the rejection rate of the offspring is 50%. A new parent is formed as a combination of the offspring weighted by their respective performance and the covariance matrix is updated through Principal Component Analysis (PCA) according to the performance of each offspring (see Appendix A of [Roslund 10] for a detailed explanation). We choose the number of *generations* (iterations) that the algorithm must complete before stopping and we monitor its convergence with the evolution of the fitness function $\mathcal{F}$ as presented on figure 6.8.

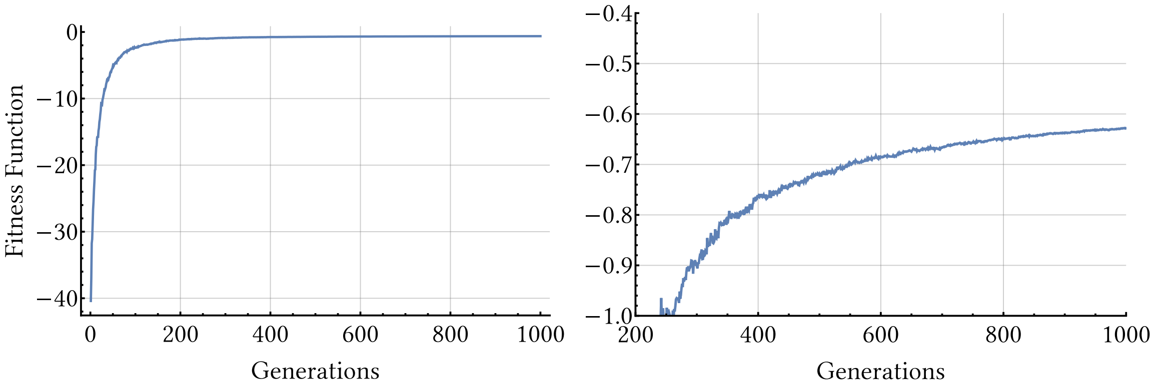

Figure 6.8: Left: Evolution of the fitness function on 1000 generations during the reconstruction of the matrix whose gate mode is a 4nm H_0 Hermite function (see figure 6.4). Right: Same than left but zoomed on $[-1, -0.4]$ after 200 generations.

In our specific situation, the search landscape of the Maximum-Likelihood reconstruction seems quite smooth as the fitness function systematically converges directly to the desired solution as shown on figure 6.8. Nevertheless, proving that there are no local maxima requires an analytic demonstration of the concavity (or convexity) of the search landscape. It is usually done using the Hessian matrix [Roslund 10]. If we were directly optimizing the set of values $\{\langle c_i \rangle\}$, the expression of $\mathcal{F}$ would suffice to demonstrate the convexity of the landscape. But our algorithm optimize $\mathcal{F}$ through the values $\{t_j\}$ of the complex lower triangular matrix $\mathbf{T}$. Still, the values $\{\langle c_i \rangle\}$ can ultimately be expressed as quadratic forms of the $\{t_j\}$ up to a normalization constant equal to $\sum_j t_j^2$. We think it constitutes a good reason to assume the absence of local maxima in our search landscape.

6.3.3 Reconstruction in the pixel basis

The subtraction matrices in the pixel basis reconstructed by Maximum-Likelihood can eventualy be characterized in terms of their Schmidt number K (or process purity $1/K$) and mode selectivity σ_0.

6.3.3.1 Reconstructed matrices

We present on figure 6.9 the reconstructed subtraction matrices corresponding to the ones shown on figure 6.4 along with the one corresponding to a gate mode $H_0 + H_1$. We also present on figure 6.10 the reconstructed subtraction matrix corresponding to figure 6.5. We do not show the imaginary part when it is measured and null within experimental uncertainties.

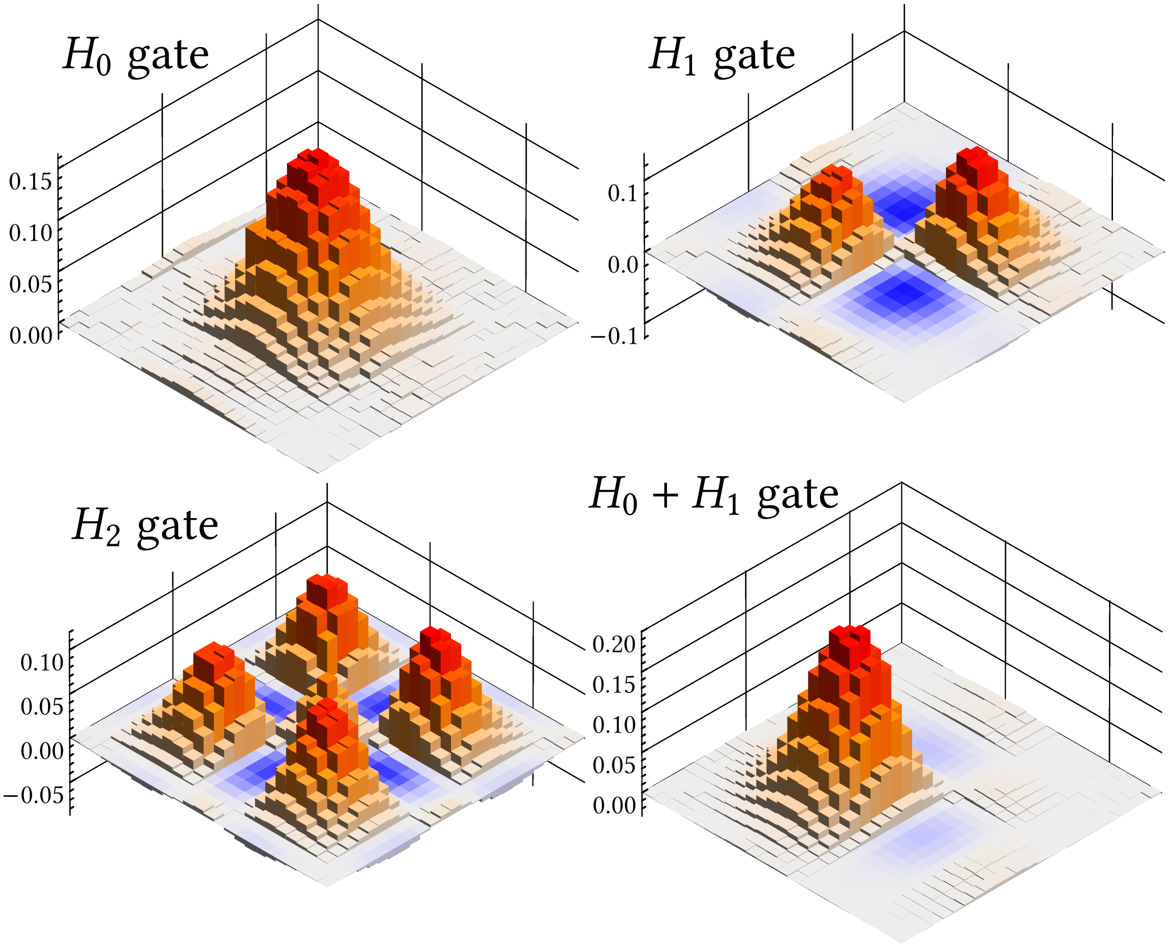

Figure 6.9: Real parts of the subtraction matrices reconstructed with the data presented on figure 6.4 along with a reconstruction for a $H_0 + H_1$ gate mode (lower right). Matrices are shown from their lower left corner.

For information, the reconstruction of those matrices with our Maximum-Likelihood algorithm uses $\lambda = 55$ offspring that must be evaluated at each iteration (*generation* in the vocabulary of evolutionary strategies) with the fitness function $\mathcal{F}$ introduced in equation

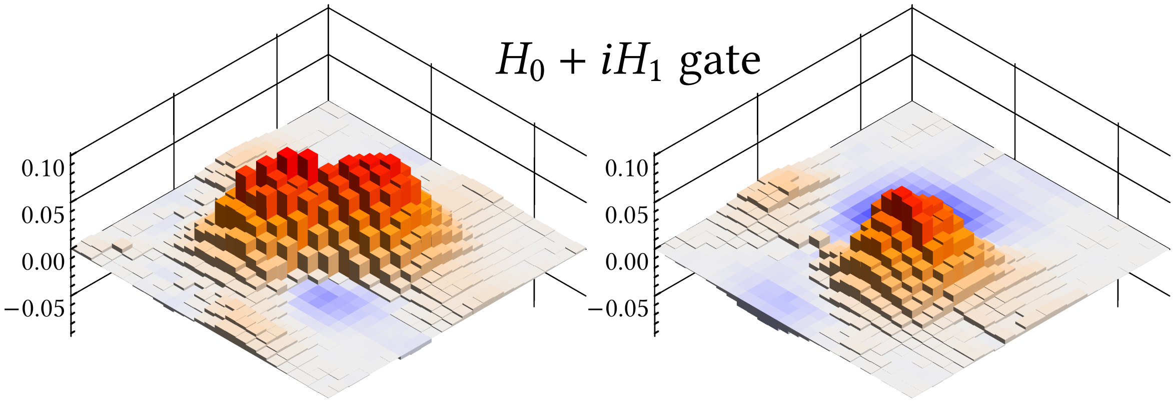

Figure 6.10: Real part (left) and imaginary part (right) of the subtraction matrices reconstructed with the data presented on figure 6.5. Matrices are shown from their lower left corner.

(6.29). Such an evaluation can be parallelized to shorten the computation. We usually performed up to 5000 iterations in about an hour with seven single-core i7-3770 CPUs clocked at 3.4GHz working in parallel.

6.3.3.2 Eigenmodes and eigenvalues

We present on figure 6.11 the first and dominating eigenmode of each reconstructed matrix presented on figures 6.9 (except for the H_0+H_1 gate mode) and 6.10. They are the Maximum-Likelihood counterpart of the subtraction modes obtained from experimental data and first presented on figure 6.7. All subtraction modes exhibit the same desired features they previously displayed when computed directly from experimental data. All previous remarks about their phase also holds here.

We present on figure 6.12 the eigenvalues of the reconstructed subtraction matrix whose gate mode is H_0. Those eigenvalues are the Maximum-Likelihood counterpart of the ones presented on figure 6.6. They are all positive, thanks to the Maximum-Likelihood under constraints and the reconstructed subtraction matrix is semi-definite positive. We do not show the eigenvalues of the other reconstructed subtraction matrices here since they all have a strongly dominating eigenvalue leading to a very empty distribution. As the matrices obtained through Maximum-Likelihood reconstruction are physical according to expression (4.15), it now makes sense to compute their Schmidt number (or process purity).

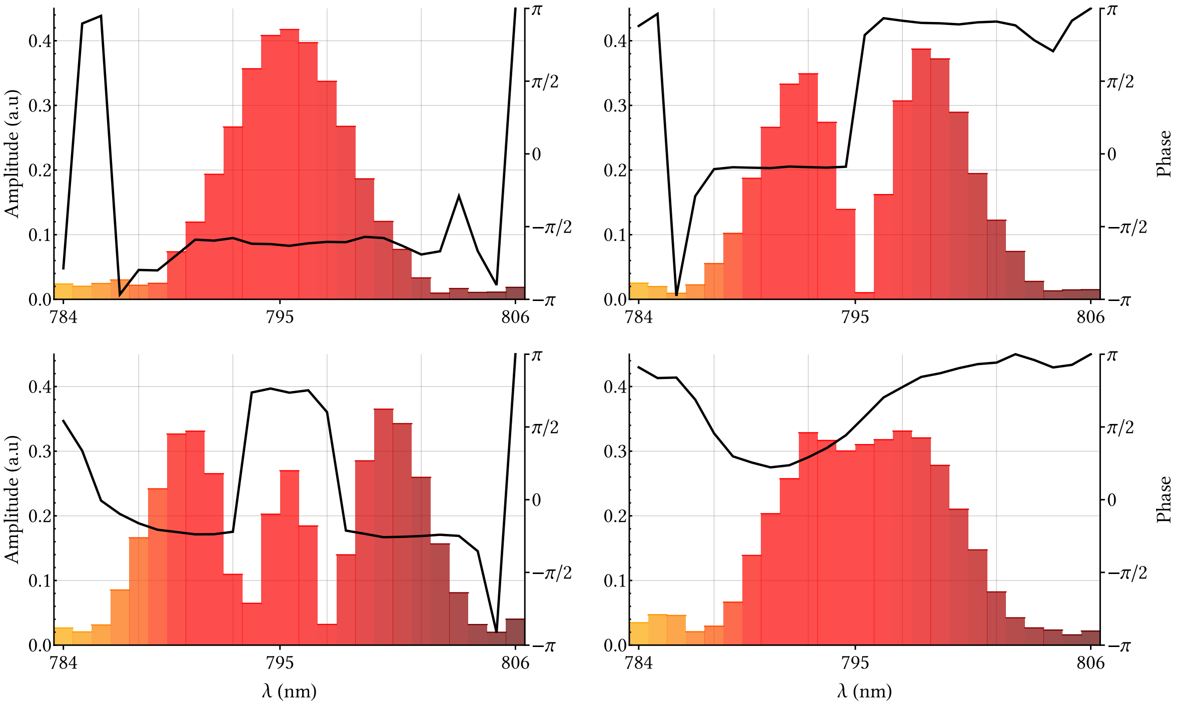

Figure 6.11: Amplitude (colored bars) and phase (solid black line) of the first eigenmode of the Maximum-Likelihood reconstructed subtraction matrices displayed on figures 6.9 and 6.10: H_0 gate (upper left), H_1 gate (upper right), H_2 gate (lower left) and $H_0 + iH_1$ gate (lower right).

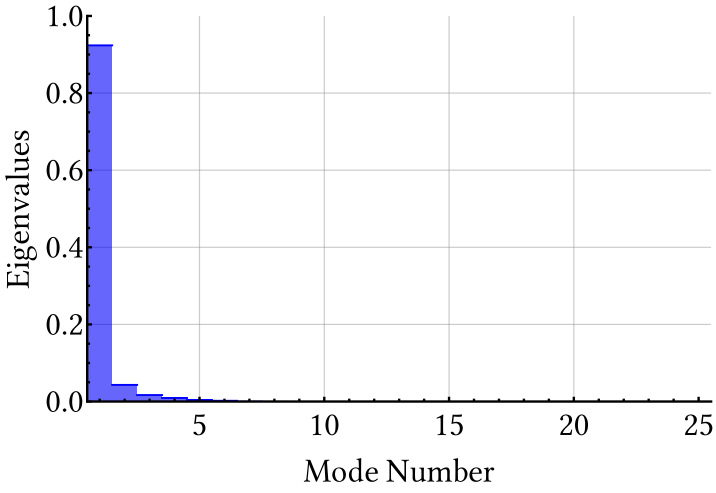

Figure 6.12: Eigenvalues of the reconstructed subtraction matrix whose gate mode is a H_0 of 4nm bandwidth (intensity FWHM).

6.3.3.3 Schmidt number and mode selectivity

We summarize the results for every Maximum-Likelihood reconstructed matrix in the following tables. The Schmidt number K along with the process purity $(1/K)$ are given. The mode selectivity σ_0 is the value of the first and dominating eigenvalue of the subtraction matrix. It is equal to the probability to subtract a photon from the first subtraction mode. All Hermite functions H_n of the gate mode belong to the 4nm family unless their bandwidth is given explicitly.

Gate Mode	K	Purity	σ_0
H_0 2nm	1.27	0.79	0.88
H_0 3nm	1.36	0.74	0.85
H_0 4nm	1.16	0.86	0.92
H_0 5nm	1.40	0.71	0.85
H_0 6nm	1.38	0.72	0.84
H_0 7nm	1.14	0.88	0.94
H_0 8nm	1.57	0.64	0.79
H_0 9nm	1.23	0.81	0.90
H_0 10nm	1.26	0.79	0.89

Gate Mode	K	Purity	σ_0
H_0	1.16	0.86	0.92
H_1	1.19	0.84	0.91
H_2	1.23	0.81	0.89
H_3	1.31	0.76	0.87
H_4	1.39	0.72	0.84
H_5	1.51	0.66	0.79
H_6	1.69	0.59	0.75

Gate Mode	K	Purity	σ_0
$H_0 + H_1$	1.16	0.86	0.92
$H_0 + iH_1$	1.36	0.74	0.85
$H_0 + H_2$	1.04	0.96	0.98
$H_0 + iH_2$	1.40	0.71	0.84
$H_2 + H_3$	1.29	0.78	0.87
$H_3 + H_4$	1.40	0.71	0.84
$H_0 + H_1 + H_2$	1.08	0.93	0.96
$H_1 + H_3 + H_4$	1.23	0.81	0.90
$H_1 + iH_3 + H_4$	1.28	0.78	0.86
$H_0 + H_1 + H_2 + H_3 + H_4$	1.17	0.85	0.92
$H_0 + H_1 + H_2 + H_3 + H_4 + H_5 + H_6$	1.16	0.86	0.93

The tables presented above demonstrate that our single-photon subtractor is fairly single-mode apart from a few cases where the Schmidt number rises above 1.50. Our measurement is not exempt from errors such as noise in the detector, variation of power (even if we renormalize each measurement), phase instabilities across the whole optical table and poor signal-to-noise ratio for frequency bands where only little optical power is available. A direct consequence of this poor signal-to-noise ratio can be found in the wings of the subtraction modes in figures 6.7 and 6.11. A pedestal appears at both edges of the different spectra. The origin of this pedestal is to be found in the subtraction matrices themselves and can be clearly identified on the reconstructed ones on figures 6.9 and 6.10 as they are exempt from random noise but still display systematic errors. For instance, on figure 6.10, a feeble but still noticeable signal can be seen on the edges of the real and imaginary parts while the matrix terms are expected to be null.

As showed by equation (6.26), the off-diagonal terms of the subtraction matrices are obtained by subtracting the two individual pixel measurements results from the two pixels measurement. In the individual pixel measurement, we try to utilize all the optical power available for each pixel. In the two pixels measurement, we also try to utilize as much optical power as possible for the two pixels while conserving the power ratio measured during the individual measurements. Additionally, an edge and a center pixel may lead to very different conversion rate. Those aspects make it difficult to perfectly cancel the off-diagonal values of the subtraction matrices and may lead to the aforementionned systematic errors.

6.4 Tomography in a natural basis

The previous section demonstrated that our single-photon subtractor was sufficiently single-mode and that the mode of subtraction that we measured matched desired target. The previous tomography was using a basis of modes that did not favor any spectral mode within its interval (see 6.2). Now that we have identified the subtraction modes for each gate mode, we can reproduce this tomography in a more appropriate basis, namely, the basis of the subtraction modes themselves.

6.4.1 The measurement basis

Our new probing basis $\{\boldsymbol{u}_k\}$ is a family of H_n Hermite functions whose H_0 has a bandwidth of 4nm (intensity FWHM) as presented on picture 6.13. Those modes are, on purpose, identical to the modes we used for the gate during the process tomography in the pixel basis (see figure 6.3.

The dimension of the measurement is reduced from $N \times N = 25^2 = 625$ pixels previously to $N \times N = 7^2 = 49$. There is thus only 49 measurements instead of 625 previously to be taken in order to reconstruct the subtraction matrices in this new basis. The acquisition time is conveniently reduced in proportion.

Also, to perform the tomography, we still had to make sure that the photon number per pulse was low and constant in each mode $\{\boldsymbol{u}_k\}$. For this purpose, we added an extra optical density on the probe beam on top of the ones that were already used for the pixel modes tomography. This extra optical density kept the average photon number per pulse below 10 for each Hermite function mode used in this tomography.

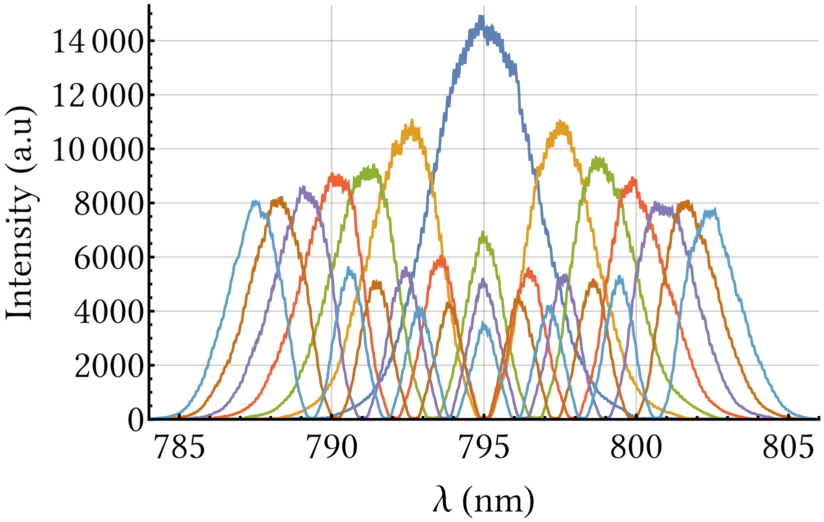

Figure 6.13: Intensity spectral profiles of the probe modes used for the tomography in a more adapted basis..

6.4.2 Raw measurement data

We performed subtraction matrix tomography for the same gate modes than the ones mentionned in subsection 6.2.3.1, except for the H_0 Hermite functions with varying bandwidths. The tomography was performed using the theory developed in subsection 6.2.2 in order to retrieve the off-diagonal terms in the new basis. We present on figure 6.14 the experimental subtraction matrices obtained with a tomography performed in the basis of Hermite functions. Our single-photon subtractor is capable of adressing each gate mode in a single-mode fashion as well as arbitrary complex superpositions of the gate modes. In the continuity of our previous measurements, we also performed the tomography of some superpositions involving a $\pi/2$ phase as presented on figure 6.15. The imaginary parts of the different matrices indicate the presence of the $\pi/2$ phase factors between the different components.

6.4.3 Maximum-Likelihood reconstruction

Just as the subtraction matrices in the pixel basis, the subtraction matrices in the Hermite functions basis almost always exhibit at least one negative eigenvalue. Even if this negative eigenvalue is extremely weak, the subtraction matrix remains unphysical. Hence similarly to the tomography in the pixel basis, we performed a Maximum-Likelihood reconstruction using our evolutionary strategy. In the basis of Hermite functions, the algorithm required ony $\lambda = 4 + \lfloor 3\log(N \times N) \rfloor = 18$ offspring at each generation (N=7 here). The evalutation of the fitness function at each generation is parallelized over six CPUs to shorten the computation time. For the tomography in the basis of Hermite functions, 1000 generations were more than enough to converge and stabilize the algorithm (actually 500 generations would suffice). The thousand generations took 130 seconds to our six single-core i7-3770 CPUs to complete.

We do not present the reconstructed matrices here as they remain fairly similar to the experimental matrices while eliminating the random noise. Systematic errors still remain. In particular, the unbalancing between the different components of a superposition remained. This unbalance can be seen on the diagonal of some experimental subtraction matrices on figures 6.14 and 6.15. Nevertheless, with reconstructed matrices, we can compute the Schmidt number of the process and quantify its purity along with its modal selectivity emphasized by the first eigenvalue σ_0 of the subtraction matrices.

Gate Mode	K	Purity	σ_0
H_0	1.03	0.97	0.98
H_1	1.11	0.90	0.95
H_2	1.17	0.85	0.92
H_3	1.25	0.80	0.89
H_4	1.35	0.74	0.85
H_5	1.33	0.75	0.85
H_6	1.26	0.79	0.88

Gate Mode	K	Purity	σ_0
$H_0 + H_1$	1.09	0.92	0.96
$H_0 + iH_1$	1.20	0.83	0.91
$H_0 + H_2$	1.16	0.86	0.92
$H_0 + iH_2$	1.15	0.87	0.93
$H_2 + H_3$	1.20	0.83	0.91
$H_3 + H_4$	1.30	0.77	0.87
$H_0 + H_1 + H_2$	1.10	0.91	0.95
$H_1 + H_3 + H_4$	1.30	0.77	0.87
$H_1 + iH_3 + H_4$	1.22	0.82	0.90
$H_0 + H_1 + H_2 + H_3 + H_4$	1.09	0.92	0.96
$H_0 + H_1 + H_2 + H_3 + H_4 + H_5 + H_6$	1.04	0.96	0.98

Those tables show that performing the process tomography in an appropriate basis of measurement leads to much faster results whose purities are generally enhanced. While the analysis in the pixel basis may seem to offer a higher resolution due to its higher number of modes, it comes with unwanted experimental errors decreasing the quality of the subtraction process parameters estimate. It is nevertheless necessary to perform it in order to reveal the eigenmodes of the process as pixels constitute a fairly unbiased basis. The tomography based on Hermite functions probe modes is more adapted to the modes to be probed. The purity obtained with those probing modes is thus more meaningful with respect to the device. The two tomographies using those two different basis of analysis are thus complementary and provide different information about our single-photon subtractor.

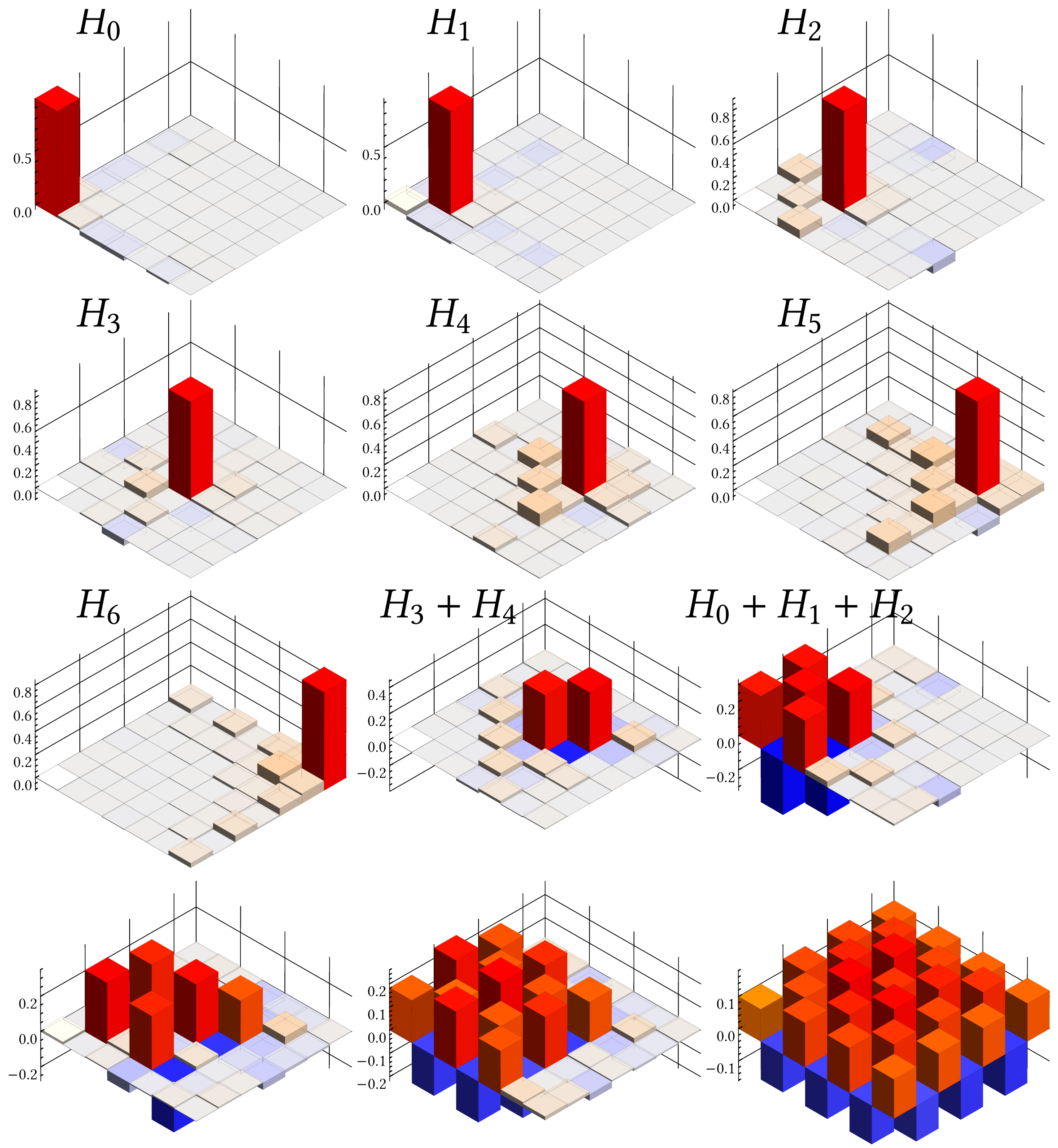

Figure 6.14: Real parts of subtraction matrices in the Hermite functions basis. Gate modes from left to right and top to bottom: H_0, H_1, H_2, H_3, H_4, H_5, H_6, $H_3 + H_4$ and $H_0 + H_1 + H_2$. The last row gate modes are not indicated on the figure for readability and are respectively, from left to right: $H_1 + H_3 + H_4$, $H_0 + H_1 + H_2 + H_3 + H_4$, and $H_0 + H_1 + H_2 + H_3 + H_4 + H5 + H_6$. Imaginary parts are expected to be null and are not displayed here as they only contain noise.

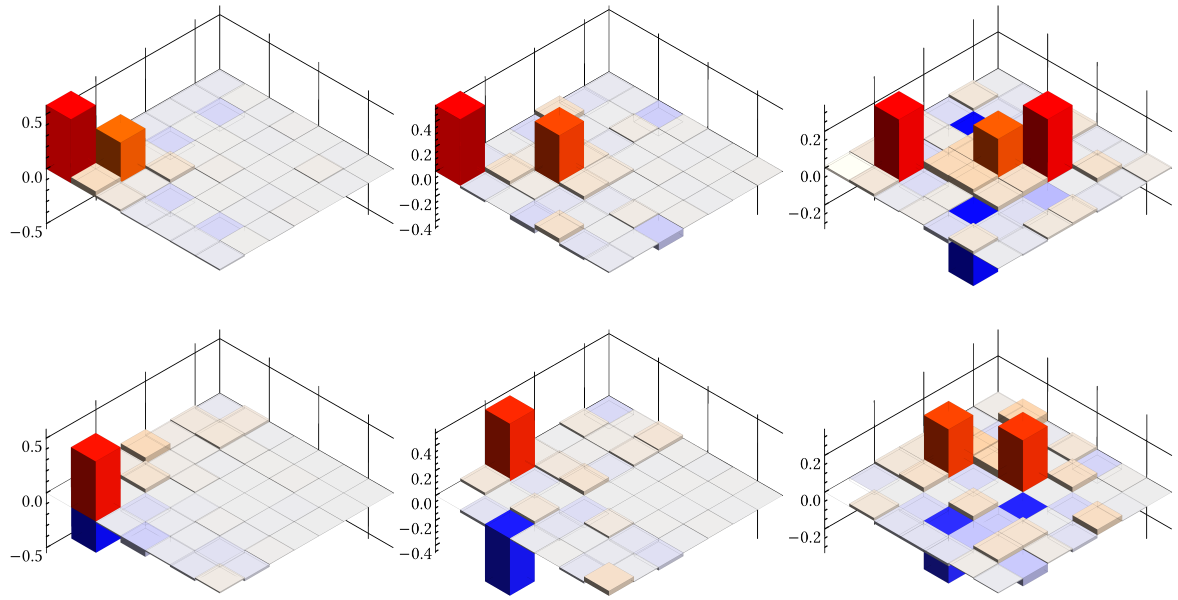

Figure 6.15: Real (upper row) and imaginary (lower row) parts of subtraction matrices in the Hermite functions basis. Gate modes from left to right: $H_0 + iH_1$, $H_0 + iH_2$, $H_1 + iH_3 + H_4$.

Conclusion & outlooks

During the course of this thesis, we have designed and built a single-photon subtractor for spectrally multimode quantum states. The construction of this device was motivated by the development of spectrally multimode squeezed vacuum presented in chapter 3. Those states contain many single-mode squeezed vacuum states embedded in broadband orthogonal spectral modes. Engineering this multimode squeezed state through single-photon subtraction requires a mode-selective device capable of preserving the state purity.

We have first developed a theoretical framework to better understand the subtraction of a single photon on a multimode quantum resource with the concept of the modal subtraction matrix. This framework has helped us identify the conditions for a single-mode subtraction as well as the effect of the interplay between the input state modes and the subtraction modes. This framework was then applied to the context of spectrally multimode light where we have discussed the difference between the legacy subtraction scheme based on a weak beamsplitter and a new scheme based on weak up-conversion.

We have then fully modeled the subtraction process based on sum-frequency generation between a signal beam and a gate beam used as a control. We have introduced a non-collinear configuration aimed at enabling a degenerate conversion process. This configuration also allows to cancel efficiently the detection noise of the single-photon detector used as an heralding device in the subtraction process. We have presented the conditions required to achieve a single-mode operation of the subtractor, the optimal design, as well as the tuning capabilities through ultrafast pulse shaping of the gate beam.

We have characterized the device at the single-photon level guaranteeing the subtraction of a single-photon only. We have measured the subtraction matrices and revealed its dominating eigenmode for many different gate modes in two different basis of analysis. Finally, we have performed a Maximum-Likelihood reconstruction of the experimental subtraction matrices through an evolutionary strategy aimed at retrieving the physical subtraction matrices. Our results outline that the device we have built is tunable, thanks to the capabilities offered by ultrafast pulse-shaping, and mode selective up to a certain modal complexity.

Nevertheless, a single-photon subtraction on a genuinely quantum state has not been demonstrated here. The process could end up being impractical if the subtraction device induces important optical losses or modal distortions. Those modal distortions could be: an important change of the spatial mode or specific ultrafast problems like an irremediable spectral phase or a detrimental angular chirp. This could be further compensated but it could require additional and potentially lossy optical elements. Though we think that our device is capable of achieving near unity process purity for the following reasons. Firstly, the optical losses are limited to reflections on the four telescope lenses interfaces and the two crystal ones, all of whom can be coated to minimize optical losses. Secondly, while misaligned lenses introduce angular chirp, the device can be built so that the ultrafast problems for the signal beam are limited to the dispersive, birefringent nature of the non-linear medium. Thirdly, a spectral phase of the gate or a later local oscillator can be adapted with the ultrafast pulse shaper.

One could state that the single-photon subtraction process tomography we have performed is nothing else than a modal analysis of the sum-frequency generation and could thus be performed with bright beams and a classical detector instead of a single-photon counter. This claim is true as the modal nature of the process has no reason to change upon the nature or average photon number of the quantum states at play. Classical tomographies often offer a better signal-to-noise ratio and thus allow to resolve the space-time dependence of the process more precisely [Rozema 15]. Nevertheless, a classical tomography performed with bright beams would lead to multiphoton conversion and thus cannot qualify as a single-photon subtractor. The only way to guarantee that only a single-photon is converted is the demonstration of the linearity of the conversion that we provided in chapter 6.

The original project of this PhD work was a quantum state tomography [Ansari 16] of the single-photon subtracted multimode squeezed vacuum. Indeed, the natural step after having characterized our device is to feed it with the multimode squeezed vacuum demonstrated in chapter 3 and perform a quantum state tomography triggered on a subtraction event. This experiment necessitates an appropriate broadband homodyne detection electronics and a fast oscilloscope to recover the target mode of the single-photon subtracted state [Morin 13]. The different subsystems have been demonstrated separately in this work and the additional techniques required are common in the community. Considering that at first, no additional phase locking of sequential operation are necessary, we are confident that this experiment can be achieved rapidly.

We also look forward to new promising improvements and projects. The first one is the spectral broadening of the beam used to generate our gate, local oscillator or probe beams. A modest broadening could be achieved using an engineered photonic crystal fiber where a coherent four-wave mixing process could easily double the available spectrum [Jiang 16]. This broadening would allow us to perform homodyne detection in spectral regions that were once out of reach and to overcome one of the main limitations of the covariance matrix measurement detailed in chapter 3.

The second project is centered on the generation of the multimode squeezed vacuum. It consists in implementing an ultrafast pulse shaper on the pump beam of the SPOPO.

The objective is to engineer the spectral phase and amplitude of the pump beam in order to optimize either the squeezing or change the eigenmodes of the parametric down-conversion process. While the interest of increasing the amount of squeezing is straightforward, it is not clear yet what kind of multipartite entanglement can be created through pump pulse shaping. An appealing possibility would be to create on-demand cluster states in an easily accessible spectral basis such as orthogonal frequency bands. A theoretical study of the feasibility of such a multimode state engineering is currently under progress.

To conclude, our single-photon subtractor constitutes a building block for multimode quantum state engineering. It is capable of producing multimode non-Gaussian states when paired with a source of multimode spectrally squeezed states. The resulting quantum state would possess multipartite entanglement and the genuine feature of quantumness through the negativity of its Wigner function. Such a state exhibits some interesting entanglement properties and provides a promising platform for quantum information related proof of concept experiments.

Appendices

Appendix A

The SPOPO cavity

The cavity is composed of thirteen broadband high reflectivity mirrors and the beam undergoes fifteen reflections on a round trip. The pump beam is not resonant.

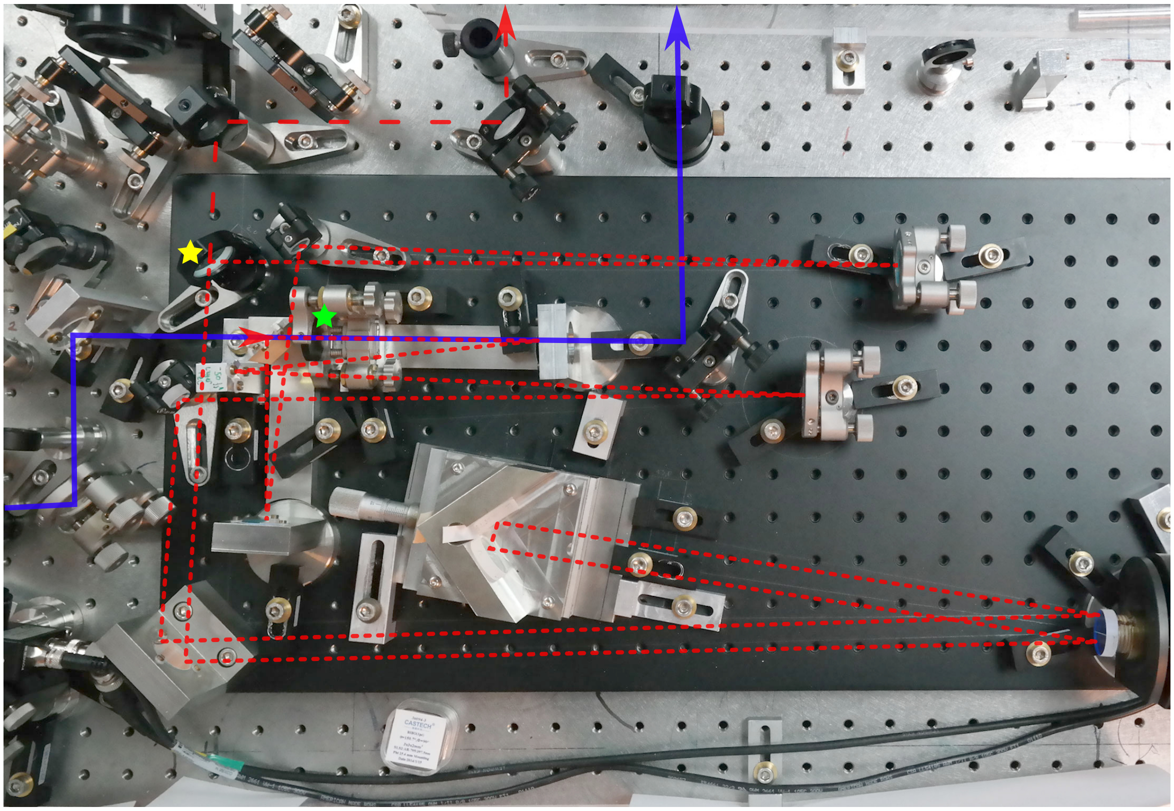

Figure A.1: Picture of the optical cavity of the SPOPO with the pump beam path (blue), the intra-cavity field path (dashed red), the crystal (green star) and the output coupler (yellow star).

Appendix B

Non-linear optics in BiBO

This appendix aims at providing the key ideas to do non-linear optics around the fundamental wavelength of $\lambda_0 = 795$nm in BiBO. For all the non-linear processes described in this thesis, we use an engineered crystal of monoclinic Bismuth Borate BiB_3O_6 commonly know as BiBO. The growth and characterization of this non-linear crystal dates back to the late 90s. It is thus younger than its older counterparts such as LBO and BBO. It offers higher non-linear coefficients for our wavelengths [Hellwig 98], along with a narrower phase-matching and transmission from UV to micrometric wavelengths [Hellwig 00]. A complete analysis of its optical properties can be found in [Ghotbi 04a]. We use BiBO in this work for Second-Harmonic Generation (SHG) [Ghotbi 04b], Parametric-Down-Conversion (PDC) [Ghotbi 06] and Sum-Frequency-Generation (SFG).

B.1 Principles of anisotropic optics

BiBO is a biaxial crystal whose refractive indices can be found in [Umemura 07] with the convention $n_x < n_y < n_z$. The Sellmeier equation and coefficients for BiBO can be seen on figure B.1 and are:

$$n = \sqrt{A + \frac{B}{\lambda^2 - C} - D\lambda^2}$$

Index	A	B	C	D
n_x	3.07403	0.03231	0.03163	0.013376
n_y	3.16940	0.03717	0.03483	0.01827
n_z	3.6545	0.05112	0.03713	0.02261

We remind a simple result of anisotropic optics that provides a way to understand how the refractive index changes with respect to the propagation direction in a birefringent medium [Zernike 73]. We consider a plane wave of wave vector $\mathbf{k}$ propagating in the birefringent medium. We denote Π the plane perpendicular to $\mathbf{k}$ containing the origin of the ellipsoid of indices $\mathscr{E}$. The intersection of Π with $\mathscr{E}$ is an ellipse E: $E = \mathscr{E} \cap \Pi$. This ellipse E has two main axes with values n_1 and n_2. The directions of those axes are the only ones

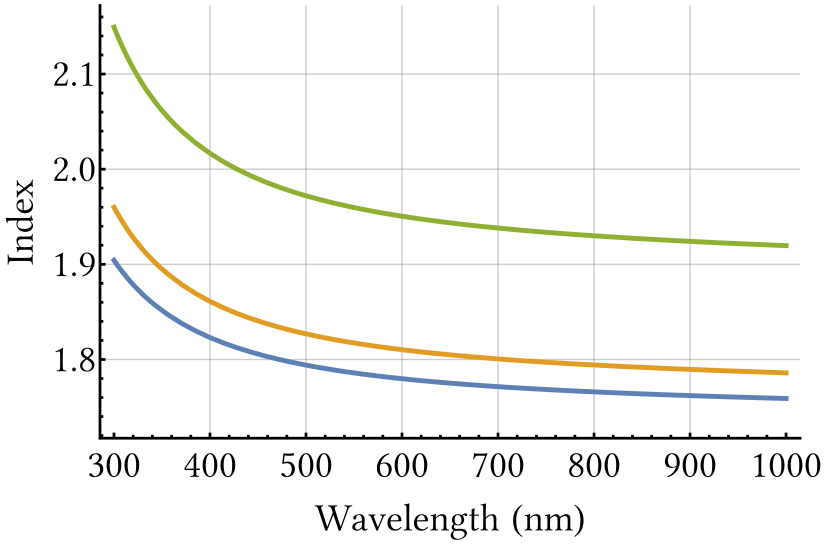

Figure B.1: n_x (blue), n_y (yellow), n_z (green) of BiBO. The values from 300nm to 474nm were extrapolated with the Sellmeier's coefficients.

where linearly polarized light can propagate while seeing refractive indices n_1 and n_2. This linearly polarized light may still undergo some walkoff ρ as it propagates. The walkoff is defined as the angle between the direction of propagation $\mathbf{k}$ and the direction of energy determined by the Poynting vector $\mathbf{\Pi}$ that always remains normal to the surface of $\mathscr{E}$.

For historical reasons, the phase-matching angles θ and ϕ that describe the rotation of the ellipsoid of indices with respect to its axes is described with geographical spherical coordinates. The coordinate system is then left-handed, ϕ is the azimuthal angle (from the xz plane to the yz plane) and θ is the elevation (from y to z) as shown on figure (this figure is missing). A refractive index $n(\lambda, \phi, \theta)$ in this system of coordinates is determined by the ellipsoid of indices through:

$$n^{-1}(\lambda, \phi, \theta) = \sqrt{\frac{\cos^2(\theta)\cos^2(\phi)}{n_x^2(\lambda)} + \frac{\cos^2(\theta)\sin^2(\phi)}{n_y^2(\lambda)} + \frac{\sin^2(\theta)}{n_z^2(\lambda)}} \tag{B.1}$$

B.2 Non-linear optics in BiBO

According to [Ghotbi 04a], BiBO can phase-match Type I ($e + e \rightarrow o$) processes with $\phi = 90^\circ$ and θ varying depending on the fundamental wavelength. It means that the fundamental waves propagates in the yz plane and the x axis is one of the main axes of the ellipse E. The two possible linear polarization are thus either on the x axis or perpendicular to it. In the Type I ($e + e \rightarrow o$) configuration, the fundamental light is polarized in the yz plane and the harmonic is polarized along x. The phase-matching index n_e for the fundamental light can be found by a rotation of the ellipsoid of indices along the x axis by taking $\phi = 90°$ in expression (B.1):

$$n_e(\lambda,\theta)^{-1} = \sqrt{\frac{\cos^2(\theta)}{n_y^2(\lambda)} + \frac{\sin^2(\theta)}{n_z^2(\lambda)}}^{-1} \tag{B.2}$$

It is then easy to model all the parametric processes described in this thesis, namely SHG, PDC and SFG through the definition of phase-matching Δk as a combination of the different wave vectors involved. The phase-matching function Φ obtained after integration on the crystal length l_c in the direction of propagation will always be:

$$\Phi(\Delta k) = \operatorname{sinc}(\Delta k\ l_c/2) \tag{B.3}$$

B.2.1 SHG in BiBO

In the case of SHG, two photons around the fundamental wavelength coming from the same beam “merge” to give birth to an harmonic photon. The optical configuration is inherently colinear and the phase-matching condition $\Delta k = 0$ is given by:

$$\Delta k(\omega_f, \omega_h) = 2k_f(\omega_f) - k_h(\omega_h) \tag{B.4}$$

where f stands for fundamental and h stands for harmonic. The wave vectors k_f and k_h are:

$$k_f(\omega_f) = \omega_f n_f(\omega_f)/c \quad \text{and} \quad k_h(\omega_h) = \omega_h n_h(\omega_h)/c \tag{B.5}$$

In BiBO, the harmonic refractive index is $n_h = n_x$. The refractive index of the fundamental wave is $n_f = n_e$. The angle θ is found through the phase matching condition for $\omega_f = \omega_0$ and $\omega_h = 2\omega_0$ so that $n_e(\omega_0, \theta) = n_x(2\omega_0)$. Given that initial spectrum presented on figure 2.1 is centered at $\lambda = 795$nm the phase-matching condition leads to $\theta = 150.81°$.

B.2.2 PDC in BiBO

In PDC, a pump photon at the harmonic frequency is “split” into two photons at the fundamental wave frequency. In this thesis, the only PDC we are interested in takes place in a colinear degenerate configuration (see chapter 2). Hence the phase-matching condition $\Delta k = 0$ is similar to (B.4). We introduce a difference between both fundamental waves as signal s and idler i:

$$\Delta k(\omega_s, \omega_i, \omega_p) = k_s(\omega_s) + k_i(\omega_i) - k_p(\omega_p) \tag{B.6}$$

where k_p and ω_p are the wave vector and optical frequency of the pump. The wave vectors k_s, k_i and k_p are:

$$k_s(\omega_s) = \omega_s n_s(\omega_s)/c \quad \text{and} \quad k_i(\omega_i) = \omega_i n_i(\omega_i)/c \quad \text{and} \quad k_p(\omega_p) = \omega_p n_p(\omega_p)/c \tag{B.7}$$

where $n_p = n_x$ and $n_s = n_i = n_e$. The latter refractive index is found with the exact same condition than in SHG and leads to the same value of θ.

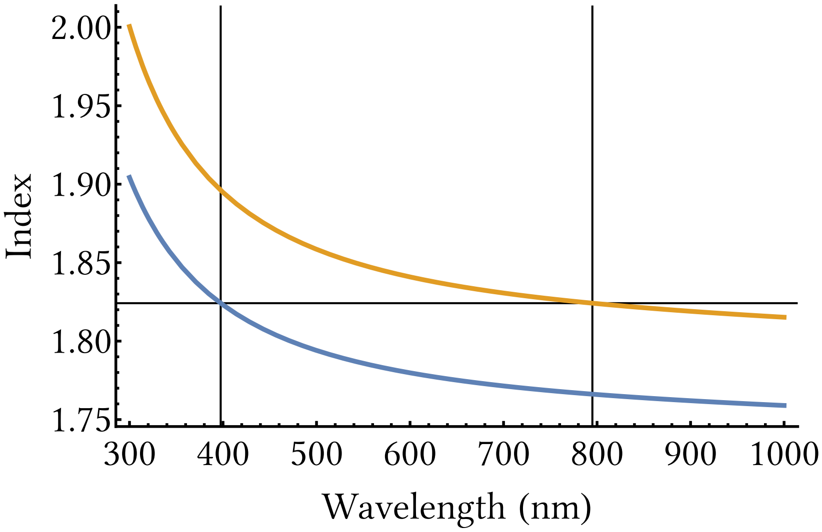

Figure B.2: n_x (blue), n_e (yellow) of BiBO. The horizontal solid black line indicate the index value where the phase-matching condition is fulfilled. The values from 300nm to 474nm were extrapolated with the Sellmeier's coefficients.

B.2.3 SFG in BiBO

In SFG, similarly to SHG, two photons around the fundamental wavelength coming from two different beams "merge" to give birth to an harmonic photon. This process can be non-colinear as detailed in chapter 5. The colinear phase-matching condition $\Delta k = 0$ is similar to (B.6) although we change the name of the photon at the harmonic frequency to *converted*. The critical phase-matching angle θ is found in the same manner. The exact value of this angle will change in a non-colinear configuration as some sine and cosine of the incident angles may appear.

B.3 Dispersion in BiBO

Like most materials, BiBO is dispersive. In ultrafast optics, the dispersion of a given material around a fundamental wavelength is often given in fs^2 assuming a Taylor development where terms above second-order are neglected. The dispersion ϕ''_{BiBO} through $l_c = 1$mm of BiBO can be computed from the Sellmeier's equations (see figure B.1) as:

$$\phi''_{BiBO} = \frac{\mathrm{d}^2\,(\mathrm{k}l_c)}{\mathrm{d}\omega^2} = \frac{l_c\lambda_0^3}{2\pi c^2}\,\frac{\mathrm{d}^2 n}{\mathrm{d}\lambda^2} \tag{B.8}$$

For $\lambda_0 = 795$nm and $n = n_e$, the dispersion ϕ''_{BiBO} is equal to 166fs^2.
For $\lambda_0 = 397.5$nm and $n = n_o$, the dispersion ϕ''_{BiBO} is equal to 480fs^2.

Appendix C

The fantasy of type II parametric interaction for QPG

As explained in chapter 5, it may be tempting to implement QPG by performing single-photon subtraction via weak parametric up-conversion in a non-linear medium set up for type II interaction. Let us consider an analytic treatment of collinear Sum-Frequency Generation (SFG).

We start from the photon-subtracted state $|\Psi^-\rangle$ of expression (5.19).

$$|\Psi^-\rangle \propto \int \mathrm{d}\omega_c\, \mathrm{d}\omega_s\; \alpha_g(\omega_c - \omega_s)\; \Phi_{SFG}\left(\Delta_k\right) \hat{a}_s\left(\omega_s\right) \hat{a}_c^{\dagger}\left(\omega_c\right) |\Psi_{in}\rangle \tag{C.1}$$

We approximate the phase-matching function Φ by a Gaussian function and we assume the parametric process to be phase-matched so that we keep only the first order of a Taylor development of the momenta:

$$\alpha_g(\omega_c - \omega_s) = \exp\left[-\Delta t^2 \left(\Omega_c - \Omega_s\right)^2\right] \quad \text{with} \quad \Delta t^2 = \frac{\lambda_0^4 2 \ln(2)}{4\pi^2 c^2 \mathrm{FWHM}^2} \tag{C.2}$$

$$\Phi_{SFG}\left(\Delta_k\right) = \exp\left[-\frac{\gamma l_c^2}{4}\left(\Omega_s\left(k_s' - k_g'\right) + \Omega_c\left(k_g' - k_c'\right)\right)^2\right] \tag{C.3}$$

$$\text{with} \quad k' = \frac{\partial k}{\partial \omega}(\omega_0) = 1/v_{\text{group}} \tag{C.4}$$

where $\gamma = 0.193$, and we have introduced k_s', k_g' and k_c' which are the inverse of the group velocities of each beam. We analyze the product $\alpha_g \Phi_{SFG}$ trying to obtain a single-mode operation by factorizing the expression so that Ω_c and Ω_s are not correlated.

C.1 Type I SFG

In Type I SFG, the single-mode interaction for SFG is achieved as we have $k_s' - k_g' = 0$. We just have to assume the pulse to be sufficiently short (or the crystal to be sufficiently long) so that $\Delta t^2 \left(\Omega_c - \Omega_s\right) \ll \gamma l_c^2 \Omega_c \left(k_g' - k_c'\right)^2 /4$ and the product $\alpha_g \Phi_{SFG}$ becomes factorized:

$$\alpha_g \Phi_{SFG}\left(\Omega_s, \Omega_c\right) = e^{-\Delta t^2 \Omega_s^2} e^{-\gamma l_c^2 \Omega_c^2 \left(k_g' - k_c'\right)/4} \tag{C.5}$$

The signal temporal mode is then only governed by the gate bandwidth and the up-converted temporal mode only depends on the mismatch of group velocities between the gate and the up-converted beam. The conversion process is then single-mode.

C.2 Type II SFG

In a Type II process, we no longer have $k_s' - k_g' = 0$. We take the example of BBO (barium borate BaB_2O_4) where it is possible to perform Type II SFG around our fundamental wavelength $\lambda_0 = 795$nm. Among the signal and gate beam, one must be ordinary and the other one extraordinary. We choose signal as extraordinary and the group velocities are respectively $v^s_{\text{group}} = 184\text{nm.fs}^{-1}$, $v^g_{\text{group}} = 178\text{nm.fs}^{-1}$ and $v^c_{\text{group}} = 175\text{nm.fs}^{-1}$. We assume a crystal length of 1mm, a gate pulse bandwidth of 6nm and we evaluate the values of each term in the exponential of the $\alpha_g \Phi_{SFG}$ product:

$$\Delta t^2 = 4.4 \times 10^3\ \text{fs}^2 \qquad \frac{\gamma l_c^2}{4}\left(k_s' - k_g'\right)^2 = 1.9 \times 10^3\ \text{fs}^2 \tag{C.6}$$

$$\frac{\gamma l_c^2}{4}\left(k_g' - k_c'\right)^2 = 3.1 \times 10^2\ \text{fs}^2 \qquad \frac{\gamma l_c^2}{2}\left(k_g' - k_c'\right)^2 = 1.5 \times 10^3\ \text{fs}^2 \tag{C.7}$$

Given the values of each term, none of them can be neglected even by increasing the crystal length or shortening the gate pulses. Switching the gate and signal beams would not help neither as the numerical values at play would not change enough to achieve a situation where the key terms can be dominating. As a consequence, it should be impossible to achieve single-mode a conversion process and therefore a single-mode single-photon subtraction.

The issue with Type II can be intuited directly from the phase-matching of the process as presented on figure C.1. On can directly see that it will not be possible to decorrelate the signal and up-converted frequencies contrary to figure 5.2 for instance.

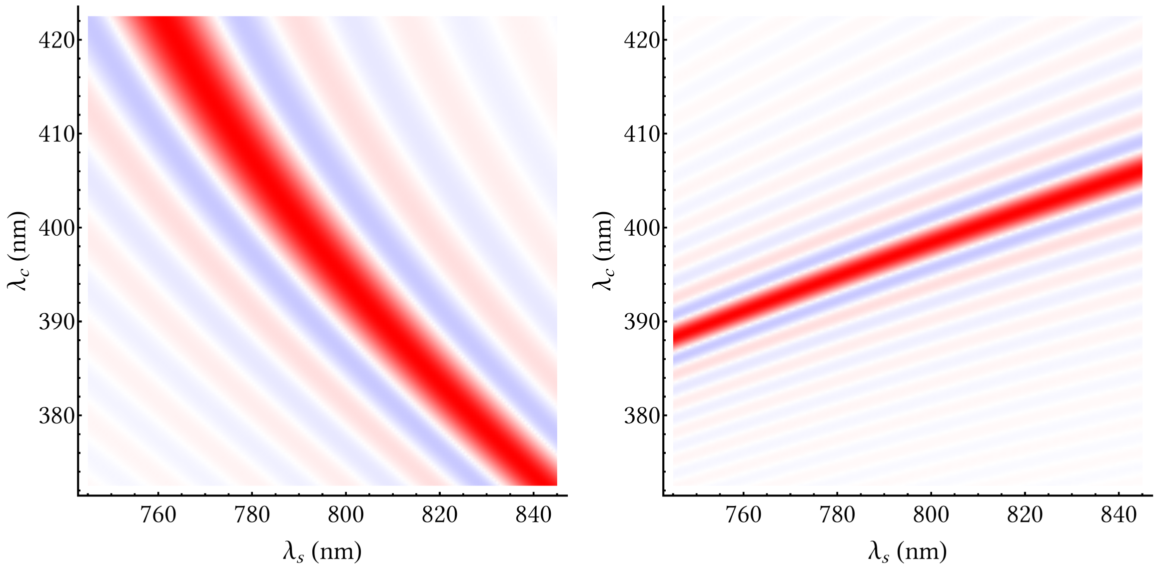

Figure C.1: Left: Phase-matching of a Type II SFG with signal as the extraordinary beam. Right: same than left but with gate as the extraordinary beam.

References

[Aasi 13]	Junaid Aasi, J Abadie, BP Abbott, Richard Abbott, TD Abbott, MR Abernathy, Carl Adams, Thomas Adams, Paolo Addesso, RX Adhikari*et al. Enhanced sensitivity of the LIGO gravitational wave detector by using squeezed states of light.* Nature Photonics, vol. 7, no. 8, pages 613–619, (Cited on page 3.)
[Akturk 10]	Selcuk Akturk, Xun Gu, Pamela Bowlan & Rick Trebino. *Spatio-temporal couplings in ultrashort laser pulses.* Journal of Optics, vol. 12, no. 9, page 093001, 2010. Online URL. (Cited on page 87.)
[Anderson 33]	Carl D Anderson. *The positive electron.* Physical Review, vol. 43, no. 6, page 491, (Cited on page 2.)
[Ansari 16]	Vahid Ansari, Markus Allgaier, Linda Sansoni, Benjamin Brecht, Jonathan Roslund, Nicolas Treps, Georg Harder & Christine Silberhorn. *Temporal-mode tomography of single photons.* arXiv preprint arXiv:1607.03001, (Cited on page 136.)
[Arvind 95]	Arvind, B. Dutta, N. Mukunda & R. Simon. *The real symplectic groups in quantum mechanics and optics.* Pramana, vol. 45, no. 6, pages 471–497, 1995. Online URL. (Cited on page 21.)
[Asaki 93]	M. T. Asaki, Chung-Po Huang, Dennis Garvey, Jianping Zhou, Henry C Kapteyn & Margaret M Murnane. *Generation of 11-fs pulses from a self-mode-locked Ti: sapphire laser.* Optics letters, vol. 18, no. 12, pages 977–979, (Cited on page 25.)
[Averchenko 11]	V. a. Averchenko, Y. M. Golubev, C. Fabre & N. Treps. *Quantum correlations and fluctuations in the pulsed light produced by a synchronously pumped optical parametric oscillator below its oscillation threshold.* European Physical Journal D, vol. 61, pages 207–214, (Cited on page 35.)

[Averchenko 14] V. Averchenko, V. Thiel & N. Treps. *Nonlinear photon subtraction from a multimode quantum field.* Physical Review A, vol. 89, no. 6, page 063808, June 2014. Online URL. (Cited on pages 15, 67, 75, 77, 84, 87, 89, and 96.)

[Averchenko 16] V. Averchenko, C. Jacquard, V. Thiel, Fabre C. & Treps N. *Multimode theory of single-photon subtraction.* New Journal of Physics, vol. 18, no. 8, page 083042, 2016. Online URL. (Cited on pages 16 and 66.)

[Back 96] Thomas Back. Evolutionary algorithms in theory and practice: evolution strategies, evolutionary programming, genetic algorithms. Oxford university press, 1996. (Cited on page 122.)

[Barnett 98] S. Barnett, L. Phillips & D. Pegg. *Imperfect photodetection as projection onto mixed states.* Optics communications, no. December, pages 45–49, 1998. Online URL. (Cited on page 77.)

[Barnett 09] Stephen M. Barnett. Quantum information. 2009. (Cited on page 66.)

[Baune 15] Christoph Baune, Jan Gniesmer, Axel Schönbeck, Christina E Vollmer, Jaromir Fiurasek & Roman Schnabel. *Strongly squeezed states at 532 nm based on frequency up-conversion.* Optics Express, vol. 23, no. 12, pages 16035–16041, 2015. Online URL. (Cited on page 3.)

[Braunstein 05] S. Braunstein. *Squeezing as an irreducible resource.* Physical Review A, vol. 71, no. 5, page 055801, may 2005. Online URL. (Cited on page 21.)

[Brecht 14a] Benjamin Brecht. *Engineering Ultrafast Quantum Frequency Conversion.* PhD thesis, Der Naturwissenschaftlichen Fakultät Paderborn, 2014. (Cited on pages 8 and 90.)

[Brecht 14b] Benjamin Brecht, Andreas Eckstein, Raimund Ricken, Viktor Quiring, Hubertus Suche, Linda Sansoni & Christine Silberhorn. *Demonstration of coherent time-frequency Schmidt mode selection using dispersion-engineered frequency conversion.* Physical Review A, vol. 90, no. 3, page 030302, sep 2014. Online URL. (Cited on page 77.)

[Cahill 69] K. E. Cahill & R. J. Glauber. *Density operators and quasiprobability distributions.* Physical Review, vol. 177, no. 5, page 1882, (Cited on page 13.)

[Cai 15] Yin Cai. *Quantum Coherent Control with an Optical Frequency Comb*. PhD thesis, ENS, 2015. (Cited on pages 34, 53, and 61.)

[Cai 16] Y. Cai, J. Roslund, G. Ferrini, F. Arzani, X. Xu, C. Fabre & N. Treps. *Reconfigurable Optical Quantum Networks Using Multimode Quantum Frequency Combs and Pulse Shaping*. arXiv preprint quant-ph/1605.02303, (Cited on page 61.)

[Caspani 10] L. Caspani, E. Brambilla & A. Gatti. *Tailoring the spatiotemporal structure of biphoton entanglement in type-I parametric down-conversion*. Phys. Rev. A, vol. 81, page 033808, Mar 2010. Online URL. (Cited on pages 87, 88, and 89.)

[Chambers 98] Lance D Chambers. Practical handbook of genetic algorithms: complex coding systems, volume 3. CRC press, 1998. (Cited on page 122.)

[Chen 14] Moran Chen, Nicolas C. Menicucci & Olivier Pfister. *Experimental realization of multipartite entanglement of 60 modes of a quantum optical frequency comb*. Physical Review Letters, vol. 112, no. 12, page 120505, 2014. Online URL. (Cited on page 3.)

[Chua 14] S S Y Chua, B J J Slagmolen, D A Shaddock & D E McClelland. *Quantum squeezed light in gravitational-wave detectors*. Classical and Quantum Gravity, vol. 31, no. 18, page 183001, 2014. Online URL. (Cited on page 11.)

[Chuang 97] Isaac L Chuang & M A Nielsen. *Prescription for experimental determination of the dynamics of a quantum black box*. Journal of Modern Optics, vol. 4412, no. 11, pages 2455–2467, 1997. Online URL. (Cited on page 108.)

[Cooper 13] Merlin Cooper, Christoph Söller & Brian J. Smith. *High-stability time-domain balanced homodyne detector for ultrafast optical pulse applications*. Journal of Modern Optics, vol. 60, no. 8, pages 611–616, 2013. Online URL. (Cited on page 43.)

[Cooper 15] Merlin Cooper, Eirion Slade, Michal Karpiński & Brian J Smith. *Characterization of conditional state-engineering quantum processes by coherent state quantum process tomography*. New Journal of Physics, vol. 17, no. 3, page 033041, 2015. Online URL. (Cited on page 110.)

[Dakna 97]	M. Dakna, T. Anhut, T. Opatrný, L. Knöll & D. G. Welsch. *Generating Schrödinger-cat-like states by means of conditional measurements on a beam splitter.* Physical Review A, vol. 55, no. 4, pages 3184–3194, 1997. Online URL. (Cited on pages 67 and 75.)
[Eckstein 11]	Andreas Eckstein, Benjamin Brecht & Christine Silberhorn. *A quantum pulse gate based on spectrally engineered sum frequency generation.* Optics express, vol. 19, no. 15, pages 13770–8, jul 2011. Online URL. (Cited on pages 4, 66, 77, and 84.)
[Eckstein 12]	Andreas Eckstein. *Mastering quantum light pulses with nonlinear waveguide interactions.* PhD thesis, Friedrich-Alexander-Universität Erlangen-Nürnberg, 2012. (Cited on page 36.)
[Ekert 95]	A. Ekert & P. Knight. *Entangled quantum systems and the Schmidt decomposition.* American Journal of Physics, vol. 63, no. 5, page 415, 1995. Online URL. (Cited on pages 15 and 88.)
[Fedorov 15]	Ilya a Fedorov, Aleksey K Fedorov, Yury V Kurochkin & a I Lvovsky. *Tomography of a multimode quantum black box.* New Journal of Physics, vol. 17, no. 4, page 043063, 2015. Online URL. (Cited on pages 110 and 121.)
[Ferraro 05]	Alessandro Ferraro, Stefano Olivares & Matteo G. A. Paris. *Gaussian states in continuous variable quantum information.* arXiv preprint quant-ph/0503237, (Cited on page 20.)
[Ferrini 13]	G Ferrini, J P Gazeau, T Coudreau, C Fabre & N Treps. *Compact Gaussian quantum computation by multi-pixel homodyne detection.* New Journal of Physics, vol. 15, no. 9, page 093015, sep 2013. Online URL. (Cited on page 61.)
[Furusawa 11]	Akira Furusawa & Peter Van Loock. Quantum teleportation and entanglement: a hybrid approach to optical quantum information processing. John Wiley & Sons, 2011. (Cited on pages 3 and 9.)
[Ghotbi 04a]	M. Ghotbi & M. Ebrahim-Zadeh. *Optical second harmonic generation properties of BiB3O6.* Optics Express, vol. 12, no. 24, pages 6002–6019, (Cited on pages 36, 143, and 144.)
[Ghotbi 04b]	M Ghotbi, M Ebrahim-Zadeh, A Majchrowski, E Michalski & I V Kityk. *High-average-power femtosecond pulse generation in the blue using BiB3O6.* Optics letters, vol. 29, no. 21, pages 2530–2, 2004. Online URL. (Cited on pages 33 and 143.)

[Ghotbi 06] M. Ghotbi, A. Esteban-Martin & M. Ebrahim-Zadeh. *BiB 3 O 6 femtosecond optical parametric oscillator.* Optics Letters, vol. 31, no. 21, page 3128, 2006. Online URL. (Cited on page 143.)

[Glauber 63] R. J. Glauber. *The quantum theory of optical coherence.* Physical Review, vol. 130, no. 6, page 2529, (Cited on pages 10 and 13.)

[Grangier 86] P. Grangier, G. Roger & A. Aspect. *Experimental Evidence for a Photon Anticorrelation Effect on a Beam Splitter: A New Light on Single-Photon Interferences.* EPL (Europhysics Letters), vol. 1, no. 4, page 173, 1986. Online URL. (Cited on page 2.)

[Grice 01] W. P. Grice, A. B. U'Ren & I. A. Walmsley. *Eliminating frequency and space-time correlations in multiphoton states.* Physical Review A. Atomic, Molecular, and Optical Physics, vol. 64, no. 6, pages 1–7, (Cited on pages 36 and 81.)

[Grynberg 10] Gilbert Grynberg, Alain Aspect & Claude Fabre. Introduction to quantum optics: from the semi-classical approach to quantized light. Cambridge University Press, 2010. (Cited on pages 8 and 40.)

[Gu 09] Mile Gu, Christian Weedbrook, Nicolas Menicucci, Timothy Ralph & Peter van Loock. *Quantum computing with continuous-variable clusters.* Physical Review A, vol. 79, no. 6, page 062318, jun 2009. Online URL. (Cited on page 61.)

[Hellwig 98] H Hellwig, J Liebertz & L. Bohatý. *Exceptional large nonlinear optical coefficients in the monoclinic bismuth borate BiB3O6 (BIBO).* Solid State Communications, vol. 109, no. 4, pages 249–251, (Cited on page 143.)

[Hellwig 00] H. Hellwig, J. Liebertz & L. Bohaty. *Linear optical properties of the monoclinic bismuth borate BiB 3 O 6.* Journal of Applied Physics, vol. 88, no. 1, pages 240–244, (Cited on page 143.)

[Heritage 85] JP Heritage, RN Thurston, WJ Tomlinson, AM Weiner & RH Stolen. *Spectral windowing of frequency-modulated optical pulses in a grating compressor.* Applied Physics Letters, vol. 47, no. 2, pages 87–89, (Cited on page 44.)

[Huang 13] YP Huang & Prem Kumar. *Mode-resolved photon counting via cascaded quantum frequency conversion.* Optics letters, vol. 38, no. 4, pages 468–470, 2013. Online URL. (Cited on page 4.)

[Hudson 74] Robin L Hudson. *When is the Wigner quasi-probability density non-negative?* Reports on Mathematical Physics, vol. 6, no. 2, pages 249–252, (Cited on page 20.)

[Husimi 40] K. Husimi. *Some formal properties of the density matrix.* Nippon Sugaku-Buturigakkwai Kizi Dai 3 Ki, vol. 22, no. 4, pages 264–314, (Cited on page 13.)

[James 01] Daniel F V James, Paul G Kwiat, William J Munro & Andrew G White. *Measurement of qubits.* Physical Review A, vol. 64, page 052312, 2001. Online URL. (Cited on pages 121, 122, and 123.)

[Jian 12] Pu Jian, Olivier Pinel, Claude Fabre, Brahim Lamine & Nicolas Treps. *Real-time displacement measurement immune from atmospheric parameters using optical frequency combs.* Opt. Express, vol. 20, no. 24, pages 27133–27146, Nov 2012. Online URL. (Cited on page 32.)

[Jiang 12] S. Jiang, N. Treps & C. Fabre. *A time/frequency quantum analysis of the light generated by synchronously pumped optical parametric oscillators.* New Journal of Physics, vol. 14, no. 4, page 043006, apr 2012. Online URL. (Cited on pages 35 and 38.)

[Jiang 16] Xin Jiang, Nicolas Y Joly, Martin A Finger, Fehim Babic, Meng Pang, Rafal Sopalla, Michael H Frosz, Samuel Poulain, Marcel Poulain, Vincent Cardin*et al. Supercontinuum generation in ZBLAN glass photonic crystal fiber with six nanobore cores.* Optics Letters, vol. 41, no. 18, pages 4245–4248, (Cited on page 136.)

[Jozsa 94] R. Jozsa. *Fidelity for Mixed Quantum States.* Journal of Modern Optics, vol. 41, no. 12, pages 2315–2323, December 1994. Online URL. (Cited on page 75.)

[Kolobov 99] M. Kolobov. *The spatial behavior of nonclassical light.* Reviews of Modern Physics, vol. 71, no. 5, pages 1539–1589, (Cited on pages 14 and 85.)

[Kurochkin 14] Y. Kurochkin, A. S. Prasad & A. I. Lvovsky. *Distillation of The Two-Mode Squeezed State.* Physical Review Letters, vol. 112, no. 7, page 070402, February 2014. Online URL. (Cited on page 73.)

[Law 00] CK Law, IA Walmsley & JH Eberly. *Continuous frequency entanglement: effective finite Hilbert space and entropy control.* Physical Review Letters, no. 3, pages 3–6, 2000. Online URL. (Cited on page 77.)

[Leonhardt 97] Ulf Leonhardt. Measuring the quantum state of light, volume 22. Cambridge university press, 1997. (Cited on page 13.)

[Lepetit 95] L. Lepetit, G. Chériaux & M. Joffre. *Linear techniques of phase measurement by femtosecond spectral interferometry for applications in spectroscopy.* Journal of the Optical Society of America B, vol. 12, no. 12, page 2467, (Cited on pages 53 and 55.)

[Lloyd 99] S. Lloyd & S. Braunstein. *Quantum computation over continuous variables.* Physical Review Letters, vol. 82, no. 8, pages 1784–1787, (Cited on page 9.)

[Lobino 08] Mirko Lobino, Dmitry Korystov, Connor Kupchak, Eden Figueroa, Barry C Sanders & a I Lvovsky. *Complete Characterization of Quantum-Optical Processes.* Science, vol. 322, no. 5901, pages 563–566, 2008. Online URL. (Cited on page 109.)

[Medeiros de Araujo 12] Renné Medeiros de Araujo. *Génération et manipulation de peignes de fréquences quantiques multimodes.* PhD thesis, UPMC, 2012. (Cited on pages 30, 35, 36, 37, 38, and 53.)

[Medeiros de Araújo 14] R. Medeiros de Araújo, J. Roslund, Y. Cai, G. Ferrini, C. Fabre & N. Treps. *Full characterization of a highly multimode entangled state embedded in an optical frequency comb using pulse shaping.* Physical Review A, vol. 89, no. 5, page 053828, may 2014. Online URL. (Cited on pages 56, 59, and 73.)

[Mehmet 10] Moritz Mehmet, Henning Vahlbruch, Nico Lastzka, Karsten Danzmann & Roman Schnabel. *Observation of squeezed states with strong photon-number oscillations.* Physical Review A - Atomic, Molecular, and Optical Physics, vol. 81, no. 1, pages 1–7, (Cited on page 3.)

[Mehmet 11] Moritz Mehmet, Stefan Ast, Tobias Eberle, Sebastian Steinlechner, Henning Vahlbruch & Roman Schnabel. *Squeezed light at 1550 nm with a quantum noise reduction of 123 dB.* Optics Express, vol. 19, no. 25, page 25763, (Cited on page 3.)

[Menicucci 06] Nicolas Menicucci, Peter van Loock, Mile Gu, Christian Weedbrook, Timothy Ralph & Michael Nielsen. *Universal Quantum*

Computation with Continuous-Variable Cluster States. Physical Review Letters, vol. 97, no. 11, page 110501, sep 2006. Online URL. (Cited on page 61.)

[Merli 76]	Pier Giorgio Merli, GianFranco Missiroli & Giulio Pozzi. *On the statistical aspect of electron interference phenomena*. Am. J. Phys, vol. 44, no. 3, pages 306–307, (Cited on page 2.)
[Michelson 94a]	Albert-A Michelson. *Les méthodes interférentielles en métrologie et l'établissement d'une longueur d'onde comme unité absolue de longueur*. J. Phys. Theor. Appl., vol. 3, no. 1, pages 5–22, (Cited on page 2.)
[Michelson 94b]	Albert Abraham Michelson. On the application of interference methods to astronomical measurements, volume 5. National Academy of Sciences, 1894. (Cited on page 1.)
[Monmayrant 10]	Antoine Monmayrant, Sébastien Weber & Béatrice Chatel. *A newcomer's guide to ultrashort pulse shaping and characterization*. Journal of Physics B: Atomic, Molecular and Optical Physics, vol. 43, no. 10, page 103001, (Cited on page 44.)
[Morgner 99]	U. Morgner, F. X. Kärtner, S. Cho, Y. Chen, H. A. Haus, J. G. Fujimoto, E. P. Ippen, V. Scheuer, G. Angelow & T. Tschudi. *Sub-two-cycle pulses from a Kerr-lens mode-locked Ti: sapphire laser*. Optics Letters, vol. 24, no. 6, pages 411–413, (Cited on page 25.)
[Morin 13]	Olivier Morin, Claude Fabre & Julien Laurat. *Experimentally accessing the optimal temporal mode of traveling quantum light states*. Physical Review Letters, vol. 111, no. November, pages 1–5, (Cited on page 136.)
[Morin 14a]	Olivier Morin. *Non-Gaussian States and Measurements for Quantum Information*. PhD thesis, UPMC, 2014. (Cited on pages 8, 12, 13, and 27.)
[Morin 14b]	Olivier Morin, Kun Huang, Jianli Liu, Hanna Le Jeannic, Claude Fabre & Julien Laurat. *Remote creation of hybrid entanglement between particle-like and wave-like optical qubits*. Nature Photonics, vol. 8, no. 7, pages 570–574, 2014. Online URL. (Cited on page 3.)
[Mosley 08]	Peter J. Mosley, Jeff S. Lundeen, Brian J. Smith, Piotr Wasylczyk, Alfred B. U'Ren, Christine Silberhorn & Ian A. Walmsley. *Heralded generation of ultrafast single photons in pure quantum states*.

Physical Review Letters, vol. 100, no. 13, pages 1–4, (Cited on pages 36 and 90.)

[Nielsen 07] Anne Nielsen & Klaus Mølmer. *Single-photon-state generation from a continuous-wave nondegenerate optical parametric oscillator.* Physical Review A, vol. 75, no. 2, page 023806, feb 2007. Online URL. (Cited on page 3.)

[O'Brien 09] Jeremy L O'Brien, Akira Furusawa & Jelena Vuckovic. *Photonic quantum technologies.* Nature Photonics, vol. 3, no. 12, pages 687–695, (Cited on page 2.)

[Ourjoumtsev 07a] A. Ourjoumtsev, A. Dantan, R. Tualle-Brouri & P. Grangier. *Increasing Entanglement between Gaussian States by Coherent Photon Subtraction.* Physical Review Letters, vol. 98, no. 3, page 030502, January 2007. Online URL. (Cited on pages 3, 71, and 73.)

[Ourjoumtsev 07b] Aexandre Ourjoumtsev. *Etude théorique et expérimentale de superpositions quantiques cohérentes et d'états intriqués nongaussiens de la lumière.* PhD thesis, UPMC, 2007. (Cited on page 13.)

[Ourjoumtsev 09] Alexei Ourjoumtsev, Franck Ferreyrol, Rosa Tualle-Brouri & Philippe Grangier. *Preparation of non-local superpositions of quasi-classical light states.* Nature Physics, vol. 5, no. 3, pages 189–192, 2009. Online URL. (Cited on page 3.)

[Parigi 07] Valentina Parigi, Alessandro Zavatta, Myungshik Kim & Marco Bellini. *Probing quantum commutation rules by addition and subtraction of single photons to/from a light field.* Science (New York, N.Y.), vol. 317, no. 5846, pages 1890–3, sep 2007. Online URL. (Cited on page 3.)

[Patera 08] Giuseppe Patera. *Quantum properties of ultra-short pulses generated by SPOPOs: multi-mode squeezing and entanglement.* PhD thesis, UPMC & Università dell'Insubria, 2008. (Cited on page 35.)

[Pinel 12] O. Pinel, P. Jian, R. Medeiros De Araujo, J. Feng, B. Chalopin, C. Fabre & N. Treps. *Generation and characterization of multimode quantum frequency combs.* Physical Review Letters, vol. 108, no. 8, pages 22–26, (Cited on pages 38 and 43.)

[Pysher 11] Matthew Pysher, Yoshichika Miwa, Reihaneh Shahrokhshahi, Russell Bloomer & Olivier Pfister. *Parallel Generation of Quadripartite Cluster Entanglement in the Optical Frequency Comb.* Physical Review Letters, vol. 107, no. 3, page 030505, jul 2011. Online URL. (Cited on page 61.)

[Rapoport 88] W R Rapoport & Chandra P Khattak. *Titanium sapphire laser characteristics.* Applied Optics, vol. 27, no. 13, page 2677, 1988. Online URL. (Cited on page 25.)

[Raussendorf 01] Robert Raussendorf & Hans J. Briegel. *A One-Way Quantum Computer.* Phys. Rev. Lett., vol. 86, pages 5188–5191, May 2001. Online URL. (Cited on page 60.)

[Raussendorf 03] Robert Raussendorf, Daniel E Browne & Hans J Briegel. *Measurement-based quantum computation on cluster states.* Physical review A, vol. 68, no. 2, page 022312, (Cited on page 61.)

[Rohde 06] Peter P. Rohde & Timothy C. Ralph. *Modelling photo-detectors in quantum optics.* Journal of Modern Optics, vol. 53, no. 11, pages 1589–1603, July 2006. Online URL. (Cited on page 77.)

[Roslund 10] Jonathan Roslund. *Optimal quantum control in the laboratory.* PhD thesis, Princeton, 2010. (Cited on pages 123 and 124.)

[Roslund 13] Jonathan Roslund, Renné Medeiros de Araújo, Shifeng Jiang, Claude Fabre & Nicolas Treps. *Wavelength-multiplexed quantum networks with ultrafast frequency combs.* Nature Photonics, no. December, pages 1–4, dec 2013. Online URL. (Cited on pages 56 and 59.)

[Rozema 15] Lee A. Rozema, Chao Wang, Dylan H. Mahler, Alex Hayat, Aephraim M. Steinberg, John E. Sipe & Marco Liscidini. *Characterizing an entangled-photon source with classical detectors and measurements.* Optica, vol. 2, no. 5, pages 430–433, (Cited on page 136.)

[Sacks 01] Z. Sacks, G. Mourou & R. Danielius. *Adjusting pulse-front tilt and pulse duration by use of a single-shot autocorrelator.* Opt. Lett., vol. 26, no. 7, pages 462–464, Apr 2001. Online URL. (Cited on page 87.)

[Schmidt 07] Erhard Schmidt. *Zur Theorie der linearen und nichtlinearen Integralgleichungen.* Mathematische Annalen, vol. 63, no. 4, pages 433–476, 1907. Online URL. (Cited on page 15.)

[Simon 98] R Simon, S Chaturvedi & V Srinivasan. *Congruences and canonical forms for a positive matrix: Application to the Schweinler-Wigner extremum principle.* arXiv preprint math-ph/9811003, (Cited on page 22.)

[Slusher 87] R. E. Slusher, P. Grangier, A. Laporta, B. Yurke & M. J. Potasek. *Pulsed squeezed light.* Physical Review Letters, vol. 59, no. 22, pages 2566–2569, (Cited on page 11.)

[Somaschi 15] N. Somaschi, V. Giesz, L. De Santis, J. C. Loredo, M. P. Almeida, G. Hornecker, S. L. Portalupi, T. Grange, C. Anton, J. Demory, C. Gomez, I. Sagnes, N. D. Lanzillotti Kimura, A. Lemaitre, A. Auffeves, A. G. White, L. Lanco & P. Senellart. *Near optimal single photon sources in the solid state.* Nature Photonics, vol. 10, no. 2, pages 1–6, 2015. Online URL. (Cited on page 3.)

[Spence 91] David E Spence, P Np Kean & Wilson Sibbett. *60-fsec pulse generation from a self-mode-locked Ti: sapphire laser.* Optics letters, vol. 16, no. 1, pages 42–44, (Cited on pages 24 and 25.)

[Su 07] Xiaolong Su, Aihong Tan, Xiaojun Jia, Jing Zhang, Changde Xie & Kunchi Peng. *Experimental preparation of quadripartite cluster and Greenberger-Horne- Zeilinger entangled states for continuous variables.* Physical Review Letters, vol. 98, no. February, pages 2–5, (Cited on pages 3 and 61.)

[Su 13] Xiaolong Su, Shuhong Hao, Xiaowei Deng, Lingyu Ma, Meihong Wang, Xiaojun Jia, Changde Xie & Kunchi Peng. *Gate sequence for continuous variable one-way quantum computation.* Nature communications, vol. 4, page 2828, nov 2013. Online URL. (Cited on page 61.)

[Sutter 99] D. H. Sutter, G. Steinmeyer, L. Gallmann, N. Matuschek, F. Morier-Genoud, U. Keller, V. Scheuer, G. Angelow & T. Tschudi. *Semiconductor saturable-absorber mirror-assisted Kerr-lens mode-locked Ti : sapphire laser producing pulses in the two- cycle regime.* Optics Letters, vol. 24, no. 9, pages 631–633, (Cited on page 25.)

[Takahashi 08] Hiroki Takahashi, Kentaro Wakui, Shigenari Suzuki, Masahiro Takeoka, Kazuhiro Hayasaka, Akira Furusawa & Masahide Sasaki. *Generation of large-amplitude coherent-state superposition via ancilla-assisted photon subtraction.* Physical Review Letters, vol. 101, no. December, pages 16–19, (Cited on page 3.)

[Takahashi 09] Hiroki Takahashi, Jonas S. Neergaard-Nielsen, Makoto Takeuchi, Masahiro Takeoka, Kazuhiro Hayasaka, Akira Furusawa & Masahide Sasaki. *Entanglement distillation from Gaussian input*

	states. Nature Photonics, vol. 4, no. 3, page 8, jul 2009. Online URL. (Cited on page 3.)
[Takahashi 10]	H. Takahashi, J. S. Neergaard-Nielsen, M. Takeuchi, M. Takeoka, K. Hayasaka, A. Furusawa & M. Sasaki. *Entanglement distillation from Gaussian input states*. Nature Photonics, vol. 4, no. February, page 8, 2010. Online URL. (Cited on page 73.)
[Taylor 09]	Geoffrey Ingram Taylor. *Interference fringes with feeble light*. In Proceedings of the Cambridge Philosophical Society, volume 15, pages 114–115, 1909. (Cited on page 2.)
[Thiel 15]	Valérian Thiel. *Modal Analysis of an Ultrafast Frequency Comb*. PhD thesis, UPMC, 2015. (Cited on pages 8, 17, 26, and 32.)
[Townsend 14]	Alex Townsend & Lloyd N. Trefethen. *Continuous analogues of matrix factorizations*. Proceedings of the Royal Society of London A: Mathematical, Physical and Engineering Sciences, vol. 471, no. 2173, 2014. Online URL. (Cited on page 15.)
[Trebino 93]	Rick Trebino & Daniel J. Kane. *Using phase retrieval to measure the intensity and phase of ultrashort pulses: frequency-resolved optical gating*. J. Opt. Soc. Am. A, vol. 10, no. 5, pages 1101–1111, May 1993. Online URL. (Cited on page 53.)
[Trebino 02]	Rick Trebino. Frequency-resolved optical gating: the measurement of ultrashort laser pulses. Springer Science, 2002. (Cited on pages 53 and 87.)
[Treps 05]	N. Treps, V. Delaubert, a. Maître, J. Courty & C. Fabre. *Quantum noise in multipixel image processing*. Physical Review A, vol. 71, no. 1, page 013820, jan 2005. Online URL. (Cited on page 14.)
[Tualle-Brouri 09]	Rosa Tualle-Brouri, Alexei Ourjoumtsev, Aurelien Dantan, Philippe Grangier, Martijn Wubs & Anders Sorensen. *Multimode model for projective photon-counting measurements*. Physical Review A, vol. 80, no. 1, page 013806, July 2009. Online URL. (Cited on pages 67 and 77.)
[Umemura 07]	Nobuhiro Umemura, Kentaro Miyata & Kiyoshi Kato. *New data on the optical properties of BiB3O6*. Optical Materials, vol. 30, no. 4, pages 532–534, (Cited on page 143.)

[Vahlbruch 16] Henning Vahlbruch, Moritz Mehmet, Karsten Danzmann & Roman Schnabel. *Detection of 15 dB Squeezed States of Light and their Application for the Absolute Calibration of Photoelectric Quantum Efficiency.* Physical Review Letters, vol. 117, no. 11, page 110801, 2016. Online URL. (Cited on pages 3, 11, and 24.)

[Valencia 07] Alejandra Valencia, Alessandro Ceré, Xiaojuan Shi, Gabriel Molina-Terriza & Juan P. Torres. *Shaping the Waveform of Entangled Photons.* Phys. Rev. Lett., vol. 99, page 243601, Dec 2007. Online URL. (Cited on page 96.)

[Van Loock 07] Peter Van Loock, Christian Weedbrook & Mile Gu. *Building Gaussian cluster states by linear optics.* Physical Review A - Atomic, Molecular, and Optical Physics, vol. 76, no. 3, pages 1–8, (Cited on page 61.)

[Vaughan 05] Joshua C Vaughan, Thomas Hornung, T Feurer & Keith a Nelson. *Diffraction-based femtosecond pulse shaping with a two-dimensional spatial light modulator.* Optics letters, vol. 30, no. 3, pages 323–325, (Cited on pages 45, 46, and 47.)

[Vogel 06] Werner Vogel & Dirk-Gunnar Welsch. Quantum optics. John Wiley & Sons, 2006. (Cited on pages 8, 11, and 13.)

[Walls 08] D.F. Walls & Gerard J. Millburn. Quantum Optics 2nd Edition. 2008. (Cited on pages 8, 11, and 13.)

[Weedbrook 12] C. Weedbrook, S. Pirandola, R. García-Patrón, N. J. Cerf, T. C. Ralph, J. H. Shapiro & S. Lloyd. *Gaussian quantum information.* Reviews of Modern Physics, vol. 84, no. 2, pages 621–669, (Cited on pages 22 and 59.)

[Wefers 95] Marc M Wefers & Keith A Nelson. *Analysis of programmable ultrashort waveform generation using liquid-crystal spatial light modulators.* Journal of the Optical Society of America B, vol. 12, no. 7, page 1343, (Cited on page 47.)

[Weiner 88] AM Weiner, JP Heritage & EM Kirschner. *High-resolution femtosecond pulse shaping.* JOSA B, vol. 5, no. 8, 1988. Online URL. (Cited on page 44.)

[Weiner 92] Andrew M. Weiner, Daniel E. Leaird, J S Patel & John R. Wullert. *Programmable Shaping of Femtosecond Optical Pulses by Use of 128-*

Element Liquid Crystal Phase Modulator. IEEE Journal of Quantum Electronics, vol. 28, no. 4, pages 908–920, (Cited on page 47.)

[Weiner 00] A. M. Weiner. *Femtosecond pulse shaping using spatial light modulators.* Review of Scientific Instruments, vol. 71, no. 5, page 1929, 2000. Online URL. (Cited on page 44.)

[Weiner 11a] A.M. Weiner. *Ultrafast optical pulse shaping: A tutorial review.* Optics Communications, vol. 284, no. 15, pages 3669–3692, 2011. Online URL. (Cited on page 44.)

[Weiner 11b] Andrew M. Weiner. Ultrafast optics, volume 72. John Wiley & Sons, 2011. (Cited on pages 24, 26, 44, 53, 55, and 101.)

[Wenger 04] Jérôme Wenger, Rosa Tualle-Brouri & Philippe Grangier. *Non-Gaussian Statistics from Individual Pulses of Squeezed Light.* Physical Review Letters, vol. 92, no. 15, page 153601, apr 2004. Online URL. (Cited on page 75.)

[Wigner 32] E. Wigner. *On the quantum correction for thermodynamic equilibrium.* Physical review, vol. 40, no. 5, page 749, (Cited on page 13.)

[Wright 15] Laura J. Wright. *Quantum Pulse Shaping by Direct Temporal Phase Modulation.* PhD thesis, University of Oxford, 2015. (Cited on page 44.)

[Wu 86] Ling An Wu, H. J. Kimble, J. L. Hall & Huifa Wu. *Generation of squeezed states by parametric down conversion.* Physical Review Letters, vol. 57, no. 20, pages 2520–2523, (Cited on page 11.)

[Yariv 89] A. Yariv. Quantum electronics. Wiley, 1989. (Cited on page 31.)

[Yokoyama 13] S. Yokoyama, R. Ukai, S. C. Armstrong, C. Sornphiphatphong, T. Kaji, S. Suzuki, J. Yoshikawa, H. Yonezawa, N. C. Menicucci & A. Furusawa. *Ultra-large-scale continuous-variable cluster states multiplexed in the time domain.* Nature Photonics, vol. 7, no. 12, pages 982–986, November 2013. Online URL. (Cited on page 73.)

[Yoshikawa 13] Jun-ichi Yoshikawa, Kenzo Makino, Shintaro Kurata, Peter van Loock & Akira Furusawa. *Creation, Storage, and On-Demand Release of Optical Quantum States with a Negative Wigner Function.* Physical Review X, vol. 3, no. 4, page 041028, dec 2013. Online URL. (Cited on page 3.)

[Yukawa 08] Mitsuyoshi Yukawa, Ryuji Ukai, Peter van Loock & Akira Furusawa. *Experimental generation of four-mode continuous-variable cluster states.* Physical Review A, vol. 78, no. 1, page 012301, jul 2008. Online URL. (Cited on page 3.)

[Yukawa 13] Mitsuyoshi Yukawa, Kazunori Miyata, Takahiro Mizuta, Hidehiro Yonezawa, Petr Marek, Radim Filip & Akira Furusawa. *Generating superposition of up-to three photons for continuous variable quantum information processing.* Optics Express, vol. 21, no. 5, page 5, 2013. Online URL. (Cited on page 3.)

[Zernike 73] Frits Zernike & John E. Midwinter. Applied nonlinear optics. John Wiley & Sons, 1973. (Cited on page 143.)